School of Physical Sciences
Department of Exploration Geophysics

DEVELOPMENT AND APPLICATION OF PROCESSING TECHNIQUES FOR SIGNAL ENHANCEMENT USING MULTISYSTEM RESISTIVITY MEASUREMENTS

Abolghasem Kamkar-Rouhani

"This thesis is presented as part of the requirements for
the award of the Degree of Doctor of Philosophy
of the
Curtin University of Technology"

November 1998

DEDICATION

To the memory of my late parents who loved me and supported me every second of their lives.

To my beloved sisters, brothers, and especially my dear wife, Zohreh.

ACKNOWLEDGEMENTS

I would like to thank all of those who have contributed in one way or another to my thesis. Many thanks go to my supervisor, Professor Norm Uren, for his guidance, encouragement, friendship, and very kind help in the final stages of completing my PhD thesis. I also wish to express my gratitude to my former supervisor, Associate Professor Umesh Das, who initiated and supervised this research thesis.

I am also thankful to all staff and graduate students in the Department of Exploration Geophysics for their assistance and friendship. I particularly thank Professor John McDonald, Mr. Paul Wilkes, Mr. Vern Wilson and Associate Professor Brian Evans for their help and fruitful suggestions. I am also grateful to Mr. Murray Hill and Mr. Levin Lee for their efforts in accessing computing facilities. I should also thank my fellow colleagues and PhD students, Mr. Brett Harris and Mr. Michael Sykes, whom I have had useful discussions during my PhD studies in the Department.

This thesis would not have been possible without the financial support provided by Iranian Ministry of Culture and Higher Education (MCHE) and Curtin University of Technology through MCHE, COSS and CISS scholarships and other support.

Finally, I would like to thank my wife, Zohreh, for her continuous support and patience through my studies.

ABSTRACT

DC electrical surveying involves the injection of current into the earth, and the measurement of the electrical potential differences this produces. A number of electrode configurations such as the Schlumberger and Wenner arrays, dipole-dipole and pole-pole geometries are in common use for electrical surveying. New acquisition systems enable the convenient collection of data with a number of common configurations at the same time. It is found however that while the recovery of layered structure from electrical surveys can be effective, the sensitivity and resolving power of such systems in detecting the presence of anomalous three-dimensional (3-D) bodies is poor. This is mainly due to the dominance of conduction pathways through the layered earth compared to the influence of small 3-D conductivity anomalies.

Theoretical relationships between the responses of various survey geometries to the layered earth may be established as is shown in this thesis, but their response to 3-D targets differs strongly. This thesis introduces a new procedure for anomalous target detection by the computation of an *apparent resistivity residual* using multi-electrode configuration survey data. This procedure, applicable to a variety of electrode geometries, reduces the dominance of the layered earth response and enhances the signal from 3-D structures.

In the development and testing of this new apparent resistivity residual, numerically modelled data were used. In order to obtain suitable test data of high accuracy it was necessary to make improvements to modelling software. For this purpose, recently developed techniques in numerical modelling such as the biconjugate gradient method, new digital linear filters for computation of Hankel transforms, and spectral formalism were employed in an integral equation approach for the software developed in this thesis.

The computed apparent resistivity residual was found to depend on the array type and dimensions, the nature of the anomalous zone, depth of the anomalous zone, geological layer geometries, and resistivity contrasts of the layers involved. While the apparent resistivity residual signature requires some measure of interpretation, it is shown to enhance the resolution and detectability of 3-D targets in a layered environment.

The presence of random noise produces some degradation in the performance of the residual technique, but a normalisation procedure has been developed to alleviate the problem. A preliminary field trial showed that survey profiles of apparent resistivity residual were able to locate a subsurface conductive anomaly in an area in Western Australia.

A transitional zone is defined as a layer in the earth where resistivity varies as a continuous function of depth. A theoretical formulation for the electrical response of an earth structure composed of anomalous 3-D bodies in the presence of transitional layers is introduced. Tests on synthetic survey data showed that the apparent resistivity residual is an effective anomaly detector in transitional layer environments.

A multisystem method of computing an apparent resistivity residual has been developed theoretically and tested on both synthetic and field data. This new approach when applied to resistivity profiling is more sensitive to, and gives greater resolution of, localised anomalies than is possible using conventional profiling procedures.

TABLE OF CONTENTS

LIST OF FIGURES

Chapter 1

INTRODUCTION

Geophysical methods are used for studying the structure and composition of the Earth's interior using measurements based on its physical properties. For example, gravity, magnetic and electrical surveys respond to density, magnetic susceptibility, and electrical conductivity of the subsurface and provide information about the nature of the concealed structures that could be useful for locating desired targets. Hence, geophysical methods can be used in exploration for minerals, hydrocarbons and other subsurface targets. Detection of these subsurface deposits depends on those contrasting physical characteristics, which differentiate them from the surrounding rocks. The choice of geophysical methods to locate a certain type of deposit is dependent on the nature of the deposit and of its host rock. A geophysical method may directly indicate the presence of the deposit, for example, magnetite may be detected by the magnetic method. In some other situations, these methods may give information that indicates whether or not conditions are favourable for the occurrence of the deposit, for example the use of the gravity or magnetic method in oil exploration to determine the depth to the basement rocks with high density or magnetic permeability.

Geophysical methods, based on the use of electric fields, include a large variety of techniques such as direct current (DC) resistivity, self-potential (SP), induced polarisation (IP), magnetotelluric (MT), ground penetrating radar (GPR), and electromagnetic (EM) methods. Among these, DC resistivity methods are often best for determining the distribution of electrical conductivity (or resistivity) of subsurface formations and also for detecting subsurface bodies which have high or relatively high electrical conductivity contrast with the surrounding media. This research work is directed at DC resistivity methods.

1.1 DC resistivity methods and their applications

DC resistivity methods have been widely used in subsurface geophysical exploration. They are also applied in geothermal and archaeological investigations as well as for engineering and environmental problems. The effective use of these methods began with the work of Schlumberger in 1912 (Ward, 1980; Kaufman and Keller, 1983; Zhdanov and Keller, 1994). DC resistivity methods are used to study lateral changes in resistivity for the location of faults, vertical contacts, contaminated zones, mineral deposits, geothermal, and archaeological investigations. They are also used to study vertical variations in resistivity for hydrological and civil engineering applications like bridge and dam site locations, particularly where horizontal stratification is expected. For groundwater exploration, DC resistivity methods appear to be almost the sole geophysical tool used.

DC resistivity methods have maintained their popularity even today as they use simple and inexpensive equipment. The methods commonly use a four-electrode system as shown in Figure 1.1. A direct or very low frequency alternating electric current is injected into the ground through one pair of electrodes (e.g. current electrodes A and B in Figure 1.1) and electric potential is measured with the second pair of electrodes (e.g. potential electrodes C and D in Figure 1.1). Then, apparent resistivity is computed on the assumption of a uniform earth. If inhomogeneities are present, they will affect the calculated apparent resistivity as electrode positions are changed.

Various configurations can be obtained by the selective placement of the current and potential electrodes (Figure 1.1). In a two-electrode (or pole-pole) configuration, only two electrodes, a current electrode A and a potential electrode M (Figure 1.1a), are actively used. The other current electrode B and the other potential electrode N are placed normal to the traverse line at large distances (at infinity, theoretically), so that they do not affect the measurements significantly. In the Wenner array, four electrodes are equally spaced along a straight line (Figure 1.1b). Thus, in the two-electrode and Wenner arrays the potential difference between two relatively widely

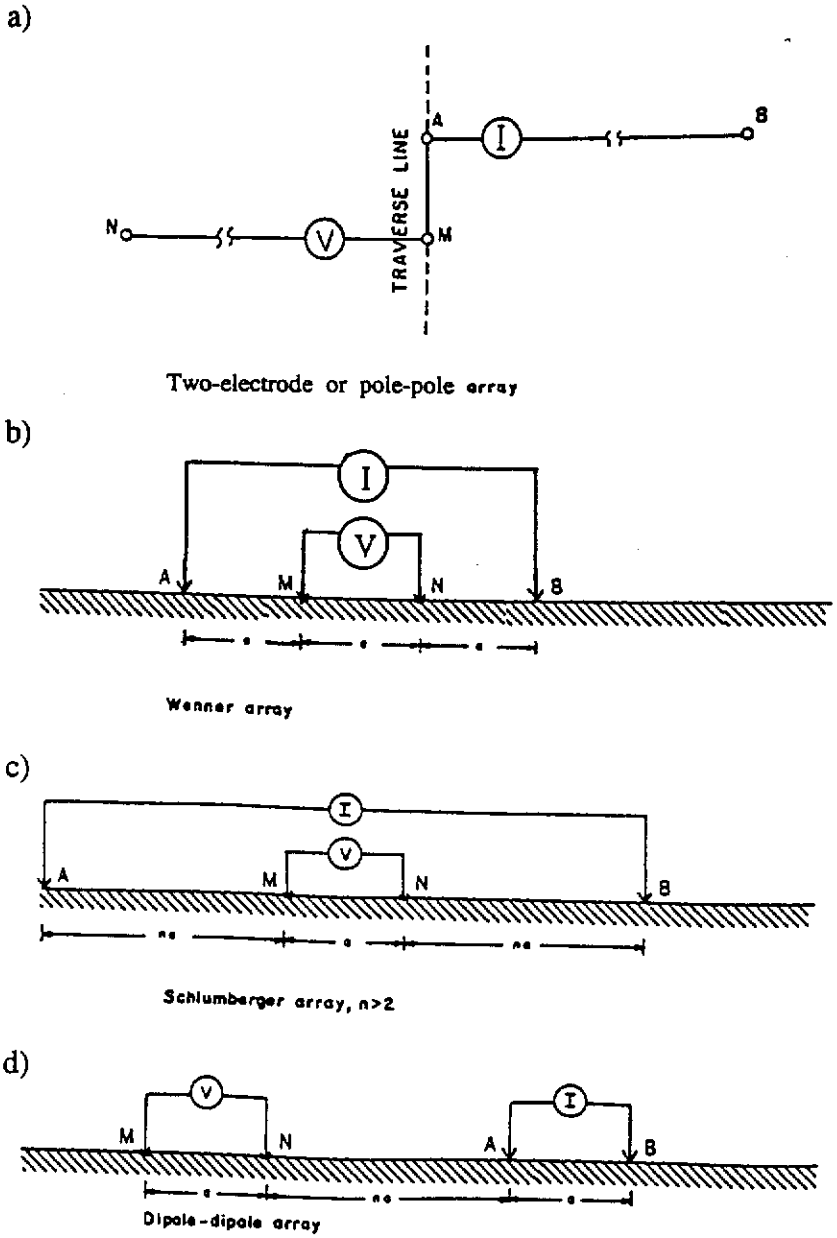

Figure 1.1. Common electrode arrays used in DC resistivity surveys: (a) two-electrode or pole-pole array (From Das and Verma, 1980), (b) Wenner array, (c) Schlumberger array, and (d) dipole-dipole array (From Sheriff, 1991).

spaced measuring electrodes is recorded. In the Schlumberger array (Figure 1.1c), two closely spaced potential measuring electrodes (M and N) are placed about the midpoint between the two current electrodes (A and B) and the system measures the potential gradient or electric field intensity at the centre of the array. In the dipole-dipole system (Figure 1.1d), the separations between the electrodes in the current electrode pair, and also between the electrodes in the potential electrode pair, are small in comparison with the distance between the pairs such that each of the two pairs of electrodes behave as dipoles. In the dipole-dipole configuration a measure of the curvature (second derivative) of the potential is recorded (Keller and Frischkecht, 1966; Koefoed, 1979a).

When these configurations are deployed over a uniform half-space, the resistivity of that half-space may be computed using the ratio of voltage to current measured with the array, together with a geometric factor specific to the array configuration. All configurations will give rise to the same computed result.

When the half-space consists of the layers with different resistivities, the current flow and the potentials produced vary with the electrode spacing, as well as with the nature of the electrode configuration. In the same way as for a uniform half-space, a resistivity may be computed. This quantity is termed apparent resistivity when the half-space is not uniform, and its value varies with the actual values of the electrode spacing.

An electrical resistivity sounding is a survey carried out by increasing electrode spacings in steps, keeping the array centred about a particular point. At each of the electrode spacings, an apparent resistivity is computed. The resistivity sounding is used to study variations of resistivity with depth. The results of the sounding are displayed as a plot of apparent resistivity against electrode spacing. The way in which the apparent resistivity varies with electrode spacing is diagnostic of the thickness and resistivities of the layers making up the half-space. These data may be inverted to obtain layer specifications consistent with the apparent resistivity sounding curve.

The shape of the sounding curve is basically similar for each of the arrays that might be used, and each may be inverted to recover possible subsurface layering structure. The curves, while similar, are not identical.

An electrical profiling technique is an alternative field procedure used for mapping resistivity variations along a survey line. In this technique to investigate a lateral variation of resistivity at some depth, a fixed electrode spacing, chosen on the basis of the nominal depth of investigation of an array, is maintained between various electrodes, and the array is moved as a whole along the traverse line (Mooney, 1980). Apparent resistivity for a fixed electrode spacing is plotted against distance along the line. Changes in the value of the computed apparent resistivity are indicative of lateral variation along the line, and thus, the resistivity measurements made by the profiling method can be used to locate the boundaries of an anomalous conductive or resistive body. In the profiling method, the nature of resistivity variations along a line is very dependent on the array dimensions, array type, layers specifications, the size, shape and depth of the non-layered anomaly, and the resistivity contrast of the structures involved. The apparent resistivity computed in this way will often differ from one array configuration to another.

There is an abundance of examples of the applications of resistivity methods for exploration and subsequent exploitation of minerals, contaminated zones, and groundwater (Mooney, 1980; Ward, 1990). Jain et al. (1973) successfully used the two-electrode and Wenner arrays with small inter-electrode spacings (0.5 to 10 m) to locate ancient gold workings in India. White (1994) applied different electrode arrays to indicate groundwater flow direction and velocity after injection of salt water into groundwater at an experimental site in New Zealand. In another study, to trace the main groundwater flow paths in the Blidworth area of Nottinghamshire in England, Barker (1990) made a series of resistivity traverses across suspected lines of fissures using a colinear dipole-dipole array. The configuration used a maximum dipole length of 25 m and a maximum distance of 150 m between the dipole centres.

The use of DC resistivity methods for engineering problems is also reported in many publications. A dipole-dipole resistivity survey was carried out by Phoenix Geoscience to locate a leak in a dam in Ontario, Canada (Ward, 1990). Smith (1986) used DC resistivity surveys using the pole-dipole array (in which an active current electrode and two potential measuring electrodes is used) to detect solution cavities beneath highways at four sites in Florida.

There are many examples of using DC resistivity methods for detecting and monitoring subsurface contaminations. A contaminated zone produces a contrast in electrical properties with its host medium. The DC resistivity methods are capable of mapping the lateral (by profiling) and vertical (by sounding) extent and the spread of contamination with time in the subsurface (Vogelsang, 1995; Annan et al., 1992). The measurements may be used to provide an image of the subsurface contamination (Benson et al., 1997). The delineation of contamination from the surface allows the development of a more efficient borehole monitoring network for more direct assessment of the rate and direction of spread of any contamination (Benson et al., 1997). These geophysical techniques, being a non-invasive technology, offer distinct advantages as they are less expensive than drilling monitoring wells (Vogelsang, 1995; Stierman et al., 1988). Vogelsang (1995) reported resistivity profiling surveys using a dipole-dipole array at two chemical disposal ditches in northern Utah, which were very successful. Frohlich et al. (1994) used DC resistivity surveys in a coastal environment near Provincetown, Massachusetts, USA to distinguish between the freshwater saturated zone and the high resistivity unsaturated and the low resistivity salt-water saturated zones in the subsurface. Barker (1990) used a Wenner resistivity survey to delineate the extent of the saline groundwater in the Milford area, east of Stafford in England. The presence of high salinity groundwater was clearly recognised from the low resistivities observed in the sounding curves obtained.

Compared to EM methods, DC resistivity surveys with less processing can indicate a clearer picture of resistivity distributions in the subsurface. However, they are subjected to many constraints in their applications. Moving the electrodes consumes considerable time and labour in field work and thus, significantly decreases the cost-

effectiveness of these methods. Because of these difficulties electrical geophysicists prefer to use EM methods for geophysical investigations in which a survey set-up can be easily moved for profiling. However, interpretations of EM measurements are more difficult than DC resistivity surveys. The measured electrical potentials by resistivity methods are converted into apparent resistivity by a simple computation and an apparent resistivity curve reflects the vertical resistivity distributions of the subsurface. A meaningful apparent resistivity value is more difficult to obtain from EM than DC resistivity data (Das, 1995). Furthermore, DC resistivity methods have relatively small sensitivity to noise compared to EM methods (Dahlin, 1996). In this regard, it should be noted that EM methods are normally useless in the vicinity of various human installations such as electric power lines, railways and buildings with metal cladding. Often such installations do not affect DC resistivity surveys to the same extent (Dahlin, 1996). However, the resolving power of DC resistivity methods is less than that of EM methods in detecting buried conductors such as certain ore bodies.

Because of these advantages and disadvantages of DC resistivity methods over EM methods, the exploration geophysicist is often confronted with the problem of choice of method for investigating subsurface anomalous bodies. The use of a combination of resistivity and EM methods is a possible compromise for better interpretation and resolution. In addition, in this way the geophysicist may obtain more information than he would get from any one of these two alone, but extra work is involved. There are several examples where such a combination of the methods yields useful results. Buselli et al. (1990) applied DC resistivity and time domain electromagnetic surveys to locate the extent of subsurface contamination near waste disposal sites in Canning Vale and Morley, Western Australia. Benson et al. (1997) applied DC resistivity and very low frequency (VLF) electromagnetic induction methods for mapping groundwater contamination in Utah County, Utah, USA. Combining these two methods was very helpful for outlining the contaminant plume produced by gasoline leaking from an underground storage tank in that area.

It is realised that if the data acquisition by resistivity methods could be made easy, the application of resistivity methods may be preferred to EM methods for some shallow subsurface investigations. With such considerations, new resistivity data acquisition systems have been developed in recent years (Barker, 1981; Griffiths and Turnbull, 1985; Overmeeren and Ritsema, 1989; Dahlin, 1996; Pazdirek and Blaha, 1996; Shi and Morgan, 1997). These new resistivity data acquisition systems typically use a multi-electrode resistivity meter equipped with a portable microcomputer, a multi-channel relay-matrix switching unit and expandable multi-electrode cables with several take-outs connected to stainless steel electrodes and power generator. The data acquisition process is monitored by the computer software, which checks that all the electrodes are connected and properly grounded before the measurements are started. These new resistivity data acquisition systems remarkably simplify field operations and reduce both the manpower needed and the data collection time. They allow resistivity measurements to be made automatically for any electrode configuration, spread along a line, with any electrode spacing using expandable multi-electrode cables. The advantages of these new resistivity data acquisition systems, mainly designed for continuous vertical sounding, also hold for profiling at any desired electrode spacing. Features of a few newly developed electrical resistivity data acquisition systems are described below.

1.2 New development in resistivity data acquisition systems

The advantages of using multi-core cables for resistivity surveying were recognised at the outset of those new developments (Overmeeren and Ritsema, 1988). As early as 1973, Van Dongen carried out resistivity sounding surveys using multi-electrode cables with a manual switchbox (Overmeeren and Ritsema, 1988). To avoid inductive coupling the cable was used for current injection only, and the potential electrodes were wired separately. For convenience, the Schlumberger configuration was used. Since then, commercially viable versions of these systems have been developed by different companies or institutions. In the following, a few resistivity

field data acquisition systems, which have been developed in recent years, are described.

The GEA-58 system

One of these new resistivity data acquisition systems, which has been developed by TNO-DGV Institute of Applied Geoscience in the Netherlands, is the GEA-58 (Figure 1.2). This microprocessor-controlled resistivity data acquisition system, which is digital and portable, combines an increased measuring accuracy with a high speed of data collection and offers great versatility in desired electrode configurations. The relay card or unit in the GEA-58 enables multi-electrode cables to be scanned automatically. The system uses standard 26-core cables with equally spaced electrode take-outs and each cable has 21 electrode positions. For shallow surveys an electrode spacing of 2 m is chosen, thus covering 40 m of profile. Either two or four cables are used. For continuous sounding, a fifth cable is recommended to roll along the spread. Each cable is mounted on a reel. By rolling along the cables in a similar way to seismic surveys, large separations between the electrodes can also be obtained. For measurements in this case (i.e. large electrode spacings) a separate current amplifier is also used. The inner cables 2 and 3, as shown Figure 1.2, are connected to 21 electrodes, leaving five cores to link with the outer cables 1 and 4, where five electrodes are connected at 8 m intervals. Cable 5 is laid out on the right-hand side of the spread, being a standby for rolling the spread along. To obtain continuous coverage along a profile, the centre of the spread moves one cable-length at a time (Figure 1.2). Former cables 3 and 4 now become the new inner cables, where all the 21 electrode positions on cable 4 are used. Cable 5 will now become active for the outer electrodes, while former cable 1 is disconnected. During the automatic scanning of the array, the operator transfers this cable and associated electrodes to the other end of the line, making them ready for the next set-up. In a Wenner resistivity survey using the GEA-58, a total of 190 measurement points may be acquired in each spread (Overmeeren and Ritsema, 1988). Detailed information about the (mainly shallow) subsurface at a high measuring speed can be obtained

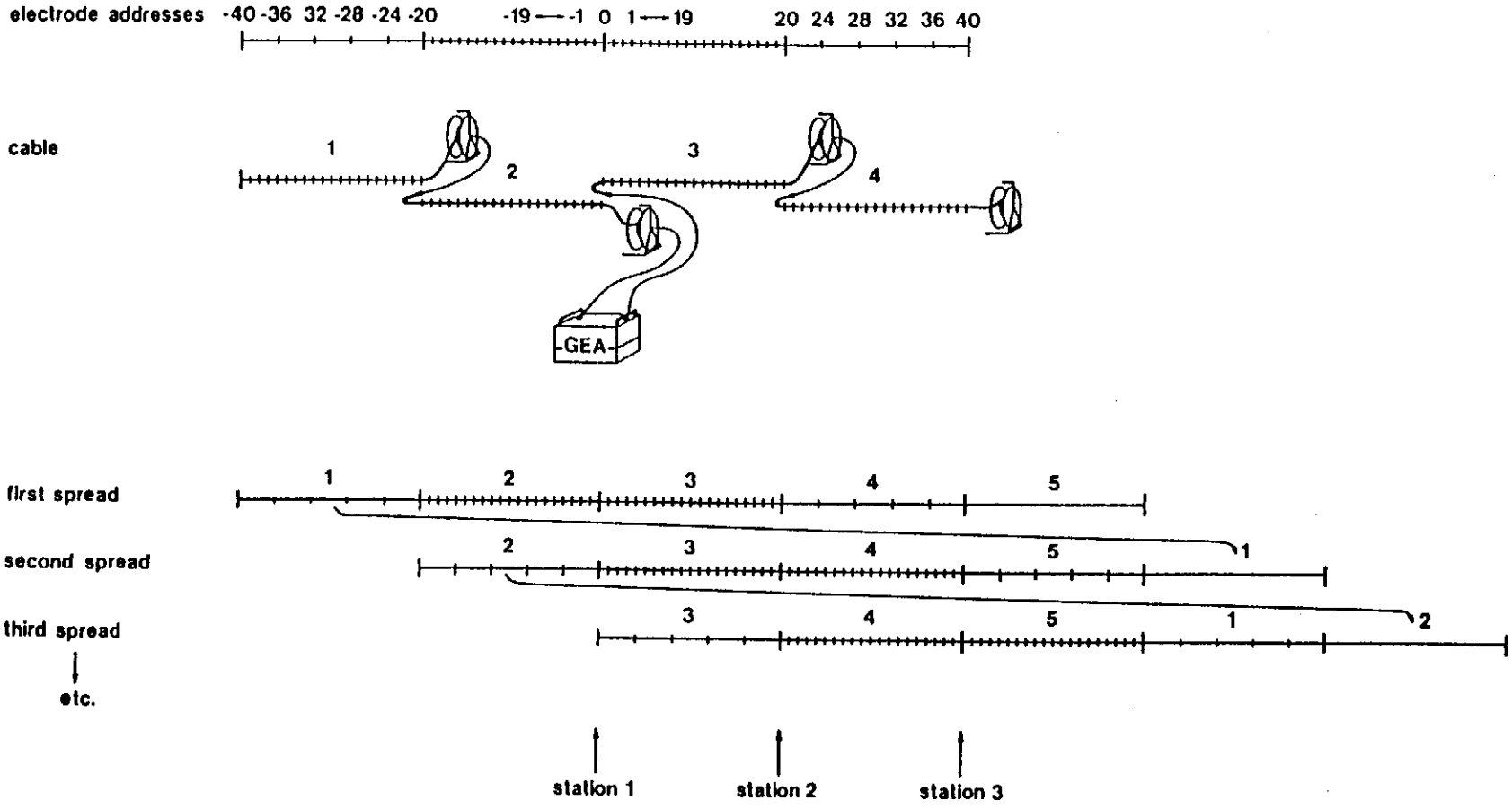

Figure 1.2. The GEA-58 multi-electrode system. This resistivity data acquisition system includes expandable multi-electrode cables with several take-outs connected to steel electrodes and power generator. The lower part of the Figure shows successive spreads established on the ground surface using the multi-electrode cables (From Overmeeren and Ritsema, 1988).

using this resistivity data acquisition system. The multi-functional concept of the GEA-58 system permits automatic scanning of any desired electrode configuration, which may thus be adapted optimally to the objectives of the survey. All operations are performed by control software, offering the operator a wide range of options by user-defined menus. The GEA-58 houses a digital voltmeter and a digital ammeter. The gain of both meters can be set manually or be adjusted automatically during the measurement process. Power is supplied by a rechargeable battery pack, attached to the bottom of the measuring unit. All relevant information, such as the electrode configuration, the measured current intensity, the electric potential difference, and the computed apparent resistivity are displayed on the screen and stored in the computer's memory. Optionally, a portable printer may be connected to the GEA-58, giving an instantaneous print-out of all controlled data. Automatic array scanning for profiling or continuous sounding is performed by the software-controlled relay-card, which connects any desired set of four electrodes to the measuring circuit. During scanning, all information concerning the electrodes involved and results obtained is displayed simultaneously. Although the GEA-58 multi-electrode system was designed mainly for shallow applications, a simple scaling factor, i.e. multicore cables with a larger spacing between the electrodes, is all that is needed to reach deeper targets with this equipment (Overmeeren and Ritsema, 1988).

Multi-electrode system with ABEM SAS 300 Terrameter

Griffiths and Turnbull (1985) have designed a multi-electrode system for resistivity data acquisition in which an 8-core cable was made up from 20 separate 50 m sections, these being reel mounted for convenience. Each reel is set up close to an electrode. All electrodes at the outset are driven into the ground at equal intervals along the chosen profile. Enough cable is unwound from each reel to enable connection to be made to the adjacent reel, thus providing electrical continuity throughout the full length of the array. The cable carries two current and two potential conductors (connected to the resistance measuring instrument, in this instance a Terrameter). One further conductor is used to operate the switching, the

remaining line being at present unused. The intention is to employ this conductor to monitor the performance of the control units. The basic unit in each control box is a Mostek type SCU microprocessor. This is used to switch one of four reed relays and so connect the associated electrode to the required measuring line. The microprocessors are controlled from a station at the end of the cable by a portable computer and an ABEM SAS 300 Terrameter is used for measurement. The operation of a single key moves the program to the next step. On the completion of the sequence the apparent resistivity data can be output to a printer or stored on magnetic tape. Although in practice the Wenner configuration is the most commonly used with this system, any other desired configuration of four electrodes spread on a line such as the Schlumberger or dipole-dipole configuration can be used and the measurements can be made in any sequence.

Multi-electrode system with ELREC T resistivity meter

In another resistivity data acquisition system used by Shi and Morgan (1997) a series of electrodes are laid out on a straight line with a constant electrode spacing. For data recording, a ELREC T resistivity meter produced by IRIS Instruments is used. The resistivity meter is connected to an intelligent node system in which the active electrodes can be selected automatically to vary source and receiver dipole spacing for each measurement. Each measurement is made automatically through the control of a microprocessor, with automatic self-potential correction, and temporal stacking signal enhancement. The internal memory stores the data as well as the station number, and position of each electrode (Shi and Morgan, 1997).

ABEM Lund imaging system

The ABEM Lund imaging system is another multi-electrode data acquisition system, which is used in resistivity surveying. In this system, in addition to data collection, processing and presentation of data in two- or three-dimensional form is also carried

out automatically. The system has a basic unit Electrode Selector ES464 which is a multi-channel relay matrix switching unit. This unit is connected to an ABEM SAS 300 C Terrameter and a notebook or handheld computer. Alternatively, an ABEM SAS 4000 Terrameter (with built-in software) can be used, and therefore, in this case no external computer is needed in the field. This system provides fast and automatic resistivity data acquisition and imaging (Dahlin, 1996).

Case studies involving new multi-electrode resistivity data acquisition systems

With these recent developments which facilitate electrical data acquisition in resistivity surveys, a surge in the application of these methods is inevitable, as the methods provide an opportunity for an interpretational advantage over other active methods. The new resistivity data acquisition systems have already been applied to a variety of applications with considerable success. Overmeeren and Ritsema (1989) used the GEA-58 data acquisition system for mapping shallow subsurface layers in the southern part of the Netherlands and also for investigating water quality in the eastern part of the Netherlands, where a number of boreholes had already been drilled. The results of these resistivity surveys showed that they could reliably contribute to the optimal selection of the drilling site. Dahlin (1996) used the ABEM Lund imaging system, for mapping of a fine sediment cover over a coarse sediment aquifer in an area close to Revinge in southern Sweden. The survey was carried out for groundwater vulnerability studies and aquifer volume estimations in the area. He also applied this acquisition system, for a geotechnical study of a planned road south of Stockholm in Sweden, to map the bedrock topography and the extent of postglacial clay cover. In addition, he applied the data acquisition system for engineering, hydrogeological and environmental applications in a number of other areas in Sweden. Based on the results obtained from the resistivity surveying in combination with a limited number of drill holes, reliable models of the subsurface were presented. Griffiths and Turnbull (1985) applied their self-designed multi-electrode acquisition system for geological mapping in an area of deeply weathered crystalline basement rocks in Zimbabwe and also for studying the location of a

geological fault in an area near Wiltshire in England. Pazdirek and Blaha (1996) after using yet another new resistivity data acquisition system, known as ME-100 and developed by Geofyzika Brno (Czech Republic), in a number of applications concluded that their data acquisition system is particularly suitable for small scale engineering sites, hydrogeological, environmental and archeological investigations where understanding complex subsurface structure in detail is important. Shi and Morgan (1997) also used one of the new data acquisition systems to detect underground limestone caves in Barbados, West Indies.

1.3 The need for doing this research

The recent developments in electrical resistivity data acquisition systems coupled with major improvements in digital computers have given a new impetus to the use of resistivity surveying, especially for shallow investigations for water and subsurface contaminations. A large volume of data for different electrode configurations can now be acquired easily in a short time. It should be possible to take advantage of the redundancy of measurement made with these systems to yield enhanced information about the subsurface.

When DC resistivity methods are used to detect subsurface anomalous zones such as contamination plumes or shallow mineralisation embedded in a layered earth, the layered earth potential contributes a major part of the total potential measured. In other words, when an anomalous conductivity zone is a target, its contribution to the total response is so low at times that the methods fail to resolve such a subsurface target. In order to increase the resolution, the large layered earth contribution to field measurements must be reduced in order to enhance the signal from a particular target. This PhD research work is directed at processing techniques based on multisystem surveys which reduce the contribution of the layered earth to the measured response. The new data acquisition systems can be advantageously used for measuring the electric potentials for a number of different electrode configurations. The development of new procedures for processing resistivity data to

enhance the resolution of the resistivity method for target detection in the subsurface will be investigated. Processing the data obtained by multi-system DC resistivity surveys should result in them becoming more effective geophysical prospecting methods.

The strategy to be used for developing new geophysical processing and interpretational technique deserves comment. Data are required to which the new procedures may be applied, and for which the causative bodies are known. Numerical simulation of field surveys is an obvious source of data. However, the computation of the electrical effects of three-dimensional anomalous conductivity zones in a layered earth is not a trivial task. Speed and accuracy as well as the theoretical formulation are challenges in this area. Much has been done in the forward modelling of the electrical anomalies (Hohmann, 1987; Zhdanov and Keller, 1994; Raiche, 1994). However, problems still remain in the mathematical formulation leading to accurate results obtained in efficient ways (Raiche, 1994; Spitzer and Wurmstich, 1995; Liu and Lamontagne, 1998).

In choosing to use numerically modelled data as a primary test of the new techniques developed in this thesis, it will be necessary to critically examine the modelling process itself, and make further improvements as required. If the modelling results used for testing are flawed, then this will cast a doubt on the validity of subsequent outcomes of the research.

1.4 Outline of the thesis

This thesis deals with development and application of processing techniques for enhanced interpretation of multisystem resistivity measurements. A mathematical formulation of the 3-D forward problem is presented with software developed to compute responses for different electrode configurations. In general, a 3-D body in the lower half-space of a two-layered earth under homogeneous or transitional overburden is studied in this PhD research work. To test the processing techniques,

synthetic data from 3-D structures are generated for various electrode configurations in different geoelectrical models. While this thesis is essentially theoretical, the practicing geophysicist will never be completely at ease with a new method unless it has been tried and proven in the field. To do this is not a trivial exercise. In fact, this aspect could constitute a whole new research project in itself. The results of preliminary field tests, though not as extensive as might be desired, are presented in this thesis as a basic reality check on the theoretical procedures which are developed in the following chapters.

In Chapter 2, the mathematical formalism for 3-D resistivity modelling using the integral equation technique is given. Two different implementations of the integral equation method are discussed to compute unknown distributions of electric charge density on the surface of a 3-D subsurface body. Computation of various Green's functions involves Hankel integrals. These integrals should be computed with high accuracy. For this purpose, new digital linear filters developed by Guptasarma and Singh (1997) are used. Evaluation of the unknown surface charges on the 3-D target requires the inversion of a large full matrix. The biconjugate gradient method is used in preference to the LU decomposition method for the computation of the surface charge density as it is expected to provide greater accuracy.

Chapter 3 presents the development and application of the processing techniques for enhancement of the signal from a target embedded in a layered earth. The 3-D resistivity forward modelling of different geoelectrical structures is carried out to obtain apparent resistivity values for common electrode arrays. The processing techniques selected, simultaneously use either Wenner and two-electrode resistivity measurements or Schlumberger and equatorial dipole-dipole resistivity measurements. For processing, numerically modelled two-system measurements are combined in a specific way to remove the layered earth contribution to the total measurements. Random noise is added to distort the responses in order to study the effectiveness of the processing techniques in the presence of noise. The processing techniques are then applied to real field data to investigate a subsurface conductive anomaly.

A *transitional layer* can be defined as a layer in which resistivity (or conductivity) varies with depth in some continuous fashion. This may be due to differential weathering of the surface layer (especially in tropical and subtropical areas) or seepage of chemicals spilled on the surface or generally any phenomenon that continuously alters the resistivity of layers. Transitional layering effects on resistivity measurements over a 3-D body are studied in Chapter 4. In this chapter, the mathematical formulation of the problem is given and then the responses of a 3-D body under a transitional cover are computed. The processing technique developed in the previous Chapter is applied to reduce the effect of layered earth consisting of transitional layers.

In Chapter 5, the conclusions and some recommendations for further research in this area are given.

Chapter 2

NUMERICAL MODELLING OF DC RESISTIVITY METHODS

The most conventional method of testing new geophysical techniques is to apply them to numerically modelled field data. That way, the correct results are known ahead of the application of the new technique. The forward modelling of 3-D resistivity responses is a difficult task. This Chapter contains a detailed review of existing forward modelling methods using the integral equation technique, and also introduces some new improvements in the computation of electrical anomalies.

2.1 Introduction

A mineral deposit or a subsurface contaminated zone may often be represented by a 3-D body in a layered earth model. Normally, the body has a resistivity (or conductivity) contrast with the host layer. A simple geoelectrical example of such a case, which is often found in the nature, is illustrated in Figure 2.1. In DC resistivity surveys, voltage measurements on the surface of the ground obtained by the profiling method may be used to delineate the body in the subsurface. However, to interpret the resistivity response of the body to the profiling method, numerical modelling of such a geoelectrical situation is very beneficial.

Forward solutions for one-dimensional (1-D) layered models have been available for many years (Bhattacharya and Patra, 1968; Koefoed, 1979a). They incorporate Fourier-Bessel integrals, which can easily be evaluated numerically. Also, inverse solutions for 1-D models have been used routinely for many years (Szaraniec,1980; Zohdy, 1989). However, calculating the response of two-dimensional (2-D) or three-dimensional (3-D) models is much more difficult, except for certain simple geometries such as spheres or cylinders. Advances in the understanding and interpretation of these geophysical methods largely depend on forward and inverse

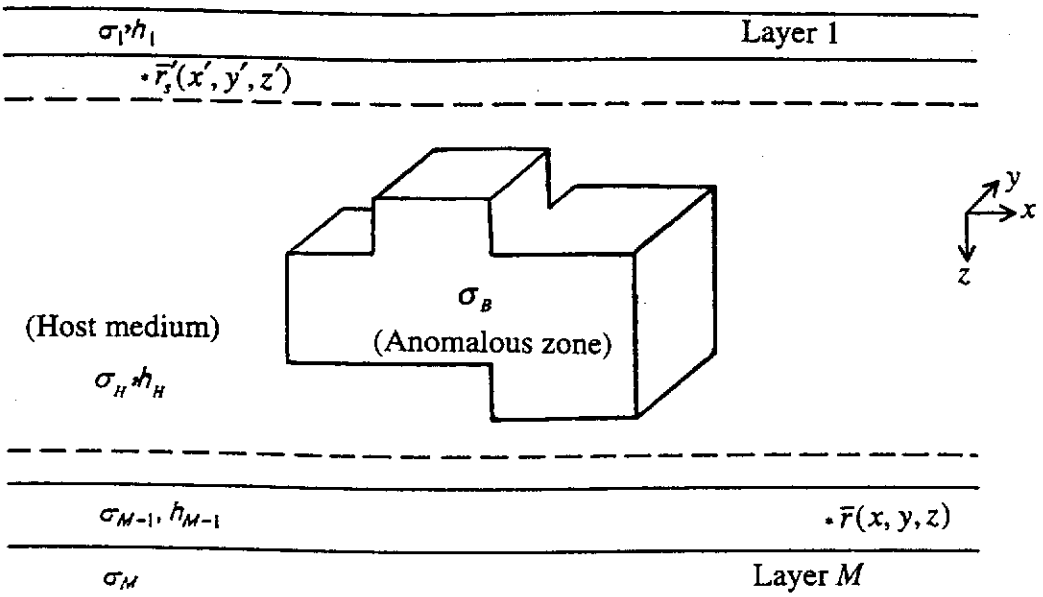

Figure 2.1. An arbitrarily shaped 3-D body in a layered earth containing M layers. The layer conductivities and thicknesses are denoted by σ_j and h_j, respectively, where $j = 1, 2, 3, ..., M$ and $h_M = \infty$. The conductivity of the body is denoted by σ_B. A constant electric current is injected at a point $\bar{r}_s'(x', y', z')$ arbitrarily located at any depth. The potential is measured at any point $\bar{r}(x, y, z)$ anywhere in the layered earth.

numerical solutions for 3-D models. This Chapter deals with the mathematical formalism for computing direct current responses of 3-D subsurface structures.

Two principal modelling classes are used for numerical modelling: (1) differential equation (DE) methods and (2) integral equation (IE) methods. The class of DE methods includes finite-difference and finite-element methods (Snyder, 1976; Best et al., 1985; Hohmann, 1987; Zhao and Yedlin; 1996a). In general, numerical solutions are achieved by approximating the relevant differential or integral equation and solving a large matrix equation. DE methods consider a grid mesh that involves a large part of the earth. The principal advantage of the DE methods is that they have the ability to solve problems for which the physical properties (e.g. resistivity) have been arbitrarily assigned different values at each element in the approximation grid or network. Thus, for this purpose the finite-difference or finite-element modelling schemes are extremely versatile (Snyder, 1976). These methods are preferable for simulating complex geology (Hohmann, 1987).

Dey and Morrison (1979) developed a 3-D finite-difference method to solve the potential distribution about a point source of current located in or on the surface of a half-space containing a 3-D conductivity distribution. They integrated the generalised Poisson's equation, which includes a spatially variable electrical conductivity, over discretised cubic element volumes of the lower half-space to obtain a system of self-adjoint difference equations. A boundary condition, on the basis of the asymptotic behaviour of the potential at large distances from the source or any material inhomogeneity, was introduced and the electric potential was calculated for simple 3-D block-shaped models. Accurate and stable results for the potential were obtained using full, banded, Cholesky decomposition of the capacitance matrix.

James (1985) had a different approach to 3-D finite-difference resistivity modelling. He applied a class of matrix transforms, known as the Polozhii transforms in his approach and obtained a very efficient finite-difference modelling algorithm. Zhao and Yedlin (1996b) presented a modified finite-difference method for 3-D DC

resistivity modelling. They made two modifications to the finite-difference method. The first modification was the use of a more accurate formula, suggested by Lowry et al. (1989), for the source singularity removal. As Lowry et al. (1989) showed, removing the source singularity by dividing the potential into the primary potential (because of the source current) and the secondary potential (caused by changes in the electrical conductivity), improved accuracy because a major proportion of the numerical error arose due to the inadequate representation of the source on a discrete grid. A result of introducing the primary potential in the 3-D DC resistivity problem was the creation of an additional effective source term. The second modification was the analytical evaluation of the volume integral of the source terms. To compute the secondary potential, a no-flow boundary condition was considered on the air-earth interface and Dirichlet conditions were used for the other boundaries. Results with an average error of less than 0.5% were obtained from applying this modified finite-difference method to various examples (Zhao and Yedlin, 1996b).

For the case of the finite-element method Coggon (1971) derived an energy functional for 2-D electromagnetic problems, including DC resistivity. A linear system of equations for interpolation weights was obtained using a trial solution based on linear interpolation on triangles. This method was extended to 3-D problems using tetrahedral elements by Pridmore et al. (1981). Distorted elements were used by Holcombe and Jiracek (1984) to show 3-D topographic variations. The boundary conditions were implemented using approximate analytic boundary conditions that model the potential in a horizontally layered earth. The near surface layers of regular hexahedral elements were replaced with distorted isoparametric elements. This distortion was attained by the introduction of a coordinate transformation into the finite-element functional.

Numerical solutions using DE methods are easy to implement. However, they result in large banded matrices (Hohmann, 1987). Although DE methods have been developed for modelling the electrical response of 3-D bodies, they have had limited success in this case. This is because these methods simply subdivide a large volume of the earth containing any inhomogeneities into a number of cells or mesh points,

and the mesh boundaries must be far from the inhomogeneities. This results in having a large number of cells with corresponding large sets of equations to solve for the unknown function values. The coefficient matrix of these equations is very big, which leads to computer storage problems and long execution times for obtaining the solution. This makes the numerical solution of 3-D electrical problems using DE methods very costly in terms of computer storage and time requirements (Best et al., 1985; Hohmann, 1987).

Unlike DE methods, an integral equation is not as flexible in its ability to handle both arbitrary geometry and variations in the properties of the medium (Snyder, 1976). Integral equation (IE) methods are well suited for studying or modelling a confined body or target in a layered earth (Schulz, 1985; Hohmann, 1987; Eskola, 1992). The IE methods are based on the accessibility of a known Green's function for a background model (Lee, 1975). This Green's function is substituted for the potential due to an anomalous body inserted into the background model. Using this technique, Lee (1975) computed the potential of a cylinder and sphere in a layered earth. Snyder (1976) formulated the integral equations for the solution of the potential field for the resistivity modelling problem with one or more anomalous inhomogeneities, each of uniform resistivity buried in an otherwise uniform space. He considered the formulation and numerical implementation only for modelling 2-D boundaries (i.e. infinte strike length) in the presence of a point current source. Dieter et al. (1969) formulated the 3-D resistivity problem into an integral equation. Schulz (1985) studied the numerical accuracy of the integral equation technique for DC resistivity methods. Das and Parasnis (1987) presented numerical computations using this technique for resistivity and induced polarisation (IP) responses due to arbitrarily shaped 3-D bodies in a layered earth. Furthermore, they compared their results with those from finite difference methods and physical tank experiments. Xu et al. (1988), also computed 3-D terrain effects for DC resistivity surveys using this technique.

For the case of a body embedded in a layered earth, IE methods have considerable computational advantages over DE methods because the unknown fields in IE methods only need to be found in the anomalous region rather than the entire region.

Thus, in IE methods there is a much smaller system matrix to solve (Hohmann, 1987; Liu and Lamontagne, 1998). Also, for a specific 3-D resistivity distribution, elements of the Green's function are computed only once and if the current electrode position changes, only the incident field in the elements needs to be recomputed. For these reasons, the computation time in IE methods is reduced dramatically compared to the DE methods. These computational advantages are important for the research work where the resistivity responses of 3-D subsurface bodies must be efficiently and accurately computed. Although formulations of IE methods involve more difficult mathematics, they have been very useful in the understanding and interpretation of the responses of a 3-D target.

In this research work, the IE technique has been adopted for 3-D DC resistivity modelling. In the following, an appraisal of the relevant mathematics for the solution of the problem using IE methods is given. Then, development of a new approach using the spectral formalism is presented for computation of the required Green's functions. Also, implementation of new digital filters for computing Hankel integrals in the expressions for the Green's functions is briefly explained. Furthermore, a new implementation of the biconjugate gradient method for the solution of the electric charge density is introduced.

2.2 Integral equation approach

We consider the situation shown in Figure 2.1; namely an arbitrarily shaped 3-D inhomogeneity in an M-layered earth. Here, we use a global Cartesian coordinate system throughout. A primed quantity for a source location and an unprimed quantity for the field point location will be used. A constant electric current I is injected at a point $\bar{r}_s'(x', y', z')$, which can be anywhere in the layered earth, either on the surface or somewhere in the subsurface including the inhomogeneous body (for a mise - a - la - masse survey). The problem is to calculate the potential at any point $\bar{r}(x, y, z)$ when a steady or direct current flows. The conductivity of the body is denoted by σ_B. The layer conductivities and thicknesses are denoted by σ_j and h_j,

respectively, where $j = 1, 2, 3, ..., M$ and $h_M = \infty$. The governing equation for the present situation can be written as:

$$\nabla . \bar{J} = I\delta(\bar{r}, \bar{r}_s'), \tag{2.1}$$

where $\bar{J}$ is the current density and $\delta(\bar{r}, \bar{r}_s')$ is the Kronecker delta which is defined as:

$$\delta(\bar{r}, \bar{r}_s') = \begin{cases} 0 & \text{if} \quad \bar{r} \neq \bar{r}_s' \\ 1 & \text{if} \quad \bar{r} = \bar{r}_s' \end{cases}. \tag{2.2}$$

For an isotropic medium, the constitutive relation is,

$$\bar{J} = \sigma \bar{E}, \tag{2.3}$$

where σ is the conductivity of a medium and $\bar{E}$ is the electric field intensity. The electric field $\bar{E}$ is related to the measured scalar potential V by

$$\bar{E} = -\nabla V. \tag{2.4}$$

Equations (2.1), (2.3), (2.4) yield the following equation:

$$-\nabla . (\sigma \nabla V) = I\delta(\bar{r}, \bar{r}_s'). \tag{2.5}$$

Expanding this equation, we obtain

$$\nabla \sigma . \nabla V + \sigma \nabla^2 V = -I\delta(\bar{r}, \bar{r}_s'), \tag{2.6}$$

or

$$\nabla^2 V = -\frac{I}{\sigma}\delta(\bar{r},\bar{r}_s') - \frac{\nabla\sigma.\nabla V}{\sigma}. \tag{2.7}$$

We know that the solution of the Poisson's equation:

$$\nabla^2 V = -\frac{\rho}{\varepsilon_\circ}, \tag{2.8}$$

is given by

$$V = \frac{1}{4\pi}\int_v \frac{\rho}{\varepsilon_\circ R} dv', \tag{2.9}$$

where ρ is the volume charge density in the total volume v, and R is given by

$$R = \sqrt{(x-x')^2 + (y-y')^2 + (z-z')^2}. \tag{2.10}$$

We write equation (2.9) as

$$V = \frac{1}{4\pi}\int_v \frac{\rho}{\varepsilon_\circ} G(\bar{r},\bar{r}')dv', \qquad \text{with } G(\bar{r},\bar{r}') = \frac{1}{R}. \tag{2.11}$$

Here the function $G(\bar{r},\bar{r}')$ is called the scalar Green's function for a whole space (i.e. a space having no boundaries). $G(\bar{r},\bar{r}')$ is the potential at a point $\bar{r}$ due to a unit current at $\bar{r}'$. A similar treatment to equation (2.7) along with the Helmholtz theorem yields,

$$V(r) = \frac{1}{4\pi}\int_v \frac{I}{\sigma}\delta(\bar{r}',\bar{r}_s')G(\bar{r},\bar{r}')dv' + \frac{1}{4\pi}\int_v \frac{\nabla\sigma.\nabla V}{\sigma} G(\bar{r},\bar{r}')dv'. \tag{2.12}$$

The first integral on the right-hand side of equation (2.12) relates to the part of the total potential V which is due to the current only at $\bar{r}_s'$. Let us assume that the

current point source is located at $\bar{r}_s'$ in a medium with a conductivity σ_s. We can write equation (2.12) in the following form:

$$V(r) = \frac{I}{4\pi\sigma_s} G(\bar{r}, \bar{r}_s') + \frac{1}{4\pi} \int_v \frac{\nabla\sigma.\nabla V}{\sigma} G(\bar{r}, \bar{r}') dv'. \tag{2.13}$$

The first term on the right-hand side of equation (2.13) is the normal potential contribution V_N to the total potential V as a result of the current injection at $\bar{r}_s'$. The second term on the right-hand side of equation (2.13) suggests that the contribution to the potential arises from the regions where there is a conductivity (or resistivity) contrast, i.e. where $\nabla\sigma$ exists. $\nabla\sigma$ exists only on the contact between the body with conductivity σ_B and the host medium with a different conductivity σ_H.

In equation (2.13), the factor $\frac{\nabla\sigma.\nabla V}{\sigma}$ can be expressed in terms of surface charge density. For this, we consider Maxwell's equation for the volume charge density ρ, given by

$$\nabla.\bar{D} = \rho. \tag{2.14}$$

Using the following constitutive relationship:

$$\bar{D} = \varepsilon_o \bar{E}, \tag{2.15}$$

we obtain from equation (2.14),

$$\nabla.\bar{E} = \frac{\rho}{\varepsilon_o}. \tag{2.16}$$

Here $\varepsilon_\circ$ is the permittivity of free space, and $\overline{D}$ is the electric displacement. From equation (2.3) and (2.16),

$$\frac{\rho}{\varepsilon_\circ} = \frac{1}{\sigma}\nabla.\bar{J} + \bar{J}.\nabla(\frac{1}{\sigma}). \tag{2.17}$$

As we have considered the inhomogeneous body to have no source inside it, we have $\nabla.\bar{J} = 0$ inside the inhomogeneity. Thus, equation (2.17) reduces to

$$\frac{\rho}{\varepsilon_\circ} = \bar{J}.\nabla(\frac{1}{\sigma}). \tag{2.18}$$

Using $\nabla(\frac{1}{\sigma}) = (-\frac{1}{\sigma^2})\nabla\sigma$, and equations (2.3), (2.4) and (2.18), we obtain

$$\frac{\rho}{\varepsilon_\circ} = \frac{\nabla V.\nabla\sigma}{\sigma}. \tag{2.19}$$

Using the above relationship given by equation (2.19), we can write equation (2.13) in the following form:

$$V(\bar{r}) = \frac{I}{4\pi\sigma_s}G(\bar{r},\bar{r}_s') + \frac{1}{4\pi}\int_v \frac{\rho}{\varepsilon_\circ}G(\bar{r},\bar{r}')dv'. \tag{2.20}$$

Thus, the second term on the right-hand side of equation (2.20) arises due to the volume charge density distribution in the inhomogeneity. In equation (2.20), while the first term represents the normal potential V_N, we denote the second term as the anomalous potential V_A, and then two kinds of potentials add up to yield the total potential V. Thus, we can write equation (2.20) as,

$$V = V_N + V_A, \tag{2.21}$$

where

$$V_N = \frac{I}{4\pi\sigma_s} G(\bar{r}, \bar{r}_s') \quad , \tag{2.22}$$

and

$$V_A = \frac{1}{4\pi} \int_v \frac{\rho}{\varepsilon_\circ} G(\bar{r}, \bar{r}') dv' \quad . \tag{2.23}$$

Now, we deal with the volume charge density ρ that exists only in the volume of the inhomogeneity. As no external source of current is considered inside the anomalous region, the charges exist only in a small volume which encloses the surface of the inhomogeneity. This is schematically shown in Figure 2.2. We consider a volume with thickness t containing all the charges. Thus, we can write $dv' = tds'$ where ds' represents an elementary surface. When t is very small, we can write $\rho t = q$ where q is the surface charge density. Replacing dv' by tds' and then ρt by q, we then write the volume integral in equation (2.20) in the form of surface integral with a surface charge density q as

$$V(\bar{r}) = \frac{I}{4\pi\sigma_s} G(\bar{r}, \bar{r}_s') + \frac{1}{4\pi} \int_S \frac{q}{\varepsilon_\circ} G(\bar{r}, \bar{r}') ds' \quad . \tag{2.24}$$

Equation (2.24) is an integral equation with the unknown surface charge density q appearing in the integrand. To obtain the potential V from this integral equation, first we need to evaluate the unknown q. If we can express the potential V in equation (2.24) in terms of q, equation (2.24) will be converted into a Fredholm integral equation of the second kind. The potential V can be written in terms of q using the boundary condition that the normal electric field is discontinuous across the surface S.

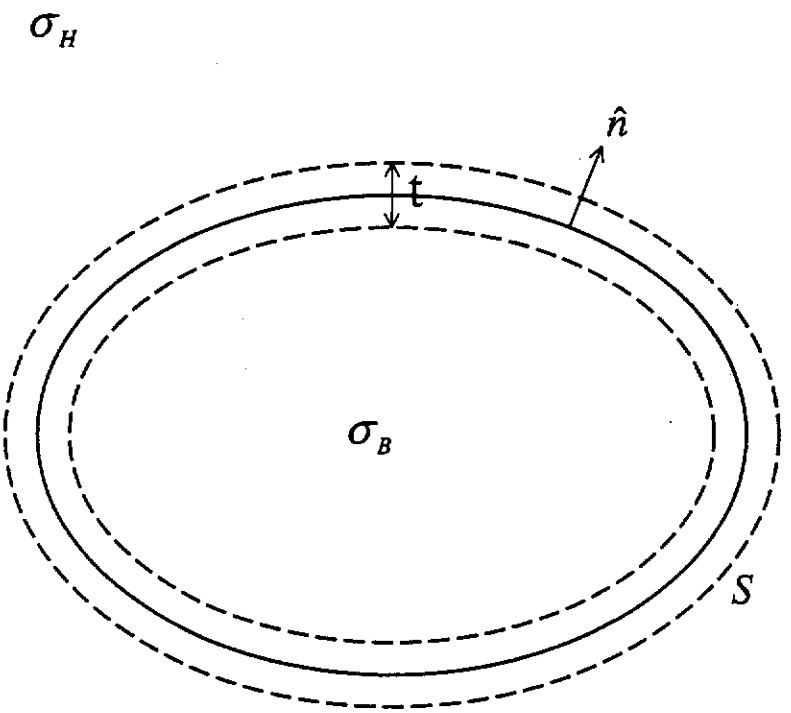

Figure 2.2. Small volume enclosing surface of the body shown in Figure 2.1. As a result of injecting current into the layered earth, shown in Figure 2.1, electrical charges are developed only in this small volume with thickness t enclosing the surface S of the body. σ_B is the conductivity of the body, σ_H is the conductivity of the host medium, and $\hat{n}$ is the outward unit vector normal to the surface S.

Boundary condition (discontinuous normal electric field)

Let us consider a small planar surface with a surface charge density q (Figure 2.3). The electric field component normal to either side of this surface is $\frac{q}{2\varepsilon_\circ}$. Therefore, we can write:

$$\hat{n}_i.\overline{E}_i = \frac{q}{2\varepsilon_\circ} \quad \text{(for the } i \text{ side of the surface),} \tag{2.25}$$

and

$$\hat{n}_j.\overline{E}_j = \frac{q}{2\varepsilon_\circ} \quad \text{(for the } j \text{ side of the surface).} \tag{2.26}$$

Here $\hat{n}_i$ and $\hat{n}_j$ are the unit vectors normal to the i and j sides of the surface, respectively. From these two equations, the following expression can be written:

$$\hat{n}_i.\overline{E}_i + \hat{n}_j.\overline{E}_j = \frac{q}{\varepsilon_\circ}. \tag{2.27}$$

Considering an outward normal unit vector $\hat{n} = \hat{n}_i = -\hat{n}_j$ (see Figure 2.3), equation (2.27) can be written as

$$\hat{n}.(\overline{E}_i - \overline{E}_j) = \frac{q}{\varepsilon_\circ}. \tag{2.28}$$

Thus, the outward normal component of the electric field is discontinuous on the surface. However, the normal component of current density is continuous across the surface S, i.e.,

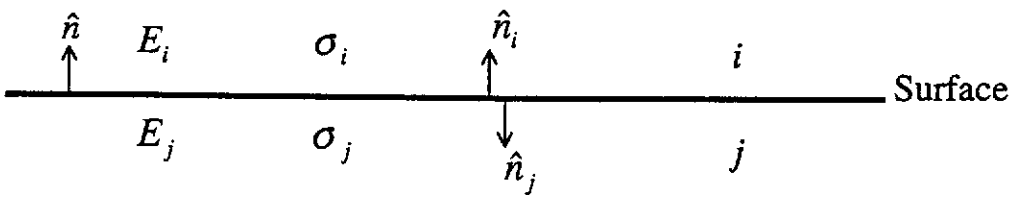

Figure 2.3. Electrical quantities on each side of a planar surface. σ_i and σ_j are the conductivities, E_i and E_j are the electric fields, and $\hat{n}_i = \hat{n}$ and $\hat{n}_j$ are the outward unit vectors normal to the i and j sides of the surface.

$$\hat{n}_i.\bar{J}_i + \hat{n}_j.\bar{J}_j = 0. \tag{2.29}$$

Considering equation (2.3), we can write equation (2.29) in the following form:

$$\sigma_i \hat{n}_i \bar{E}_i + \sigma_j \hat{n}_j \bar{E}_j = 0. \tag{2.30}$$

Multiplying equation (2.27) by σ_j and subtracting it from equation (2.30), we have

$$\hat{n}.\bar{E}_i = \frac{-\sigma_j}{\sigma_i - \sigma_j}\frac{q}{\varepsilon_\circ}. \tag{2.31}$$

Considering equations (2.4) and (2.31) for the case of a body of conductivity σ_B embedded in a host medium of conductivity σ_H (Figure 2.1), we obtain

$$\hat{n}.\nabla V = \frac{\sigma_B}{\sigma_H - \sigma_B}\frac{q}{\varepsilon_\circ}. \tag{2.32}$$

Applying spatial normal derivatives to both sides of equation (2.24), we will have

$$\hat{n}.\nabla V(\bar{r}) = \frac{I}{4\pi\sigma_s}\hat{n}.\nabla G(\bar{r},\bar{r}_s') + \frac{1}{4\pi}\int_S \frac{q}{\varepsilon_\circ}\hat{n}.\nabla G(\bar{r},\bar{r}')ds' \ . \tag{2.33}$$

Equations (2.32) and (2.33) yield

$$\frac{\sigma_B}{\sigma_H - \sigma_B}\frac{q}{\varepsilon_\circ} = \frac{I}{4\pi\sigma_s}\hat{n}.\nabla G(\bar{r},\bar{r}_s') + \frac{1}{4\pi}\int_S \frac{q}{\varepsilon_\circ}\hat{n}.\nabla G(\bar{r},\bar{r}')ds'. \tag{2.34}$$

Defining $Q = \frac{q}{\varepsilon_\circ}$, we can rewrite equation (2.34) in the following form:

$$\frac{\sigma_B}{\sigma_H - \sigma_B} Q = \frac{I}{4\pi\sigma_s} \hat{n}.\nabla G(\bar{r}, \bar{r}_s') + \frac{1}{4\pi} \int_S Q\hat{n}.\nabla G(\bar{r}, \bar{r}') ds' . \tag{2.35}$$

Now equation (2.35) is the Fredholm integral equation of the second kind and we will solve it for the unknown surface charge density Q.

There are several methods which can be used to solve equation (2.35) for Q. Among these methods, we discuss the following two: (1) moment method with pulse basis function and point collocation, and (2) method of weighted residuals.

2.2.1 Moment method with pulse basis function and point collocation

To solve equation (2.35) for Q using this method, we discretise the surface of the inhomogeneous body into N elementary cells as shown in Figure 2.4. After discretisation, we write the integral term (second term) on the right-hand side of equation (2.35) in the following form:

$$\int_S Q\hat{n}.\nabla G(\bar{r}, \bar{r}') ds' = \sum_{n=1}^{N} \int_{S_n} Q^n \hat{n}.\nabla G(\bar{r}, \bar{r}_n') ds' . \tag{2.36}$$

Here S_n is an elementary cell on the surface of the inhomogeneous body at a location $\bar{r}_n'$. Q^n is the surface charge density on cell n. To simplify the computational problem of obtaining the unknown Q, a uniform constant surface charge density distribution is considered on the surface of each elementary cell. To justify this assumption and reduce the error in computations, a sufficiently small size of elementary cells is used. Each surface cell S_n on the right-hand side of equation (2.36) is considered as a source and the computations of the Green's function are carried out at the centre of each surface cell (point collocation), and then, the contributions from the source cells are added together. However, when the field point is inside a source cell, a singularity occurs. In this case, a special computational

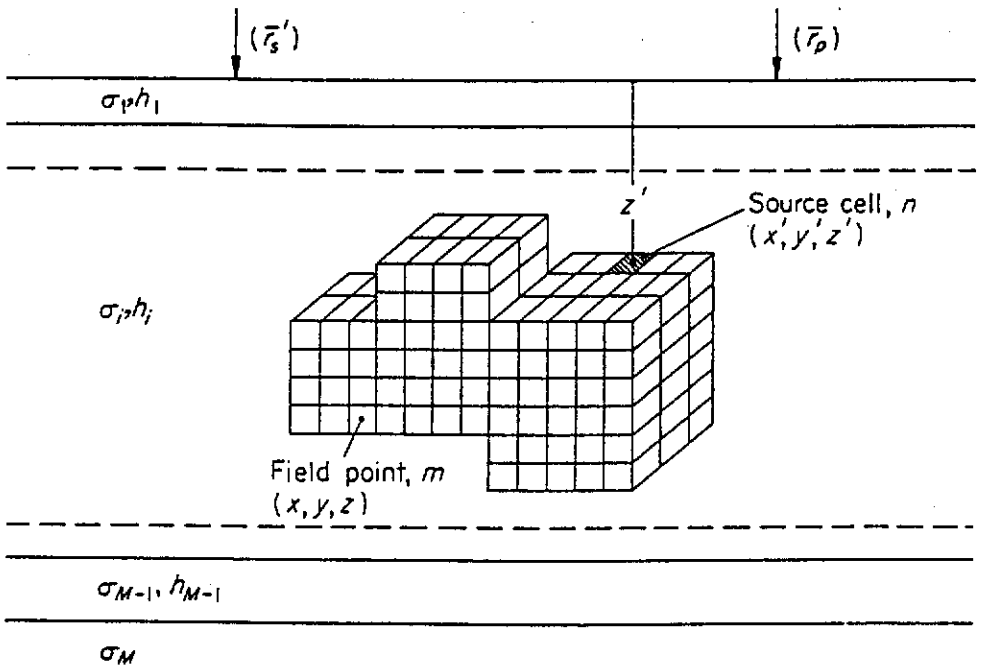

Figure 2.4. A 3-D body in a layered earth excited by a point source on the ground surface. $\bar{r}_s'$ is the direct current source point, and $\bar{r}_p$ is the measuring potential point. The layered earth contains M layers. The layer conductivities and thicknesses are denoted by σ_j and h_j, respectively, where $j = 1, 2, 3, ..., M$ and $h_M = \infty$. The body with conductivity σ_B is discretised to N surface elementary cells. Applying the moment method with basis function and point collocation, $m(x, y, z)$ at the centre of a surface cell is the field point and $n(x', y', z')$ is the source cell.

treatment is needed. For the nth source cell and mth field point, we can write equation (2.36) as

$$\int_S Q\hat{n}.\nabla G(\bar{r}_m,\bar{r}')ds' = \sum_{\substack{n=1\\ n\neq m}}^{N-1}\int_{S_n} Q^n\hat{n}.\nabla G(\bar{r}_m,\bar{r}_n')ds' + \int_{\substack{S_n\\ n=m}} Q^n\hat{n}.\nabla G(\bar{r}_m,\bar{r}_n')ds' . \quad (2.37)$$

Computation of the first term on the right-hand side of equation (2.37) gives no problem. The singularity occurs in the second term on the right-hand side of equation (2.37) because of the involvement of $\frac{1}{R}$ in the Green's function. To avoid computational difficulties, we separate the relevant Green's function into the whole-space part and reflected part contributions. Therefore, we can write the second integral on the right-hand side of equation (2.37) in the following form:

$$\int_{\substack{S_n\\ n=m}} Q^n\hat{n}.\nabla G(\bar{r}_m,\bar{r}_n')ds' = \int_{\substack{S_n\\ n=m}} Q^n\hat{n}.\nabla G^W(\bar{r}_m,\bar{r}_n')ds' + \int_{\substack{S_n\\ n=m}} Q^n\hat{n}.\nabla G^R(\bar{r}_m,\bar{r}_n')ds' . \quad (2.38)$$

Here, the superscripts W and R on G denote the whole space and reflected contributions to Green's function, respectively. G without a superscript involves both contributions. The reflection term [second term on the right-hand side of equation (2.38)] does not produce any computational problem as the field point and image source are separated. A singularity occurs only in the whole-space term appearing as the first term on the right-hand side of equation (2.38). The solution of the first integral on the right-hand side of equation (2.38) is $-2\pi Q^n$ for $n=m$ (Kellogg, 1953). Therefore, equation (2.37) can be written as

$$\int_S Q\hat{n}.\nabla G(\bar{r}_m,\bar{r}')ds' = \sum_{\substack{n=1\\ n\neq m}}^{N-1}\int_{S_n} Q^n\hat{n}.\nabla G(\bar{r}_m,\bar{r}_n')ds' - 2\pi Q^n + \int_{\substack{S_n\\ n=m}} Q^n\hat{n}.\nabla G^R(\bar{r}_m,\bar{r}_n')ds' . \quad (2.39)$$

Equations (2.35) and (2.39) at a field point m yield

$$\frac{4\pi\sigma_B}{\sigma_H-\sigma_B}Q^n_{n=m}=\frac{I}{\sigma_s}\hat{n}.\nabla G(\bar{r}_m,\bar{r}_s')+\sum_{\substack{n=1\\n\neq m}}^{N-1}\int_{S_n}Q^n\hat{n}.\nabla G(\bar{r}_m,\bar{r}_n')ds'-2\pi Q^n_{n=m}+\int_{S_n}Q^n\hat{n}.\nabla G^R(\bar{r}_m,\bar{r}_n')ds'. \tag{2.40}$$

After simplification, this equation can be written as

$$\frac{2\pi(\sigma_H+\sigma_B)}{\sigma_H-\sigma_B}Q^n_{n=m}=\frac{I}{\sigma_s}\hat{n}.\nabla G(\bar{r}_m,\bar{r}_s')+\sum_{\substack{n=1\\n\neq m}}^{N-1}\int_{S_n}Q^n\hat{n}.\nabla G(\bar{r}_m,\bar{r}_n')ds'+\int_{S_n}Q^n\hat{n}.\nabla G^R(\bar{r}_m,\bar{r}_n')ds'. \tag{2.41}$$

Now we assume that the surface charge density is constant on each cell (pulse basis function is considered). Therefore, we can write equation (2.41) in the following form:

$$-\frac{I}{\sigma_s}\hat{n}.\nabla G(\bar{r}_m,\bar{r}_s')=\sum_{\substack{n=1\\n\neq m}}^{N-1}Q^n\int_{S_n}\hat{n}.\nabla G(\bar{r}_m,\bar{r}_n')ds'+Q^n\int_{S_n}\hat{n}.\nabla G^R(\bar{r}_m,\bar{r}_n')ds'-CQ^n_{n=m}. \tag{2.42}$$

In the above equation, we have used

$$C=\frac{2\pi(\sigma_H+\sigma_B)}{\sigma_H-\sigma_B}. \tag{2.43}$$

Introducing

$$\hat{n}.\bar{E}_m^i=\frac{-\hat{n}.\nabla G(\bar{r}_m,\bar{r}_s')}{\sigma_s}I \tag{2.44}$$

as the outward normal component of the electric field normalised with σ_s, we write equation (2.42) as

$$\hat{n}.\overline{E}_m^i = \sum_{\substack{n=1 \\ n\neq m}}^{N-1} Q^n \int_{S_n} \hat{n}.\nabla G(\bar{r}_m, \bar{r}_n')ds' + Q^n \int_{\substack{S_n \\ n=m}} \hat{n}.\nabla G^R(\bar{r}_m, \bar{r}_n')ds' - CQ^n \,. \qquad (2.45)$$

Collecting Q^n on the right-hand side,

$$\hat{n}.\overline{E}_m^i = \sum_{n=1}^{N} (\Gamma^{mn} - \delta^{mn})Q^n \,, \qquad (2.46)$$

where

$$\Gamma^{mn} = \int_{S_n} \hat{n}.\nabla G(\bar{r}_m, \bar{r}_n')ds' \,, \quad \text{and} \quad \delta^{mn} = 0 \qquad \text{if} \quad m \neq n \,, \qquad (2.47)$$

and

$$\Gamma^{mn} = \int_{S_n} \hat{n}.\nabla G^R(\bar{r}_m, \bar{r}_n')ds' \,, \quad \text{and} \quad \delta^{mn} = C \qquad \text{if} \quad m = n \,. \qquad (2.48)$$

Defining,

$$K^{mn} = \Gamma^{mn} - \delta^{mn} \,, \qquad (2.49)$$

equation (2.46) becomes

$$\hat{n}.\overline{E}_m^i = \sum_{n=1}^{N} K^{mn} Q^n \,. \qquad (2.50)$$

Considering the field point at the centre of each cell (point collocation) ($m = 1, 2, ..., N$), we obtain from equation (2.50) the following partitioned matrix equations:

$$|E| = |K||Q| \,. \qquad (2.51)$$

Computing the normal component of the required Green's functions, i.e. $\hat{n}.G(\bar{r}_m, \bar{r}_s')$, $\hat{n}.G(\bar{r}_m, \bar{r}_n')$, and $\hat{n}.G^R(\bar{r}_m, \bar{r}_n')$, the elements of $|E|$ and $|K|$ are computed, and then, matrix inversion of equation (2.51) will result in the computation of the elements of $|Q| = \left|\frac{q}{\varepsilon_\circ}\right|$ on the surface of each cell. Finally, the potential at any point $\bar{r}_p$ outside the inhomogeneity can be obtained by using equation (2.24) as

$$V(\bar{r}_p) = \frac{I}{4\pi\sigma_s} G(\bar{r}_p, \bar{r}_s') + \frac{1}{4\pi} \sum_{n=1}^{N} \frac{q^n}{\varepsilon_\circ} \int_{S_n} G(\bar{r}_p, \bar{r}_n') ds \,. \tag{2.52}$$

In Figure 2.5, we consider a two-layered earth, in which an inhomogeneity (or body) with conductivity σ_B (or resistivity ρ_B) is embedded in the lower half-space with conductivity $\sigma_2 = \sigma_H$ (or resistivity $\rho_2 = \rho_H$). In this case, the external source is a current electrode at $\bar{r}_s'$ on the ground surface. In this situation, we have $\sigma_s = \sigma_1$, and thus, the layered earth potential $V_N(\bar{r}_p)$ is expressed as

$$V_N(\bar{r}_p) = \frac{I}{2\pi\sigma_1} G(\bar{r}_p, \bar{r}_s') \,. \tag{2.53}$$

Different Green's functions, $G(\bar{r}_m, \bar{r}_s')$, $G(\bar{r}_m, \bar{r}_n')$, and $G^R(\bar{r}_m, \bar{r}_n')$ for evaluating $|Q|$ [used in equations (2.44)-(2.48)], and $G(\bar{r}_p, \bar{r}_s')$ and $G(\bar{r}_p, \bar{r}_n')$ for computing $V(\bar{r}_p)$ [used in equation (2.52)], are shown in Figure 2.5. In this Figure, $G(\bar{r}_p, \bar{r}_s')$ represents the potential at point $\bar{r}_p$ due to the unit current source at $\bar{r}_s'$ on the surface of the layered earth, $G(\bar{r}_m, \bar{r}_s')$ represents the potential at the centre of an elementary cell due to the current point source at $\bar{r}_s'$, $G(\bar{r}_m, \bar{r}_n')$ represents the potential at the centre of an elementary cell due to the surface charge density at $\bar{r}_n'$, and $G(\bar{r}_p, \bar{r}_n')$ represents the potential at point $\bar{r}_p$ due to the surface charge density at $\bar{r}_n'$. Expressions for various Green's functions using the spectral formalism will be

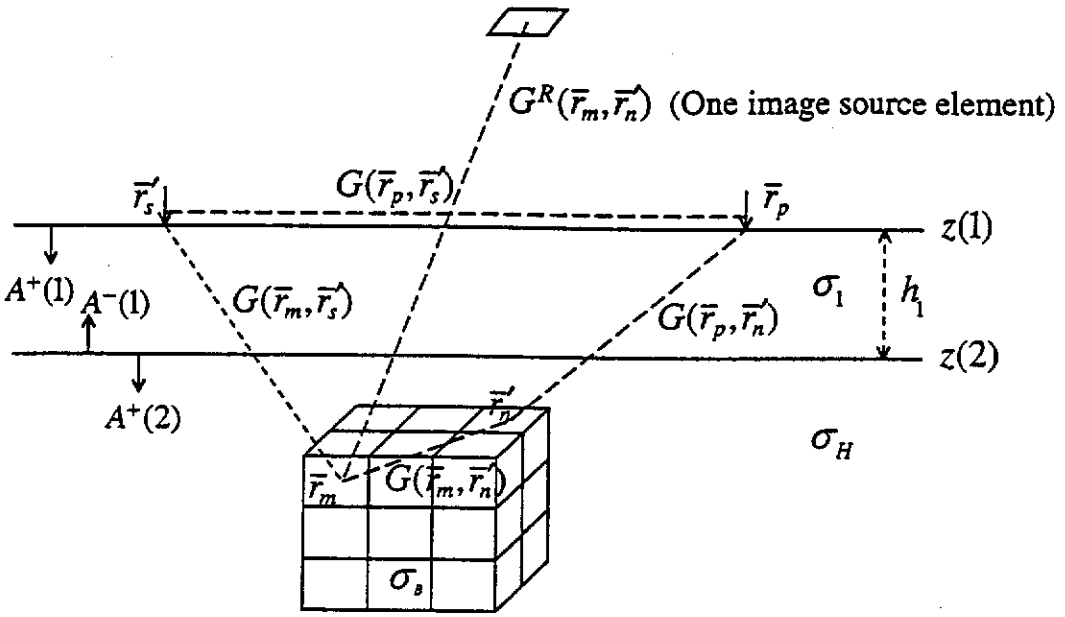

Figure 2.5. The Green's functions required for computation of the body response. $G(\bar{r}_p,\bar{r}_s')$ is the Green's function for the layered earth potential at point $\bar{r}_p$ due to the current point source at $\bar{r}_s'$, $G(\bar{r}_m,\bar{r}_s')$ is the Green's function for the electric field at the centre of a surface cell ($\bar{r}_m$) due to the current point source at $\bar{r}_s'$, $G(\bar{r}_m,\bar{r}_n')$ is the Green's function for the interaction between the cells, and $G(\bar{r}_p,\bar{r}_n')$ is the Green's function for the anomalous potential at $\bar{r}_p$ due to the surface charge density at $\bar{r}_n'$. The body with conductivity σ_B is located in the lower half-space (host medium with conductivity σ_H) of a two-layered earth in which σ_1 and h_1 are, respectively, the conductivity and thickness of the first (overburden) layer. $z(1)$ and $z(2)$ are the depths to the layers. $A^+(1)$, $A^-(1)$ and $A^+(2)$ are the amplitudes (coefficients) at interfaces.

discussed later in this Chapter. The computed potential V for an electrode configuration is converted into apparent resistivity ρ_a by a simple transformation given by the expression

$$\rho_a = K\frac{V}{I}, \tag{2.54}$$

where K is a geometric factor and I is the electric current injected into the ground through the current electrode.

2.2.2 Method of weighted residuals

In the previous section, applying the pulse basis function we considered the surface charge density to be constant on each elementary cell. Here, we use a different method, known as the method of weighted residuals, for the distribution of the charge density Q on the surface of an inhomogeneity. Taking the terms containing Q in equation (2.35) to one side, we obtain

$$Q - \frac{\sigma_H - \sigma_B}{4\pi\sigma_B}\int_S Q\hat{n}.\nabla G(\bar{r},\bar{r}')ds' = \frac{I(\sigma_H - \sigma_B)}{4\pi\sigma_s\sigma_B}\hat{n}.\nabla G(\bar{r},\bar{r}_s') \ . \tag{2.55}$$

Factorising Q on the left-hand side of equation (2.55), we obtain

$$[I - \gamma\int_S \hat{n}.\nabla G(\bar{r},\bar{r}')ds']Q = \frac{I}{\sigma_s}\gamma\hat{n}.\nabla G(\bar{r},\bar{r}_s') . \tag{2.56}$$

In the above scalar equation, I is the identity operator and γ is given by

$$\gamma = \frac{\sigma_H - \sigma_B}{4\pi\sigma_B} . \tag{2.57}$$

Considering equation (2.57), γ has a fixed or constant value, since in this case the host medium and the body have constant conductivities. Equation (2.56) can be written in the following simple form

$$LQ = s, \tag{2.58}$$

where L is the linear integral operator, given by

$$L = 1 - \gamma \int_S \hat{n}.\nabla G(\bar{r}, \bar{r}')ds', \tag{2.59}$$

and s is the source term, expressed by

$$s = \frac{I}{\sigma_s} \gamma \hat{n}.\nabla G(\bar{r}, \bar{r}_s') \ . \tag{2.60}$$

Using the method of weighted residuals, we approximate the surface charge density Q by an N-term sum of suitably linear basis functions, i.e.

$$Q \approx \hat{Q} = \sum_{n=1}^{N} a_n Q_n, \tag{2.61}$$

where the coefficients a_n are to be determined.

Substituting the approximation (2.61) in equation (2.58) yields

$$\sum_{n=1}^{N} a_n L Q_n(\bar{r}') + \varepsilon = s, \tag{2.62}$$

where ε is the residual arising from the use of the approximation $\hat{Q}$ instead of Q. Now, we have to determine the coefficients a_n so that the residual is forced to zero. For this, we define a set of N weighting (or test) functions w_m and a suitable inner

product. Taking the inner product of equation (2.62) with each weighting function w_m yields

$$\sum_{n=1}^{N} a_n < w_m, LQ_n > + < w_m, \varepsilon > = < w_m, s > \quad \text{for } m = 1, 2, \ldots, N. \tag{2.63}$$

The weighted residuals, $< w_m, \varepsilon >$, are set to zero for all m. This forces the residual ε to be orthogonal to the weighting functions. Thus, equation (2.63) becomes

$$\sum_{n=1}^{N} a_n < w_m, LQ_n > = < w_m, s > \quad \text{for } m = 1, 2, \ldots, N. \tag{2.64}$$

Equation (2.64) is a set of linear algebraic equations deduced from the original integral equation (2.58). We can write equation (2.64) in the following matrix equation

$$\boldsymbol{Ta} = \boldsymbol{s}, \tag{2.65}$$

where the elements of matrix $\boldsymbol{T}$ are given by

$$T_{mn} = < w_m, LQ_n >, \tag{2.66}$$

and the elements of vector $\boldsymbol{s}$ are given by

$$s_m = < w_m, s >. \tag{2.67}$$

Equation (2.65) is to be solved for $\boldsymbol{a}$, the vector of unknown coefficients. Then we obtain $\hat{Q}$, the approximation for Q, from equation (2.61). The difficulty in this method, from numerical point of view, is to choose the basis functions Q_n and the weighting functions w_m that approximate the unknown function Q well and also provide a stable solution. In addition, the elements of matrix $\boldsymbol{T}$ must be relatively

easy to evaluate. Otherwise, it results in numerical difficulties, which make the solution very difficult or impossible.

2.3 Spectral formalism for Green's function computation

In the classical method of propagator matrix formalism for computing the electrical potential (or Green's functions) as a result of a direct current electric source in a layered earth, the field quantities at two different levels are expressed in terms of each other via a propagator matrix. In this formalism the general expression for the electrical potential at any point is given by

$$V(r_m, z_m) = \frac{1}{2\pi}\int_0^\infty [c_1 e^{-\lambda(z_m - z_{ref})} + c_2 e^{\lambda(z_m - z_{ref})}] J_0(\lambda r_m) d\lambda, \tag{2.68}$$

where r_m is the horizontal separation between the source and field point, z_m is the depth of the field point measured from a reference depth z_{ref}, c_1 and c_2 are coefficients, λ is the integration variable and J_0 is the Bessel function of the first kind of order zero. The exponentials with positive arguments (or hyperbolic functions) that occur in the expression may cause a computer overflow problem in the numerical computation. Although exponentials with positive arguments using this formalism can be avoided in some cases, for a buried source when the propagation has to be carried out beyond the source level the problem of positive exponentials cannot be avoided. This difficulty can be overcome in the spectral formalism (Das and de Hoop, 1995) by using only exponential functions with non-positive arguments. This spectral formalism is presented in the first section of Appendix A for ready reference. In later section of Appendix A, it is used for the computations of various Green's functions.

We consider a two-layered earth model in which a 3-D body is embedded in the lower half-space (Figure 2.5). In this Figure, $z(1)$ and $z(2)$ are the depths of the air-earth interface and the second interface separating the overburden and the lower half-

space, respectively. We use the spectral formalism to obtain the various Green's functions required for our computations. Here, we use the suffixes *ab* which indicate computation of the electric potential at *a* due to a unit current at *b*.

For the Green's function $G(\bar{r}_p, \bar{r}_s')$, which represents the potential at point $\bar{r}_p$ due to the unit current source at $\bar{r}_s'$ on the surface of the layered earth, using the spectral formalism we write

$$G(\bar{r}_p, \bar{r}_s') = \frac{1}{2\pi}\int_0^\infty [A_{ps}^+(1)e^{-\lambda(z_p - z(1))} + A_{ps}^-(1)e^{-\lambda(z(2)-z_p)}]J_0(\lambda r_p)\lambda d\lambda . \qquad (2.69)$$

Considering Figure 2.6, the field point at $\bar{r}_p$ is located on the surface where $z_p = z(1)$, and also we have $z(2) - z_p = h_1$ where h_1 is the thickness of the first layer. Thus, we can write equation (2.69) as

$$G(\bar{r}_p, \bar{r}_s') = \frac{1}{2\pi}\int_0^\infty [A_{ps}^+(1) + A_{ps}^-(1)e^{-\lambda h_1}]J_0(\lambda r_p)\lambda d\lambda . \qquad (2.70)$$

To determine the coefficients $A_{ps}^+(1)$ and $A_{ps}^-(1)$, we use the relevant equations presented in Appendix A. We obtain (see Appendix A)

$$A_{ps}^+(1) = \frac{I}{\lambda}\frac{1}{\sigma_0(1+k_1e^{-2\lambda h_1}) + \sigma_1(1-k_1e^{-2\lambda h_1})}, \qquad (2.71)$$

and

$$A_{ps}^-(1) = \frac{I}{\lambda}\frac{k_1e^{-\lambda h_1}}{\sigma_0(1+k_1e^{-2\lambda h_1}) + \sigma_1(1-k_1e^{-2\lambda h_1})}, \qquad (2.72)$$

where k_1 is defined as

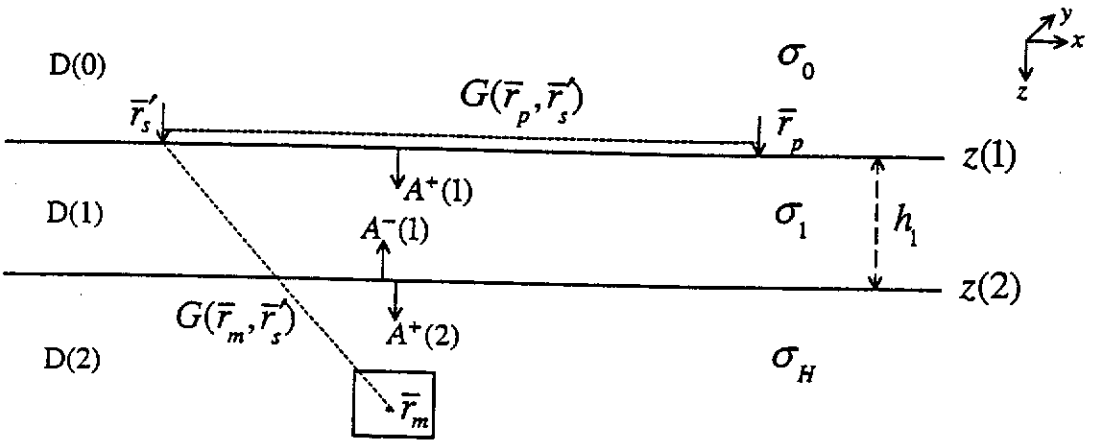

Figure 2.6. The geometry of a two-layered earth with a point source on the surface. Considering the source at $\bar{r}_s'$ and field points at $\bar{r}_p$ and $\bar{r}_m$, the Green's functions $G(\bar{r}_p, \bar{r}_s')$ and $G(\bar{r}_m, \bar{r}_s')$ are determined using the spectral formalism. σ_0, σ_1 and σ_H are the conductivities of domains D(0), D(1) and D(2), respectively. h_1 is the thickness of domain D(1). $z(1)$ and $z(2)$ are the depths to the domains D(1) and D(2), respectively. $A^+(1)$, $A^-(1)$ and $A^+(2)$ are the amplitudes (coefficients) at interfaces.

$$k_1 = \frac{\sigma_1 - \sigma_H}{\sigma_1 + \sigma_H}. \tag{2.73}$$

Here, σ_0 is the conductivity of the uppermost layer D(0) in Figure 2.6, σ_1 is the conductivity of the first layer [overburden D(1)], and σ_H is the conductivity of the host medium D(2). Substituting equations (2.71) and (2.72) in equation (2.70) yields

$$G(\bar{r}_p, \bar{r}_s') = \frac{I}{2\pi}\int_0^\infty \frac{(1+k_1 e^{-2\lambda h_1})}{\sigma_0(1+k_1 e^{-2\lambda h_1}) + \sigma_1(1-k_1 e^{-2\lambda h_1})} J_0(\lambda r_p) d\lambda. \tag{2.74}$$

Considering that the uppermost medium above the earth surface is air, we have $\sigma_0 = 0$. Thus, for this case equation (2.74) is written as

$$G(\bar{r}_p, \bar{r}_s') = \frac{I}{2\pi\sigma_1}\int_0^\infty \frac{1+k_1 e^{-2\lambda h_1}}{1-k_1 e^{-2\lambda h_1}} J_0(\lambda r_p) d\lambda. \tag{2.75}$$

To obtain the Green's function $G(\bar{r}_m, \bar{r}_s')$, as shown in Figure 2.6, we consider the field point $\bar{r}_m$ at the centre of an elementary surface cell of the body. The expression for the Green's function $G(\bar{r}_m, \bar{r}_s')$ for this case is written in the following form:

$$G(\bar{r}_m, \bar{r}_s') = \frac{1}{2\pi}\int_0^\infty A_{ms}^+(2) e^{-\lambda(z_m - z(2))} J_0(\lambda r_m) \lambda d\lambda. \tag{2.76}$$

Again, considering Figure 2.6, we have $z(2) = z_s' + h_1$ where z_s' is the depth to the current point source at r_s'. Thus, we can write equation (2.76) in the following form:

$$G(\bar{r}_m, \bar{r}_s') = \frac{1}{2\pi}\int_0^\infty A_{ms}^+(2) e^{-\lambda(z_m - z_s' - h_1)} J_0(\lambda r_m) \lambda d\lambda. \tag{2.77}$$

In this case, we obtain the coefficient $A_{ms}^+(2)$ (see Appendix A) as

$$A_{ms}^{+}(2)=\frac{I}{\lambda}\frac{(1+k_1)e^{-\lambda h_1}}{\sigma_0(1+k_1e^{-2\lambda h_1})+\sigma_1(1-k_1e^{-2\lambda h_1})}, \tag{2.78}$$

where k_1 is given by equation (2.73). Substituting equation (2.78) in equation (2.77), we obtain the expression for the Green's function $G(\bar{r}_m,\bar{r}_s')$ as

$$G(\bar{r}_m,\bar{r}_s')=\frac{I}{2\pi}\int_0^{\infty}\frac{(1+k_1)e^{-\lambda(z_m-z_s')}}{\sigma_0(1+k_1e^{-2\lambda h_1})+\sigma_1(1-k_1e^{-2\lambda h_1})}J_0(\lambda r_m)d\lambda. \tag{2.79}$$

Since $\sigma_0=0$, we can write equation (2.79) for this case as

$$G(\bar{r}_m,\bar{r}_s')=\frac{I}{2\pi\sigma_1}\int_0^{\infty}\frac{(1+k_1)e^{-\lambda(z_m-z_s')}}{1-k_1e^{-2\lambda h_1}}J_0(\lambda r_m)d\lambda. \tag{2.80}$$

The Green's function $G(\bar{r}_p,\bar{r}_n')$, shown in Figure 2.7, is of the same form as $G(\bar{r}_p,\bar{r}_s')$ but with different coefficients, i.e.

$$G(\bar{r}_p,\bar{r}_n')=\frac{1}{2\pi}\int_0^{\infty}[A_{pn}^{+}(1)+A_{pn}^{-}(1)e^{-\lambda h_1}]J_0(\lambda r_p)\lambda d\lambda. \tag{2.81}$$

The coefficients $A_{pn}^{+}(1)$ and $A_{pn}^{-}(1)$ are obtained (see Appendix A) as

$$A_{pn}^{+}(1)=\frac{I}{2\lambda\sigma_H}\frac{(1-k_1)\dfrac{\sigma_1-\sigma_0}{\sigma_1+\sigma_0}e^{-\lambda(z_n'-z_p)}}{1-k_1\dfrac{\sigma_1-\sigma_0}{\sigma_1+\sigma_0}e^{-2\lambda h_1}}, \tag{2.82}$$

and

$$A_{pn}^{-}(1)=\frac{I}{2\lambda\sigma_H}\frac{(1-k_1)e^{-\lambda(z_n'-z_p-h_1)}}{1-k_1\dfrac{\sigma_1-\sigma_0}{\sigma_1+\sigma_0}e^{-2\lambda h_1}}, \tag{2.83}$$

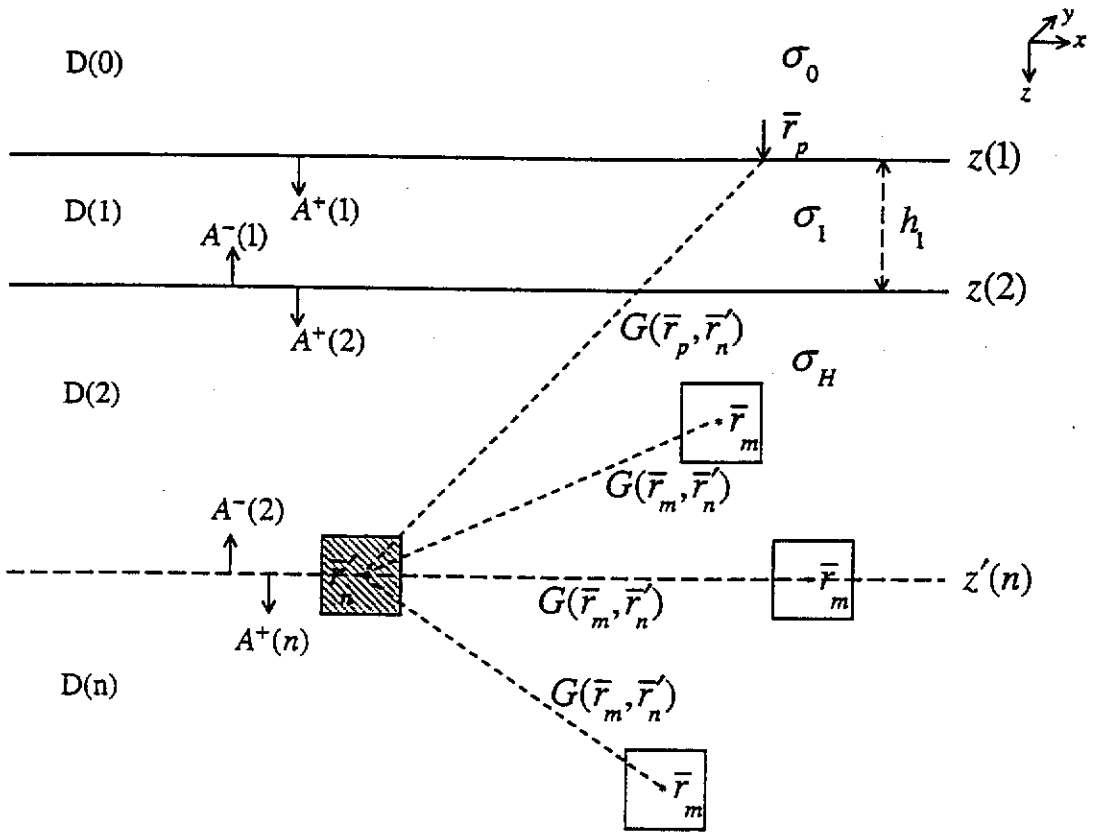

Figure 2.7. The geometry of a two-layered earth with a fictitious horizontal interface at the source cell. Considering the source cell at $\bar{r}_n'$ and field points at $\bar{r}_p$ and $\bar{r}_m$, the Green's functions $G(\bar{r}_p, \bar{r}_n')$ and $G(\bar{r}_m, \bar{r}_n')$ are determined using the spectral formalism. σ_0 and σ_1 are the conductivities of domains D(0) and D(1), respectively. σ_H is the conductivity of domain D(2) that is the same conductivity as for domain D(n). h_1 is the thickness of domain D(1). $z(1)$, $z(2)$ and $z'(n)$ are the depths to the domains D(1) and D(2) and D(n), respectively. $A^+(1)$, $A^-(1)$, $A^+(2)$, $A^-(2)$ and $A^+(n)$ are the amplitudes (coefficients) at interfaces.

where $z_n' = z'(n)$ is the depth to the source element (Figure 2.7). Equations (2.81), (2.82) and (2.83) yield

$$G(\bar{r}_p, \bar{r}_n') = \frac{I}{4\pi\sigma_H} \int_0^\infty \frac{(1-k_1)\dfrac{2\sigma_1}{\sigma_1+\sigma_0} e^{-\lambda(z_n'-z_p)}}{1-k_1\dfrac{\sigma_1-\sigma_0}{\sigma_1+\sigma_0} e^{-2\lambda h_1}} J_0(\lambda r_p) d\lambda . \tag{2.84}$$

Again $\sigma_0 = 0$, so we can write equation (2.84) for this case as

$$G(\bar{r}_p, \bar{r}_n') = \frac{I}{4\pi\sigma_H} \int_0^\infty \frac{(1-k_1)2e^{-\lambda(z_n'-z_p)}}{1-k_1 e^{-2\lambda h_1}} J_0(\lambda r_p) d\lambda . \tag{2.85}$$

To obtain the Green's function $G(\bar{r}_m, \bar{r}_n')$, we consider Figure 2.7, in which both the field point $\bar{r}_m$ and the source at $\bar{r}_n'$, are located in the lower half-space of a two-layered earth. Three depth locations of the field point $\bar{r}_m$ above, at, and below the source element are considered. The Green's functions $G(\bar{r}_m, \bar{r}_n')$ corresponding to these locations are

$$G(\bar{r}_m, \bar{r}_n') = \frac{1}{2\pi} \int_0^\infty [A_{mn}^+(2) e^{-\lambda(z_m - z(2))} + A_{mn}^-(2) e^{-\lambda(z_n'-z_m)}] J_0(\lambda r_m) \lambda d\lambda \quad \text{for} \quad z_m < z_n', \tag{2.86}$$

and

$$G(\bar{r}_m, \bar{r}_n') = \frac{1}{2\pi} \int_0^\infty A_{mn}^+(n) e^{-\lambda(z_m - z_n')} J_0(\lambda r_m) \lambda d\lambda \quad \text{for} \quad z_m \geq z_n', \tag{2.87}$$

where z_m is the depth to the field point $\bar{r}_m$ and z_n' is the depth to the source element. The coefficients $A_{mn}^+(2)$, $A_{mn}^-(2)$ and $A_{mn}^+(n)$ in the above expressions are obtained (see Appendix A) as

$$A_{mn}^{+}(2)=\frac{I}{2\lambda\sigma_H}\frac{(\frac{\sigma_1-\sigma_0}{\sigma_1+\sigma_0}e^{-2\lambda h_1}-k_1)e^{-\lambda(z_n'-z(2))}}{1-k_1\frac{\sigma_1-\sigma_0}{\sigma_1+\sigma_0}e^{-2\lambda h_1}}, \tag{2.88}$$

$$A_{mn}^{-}(2)=\frac{I}{2\lambda\sigma_H}, \tag{2.89}$$

and

$$A_{mn}^{+}(n)=\frac{I}{2\lambda\sigma_H}\frac{(1-k_1\frac{\sigma_1-\sigma_0}{\sigma_1+\sigma_0}e^{-2\lambda h_1})+(\frac{\sigma_1-\sigma_0}{\sigma_1+\sigma_0}e^{-2\lambda h_1}-k_1)e^{-2\lambda z'}}{1-k_1\frac{\sigma_1-\sigma_0}{\sigma_1+\sigma_0}e^{-2\lambda h_1}e^{-2\lambda h_1}}. \tag{2.90}$$

Substituting equations (2.88) and (2.89) in equation (2.86) yields

$$G(\bar{r}_m,\bar{r}_n')=\frac{I}{4\pi\sigma_H}\int_0^{\infty}\frac{(1-k_1\frac{\sigma_1-\sigma_0}{\sigma_1+\sigma_0}e^{-2\lambda h_1})e^{-\lambda(z_n'-z_m)}+(\frac{\sigma_1-\sigma_0}{\sigma_1+\sigma_0}e^{-2\lambda h_1}-k_1)e^{-\lambda(z_m+z_n'-2z(2))}}{1-k_1\frac{\sigma_1-\sigma_0}{\sigma_1+\sigma_0}e^{-2\lambda h_1}}.$$
$$.J_0(\lambda r_m)d\lambda \quad \text{for} \quad z_m<z_n'. \tag{2.91}$$

Also, substituting equation (2.90) in equation (2.87), we obtain

$$G(\bar{r}_m,\bar{r}_n')=\frac{I}{4\pi\sigma_H}\int_0^{\infty}\frac{(1-k_1\frac{\sigma_1-\sigma_0}{\sigma_1+\sigma_0}e^{-2\lambda h_1})e^{-\lambda(z_m-z_n')}+(\frac{\sigma_1-\sigma_0}{\sigma_1+\sigma_0}e^{-2\lambda h_1}-k_1)e^{-\lambda(z_m+z_n'-2z(2))}}{1-k_1\frac{\sigma_1-\sigma_0}{\sigma_1+\sigma_0}e^{-2\lambda h_1}}.$$
$$.J_0(\lambda r_m)d\lambda \quad \text{for} \quad z_m\geq z_n'. \tag{2.92}$$

Equations (2.91) and (2.92) can be written in the following form:

$$G(\bar{r}_m,\bar{r}_n')=\frac{I}{4\pi\sigma_H}\int_0^\infty \frac{(1-k_1\frac{\sigma_1-\sigma_0}{\sigma_1+\sigma_0}e^{-2\lambda h_1})e^{-\lambda|z_m-z_n'|}+(\frac{\sigma_1-\sigma_0}{\sigma_1+\sigma_0}e^{-2\lambda h_1}-k_1)e^{-\lambda(z_m+z_n'-2z(2))}}{1-k_1\frac{\sigma_1-\sigma_0}{\sigma_1+\sigma_0}e^{-2\lambda h_1}}$$

$$.J_0(\lambda r_m)d\lambda. \tag{2.93}$$

Considering that the uppermost medium above the earth surface is air, we have $\sigma_0=0$. Thus, equation (2.93) for this case is written as

$$G(\bar{r}_m,\bar{r}_n')=\frac{I}{4\pi\sigma_H}\int_0^\infty \frac{(1-k_1e^{-2\lambda h_1})e^{-\lambda|z_m-z_n'|}+(e^{-2\lambda h_1}-k_1)e^{-\lambda(z_m+z_n'-2z(2))}}{1-k_1e^{-2\lambda h_1}}J_0(\lambda r_m)d\lambda. \tag{2.94}$$

The various expressions for the Green's functions are of the form:

$$f(\bar{r}_a,\bar{r}_b')=\int_0^\infty K_{ab}(\lambda)J_i(\lambda r_a)d\lambda, \tag{2.95}$$

where J_i is the Bessel function of the first kind of order i and $K_{ab}(\lambda)$ is the function which involves the coefficients and exponential terms. Using the filter weights, the above expression (2.95) is computed in the following way:

$$f(\bar{r}_a,\bar{r}_b')=\int_0^\infty K_{ab}(\lambda)J_i(\lambda r_a)d\lambda=\frac{1}{r_a}\sum_{i=1}^{n}K_{ab}(\lambda_i)W_i, \tag{2.96}$$

where W_i are the n filter weights. $K_{ab}(\lambda_i)$ is computed for different values of λ_i, given by

$$\lambda_i=(\frac{1}{r_a})\times 10^{[a+(i-1)d]},\qquad i=1,2,\ldots,n. \tag{2.97}$$

Here a is the shift (for placement of the starting point for sampling the input function), and d is the sampling interval or spacing.

In the computations for Hankel integrals appearing in numerical integrations (e.g. numerical computations of the integrals in the above Green's functions expressions), we used a 61-point filter for Hankel J_0 transforms given by Koefoed et al. (1972) and a 14-point filter for Hankel J_1 transforms given by Das (1982). However, the required accuracy of the computations could not be achieved for some geoelectrical situations. For this reason, later we used a 120-point filter for the J_0 kernel and a 140-point filter for the J_1 kernel, both given by Guptasarma and Singh (1997). In these new filters, the filter weights, the values of the shift a and the sampling interval or spacing s were designed to be restricted to 12 significant digits. All the digits of the filter parameters need to be retained in order to have good error performance.

2.4 Conjugate gradient method

Solving the partitioned matrix equation in the 3-D resistivity modelling problem using the integral equation technique is a crucial stage in the modelling since the unknown electric charges are determined from the solution. To solve these matrix equations, either direct or iterative methods may be used. Although direct methods such as LU decomposition always provide solutions to the matrix equations, they become inefficient when the coefficient matrix is large. Furthermore, direct methods are more likely to be affected by round-off errors. On the contrary, iterative (or indirect) methods for the case of large matrix equations have some advantages over direct methods. For example, they are more economical in computer memory requirements, and also they are self-correcting if an error is made in the process (iterations) leading to the solution. The conjugate gradient technique, which is one of the most efficient iterative methods available, can be used for this purpose. The conjugate gradient method has several algorithms. The simplest, called the classical or ordinary conjugate gradient algorithm, solves a matrix equation only in the case where the coefficient matrix is symmetric and positive definite. Here, we are faced with

partitioned matrix equations where the coefficient matrix is not necessarily symmetric or positive definite. Hence, we use the biconjugate gradient approach. In the following, a new implementation of the biconjugate gradient method for the solution of the electric charge density is presented.

Once the elements of $|E|$ and $|K|$ partitioned matrices are computed using various Green's functions, we may solve equation (2.51) for $|Q|$. This requires us to compute $|K^{-1}|$. We solve equation (2.51) using the biconjugate gradient method. In the ordinary conjugate gradient method, the function minimisation is carried out by generating a succession of search directions and improved minimisers and after N iterations the solution is obtained. However, the biconjugate gradient method, in general, does not have a simple connection with function minimisation. The advantage of the biconjagate gradient method is that it does not square the condition number of the original matrix equation, but since at each iteration no function is minimised, the method is not guaranteed to converge until N iterations. However, the rate of convergence can be quite fast if the eigenvalues are bunched together (Sarkar et al., 1988). The biconjugate gradient method uses two similar conjugate search direction vectors p_i and $\bar{p}_i$ resulting in two residual vectors ε_i and $\bar{\varepsilon}_i$ (for $i = 1, 2, ...$). These quantities correspond to the matrix K and its transpose K^T. We supply the initial vectors ε_1 and $\bar{\varepsilon}_1$, and set $p_1 = \varepsilon_1$, $\bar{p}_1 = \bar{\varepsilon}_1$. Then we compute quantities α_1 and β_1 using the following equations. In general, we carry out the following recurrence:

$$\alpha_i = \frac{\bar{\varepsilon}_i . \varepsilon_i}{\bar{p}_i . K . p_i}, \tag{2.98}$$

$$\varepsilon_{i+1} = \varepsilon_i - \alpha_i . K . p_i, \tag{2.99}$$

$$\bar{\varepsilon}_{i+1} = \bar{\varepsilon}_i - \alpha_i . K^T . \bar{p}_i, \tag{2.100}$$

$$\beta_i = \frac{\bar{\varepsilon}_{i+1}.\varepsilon_{i+1}}{\bar{\varepsilon}_i.\varepsilon_i}, \tag{2.101}$$

$$p_{i+1} = \varepsilon_i + \beta_i.p_i, \tag{2.102}$$

$$\bar{p}_{i+1} = \bar{\varepsilon}_i + \beta_i.\bar{p}_i. \tag{2.103}$$

If the recurrence does not break down earlier because one of the denominators is zero, it must terminate after $m \leq N$ steps with $\varepsilon_{m+1} = \bar{\varepsilon}_{m+1} = 0$ (Press et al., 1992).

Solving equation (2.51) by the biconjugate gradient algorithm requires an initial guess Q_1 for the solution. Therefore, the residual ε_1 will be

$$\varepsilon_1 = E - K.Q_1. \tag{2.104}$$

Also, we choose $\bar{\varepsilon}_1 = \varepsilon_1$. Carrying out the recurrence expressed in equations (2.98) to (2.103), we build up the sequence of improved estimates for Q:

$$Q_{i+1} = Q_i + \alpha_i.p_i. \tag{2.105}$$

This equation guarantees that the residual ε_{i+1} corresponding to Q_{i+1} in the recurrence is equal to $E - K.Q_{i+1}$. Since $\varepsilon_{m+1} = 0$, Q_{m+1} is the solution to equation (2.51).

The ordinary conjugate gradient algorithm is the special case of the biconjugate gradient algorithm when K is symmetric. The above computations become easier since for this case, we consider $\bar{\varepsilon}_1 = \varepsilon_1$ and then $\bar{\varepsilon}_i = \varepsilon_i$ and $\bar{p}_i = p_i$.

The rate of convergence is related to the condition number and the eigenspectrum of the coefficients matrix (Spitzer and Wurmstich, 1995). The rate of convergence of conjugate gradient algorithms or methods may be accelerated by preconditioning of

the coefficients matrix (i.e. matrix K here). This suggests that applying these methods to the preconditioned form of equation (2.51) yields the following equivalent equation system, which is to be solved.

$$(\tilde{K}^{-1}.K).Q = \tilde{K}^{-1}.E, \tag{2.106}$$

where $\tilde{K}^{-1}$ is an approximate inverse of K (i.e. $\tilde{K}$ is close to K) so that $\tilde{K}^{-1}.K \approx 1$. This idea allows the algorithm to converge in fewer steps. The matrix $\tilde{K}$ is called a preconditioner and the algorithm in this case is known as the preconditioned biconjugate gradient (PBCG) method. In the PBCG algorithm, an additional set of vectors η_i and $\overline{\eta}_i$ is introduced and defined by

$$\tilde{K}.\eta_i = \varepsilon_i, \tag{2.107}$$

and

$$\tilde{K}^T.\overline{\eta}_i = \overline{\varepsilon}_i. \tag{2.108}$$

Then, we modify the definitions of α_i, β_i, p_{i+1}, and $\overline{p}_{i+1}$ given in equations (2.98), (2.101), (2.102) and (2.103), respectively, in the following:

$$\alpha_i = \frac{\overline{\varepsilon}_i.\eta_i}{\overline{p}_i.K.p_i}, \tag{2.109}$$

$$\beta_i = \frac{\overline{\varepsilon}_{i+1}.\eta_{i+1}}{\overline{\varepsilon}_i.\eta_i}, \tag{2.110}$$

$$p_{i+1} = \eta_i + \beta_i p_i, \tag{2.111}$$

$$\overline{p}_{i+1} = \overline{\eta}_i + \beta_i \overline{p}_i. \tag{2.112}$$

In the computer program for the preconditioner $\tilde{K}$, we use the trivial diagonal part of the matrix K. Also in the program iteration stops when $\frac{|K.Q-E|}{|K|}$ is less than an input quantity known as desired convergence tolerance, which is chosen to be a very small number. In the computer program implementing the technique, we have considered this quantity to be 10^{-9}. If we make this quantity smaller, although the accuracy of the solution increases, the number of iterations also increases, which results in increasing computer time for numerical computation leading to the solution and also probably increases the accumulation of round-off error. This may cause computational difficulties because of limit in computer memory.

2.5 Discussion

Using a general spectral formalism, in which the current source electrode can be put at any point in a layered earth, the problem of computing the electric potential for the borehole case is simplified. The propagator matrix formalism is not suitable in this case since we may be faced with significant errors and instability in the numerical computation due to the appearance of exponentials with positive arguments in the expression for the electrical potential. In the spectral formalism, the use of exponentials with non-positive arguments results in numerical stability of the computations. As shown earlier in this Chapter, a body embedded in a layered earth can be cut across by a horizontal interface and accordingly the Green's function $G(\bar{r}_m, \bar{r}_n')$ can be easily calculated using the spectral formalism.

The biconjagate gradient method, used to solve the partitioned matrix equations for the electric charge density column vector Q, should provide higher accuracy than the LU decomposition method. By preconditioning of the coefficient matrix in the matrix equation the convergence of the algorithm is attained faster and the solution is obtained in fewer steps.

Applying new digital linear filters for Hankel J_0 and J_1 transforms, given by Guptasarma and Singh (1997), the accuracy of the computations is improved as these new filters with12-digit weights produce much smaller errors than the errors made by all other filters available for these transforms.

In this Chapter, we developed the theoretical considerations required for modelling resistivity responses of 3-D anomalies. This development is used to compute resistivity responses for different electrode configurations, enabling the development of processing techniques for signal enhancement discussed in the next Chapter.

Chapter 3

DEVELOPMENT OF PROCESSING TECHNIQUES FOR SIGNAL ENHANCEMENT

3.1 Introduction

A few attempts have been made in the past to improve target detectability or resolution by resistivity methods. In order to improve the anomalous response of a buried target in the subsurface, Brizzolari and Bernabini (1979) arranged the electrodes in special ways to focus the electric currents towards it. Focussing is obtained by sending a positive current from two or more current electrodes. The negative pole is supposed to be at a large distance. They used two different focussed electrode arrangements, which include the tri-electrode and penta-electrode configurations, for studying anomalies of some regular shaped bodies as well as buried cavities in the field. With these focussed electrode arrangements the current lines are directed downward resulting in a larger depth of penetration. In comparison with classical electrode configurations such as the Schlumberger array, these focussed electrode arrangements were found to give better signal-to-noise ratios. When superficial noise is small, the study shows that the focussed electrode arrangements can detect buried bodies or cavities, which cannot be localised with common, more conventional configurations. Focussed electrode arrangements are also used in resistivity well logging to force the electric current to a specific subsurface area in order to obtain more information from that area.

Also, in order to achieve higher resolution than can be obtained with a classical four-electrode data acquisition system, Shi and Morgan (1997) have outlined a new way to obtain resistivity data using a new multi-electrode data acquisition system (see Chapter 1) with a spatially varying source dipole (Figure 3.1). The measurement starts with injecting current into the ground at the number 1 electrode (Figure 3.1) with the current sink located at the *n*th electrode. Potential differences are measured

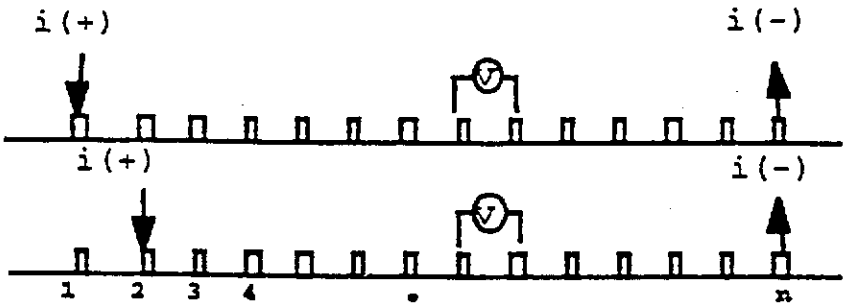

Figure 3.1. Field arrangement used by Shi and Morgan. In this arrangement, resistivity measurements are obtained using a multi-electrode data acquisition system with a spatially varying source dipole. A procedure is used for the resistivity data acquisition along the profile line, which leads to improved resolution of resistivity methods (From Shi and Morgan, 1997).

along the line of the current electrode pair. Then the current is injected into the ground at the number 2 electrode, while the current sink remains at the *n*th electrode, and the measurements are repeated. This procedure continues until all electrodes have been excited. The entire procedure is then repeated after reversing the geometry of the source dipole, i.e. the current sink is moved to the number 1 electrode, and the source is scanned starting from the *n*th electrode. Data collected in this way, using an inversion procedure, can lead to better resolution and mapping of subsurface structures, especially for those structures with laterally varying electrical properties.

In this Chapter, we present two new combinations of multisystem resistivity measurements, which lead to the development of new processing techniques for resistivity signal enhancement. Numerically modelled data are used to test these processing techniques. The effects of random noise on these techniques are also presented. Finally, these techniques are applied to real field data to investigate a subsurface conductive anomaly.

3.2 Multisystem measurements for signal enhancement

DC resistivity methods have low resolution and suffer from the smearing of the anomalous target response by the host medium. The response of the host medium, which is generally relatively very large, compared to that of the anomalous body, is superimposed on it. As a result, target detection by these methods is quite difficult.

In this thesis, we consider the common case of a horizontally layered host medium containing an anomalous 3-D body. We develop some processing techniques, which will reduce the contribution of the horizontally or subhorizontally layered earth to the total measured response, and thus, enhance the anomalous 3-D target response. The process to be developed uses multisystem resistivity measurements, i.e. the measurements of electrical potentials by different electrode configurations along a profile line. This is shown in Figure 3.2 where two combinations of electrode

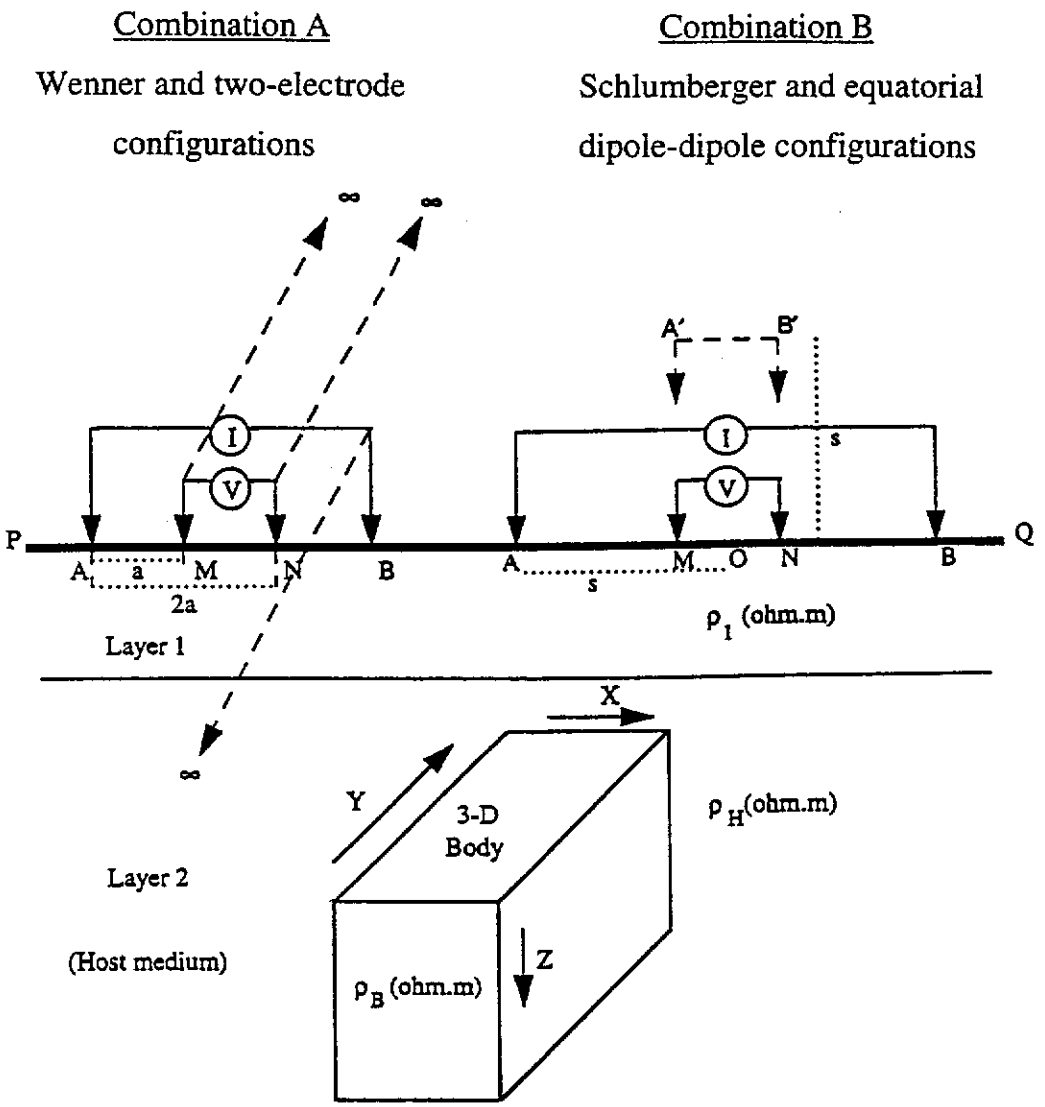

Figure 3.2. Field layout for multisystem resistivity measurements including two combinations A and B. Combination A involves the Wenner and two-electrode configurations and combination B involves the Schlumberger and equatorial dipole-dipole configurations. These combinations are used in the new processing techniques to enhance the anomalous 3-D body response.

configurations are indicated. Combination A involves the Wenner and two-electrode configurations and combination B involves the Schlumberger and equatorial dipole-dipole arrays. In the following, we discuss the development of the mathematical forward modelling theory. Based on that, multisystem measurements are computed and processed to reduce the layering contribution to the total measured signal.

In this section, two different techniques are presented for processing 3-D resistivity profiling measurements using a combination of electrode arrays (i.e. combination A or B as shown in Figure 3.2) to enhance the detectability of a subsurface body. The profiling measurements by different electrode arrays used in combinations A and B are made as follows. For resistivity profiling along a line PQ (Figure 3.2) using the Wenner configuration *AMNB*, in which the electrodes *A*, *M*, *N* and *B* are equally spaced with inter-electrode spacing a, voltage differences between the potential electrodes *MN* are measured after injecting an electric current into the ground using the current electrode pair *AB*. For potential measurement by the two-electrode configuration, two sets of active electrodes *AM* and *AN* are used to measure the potentials with spacings $AM=a$ and $AN=2a$. For the Schlumberger array *AMNB* (combination B), with a separation $\frac{AB}{2} = s$, after injecting of an electric current into the ground using the current electrode pair *AB*, the potential difference between two closely spaced potential measuring electrodes *MN* is measured. Then, for an equatorial dipole-dipole configuration $A'MNB'$ with dipole separation equal to s (i.e. $A'M = B'N = s$), we inject an electric current into the ground using the current electrode pair $A'B'$, and then measure the voltage difference between the same potential electrodes *M* and *N* used by the Schlumberger configuration. Any of these combinations measures the electric potential along a profiling line. The actual electrode spacings a and s are selected on the basis of nominal depth of investigation.

With the concept in mind, for signal enhancement through redundant field measurements using different geometries, the mathematical aspects need to be explored. If a theoretical justification can be developed, then field testing of the idea can follow. In section 3.2.1 and its subsections, the concept, theory and numerical

examples will be explored with the Wenner and two-electrode systems. Then in section 3.2.2 and its subsections, we examine the concept and theory for the Schlumberger and equatorial dipole-dipole systems with numerical examples.

3.2.1 Wenner and two-electrode measurements

The potential of a two-electrode configuration *AM*, i.e. the potential at potential electrode *M* due to a direct current point source at current electrode *A* (Figure 3.2) over a horizontally layered earth is expressed by (Koefoed, 1979a)

$$V_T(a = AM) = \frac{I}{2\pi}\int_0^\infty T(\lambda)J_0(\lambda a)d\lambda\,. \tag{3.1}$$

Here I is the electric current injected into the ground using electrode *A* on the ground surface, a=*AM* is the separation between the two active electrodes (i.e. the current electrode *A* and the potential point *M*). For the source and measuring point locations *A* and *M*, $T(\lambda)$ which includes the coefficients A^+ and A^- and the exponential terms, can be obtained using the spectral formalism discussed in Appendix A. The above expression changes to the following when the electrodes *A* and *N* are used as the two active electrodes of the two-electrode configuration (Figure 3.2):

$$V_T(2a = AN) = \frac{I}{2\pi}\int_0^\infty T(\lambda)J_0(\lambda 2a)d\lambda\,. \tag{3.2}$$

Now the potential difference measured by the Wenner configuration *AMNB* with an inter-electrode spacing a is given by

$$V_W(a) = V_T(AM = a) - V_T(AN = 2a) - V_T(BM = 2a) + V_T(BN = a)\,. \tag{3.3}$$

Equation (3.3) can be written as

$$V_W(a) = 2V_T(a) - 2V_T(2a). \tag{3.4}$$

Using equations (3.1) and (3.2), we obtain the expression for the potential difference measured by the Wenner configuration in the following form:

$$V_W(a) = \frac{I}{\pi}\int_0^\infty T(\lambda)[J_0(\lambda a) - J_0(\lambda 2a)]d\lambda. \tag{3.5}$$

Suppose we measure the electric potentials using a Wenner system with an inter-electrode spacing a and again with a two-electrode system with spacings a and $2a$. Then using these measurements we obtain

$$V_W(a) - 2V_T(a) + 2V_T(2a) = 0. \tag{3.6}$$

The apparent resistivity expression corresponding to the voltage equation is then obtained by multiplying equation (3.4) by $\frac{2\pi a}{I}$, which is (Das and Verma, 1980)

$$\rho_{aW}(a) = 2\rho_{aT}(a) - \rho_{aT}(2a). \tag{3.7}$$

Thus, we can write

$$\rho_{aW}(a) - 2\rho_{aT}(a) + \rho_{aT}(2a) = 0. \tag{3.8}$$

Considering equation (3.1) we can obtain the apparent resistivity expression for a two-electrode configuration with spacing a as

$$\rho_{aT}(a) = a\int_0^\infty T(\lambda)J_0(\lambda a)d\lambda. \tag{3.9}$$

Similarly, considering equation (3.2) we write the apparent resistivity expression for a two-electrode configuration with spacing $2a$ as

$$\rho_{aT}(2a) = 2a\int_0^\infty T(\lambda)J_0(\lambda 2a)d\lambda\,. \tag{3.10}$$

Also, using equation (3.5) we can obtain the apparent resistivity expression for a Wenner configuration with inter-electrode spacing a in the following form:

$$\rho_{aW}(a) = 2a\int_0^\infty T(\lambda)[J_0(\lambda a) - J_0(\lambda 2a)]d\lambda\,. \tag{3.11}$$

Equations (3.9), (3.10) and (3.11) also confirm the relationship between the two-electrode and Wenner apparent resistivities for a layered earth given in equation (3.7).

3.2.1.1 Signal enhancement

Equation (3.7) holds only for a layered earth free of any inhomogeneity (Das and Verma, 1980), and thus, this equation contains only the layered earth component of the potential since there is no anomalous potential in this case. If there is an inhomogeneity in the layered earth, as shown in Figure 3.2, this equation does not hold because in this situation, in addition to the layered earth potential, there will be an anomalous potential due to the presence of the inhomogeneity. In the profiling method to detect a 3-D body (Figure 3.2) by an electrode array, a total electric potential V^t is measured. This potential can be written as

$$V^t = V^l + V^b\,. \tag{3.12}$$

Here, V^l is the primary layered earth electric potential due to only the electric current injection into the layered earth (if the 3-D target is absent, the primary layered earth potential will be equal to the total potential). V^b is the anomalous electric potential contribution due to the electric charges developed on the surface of the anomalous body. It involves the layered earth interaction through a scalar Green's

function, as explained in Chapter 2. V^t measured by an electrode configuration is converted into apparent resistivity ρ_a^t by expression

$$\rho_a^t = K\frac{V^t}{I}, \tag{3.13}$$

where K is a geometric factor. Using equation (3.12), we can write equation (3.13) in the following form:

$$\rho_a^t = K\frac{V^l}{I} + K\frac{V^b}{I} = \rho_a^l + \rho_a^b. \tag{3.14}$$

Here, ρ_a^t is the total apparent resistivity, ρ_a^l is the layered earth contribution and ρ_a^b is anomalous body contribution to the total apparent resistivity measurement. Using equation (3.14), we can write for the two electrode configuration *AM* (Figure 3.2) with spacing a=*AM*,

$$\rho_{aT}^t(a) = \rho_{aT}^l(a) + \rho_{aT}^b(a). \tag{3.15}$$

Similarly, considering *AN*=$2a$ for the two-electrode configuration *AN*, we can write the apparent resistivity $\rho_{aT}^t(2a)$ as

$$\rho_{aT}^t(2a) = \rho_{aT}^l(2a) + \rho_{aT}^b(2a). \tag{3.16}$$

Also, employing a Wenner configuration *AMNB* with an inter-electrode spacing a, apparent resistivity $\rho_{aW}^t(a)$ for the Wenner system can be written as

$$\rho_{aW}^t(a) = \rho_{aW}^l(a) + \rho_{aW}^b(a). \tag{3.17}$$

In the absence of the body, the anomalous body contribution to the apparent resistivity (i.e. ρ_a^b) in equations (3.15)-(3.17) disappears, and thus in these equations,

$\rho_a^t = \rho_a^l$. In this case, equation (3.17) using equations (3.13) and (3.4), can be written as

$$\rho_{aW}^l(a) = 2\rho_{aT}^l(a) - \rho_{aT}^l(2a), \tag{3.18}$$

which is the same as equation (3.7). Thus, in the absence of an anomalous body, subtraction of the right-hand side of equation (3.18) from the left-hand side of this equation is equal to zero. However, in the presence of an anomalous body (where there is the anomalous body contribution in addition to the layered earth contribution to the apparent resistivity obtained by an electrode configuration), this subtraction yields an *apparent resistivity residual* $R(a)$ along a profile line given by

$$R(a) = \rho_{aW}^t(a) - 2\rho_{aT}^t(a) + \rho_{aT}^t(2a). \tag{3.19}$$

Computation of the residual $R(a)$ reduces considerably the primary layered earth contributions V^l to the measured potentials V^t in the two-electrode and Wenner apparent resistivity computations, and thus, includes mainly the anomalous contributions V^b due to the inhomogeneous body (Kamkar-Rouhani and Das, 1996a).

Equation (3.19) expresses the essence of a new processing technique which enhances the signal from, or resolution of, a target by reducing the contribution of (sub)horizontal layering effects to the total response. Thus, this new processing method operates as a filter. As noticed, in this processing technique at a profiling station three resistivity measurements (one measurement using the Wenner array with an inter-electrode spacing a and two measurements using the two-electrode array with spacings a and $2a$) are needed. Hence, the processing technique, in addition to its simplicity, uses data redundancy, which permits the attenuation of some distorting effects. Considering a need for three resistivity measurements at each station to use this processing technique, a considerable amount of data is required along each profile. The recent developments in the resistivity field data acquisition systems (see

Chapter 1) enable us to collect easily in a short time the large number of resistivity data required in this processing technique.

3.2.1.2 Numerical examples

Computations of apparent resistivity and corresponding *apparent resistivity residual* responses were carried out for a large number of models. Some of them are presented in this section. The models studied here include one 3-D body and multiple 3-D bodies in the lower half-space of a two-layered earth. In this section, to study these models, we put them into three categories: (1) a symmetric body, (2) an asymmetric body, and (3) multiple bodies. The computer program, developed for numerical modelling, uses elementary surface cells to simulate the body.

3.2.1.2.1 Symmetric body

Consider a conductive prismatic body with dimensions $50\times150\times100$ m and with a resistivity of $\rho_B = 5$ ohm.m, located in the lower half-space of a two-layered earth (Figure 3.3a). The body is located at a depth of 50 m below the ground surface. The resistivity of the host medium is $\rho_H = 200$ ohm.m. The first layer (overburden) has a resistivity of $\rho_1 = 800$ ohm.m and a thickness of $h_1 = 25$ m.

We place the model in a Cartesian coordinate system with its origin at a point vertically above the centre of the body on the surface of the ground. Following the resistivity profiling method, the two-electrode and Wenner apparent resistivity measurements are computed with different electrode spacings along a profile line PQ (Figure 3.3a) on the surface passing through the origin of the Cartesian coordinate system. Thus, in this coordinate system the line PQ is at $y = 0$. The body is placed symmetrically below the origin between –25 to 25 m in the x-direction, -75 to 75 m in the y-direction and 50 to 150 m in the z-direction (Figure 3.3a).

a)

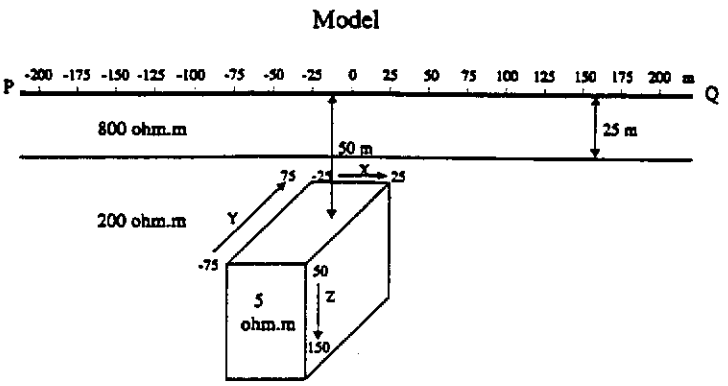

b)

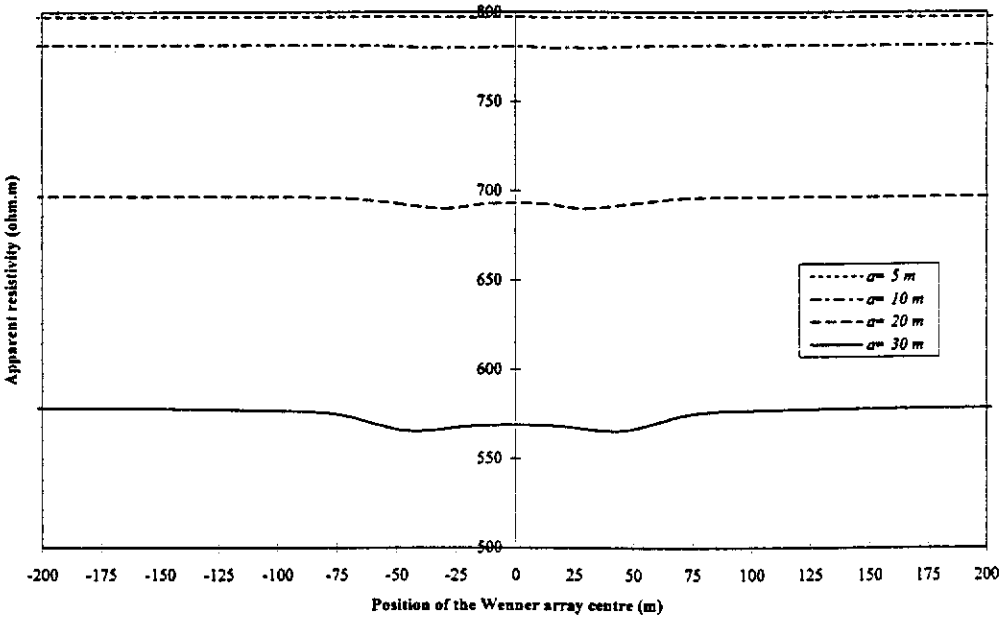

c)

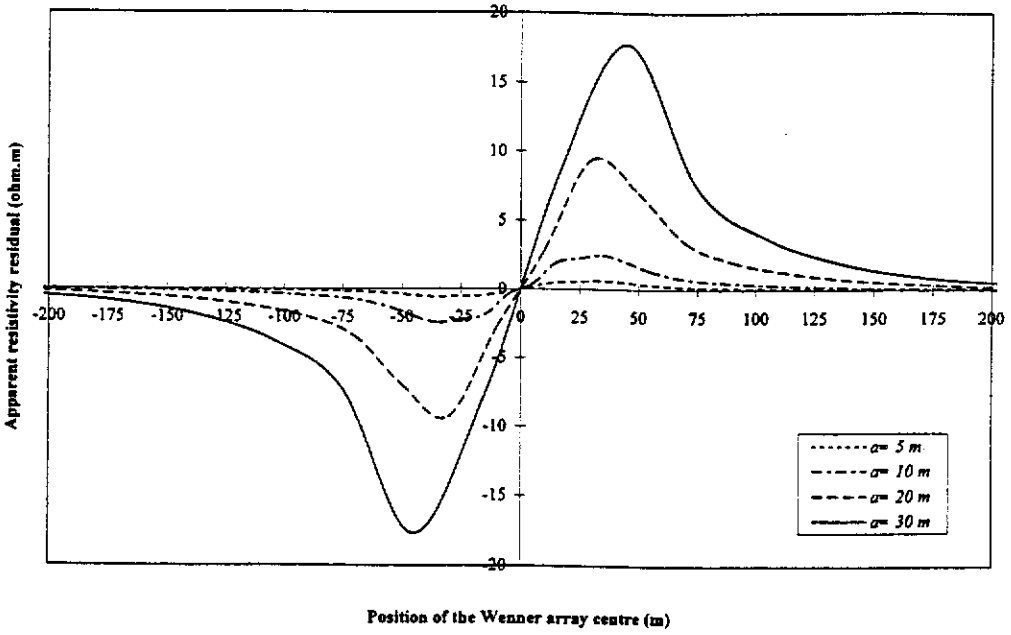

Figure 3.3. Survey combination A results for a symmetric conductive body with a resistive overburden. (a) Model, (b) Wenner apparent resistivity profiles along PQ, and (c) corresponding apparent resistivity residual response.

Figure 3.3b presents Wenner apparent resistivity profiles with different electrode spacings 5, 10, 20 and 30 m along the line PQ (Figure 3.3a) on the surface passing through the point vertically above the centre of the 3-D body. Although the body can be detected by the Wenner profiles with larger electrode spacings, the spatial resolution of the method is relatively poor. For this model the corresponding apparent resistivity residual responses, which have been calculated using equation (3.19), are plotted against the position of the centre of the Wenner array and indicated in Figure 3.3c. These *apparent resistivity residual* profiles indicate large variations in the anomalies. The negative and positive peaks of the residual profiles approximately occur at the lateral edges of the body. The crossover of an anomaly occurs at a point vertically above the centre of the body. However, with larger electrode spacings, the residual profiles show larger and wider responses and the peaks in these cases occur beyond the lateral edge of the body. The residual profiles go to zero far away from the body. This indicates that where the body is located a long distance away, the apparent resistivity residual is almost zero as if there were no body to create it (as the case of a layered earth free of an inhomogeneity). Comparing the Wenner apparent resistivity profiles (Figure 3.3b) with the corresponding apparent resistivity residual profiles (Figure 3.3c), we can see that the latter greatly enhances the anomalous effects (due to the body) and clearly indicates the presence of the anomalous 3-D body.

The model shown in Figure 3.4a consists of the anomalous conductive body from Figure 3.3a placed in a more resistive host medium. The overburden layer has a resistivity of $\rho_1 = 200$ ohm.m and a thickness of $h_1 = 25$ m. The second layer, host to the conductivity anomaly, has a resistivity of $\rho_H = 800$ ohm.m. As in the previous model (Figure 3.3a), the line PQ on the surface passing the point vertically above the centre of the 3-D body is used as the profile line along which the resistivity measurements are computed.

In Figures 3.4b and 3.4c, we show the Wenner apparent resistivity profiles and the corresponding apparent resistivity residual profiles, respectively, for different electrode spacings of 5, 10, 20 and 30 m along the line PQ over the symmetric model

a)

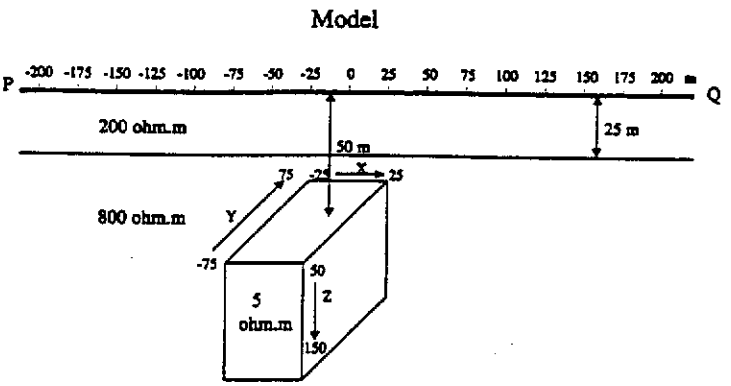

b)

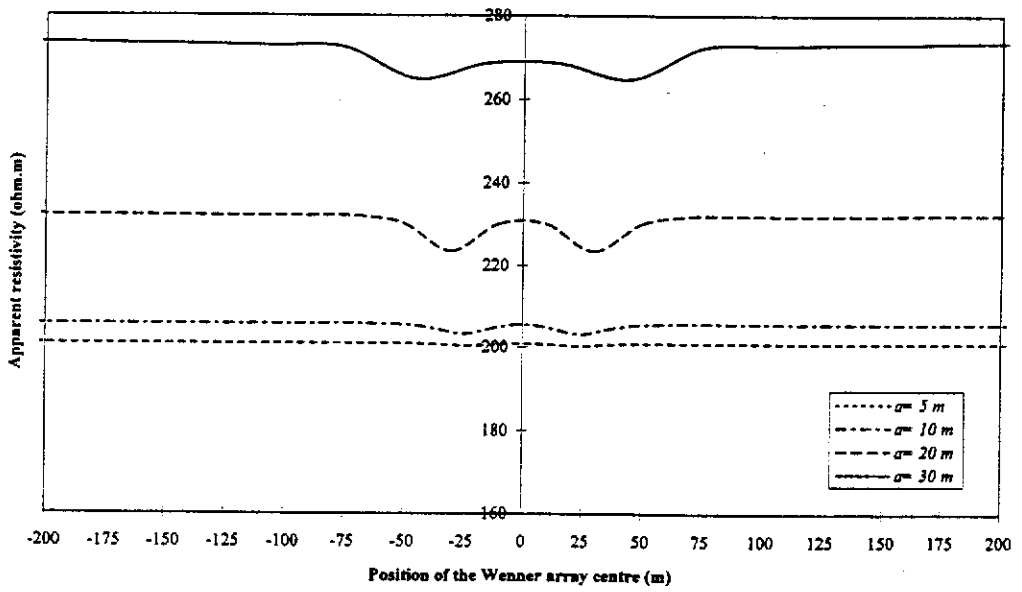

c)

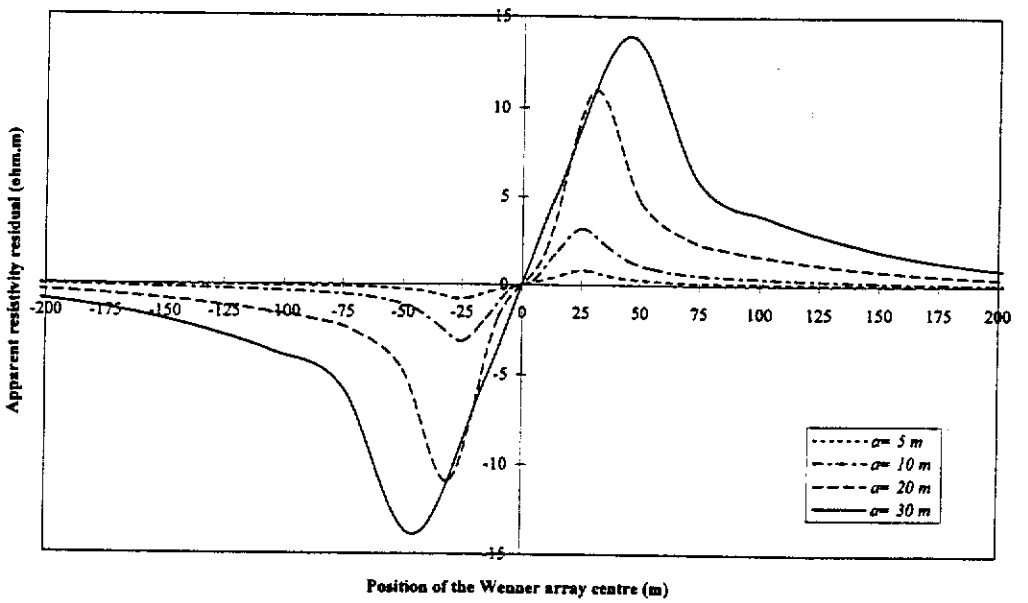

Figure 3.4. Survey combination A results for a symmetric conductive body in a host medium with high resistivity contrast. (a) Model, (b) Wenner apparent resistivity profiles along PQ, and (c) corresponding apparent resistivity residual response.

shown in Figure 3.4a. In this case, the presence of the body can be seen somewhat from the Wenner apparent resistivity profiles with the larger electrode spacings. However, the apparent resistivity residual profiles (Figure 3.4c) show the presence of the body much better than the Wenner apparent resistivity profiles (Figure 3.4b). As discussed earlier, this is because the layering effects have been reduced considerably in the apparent resistivity residual computation. The residual is mainly due to the presence of the anomalous body. The residual profiles, shown in Figure 3.4c, indicate large variations in the anomalies. In this case the crossover of a residual anomaly is at a point vertically above the centre of the body. In addition, the negative and positive peaks of the residual profiles approximately occur at the lateral edges of the body, and thus, indicate the location of the body. The profiles gradually tend to zero far away from the body. The considerably enhanced signal from the body in the residual profiles indicates the effectiveness of the method in the detection of the edges of the body.

Comparing Figures 3.3 and 3.4, we notice a higher resistivity contrast between the body and the host medium for the model shown in Figure 3.4. For this reason, larger Wenner apparent resistivity anomalies are seen in Figure 3.4. Thus, the body detection by the Wenner apparent resistivity profiles for the model in Figure 3.4 is better than that in Figure 3.3. However, applying the processing technique, we can see higher residual responses for the model shown in Figure 3.3 while the Wenner profiles for this model do not show large anomalies (due to less resistivity contrast between the body and the host medium). Where the overburden is more resistive, less electric current channelling in the overburden occurs, and thus, more current will travel in the lower medium.

A *resistive* body placed in the lower half-space of a two-layered earth model is shown in Figure 3.5a. The geometry of this model is the same as that of models shown in Figures 3.3a and 3.4a. However, the resistivity parameters of the model are different from those of models presented in Figures 3.3a and 3.4a. In Figure 3.5a, the body with a resistivity of $\rho_B = 1000$ ohm.m is placed in a host medium with resistivity of

a)

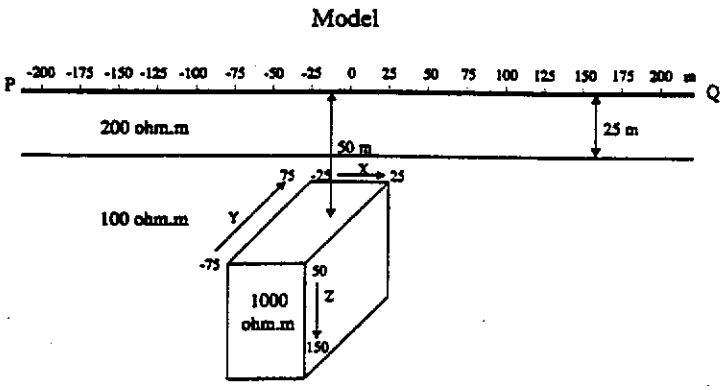

b)

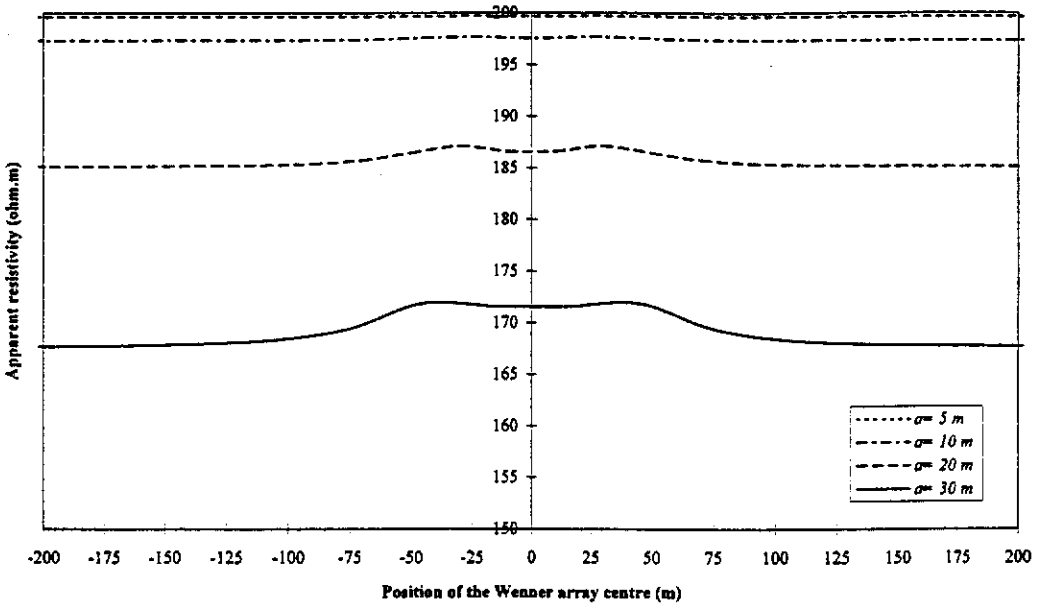

c)

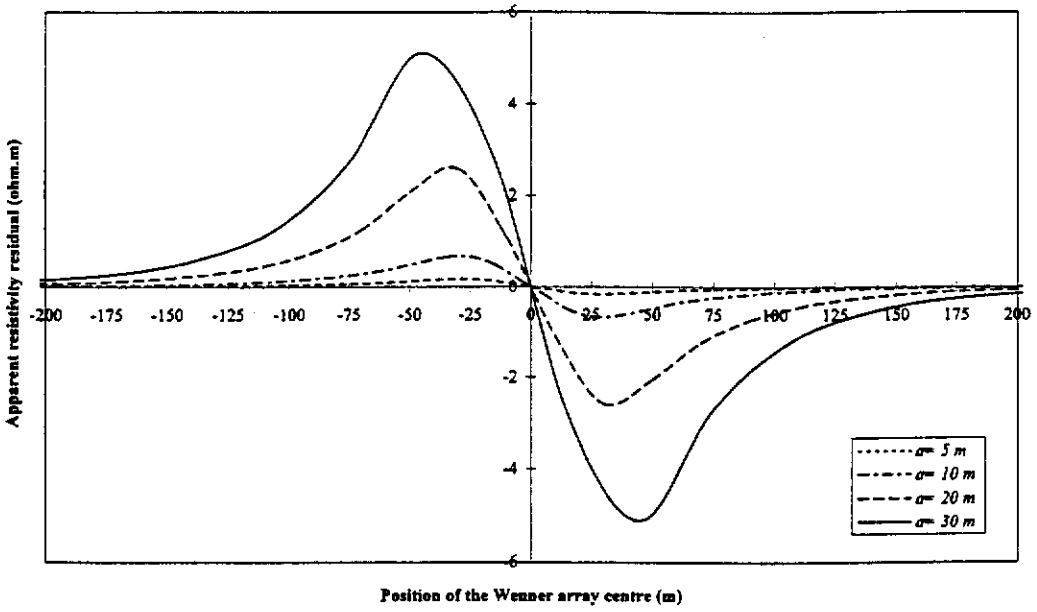

Figure 3.5. Survey combination A results for a symmetric resistive body. (a) Model, (b) Wenner apparent resistivity profiles along PQ, and (c) corresponding apparent resistivity residual response.

$\rho_H = 100$ ohm.m. The overburden layer in this model has a resistivity of $\rho_1 = 200$ ohm.m.

In Figure 3.5b, we show the Wenner apparent resistivity profiles with various electrode spacings along the line PQ over the resistive body shown in Figure 3.5a. The corresponding residual response for this model is shown in Figure 3.5c. The Wenner apparent resistivity profiles with larger electrode spacing in this case also roughly reveal the existence of the resistive body, but it is very difficult to estimate the location of the body from the Wenner apparent resistivity profiles since the resolution of the method is low. However, we can determine the approximate location of the body more effectively from the apparent resistivity residual profiles shown in Figure 3.5c. The maximum and minimum points of the residual profiles in this figure indicate the approximate location of the lateral edges of the prismatic resistive body. Also, the centre of the body in the residual profiles can be discerned from where the profiles cross over the horizontal axis. Thus, the residual profiles obtained from this processing technique improve both the detectability and the resolution of the resistivity profiling method in the presence of 3-D subsurface bodies.

It is noticed that according to the profiling direction, the lateral edges of the resistive body in the left-hand side and the right-hand side are represented, respectively, by positive and negative peaks on the apparent resistivity residual profiles (Figure 3.5c). However, for a conductive body the left-hand side and the right-hand edges are indicated on the apparent resistivity residual profiles by negative and positive peaks, respectively, as seen in Figures 3.3c and 3.4c.

3.2.1.2.2 Asymmetric body

We now consider an asymmetric conductive body in the lower half-space of a two-layered earth as shown in Figure 3.6a. In this figure, we have shown only the side

a)

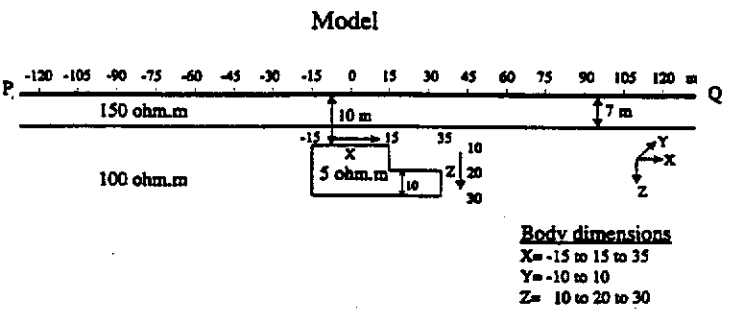

b)

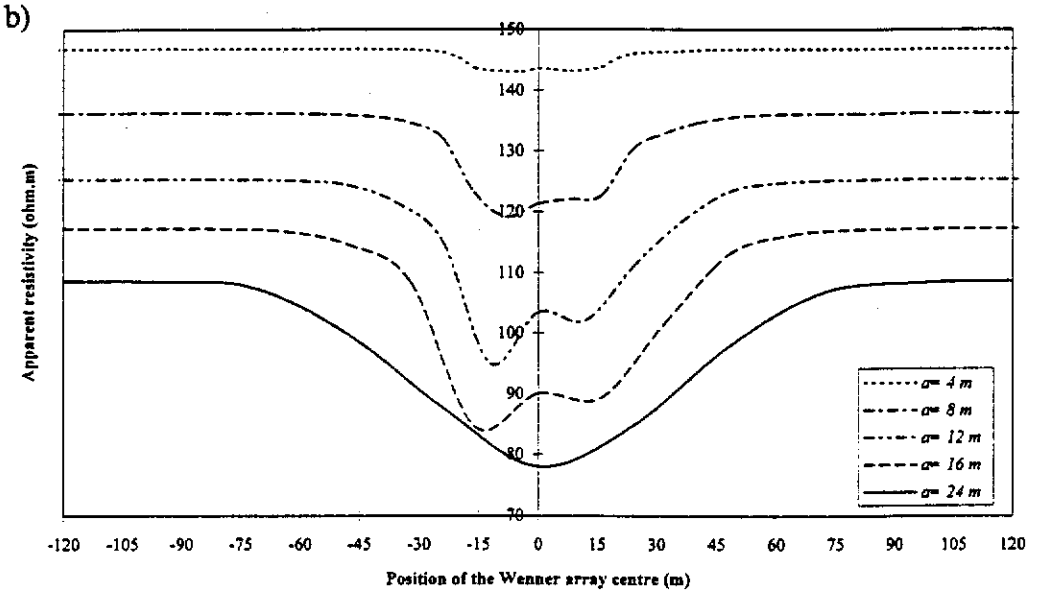

c)

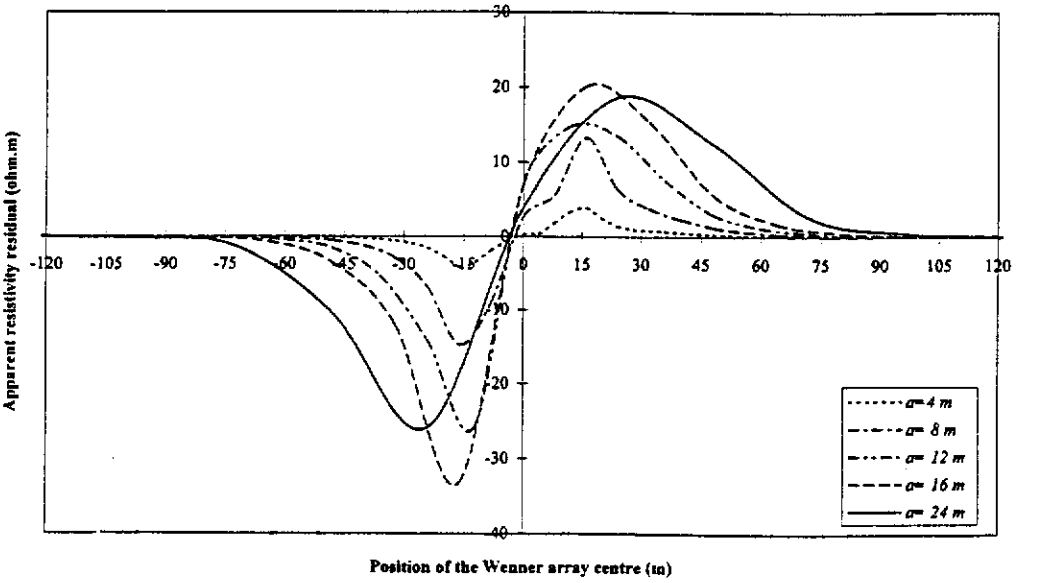

Figure 3.6. Survey combination A results for an asymmetric body. (a) Model, (b) Wenner apparent resistivity profiles along PQ, and (c) corresponding apparent resistivity residual response.

elevation of the model (i.e. in the x-z plane) to make it easy to understand the resistivity and residual profiles with reference to the model. The body, at a depth of 10 m below the ground surface, extends from -10 to 10 m in the y-direction, –15 to 35 m in the x-direction and 10 to 30 m in the z-direction. From –15 to 15 m in the x-direction, the body has a thickness of 20 m, while from 15 to 35 m in this direction, the body has a thickness of 10 m. Thus, a sharp middle edge is seen in the body at x = 15 m. This asymmetric conductive body with resistivity of $\rho_B = 5$ ohm.m is located in a host medium with resistivity of $\rho_H = 100$ ohm.m. The first layer (overburden) has a resistivity of $\rho_1 = 150$ ohm.m and a thickness of $h_1 = 7$ m.

The Wenner apparent resistivity profiles and the corresponding apparent resistivity residual profiles for electrode spacings of 4, 8, 12, 16 and 24 m over this asymmetric body are illustrated in Figures 3.6b and 3.6c, respectively. The variations in the Wenner apparent resistivity profiles over the body indicate the presence of the body, especially for greater electrode spacings (e.g. a= *12 m* and a= *16 m*). A more gently sloping gradient is seen on the right-hand side of the Wenner apparent resistivity profiles indicating that the body on this side is deeper than the left-hand side. However it is very difficult or near impossible to locate the lateral edges including the sharp middle edge of the body.

The apparent resistivity residual profiles (Figure 3.6c) indicate large asymmetric variations. The crossover of the residual profiles approximately shows the centre of that part of the body forming its uppermost surface bounded by the lateral left and middle edges. Approximate locations of the left and sharp middle edges of the body enclosing the upper surface of the body can be estimated from the negative and positive peaks of the residual profiles. However, recognising the far right lateral edge of the body, where the body is deeper and thiner, is difficult from the residual profiles. The residual profiles after turning the maximum peak on the right-hand side gradually (low dipping) go to zero unlike these profiles on the left-hand side, which more steeply go to zero. This gentle gradient on the residual profiles clearly indicates that the body is extended to the right-hand side at a greater depth.

It is noticed that the apparent resistivity profiles over the centre of the conductive body in Figure 3.6b, and also Figures 3.3b and 3.4b, show a small peak (indicating an increase in the apparent resistivity) rather than a trough (low apparent resistivity) although the body itself is more conductive than the surrounding environment. This peak is more considerable for larger electrode spacings (except for very large electrode spacing $a=24\ m$ in Figure 3.6b). A possible explanation for this is that computed resistivity anomalies are ultimately due to the development of charges on the surface of the body (at the contact of two media). For example, for a small electrode spacing the current may be entering the body from above, so that charge of some sign is developed on the upper surface of the body. Similarly, for large electrode spacings in relevant geometries the current may enter from below and a charge of that same sign is developed on the lower surface of the body. Thus, the nature of the anomalous body is very dependent on electrode spacings used, shape and size of the body and the resistivity contrasts of the layered and non-layered structures involved.

Modelling other asymmetric bodies of arbitrary shape showed that the residual profiles could easily indicate the edges enclosing the upper surface of a body. However, it seems that detecting other edges, which may be located at deeper levels, is difficult except for the cases where the edges are sufficiently laterally displaced. This is assumed to be because preferential electric current channelling occurs in the upper parts of the body. As a result, small current channelling occurs in the lower parts of the body so that it makes difficult the detection of the edges in the lower parts of the body using any DC resistivity profiling method. If the edges of the body at the upper surface of the body are sufficiently laterally displaced from the edges at the lower parts of the body, the apparent resistivity profiles indicate the latter edges by positive or negative peaks as well.

A conductive body with a long extension in the x-direction placed in the lower half-space of a two-layered earth model is shown in Figure 3.7a. In this figure also only the side elevation of the model (i.e. in the x-z plane) is shown. The body is located at a depth of 10 m below the ground surface. The body with dimensions

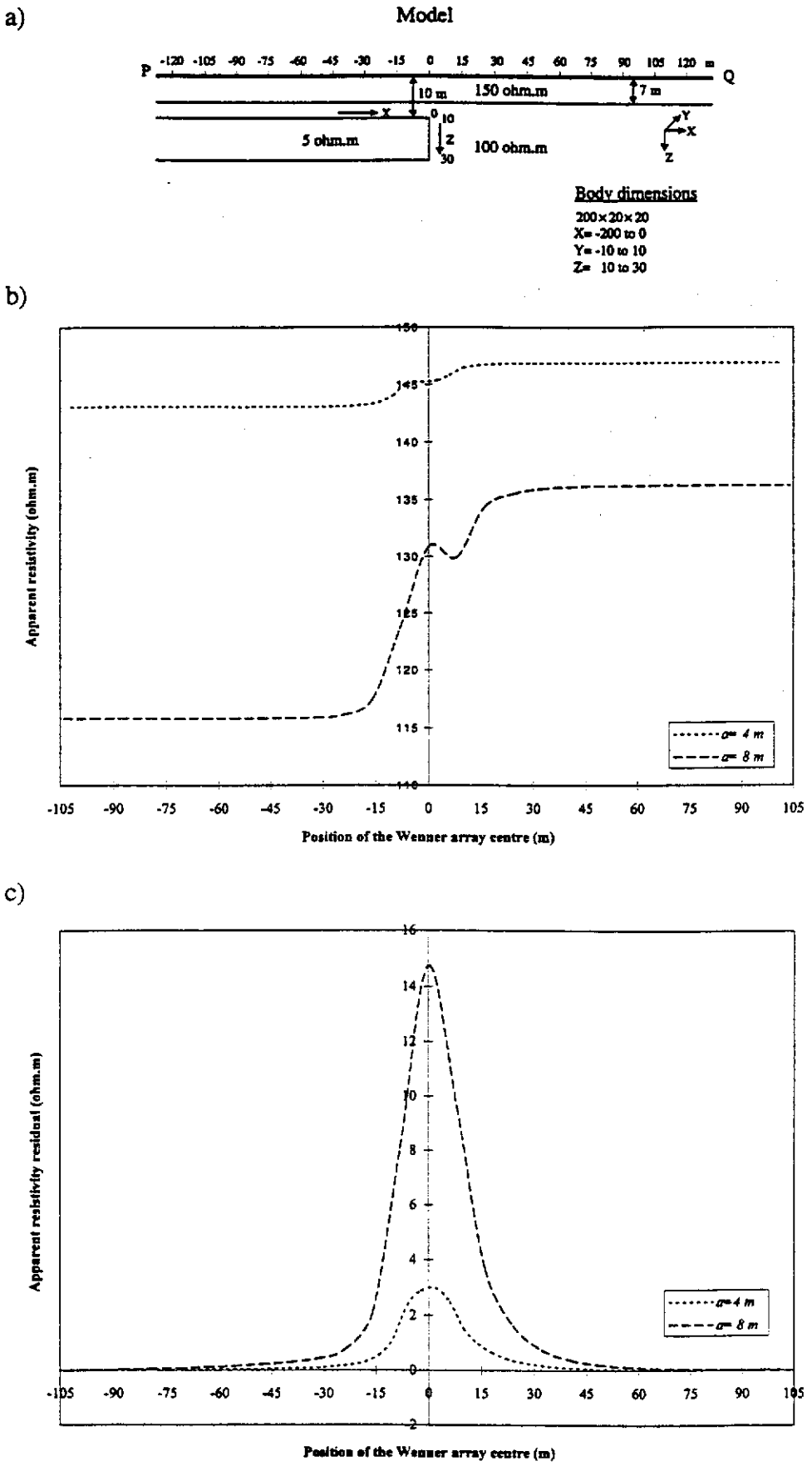

Figure 3.7. Survey combination A results for a body with a long extension in the x-direction and sharp edges. (a) Model, (b) Wenner apparent resistivity profiles along PQ, and (c) corresponding apparent resistivity residual response.

$200\times20\times20$ m is situated between –200 to 0 m in the x-direction, -10 to 10 m in the y-direction, and 10 to 30 m in the z-direction. As can be seen from the figure, the left edge of the body (in the x-direction) has not been shown since it is located at a relatively large distance along the profile line PQ. This conductive body with resistivity of $\rho_B = 5$ ohm.m is located in a host medium with resistivity of $\rho_H = 100$ ohm.m. The first layer (overburden) has a resistivity of $\rho_1 = 150$ ohm.m and a thickness of $h_1 = 7$ m.

Figures 3.7b and 3.7c represent the Wenner apparent resistivity profiles and the corresponding apparent resistivity residual profiles for electrode spacings 4 and 8 m over the right-hand side of the body. As can be seen from Figure 3.7b, the Wenner apparent resistivity profiles are flat (parallel to the horizontal axis) over that part of the body, which is not close to the edge of the body. Over the right edge of the conductive body, a gradual increase in apparent resistivity values is seen, which is followed by a small change in the trend of the resistivity profiles. Another small change in the trend of the resistivity profiles occurs as we move away from the edge of the body. This kink which occurs in the computed Wenner apparent resistivity profiles over the edge of body, is also seen in the examples presented by Van Nostrand and Cook (1966). At a further distance from the edge at the right-hand side of the body, the resistivity profiles show no variation since the apparent resistivity data do not change at great distances from the edge of the body. In this case, the edge of the body can be detected by the peak produced in the residual response (Figure 3.7c). At either side of the edge, whether over the body or not, the residual profiles dramatically decrease and go to zero. The only peak in the residual profiles, indicating the right-hand edge of the body, is positive and thus, it indicates that the body is conductive. A negative peak (not shown) occurs over the left side of the body.

The body, shown in Figure 3.7a, has sharp lateral edges. In Figure 3.8a, we consider the body to have a dipping edge on its right-hand side. Figures 3.8b and 3.8c show, respectively, the Wenner apparent resistivity profiles and the corresponding apparent

a)

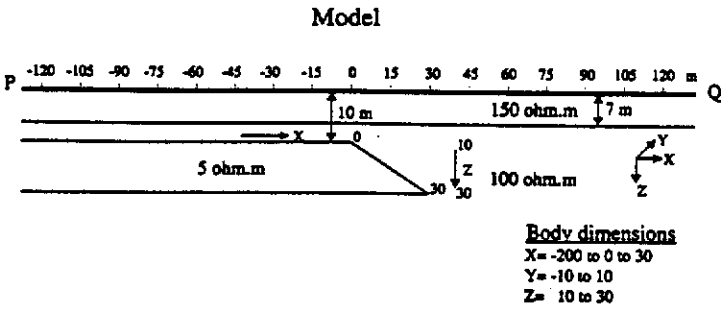

b)

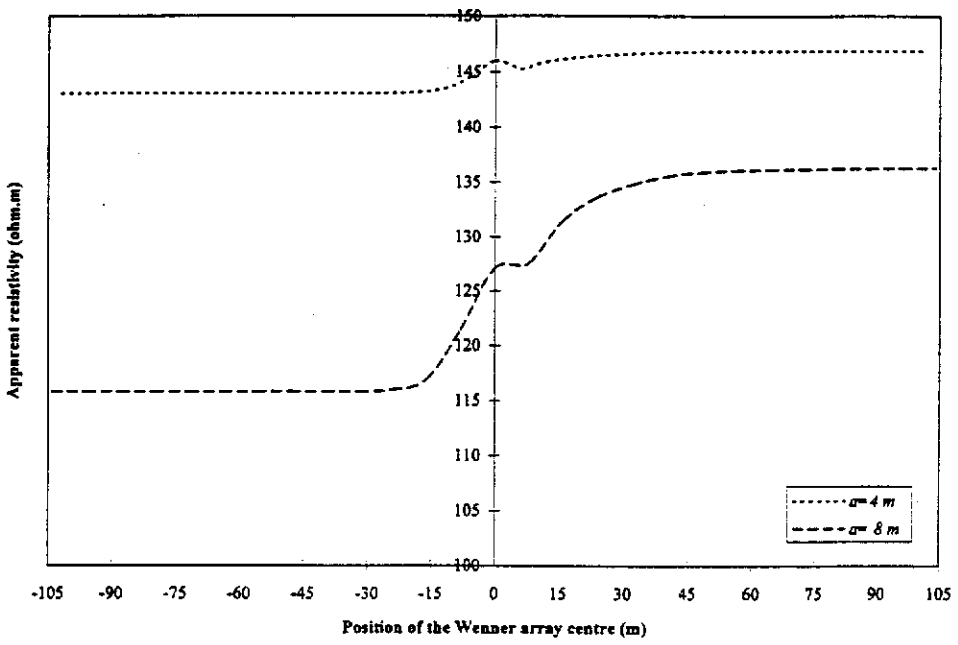

c)

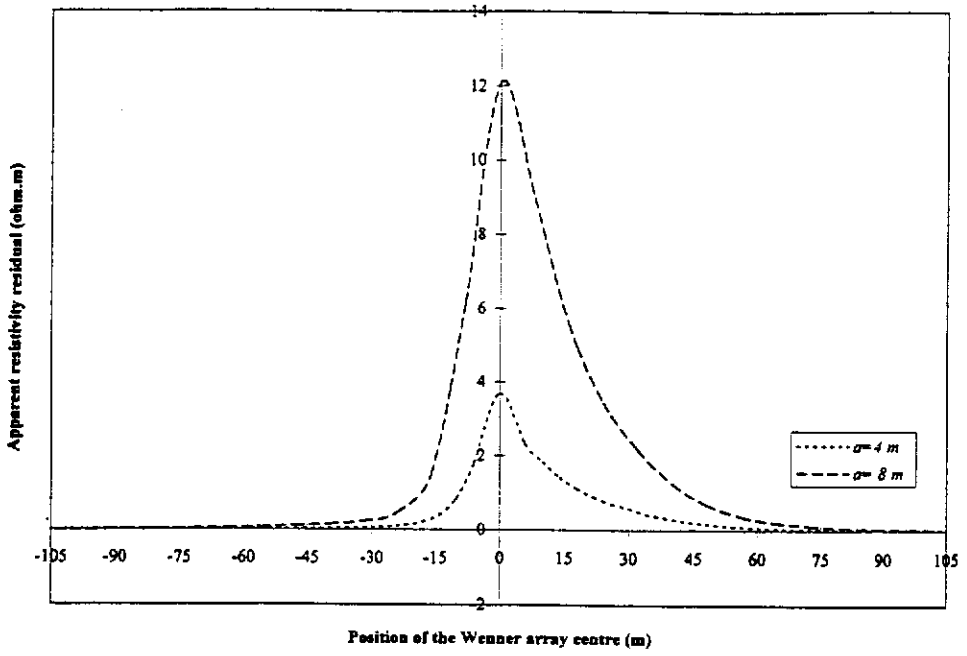

Figure 3.8. Survey combination A results for a body with a long extension in the *x*-direction and dipping edge. (a) Model, (b) Wenner apparent resistivity profiles along PQ, and (c) corresponding apparent resistivity residual response.

resistivity residual profiles for electrode spacings 4 and 8 m over the right-hand side of this asymmetric body which has a long extension in the negative x-direction. As in the previous example, the left-hand side of the body (including left edge of the body) is not shown. Also in this example only one peak in the residual response can be seen, which indicates the right-hand edge of the body. The residual profiles go to zero on the left-hand side of the peak more sharply than on the right-hand side of the peak. This implies the asymmetric shape of the body, which does not end suddenly in its right-hand side. The only peak in the residual profiles, occurring vertically above the right edge point at the top of the body, is positive which indicates that the body is conductive. The Wenner apparent resistivity profiles although are parallel to the horizontal axis on both sides of the edge of the body and have considerable variations vertically above the right-edge of the body, do not give a good indication of the structure.

3.2.1.2.3 Multiple bodies

A two-layered earth model containing two bodies of different sizes at different depths is presented in Figure 3.9a. One of the bodies with dimensions $20\times40\times20$ m is located at a depth of 30 m below the surface. The other body, which is larger and deeper, has dimensions $40\times120\times100$ m and is located at a depth of 50 m below the surface. Both bodies are conductive with the same resistivity of $\rho_B = 5$ ohm.m. The resistivity of host medium is $\rho_H = 800$ ohm.m. The first layer (overburden) has a resistivity of $\rho_1 = 200$ ohm.m and a thickness of $h_1 = 25$ m.

Figures 3.9b and 3.9c present, respectively, the Wenner apparent resistivity profiles and the corresponding residual profiles for electrode spacings 5, 10 and 20 m over these two bodies. Although one of the bodies is much smaller than the other, it is located at a shallower depth, hence it has greatly affected the Wenner apparent resistivity and residual profiles obtained using smaller electrode spacings. The Wenner apparent resistivity profiles show some variations, which imply the presence

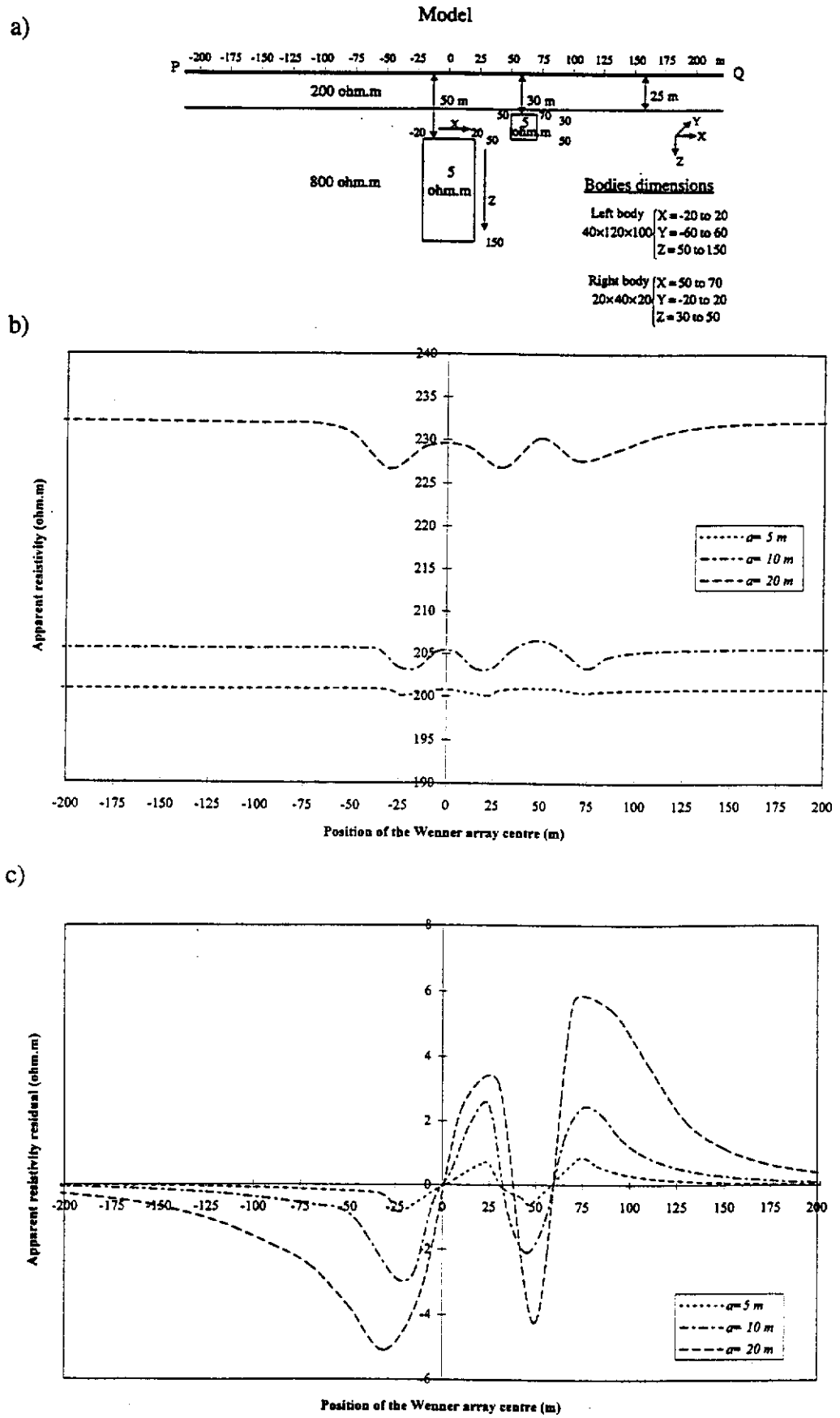

Figure 3.9. Survey combination A results for two bodies. (a) Model, (b) Wenner apparent resistivity profiles along PQ, and (c) corresponding apparent resistivity residual response.

of the anomalies (bodies) but they cannot give much detail about the bodies due to low resolution of that resistivity method. However the residual profiles do indicate more detail about the bodies. The negative and positive peaks of the residual profiles approximately indicate the lateral edges of the bodies. The centre of each body is represented by the crossover of residual profiles between the negative and positive peaks.

By adding another body with dimensions $30\times60\times80$ m at depth of 40 m to the model shown in Figure 3.9a, we will have a model composed of three bodies with different sizes located at different depths as shown in Figure 3.10a. For simplicity we consider each of these bodies to have a resistivity $\rho_B = 5$ ohm.m. The Wenner apparent resistivity profile and the corresponding residual response for this model are illustrated in Figures 3.10b and 3.10c, respectively. In this case also the bodies located at a shallower depth have a greater effect on the resistivity and residual profiles with smaller electrode spacings. As usual the negative and positive peaks of the residual profiles approximately indicate the lateral edges of the bodies, and the centre of each body is represented by the crossover of residual profiles between the negative and positive peaks.

In this case where multiple bodies are embedded in a layered earth, how much each body affects the apparent resistivity residual profiles, depends on several parameters including the resistivities and thicknesses of the layers, and also the resistivity, depth, thickness, and the lateral extent of the body as well as on the electrode spacings of the survey. A shallow, thick and extensive body has a great effect on the variation of the residual profiles while a deep and small body has little effect on the residual profiles. Thus, we can differentiate the responses of these bodies in the residual profiles. Also, if the resistivity contrast between the body and the host medium is greater, the effect of the body on the residual profiles will be larger. The method is successful in resolving the presence of bodies, which are sufficiently laterally displaced. However, where overlap occurs, discrimination is less successful (Kamkar-Rouhani, 1997). In any case, one important and interesting fact about the processing technique is that the apparent resistivity residual profiles invariably cross

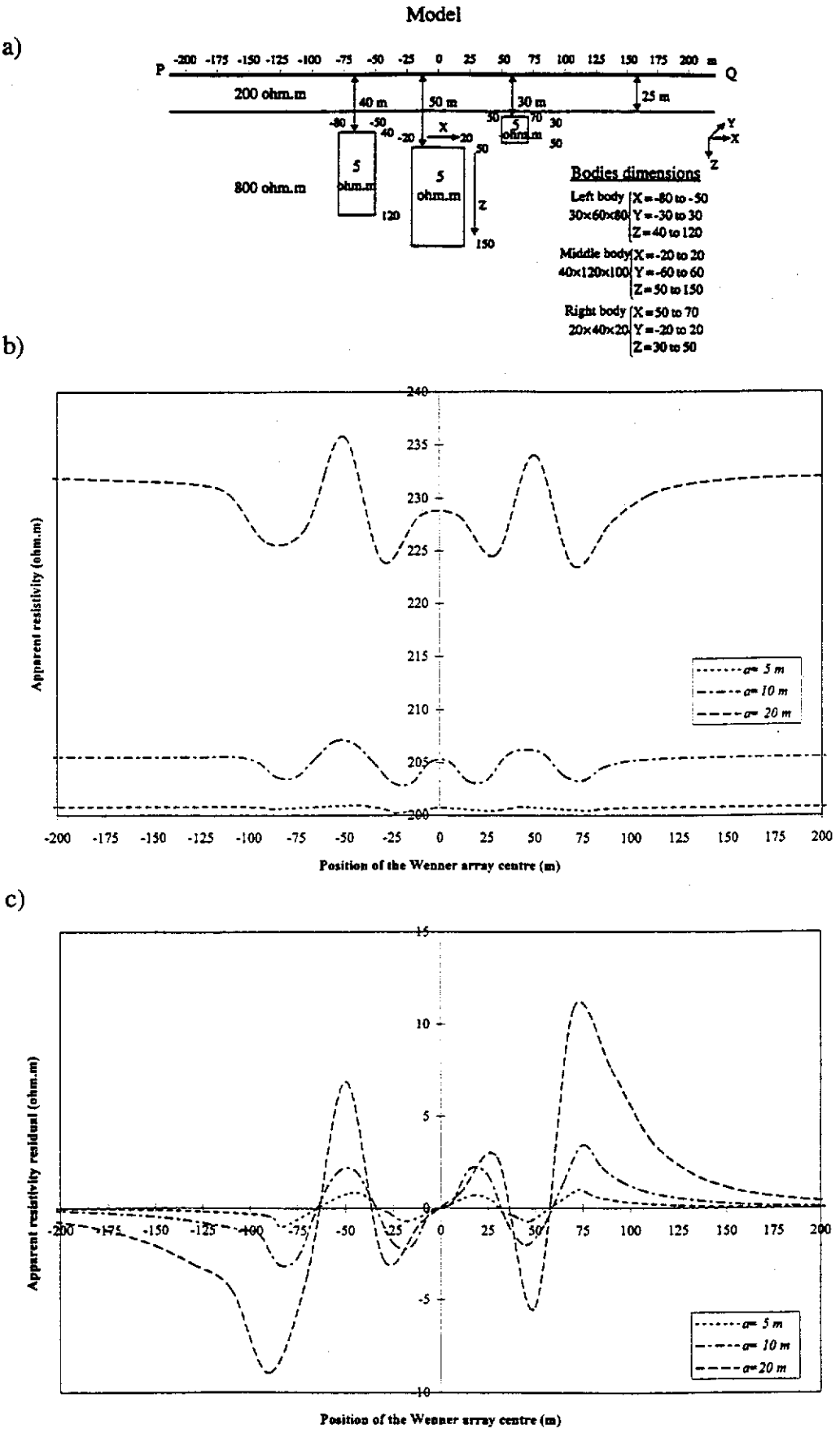

Figure 3.10. Survey combination A results for three bodies. (a) Model, (b) Wenner apparent resistivity profiles along PQ, and (c) corresponding apparent resistivity residual response.

the horizontal axis vertically above the centre of a body. In the case of an asymmetric body, the apparent resistivity residual profiles would appear to meet the horizontal axis vertically above the centre of the part of the body nearest the surface.

3.2.2 Schlumberger and equatorial dipole-dipole measurements

We now consider profiling by another combination of survey geometries.

The potential difference measured by a Schlumberger configuration *AMNB* (Figure 3.2 – combination B) with separation $s = \frac{AB}{2}$ over a layered earth is expressed by a combination of the potentials measured by two-electrode configurations. These two-electrode configurations are composed of all possible arrangements of the current electrodes *A* and *B* with the potential electrodes *M* and *N* (Kamkar-Rouhani and Das, 1996b). The potentials, measured by these two-electrode configurations, are combined in the following form to compute the potential difference in the Schlumberger configuration *AMNB*:

$$V_S(s = \frac{AB}{2}) = V_T(AM) - V_T(AN) - V_T(BM) + V_T(BN). \tag{3.20}$$

Considering Figure 3.2 (combination B), we have $AM = BN = s - b$ and $AN = BM = s + b$, where $b = \frac{MN}{2} = MO = ON$. Also, for an electric current *I* injected into the ground via the current electrodes *A* and *B*, we have $V_T(AM) = V_T(BN)$, and $V_T(AN) = V_T(BM)$. Thus, we can write equation (3.20) as

$$V_S(s = \frac{AB}{2}) = 2V_T(AM = s - b) - 2V_T(AN = s + b). \tag{3.21}$$

Using equation (3.1), we can write

$$V_T(AM = s-b) = \frac{I}{2\pi}\int_0^\infty T(\lambda)J_0(\lambda s - \lambda b)d\lambda\,, \tag{3.22}$$

and

$$V_T(AN = s+b) = \frac{I}{2\pi}\int_0^\infty T(\lambda)J_0(\lambda s + \lambda b)d\lambda\,. \tag{3.23}$$

Substituting equations (3.22) and (3.23) in equation (3.21), we obtain

$$V_S(s) = \frac{I}{\pi}\int_0^\infty T(\lambda)[J_0(\lambda s - \lambda b) - J_0(\lambda s + \lambda b)]d\lambda\,. \tag{3.24}$$

Similarly, we obtain the potential difference measured by the equatorial dipole-dipole configuration $A'MNB'$ (Figure 3.2 – combination B) with separation s as

$$V_E(s) = 2V_T(A'M = s) - 2V_T(A'N = \sqrt{s^2 + 4b^2})\,. \tag{3.25}$$

Using equation (3.1), we obtain

$$V_E(s) = \frac{I}{\pi}\int_0^\infty T(\lambda)[J_0(\lambda s) - J_0(\lambda\sqrt{s^2 + 4b^2})]d\lambda\,. \tag{3.26}$$

We can obtain the apparent resistivity expressions for the Schlumberger and equatorial dipole-dipole configurations using equation (2.54). The apparent resistivity for the Schlumberger configuration is

$$\rho_{as}(s) = \frac{s^2 - b^2}{2b}\int_0^\infty T(\lambda)[J_0(\lambda s - \lambda b) - J_0(\lambda s + \lambda b)]d\lambda\,, \tag{3.27}$$

and for the equatorial dipole-dipole configuration,

$$\rho_{aE}(s) = \frac{s\sqrt{s^2+4b^2}}{\sqrt{s^2+4b^2}-s}\int_0^\infty T(\lambda)[J_0(\lambda s) - J_0(\lambda\sqrt{s^2+4b^2})]d\lambda\,. \tag{3.28}$$

The apparent resistivity for the Schlumberger configuration can also be expressed by the following expression (Koefoed, 1979a):

$$\rho_{aS}(s) = -\frac{2\pi s^2}{I}\frac{\partial V_T(s)}{\partial s}. \tag{3.29}$$

The expression for V_T is given by equation (3.1). Differentiating this equation with respect to s, and substituting the differentiation in equation (3.29) yields

$$\rho_{aS}(s) = s^2\int_0^\infty \lambda T(\lambda)J_1(\lambda s)d\lambda\,, \tag{3.30}$$

where J_1 is the Bessel function of the first kind of order one.

Bhattacharya and Patra (1968) have shown that for the case of a layered earth free of any inhomogeneous body the apparent resistivity expression for the equatorial dipole-dipole configuration $A'MNB'$ with the dipole-dipole separation s (Figure 3.2), is the same as that for the Schlumberger configuration $AMNB$ with separation $s = \frac{AB}{2}$, i.e.

$$\rho_{aE}(s) = \rho_{aS}(s)\,. \tag{3.31}$$

Equation (3.31) simply states that the apparent resistivities of the Schlumberger and equatorial dipole-dipole configurations over a layered earth are equivalent.

3.2.2.1 Signal enhancement

In Figure 3.2, a 3-D target under an overburden layer is embedded in a host medium. Voltage differences between the potential electrodes *MN* (Figure 3.2 – combination B) are measured by the Schlumberger ($AMNB$) and the equatorial dipole-dipole ($A'MNB'$) configurations along a profile PQ on the surface of the earth. As we said earlier in section 3.2.1.1, the total electric potential V^t measured by an electrode configuration may be written as the sum of the primary layered earth electric potential V^l and the anomalous electric potential V^b due to electric charges on the surface of the body (Figure 3.2), i.e.,

$$V^t = V^l + V^b. \tag{3.32}$$

In this equation, if the contribution of the layered earth potential V^l can be reduced, the residual will contain mainly the anomalous potential V^b.

In a similar way to that in section 3.2.1.1, the potential V^t measured by an electrode configuration is converted into apparent resistivity ρ_a^t by a simple transformation given by the expression

$$\rho_a^t = K\frac{V^t}{I}, \tag{3.33}$$

where K is a geometric factor. Considering equation (3.32), we can write equation (3.33) in the following form:

$$\rho_a^t = K\frac{V^l}{I} + K\frac{V^b}{I} = \rho_a^l + \rho_a^b. \tag{3.34}$$

Here, ρ_a^t is the total apparent resistivity, ρ_a^l is the layered earth contribution and ρ_a^b is anomalous body contribution to the total apparent resistivity. Using equation

(3.34), we can write for the Schlumberger configuration with separation $s = \frac{AB}{2}$ (Figure 3.2 – combination B),

$$\rho_{aS}^{t}(s) = \rho_{aS}^{l}(s) + \rho_{aS}^{b}(s). \tag{3.35}$$

Also, for the equatorial dipole-dipole configuration with the dipole-dipole separation s (Figure 3.2 – combination B), we have

$$\rho_{aE}^{t}(s) = \rho_{aE}^{l}(s) + \rho_{aE}^{b}(s). \tag{3.36}$$

In the above equations, $\rho_{aE}^{l}(s) = \rho_{aS}^{l}(s)$ [see equation (3.31)]. In the absence of the body, the second term on the right-hand side of equations (3.35) and (3.36) [i.e. ρ_{a}^{b}] disappears, and thus, we obtain $\rho_{aE}^{t} = \rho_{aS}^{t}$. In the presence of an anomalous body, subtraction of equation (3.35) from (3.36) yields an *apparent resistivity residual R(s)* along a profile line given by

$$R(s) = \rho_{aE}^{t}(s) - \rho_{aS}^{t}(s). \tag{3.37}$$

It is obvious that if there is no anomalous body in the layered earth, $R(s) = 0$. Thus, the apparent resistivity residual *R(s)* is dependent on the anomalous potentials. The contributions of layered earth to the apparent resistivity computations in equation (3.37) are considerably lessened, and consequently, the resistivity response of localised anomalies in the subsurface is enhanced (Kamkar-Rouhani and Das, 1997). Thus, this simple processing technique, which is just subtraction of the two sets of data acquired by the Schlumberger and equatorial dipole-dipole arrays, should result in improved resolution and detection of 3-D subsurface structures. Like the other processing technique, explained in section 3.2.1, this technique also operates as a filter since it removes a major contribution of (sub)horizontal layering to the total response.

3.2.2.2 Numerical examples

The models studied here consist of a single 3-D body and multiple 3-D bodies of arbitrarily shape in the lower half-space of a two-layered earth. Three models are discussed: (1) a symmetric body, (2) an asymmetric body, and (3) multiple bodies. In order to compare their results, these models are selected mostly the same as the models presented in section 3.2.1.2 where we considered the case of signal enhancement using the Wenner and two-electrode measurements.

3.2.2.2.1 Symmetric body

We consider a conductive prismatic body with dimensions $50\times150\times100$ m and with a resistivity of $\rho_B = 5$ ohm.m located symmetrically at depth of 50 m below the ground surface as shown in Figure 3.11a. The resistivity of the host medium is $\rho_H = 200$ ohm.m. The first layer (overburden) has a resistivity of $\rho_1 = 800$ ohm.m and a thickness of $h_1 = 25$ m.

Applying the resistivity profiling method, we compute the equatorial dipole-dipole and Schlumberger apparent resistivity measurements with different electrode spacings along a line PQ (Figure 3.11a) on the surface passing through the point vertically above the centre of the 3-D body. Figure 3.11b presents the Schlumberger apparent resistivity profiles with electrode separations (AB/2) 5, 10, 20 and 30 m along the line PQ over the symmetric body shown in Figure 3.11a. The Schlumberger profiles with larger separations show small variations over the body. Thus, it is possible to detect the body from these Schlumberger profiles. However, the resolution of the resistivity method is quite low. For this model, the corresponding residual response, which has been calculated using equation (3.37), is shown in Figure 3.11c. The apparent resistivity residual profiles indicate large variations in the anomalies. The lateral edges of the body are recognised from the minimum peaks (or small upward peaks between two minimum peaks) on the residual profiles. However for large

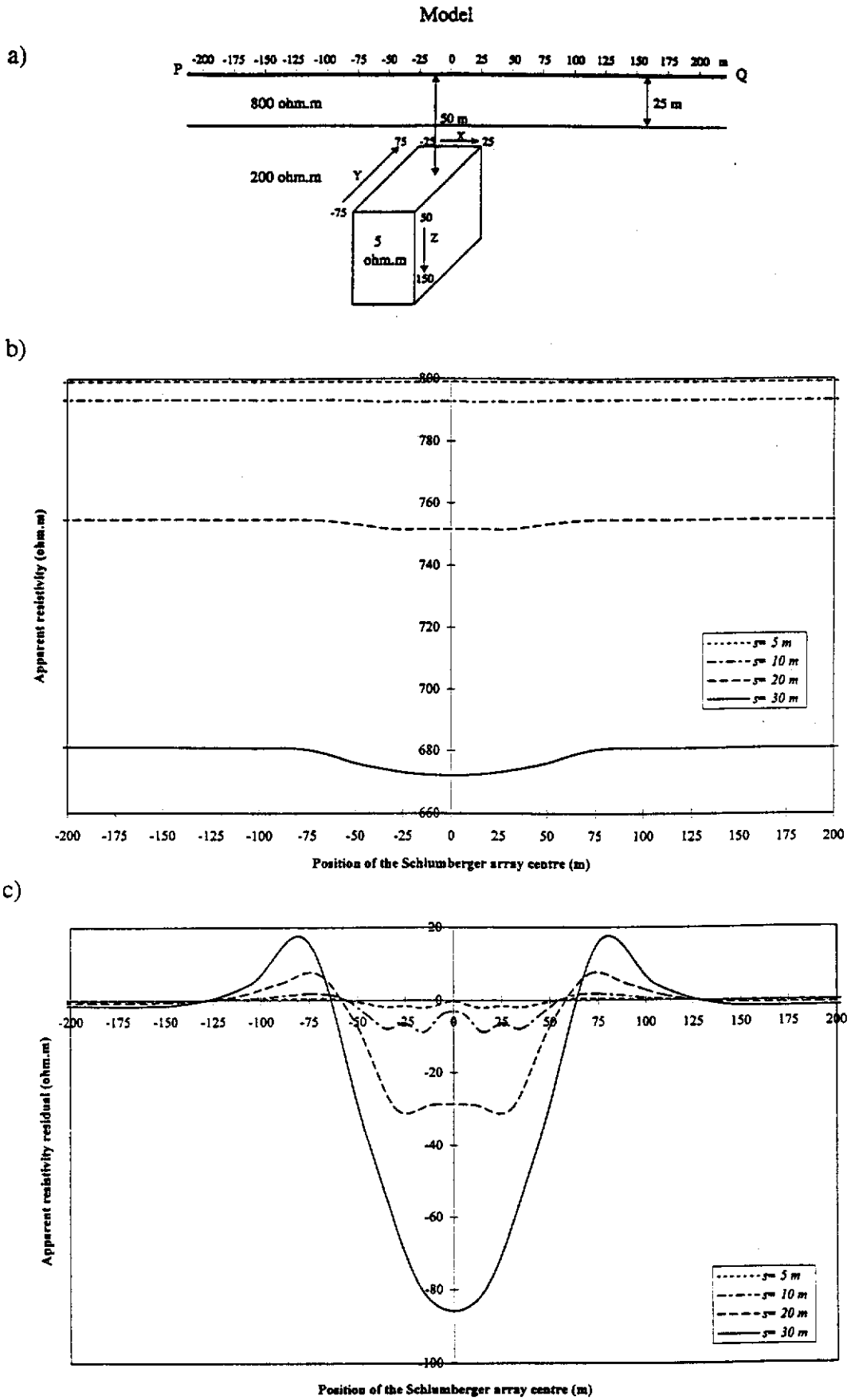

Figure 3.11. Survey combination B results for a symmetric conductive body with a resistive overburden. (a) Model, (b) Schlumberger apparent resistivity profiles along PQ, and (c) corresponding apparent resistivity residual response.

electrode separations these peaks disappear and in such cases we see only a minimum peak, which occurs vertically above the centre of the body. For smaller electrode separations, the centre of the body is represented on the residual profiles by a small upward peak between the peaks indicating the lateral edges of the body. It is also seen from the residual profiles that they go to zero far away from the body. This indicates that where the body is located at a long distance away, the apparent resistivity residual is almost zero as if there is no body to create it (as the case of a layered earth free of an inhomogeneity). A comparison between the Schlumberger apparent resistivity profiles (Figure 3.11b) and the corresponding residual response (Figure 3.11c) shows that the residual response greatly improves the anomalous effects due to the body and clearly indicates the location of the body. Thus this simple processing technique, which is just a subtraction of the two sets of resistivity measurements obtained by the Schlumberger and equatorial dipole-dipole configurations, results in enhanced resolution of the subsurface anomalous targets.

Another model, shown in Figure 3.12a, consists of the anomalous conductive body from Figure 3.11a placed in a more resistive host medium. In this model, the overburden layer has a resistivity of $\rho_1 = 200$ ohm.m and a thickness of $h_1 = 25$ m. The host medium for the conductive body has a resistivity of $\rho_H = 800$ ohm.m.

Figures 3.12b and 3.12c give the Schlumberger apparent resistivity and the corresponding apparent resistivity residual profiles for electrode spacings (AB/2) 5, 10, 20 and 30 m along the line PQ over the symmetric model shown in Figure 3.12a. The presence of the body can be detected from the Schlumberger profiles with larger electrode spacings. However, we see that the residual profiles show much greater responses, caused by the anomalous body. This is due to the signal enhancement effect of the apparent resistivity residual. The Schlumberger profiles have a low sensitivity to the presence of the anomalous body, while the residual profiles generally indicate larger and sharper anomalies. The lateral edges of the body are indicated on the residual profiles by the minimum peaks. For large electrode separations the peaks (indicating the edges of the body) are not visible and only the central minimum peak on the residual profiles occurs vertically above the centre of

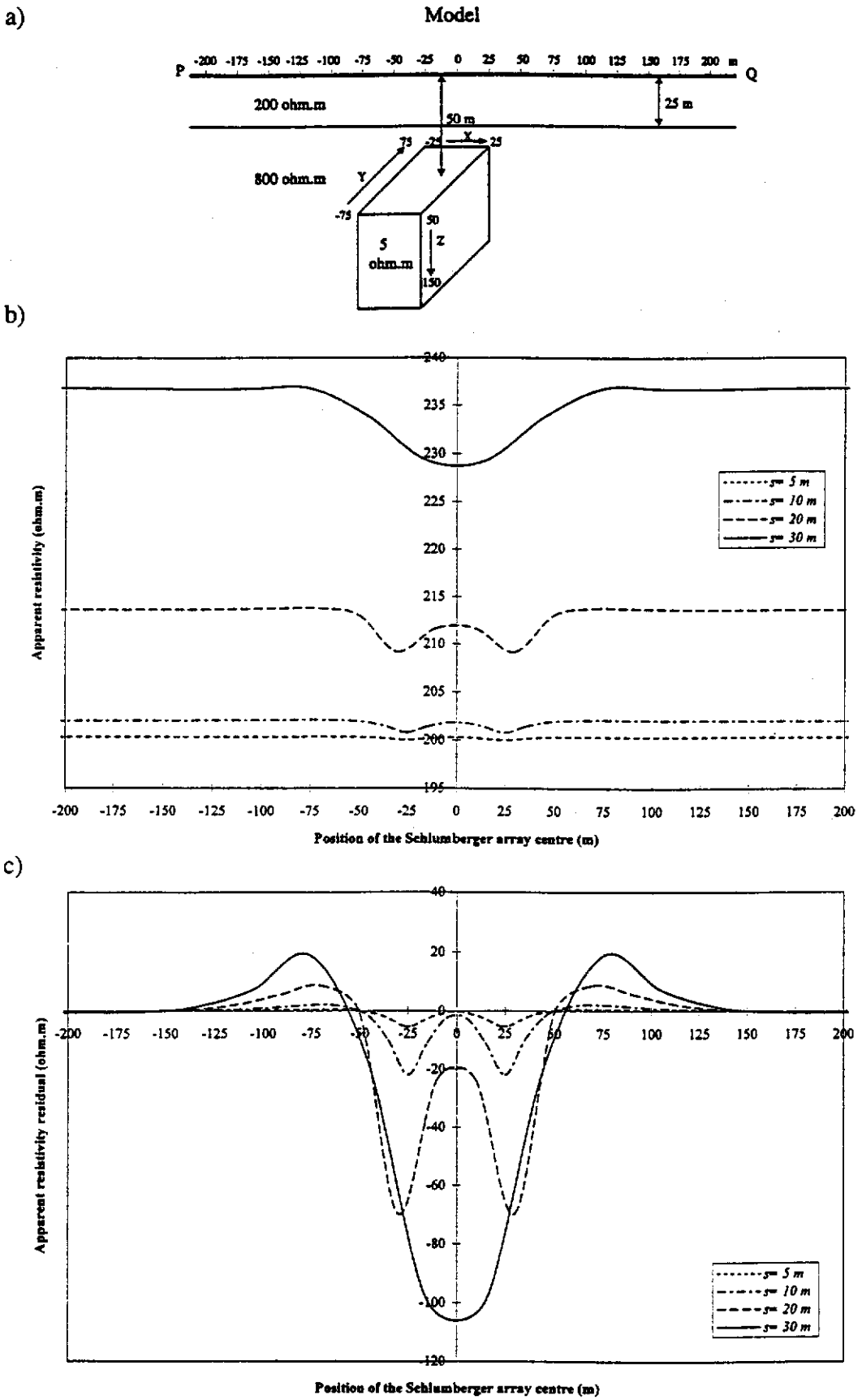

Figure 3.12. Survey combination B results for a symmetric conductive body in a host medium with high resistivity contrast. (a) Model, (b) Schlumberger apparent resistivity profiles along PQ, and (c) corresponding apparent resistivity residual response.

the body. For smaller electrode separations, the centre of the body is represented on the residual profiles by a small upward peak between the minimum peaks which indicate the edges of the body. At a greater distance away from the body, the residual profiles tend to zero again.

Because of the greater resistivity contrast between the body and the host medium in the model in Figure 3.12, the Schlumberger apparent resistivity anomalies over the body in this model are greater than those for the model in Figure 3.11.

In another example, we place a *resistive* body in the lower half-space of a two-layered earth model as shown in Figure 3.13a. The geometry of this model is the same as that of models shown in Figures 3.11a and 3.12a. However, the resistivity parameters of the model are different. In this example, the resistive body with resistivity $\rho_B = 1000$ ohm.m is placed in a host medium with resistivity of $\rho_H = 100$ ohm.m. The resistivity of overburden layer in this model is $\rho_1 = 200$ ohm.m.

For this model the Schlumberger profiles and the corresponding residual response with different separations are presented in Figures 3.13b and 3.13c, respectively. The Schlumberger profiles for this case show poor apparent resistivity signals from the body. The residual profiles, however, indicate a distinctly enhanced response from the anomalous resistive body, which are quite distinguishable from those of non-anomalous regions. The position of the lateral edges of the body can be estimated from the residual profiles as the maximum peaks of the residual profiles approximately occur at the lateral edges of the body. However, for large electrode spacings only one maximum peak is produced, which occurs vertically above the centre of the resistive body. The centre of the body for smaller electrode spacings in this case is represented by a small minimum peak between two maximum peaks (indicating the edges of the body). The residual response for this model is similar to that in Figure 3.11c or 3.12c but of reverse polarity since the body in this model is more resistive than its host medium. As evidenced by the examples shown here the residual peaks are either maximum or minimum, depending on whether the body is resistive or conductive compared with its host rock.

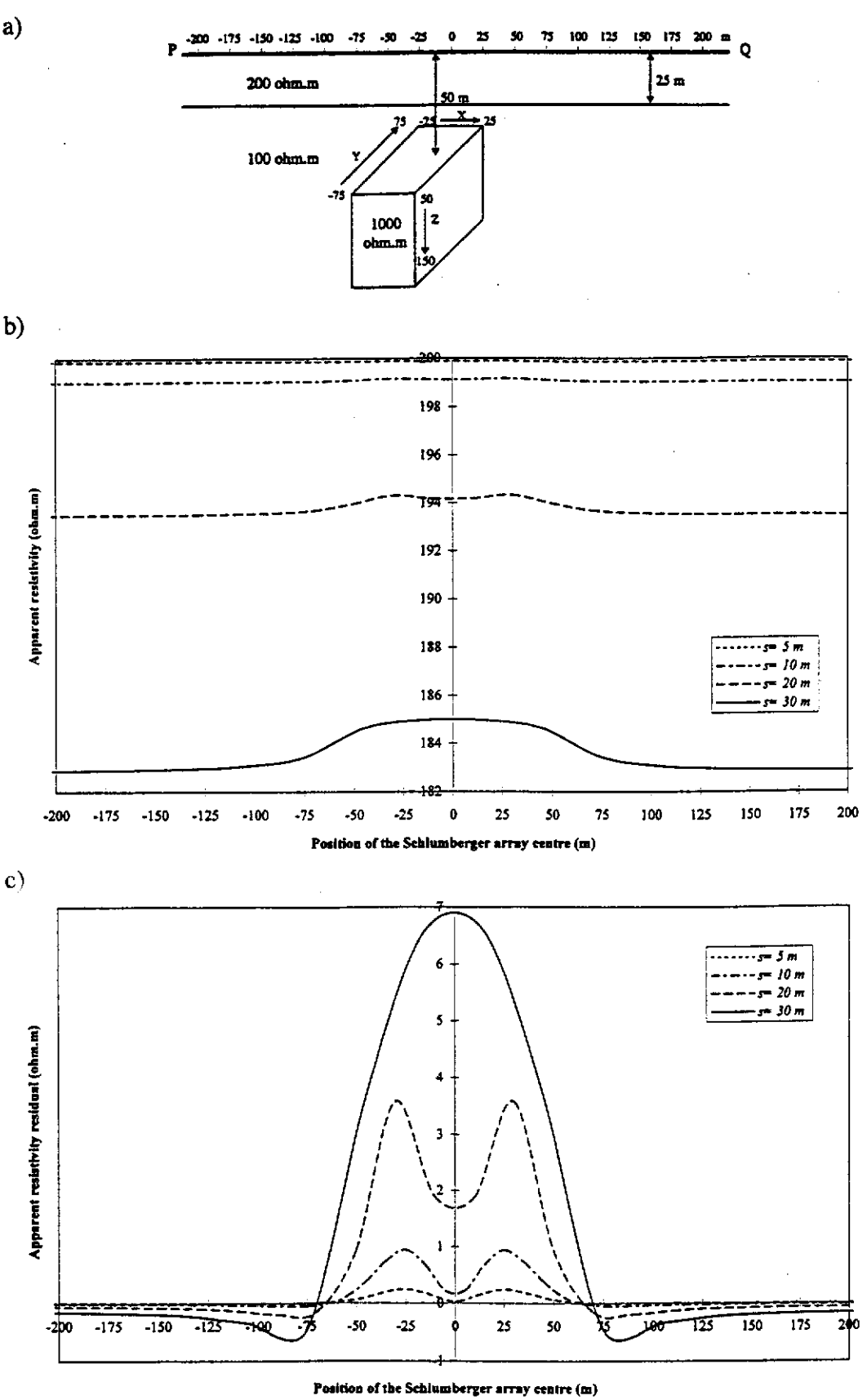

Figure 3.13. Survey combination B results for a symmetric resistive body. (a) Model, (b) Schlumberger apparent resistivity profiles along PQ, and (c) corresponding apparent resistivity residual response.

3.2.2.2.2 Asymmetric body

An asymmetric conductive body in the lower half-space of a two-layered earth is shown in Figure 3.14a. In this figure, only the side elevation of the model (i.e. in the x-z plane) is shown. The body at depth of 50 m below the ground surface extends from -75 to 75 m in the y-direction, –25 to 50 m in the x-direction and 50 to 150 m in the z-direction. From –25 to 25 m in the x-direction, the body has a thickness of 100 m, while at 25 to 50 m in this direction, the body has a thickness of 50 m. Thus, a sharp middle edge is seen in the body at x = 25 m. This asymmetric conductive body with resistivity of $\rho_B = 5$ ohm.m is located in a host medium with resistivity of $\rho_H = 800$ ohm.m. The first layer (overburden) has a resistivity of $\rho_1 = 200$ ohm.m and a thickness of $h_1 = 25$ m.

In Figure 3.14b, we show the Schlumberger apparent resistivity profiles along the line PQ (Figure 3.14a) for electrode spacings (AB/2) of 5, 10, 20 and 30 m over the asymmetric body. From the Schlumberger profiles, especially with large spacings (i.e. s= AB/2= 20 and 30 m), the existence of the asymmetric anomalous body is evident as the Schlumberger apparent resistivity profiles have more gradual dips on the right-hand side than on the left-hand side of the profiles. This indicates a greater depth in the right-hand side of the body than that of the left-hand side of the body, but resolution is poor. The corresponding apparent resistivity residual response, shown in Figure 3.14c, indicates large asymmetric variations. Except for the large spacing (i.e. s=AB/2=30 m), the minimum points of the residual profiles locate the lateral edges of the body. However it seems to be difficult from the residual graph to recognise the location of the edge of the body on its far right-hand side. The small peak between two minimum points in the residual response occurs vertically above the centre of the top section of the body nearest the surface. For spacing s=AB/2=30 m, the only minimum point indicates the centre of the body. The residual profiles at a long distance from the body go to zero. It is also noted that the residual profiles have a more gentle slope on the right-hand side than those in the left-hand side, which clearly indicates a greater depth in the right-hand side of the body than that of the left-hand side of it.

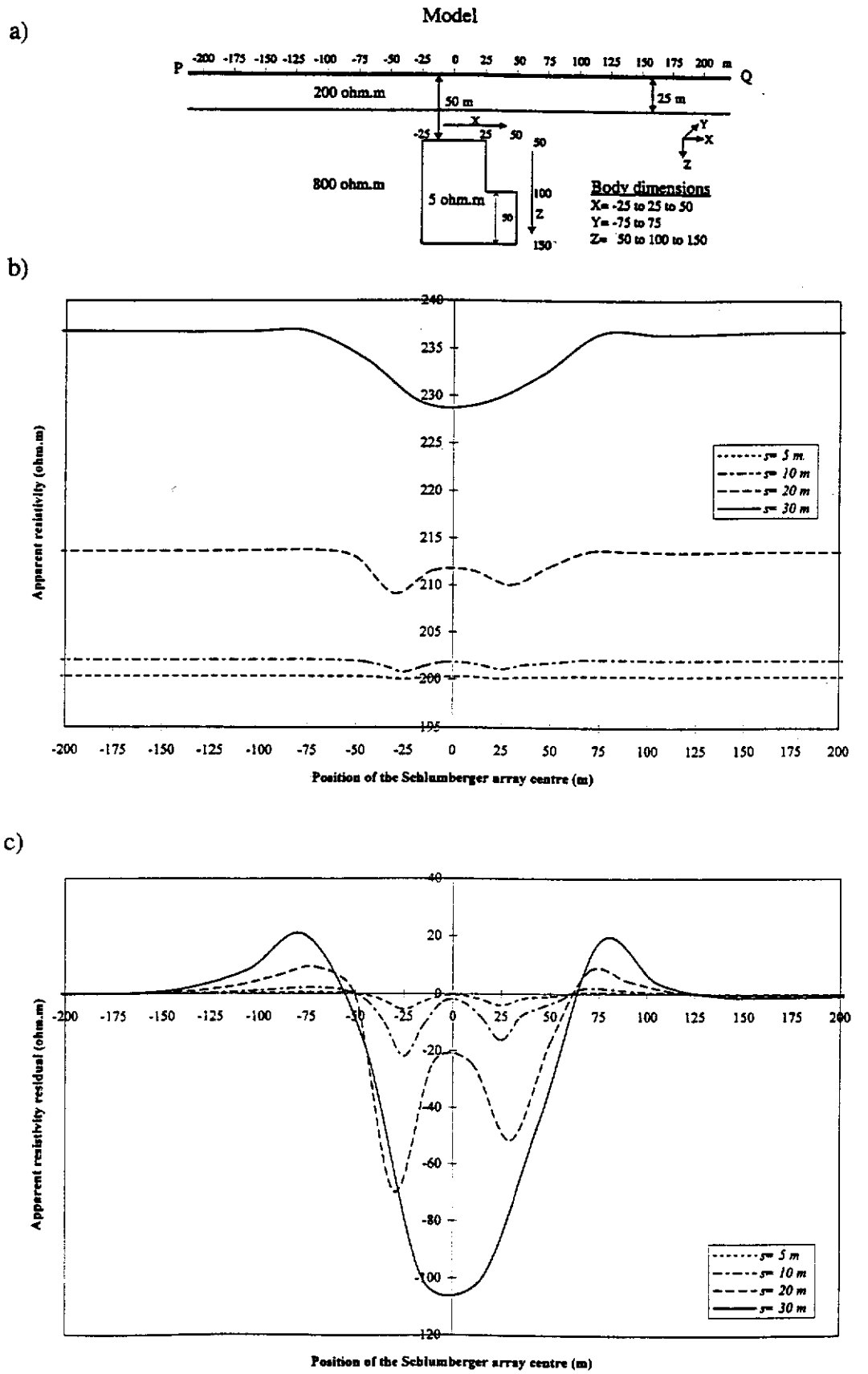

Figure 3.14. Survey combination B results for an asymmetric body. (a) Model, (b) Schlumberger apparent resistivity profiles along PQ, and (c) corresponding apparent resistivity residual response.

3.2.2.2.3 Multiple bodies

Consider two bodies of different sizes are placed at different depths in a two-layered earth as shown in Figure 3.15a. One of the bodies with dimensions $20\times40\times20$ m is placed at a depth of 30 m below the surface. The other body, which is larger and deeper, has dimensions $40\times120\times100$ m and is placed at depth of 50 m below the surface. Both bodies are conductive with the same resistivity of $\rho_B = 5$ ohm.m. The resistivity of the host medium is $\rho_H = 800$ ohm.m. The first layer (overburden) has a resistivity of $\rho_1 = 200$ ohm.m and a thickness of $h_1 = 25$ m.

The Schlumberger apparent resistivity profiles and the corresponding residual profiles for separations (AB/2) 5, 10, 20 and 30 m over these two bodies are illustrated in Figures 3.15b and 3.15c, respectively. Although one of the bodies is much smaller than the other, since it is located at a shallower depth, it has more greatly affected the Schlumberger profiles and residual profiles obtained with smaller electrode separations. The presence of one body affects the current flow through the other. The effects of each body cannot be considered in isolation. The Schlumberger apparent resistivity profiles show some variations over the bodies, which imply the presence of the anomalous bodies but they do not give much detail about the bodies due to the low sensitivity and resolution of the resistivity method. The residual profiles indicate the presence of bodies and their approximate locations much more effectively. However, in this case the two bodies are close together, and we see that in both the Schlumberger apparent resistivity and the apparent resistivity residual profiles, the close proximity of the bodies causes the profiles to be distorted. Thus, the location of the bodies from the apparent resistivity residual response is not quite as clear as that in the previous examples. Despite this, the approximate location of the lateral edges and centres of the bodies can be estimated from the minimum and small maximum peaks on the residual profiles as explained in the previous examples.

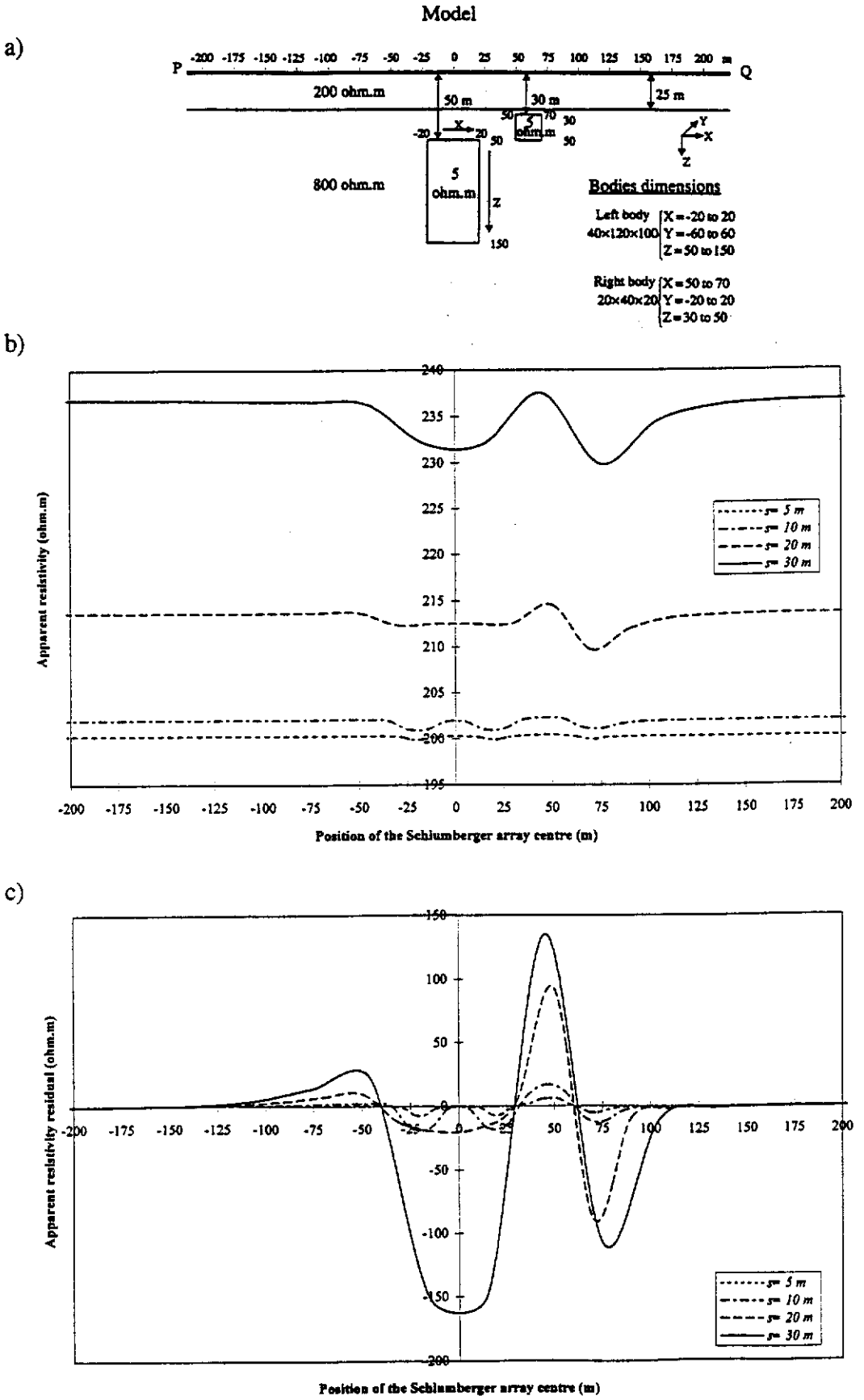

Figure 3.15. Survey combination B results for two bodies. (a) Model, (b) Schlumberger apparent resistivity profiles along PQ, and (c) corresponding apparent resistivity residual response.

Generally for the case of multiple bodies embedded in a layered earth, the effect of each body on the apparent resistivity residual profiles, depends on the geometry and resistivity parameters of the model including the resistivity of the body and layers, depth, thickness, and the lateral extent of the body as well as on the electrode spacings of the survey. A shallow, thick and extensive body has a great effect on the residual profiles while a deep and small body has little effect on the residual profiles. In addition, if the resistivity contrast between the body and the host medium is greater, the effect of the body on the residual profiles will generally be larger. The residual response is less successful in recognising the individual locations of anomalous bodies if they are close together or if overlapping occurs.

3.2.3 Effect of noise on the resistivity and residual responses

In order to see how noise affects 3-D resistivity and residual responses, we generated some random noise with the computer modelling program. To do this, a negative or positive percentage of the potential difference is randomly added to the actual potential difference in the program and the apparent resistivity and apparent resistivity residual were computed using these noisy potential values. In Figures 3.16b and 3.16c we demonstrate the effect of noise on the Wenner apparent resistivity profile and the corresponding apparent resistivity residual response with electrode spacing 20 m for the model shown in Figure 3.16a. The maximum level of random noise in this example is $\pm 1\%$. For comparison, we have also shown in Figures 3.16b and 3.16c, respectively, the actual (free of noise) Wenner apparent resistivity profile and the corresponding apparent resistivity residual response with the same electrode spacing (i.e. 20 m) for the same model shown in Figure 3.16a. Also it should be mentioned that we have used the same axis scale for the resistivity and residual graphs shown in this section. As can be seen from Figure 3.16b the noisy Wenner apparent resistivity profile is very bumpy, which makes difficult the detection of the body from this Wenner resistivity profile. The corresponding noisy residual profile is also very bumpy. However, although it is difficult, it may be possible to locate the body from this noisy residual profile. In this case, the effect of

a)

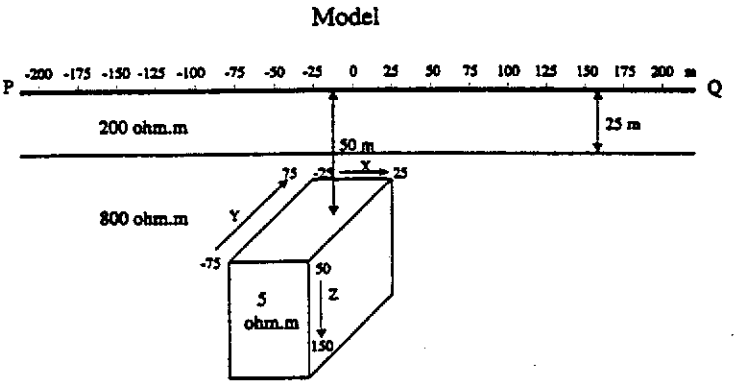

b)

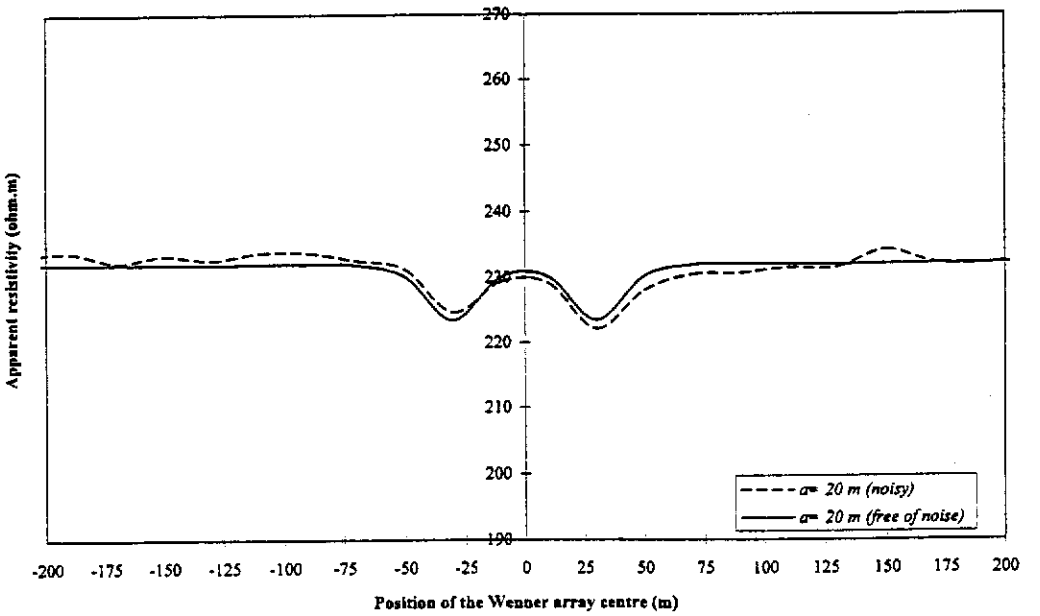

c)

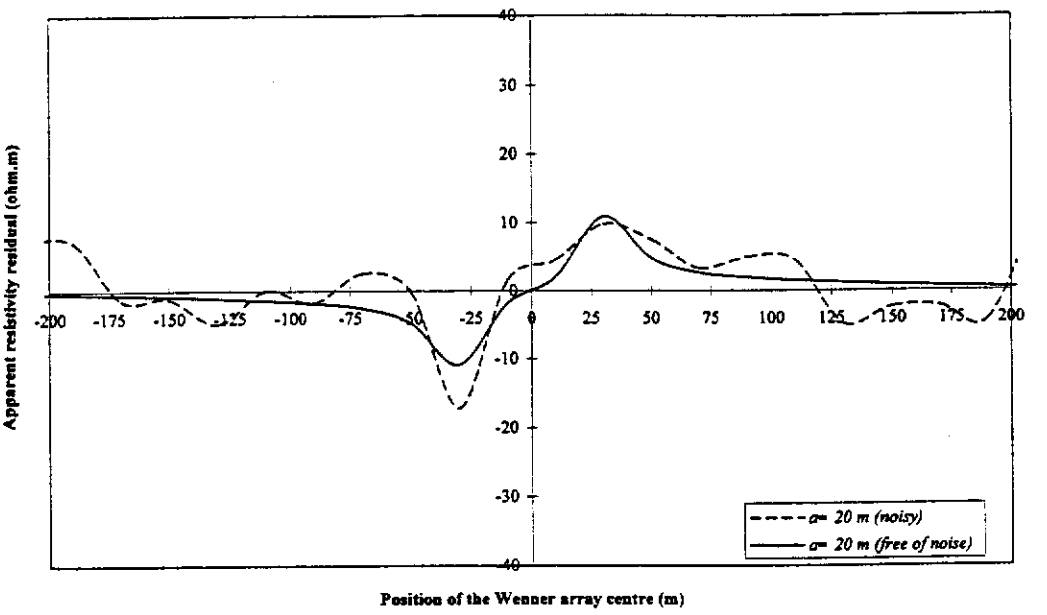

Figure 3.16. Effect of noise on the survey combination A results for a symmetric body. (a) Model, (b) Wenner apparent resistivity profiles along PQ, and (c) corresponding apparent resistivity residual response. In this case, the maximum level of random noise, added to the apparent resistivity values, is $\pm 1\%$.

noise on the apparent resistivity residual profile is not so great that it prevents us from detecting the body though it is difficult to accurately recognise the centre and lateral edges of the body. However, comparing the effect of noise on the Wenner apparent resistivity profile with that on the noisy apparent resistivity residual profile, we easily see that the noise has affected the residual profile much more than the Wenner apparent resistivity profile, and thus the noisy residual profile is more distorted than the noisy Wenner apparent resistivity profile. This is because the noisy residual profile has been obtained by adding the noisy Wenner apparent resistivity component to two other noisy two-electrode apparent resistivity components (using two different electrode spacings) having different coefficients [see equation (3.19)]. Thus, the residual computation strengthens the noise which is seen more strongly than on the Wenner apparent resistivity profile. This effect points to the weakness of the residual apparent resistivity technique.

Increasing the level of random noise by more than $\pm 1\%$ of the potential difference distorts the Wenner apparent resistivity profiles and the corresponding apparent resistivity residual profiles even more, and recognising the signal due to the body from the noise becomes nearly impossible. Therefore, one cannot detect or locate the body from these noisy resistivity or residual profiles confidently.

Figures 3.17b and 3.17c show the effect of noise on a Schlumberger apparent resistivity profile and the corresponding apparent resistivity residual response with a maximum level of random noise equal to $\pm 1\%$ for the model shown in Figure 3.17a (the same model as Figure 3.16a) and separation (AB/2) equal to 20 m. In these figures, as in the previous ones, various small and large irregularities are seen in both the resistivity and residual graphs. These irregularities cause a problem in detecting the body from the Schlumberger resistivity profiles. However from the corresponding residual profiles, it is still quite possible to find the presence of the body and its location approximately. In this case also if the maximum level of noise is increased, the irregularities created due to the noise, in some cases, may be mistaken for the signal from some anomalous body.

a)

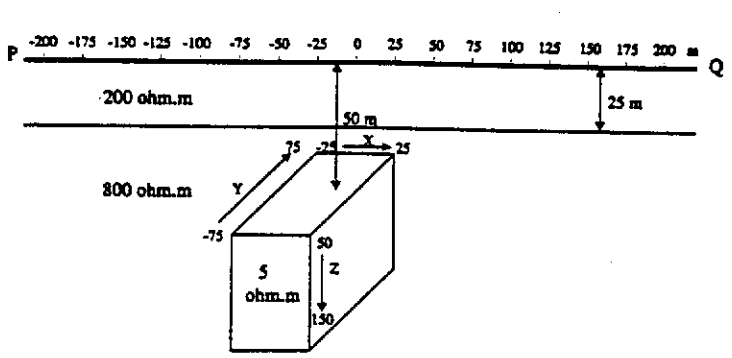

b)

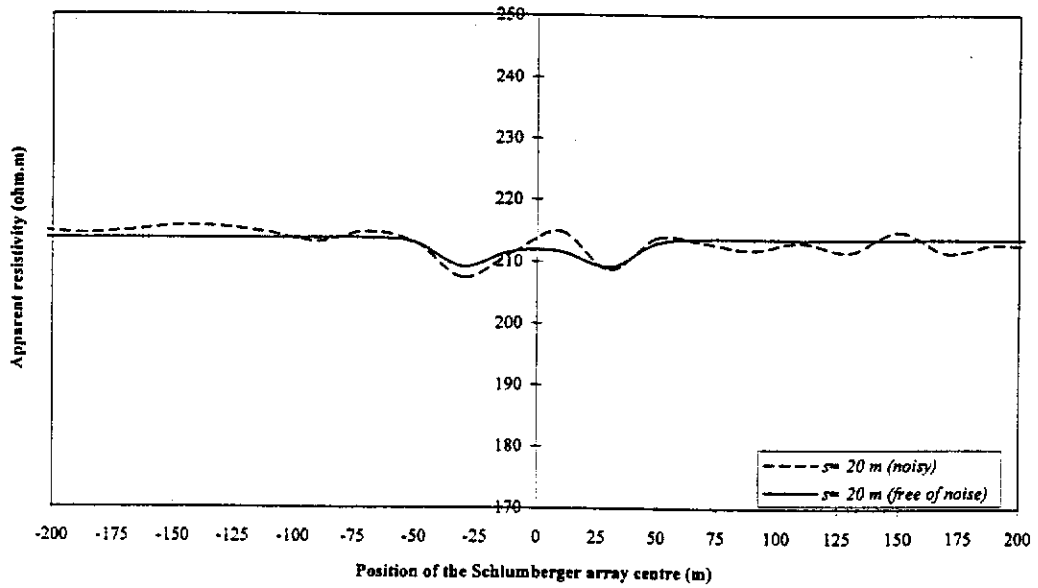

c)

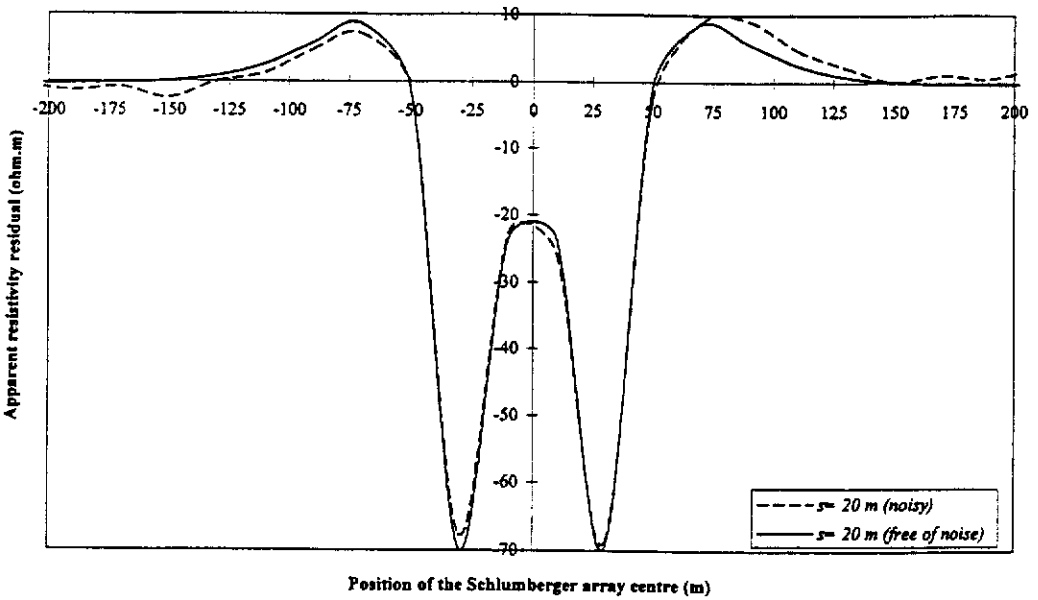

Figure 3.17. Effect of noise on the survey combination B results for a symmetric body. (a) Model, (b) Schlumberger apparent resistivity profiles along PQ, and (c) corresponding apparent resistivity residual response. In this case, the maximum level of random noise, added to the apparent resistivity values, is $\pm 1\%$.

A comparison between the two noisy apparent resistivity residual profiles (shown in Figures 3.16c and 3.17c), obtained using the multisystem combinations A and B (Figure 3.2), indicates that a given level of noise distorts the residual profiles resulting from the multisystem combination A far more than the residual profiles resulting from the multisystem combination B. The reason seems to be that more apparent resistivity data are used in the apparent resistivity residual computation from the multisystem combination A than the multisystem combination B [cf. equations (3.19) and (3.37)]. Adding $\pm 1\%$ random noise to each one of the Wenner and two-electrode apparent resistivity components in the right-hand side of equation (3.19), results in having up to $\pm 4\%$ noise in the corresponding apparent resistivity residual. However, adding $\pm 1\%$ random noise to each one of the Schlumberger and equatorial dipole-dipole apparent resistivity components in the right-hand side of equation (3.37), results in having up to $\pm 2\%$ noise in the corresponding apparent resistivity residual. Thus, more random noise is actually added to the case shown in Figure 3.16c than the case shown in Figure 3.17c. As a result more distortion of the actual residual response is seen in Figure 3.16c than that in Figure 3.17c. The fact that for the same model, the residual obtained from the multisystem combination B (Figure 3.17c) produces a higher amplitude anomaly than that from the multisystem combination A, is also an advantage for the multisystem combination B from the view point of the detection of the body in noisy areas. When we add a given level of noise to the apparent resistivity data of the above-mentioned configurations, although it distorts both residual profiles (obtained from the multisystem combinations A and B), the detection of the body from the residual profile obtained by the multisystem combination B is superior. This is because in addition to the lower noise level for the residual obtained from the multisystem combination B than that from the multisystem combination A (i.e. $\pm 2\%$ compared to $\pm 4\%$, respectively), we have a bigger residual anomaly response obtained by combination B than that obtained by combination A. Thus, the effect of noise on the residual response obtained by the multisystem combination B (shown in Figure 3.17c) is not as great as that on the residual response obtained by the multisystem combination A (shown in Figure 3.16c).

3.2.4 General apparent resistivity residual concept

An apparent resistivity residual may be defined as a weighted difference between apparent resistivity values obtained using different arrays in a profiling technique. The resultant difference will enhance the response differences of the arrays to the presence of anomalous bodies, by removing the approximate common response to the layered environment.

The resulting apparent resistivity residual calculated in this way along a profile is then primarily an indicator of anomalous conductivity zones. The character of the computed residual depends on the way it was derived from the profiling arrays. Further study of the apparent resistivity residual is needed to completely characterise its nature. It is to be expected that this will depend on the array dimensions, array types used in computing the residual response, the nature of anomalous zone, depth of anomalous zone, layer specifications, and the resistivity relationship between the anomalous zone and its host rock.

Examples of the apparent resistivity residual, as an initial study in this thesis, were obtained from multisystem resistivity measurement combinations A (i.e. Wenner and two-electrode resistivity measurements) and B (i.e. Schlumberger and equatorial dipole-dipole resistivity measurements). As can be seen for each model the computed apparent resistivity residual profile obtained from the multisystem combination A is quite different from that obtained from the multisystem combination B [cf. equations (3.19) and (3.37)]. Consequently, the interpretation of the apparent resistivity residual data obtained by these two multisystem combinations must be different. It was shown that when using the apparent resistivity residual profiles obtained using combination A, the approximate location of the edges of a conductive or resistive body is indicated by the negative and positive peaks in the residual profiles. However, using the apparent resistivity residual profiles obtained using combination

B, the location of the edges of a body are estimated from the minimum (if the body is conductive) or maximum (if the body is resistive) peaks in those residual profiles.

From a comparison of the examples presented in this thesis, we find that the residual profiles obtained by combination B are not as good and reliable as those obtained by combination A for accurately locating a body in the subsurface. On the other hand, the residual response obtained by combination B is much more immune to random noise than that obtained by combination A. This will have consequences for field applications.

A problem, that we usually face in locating the lateral edges of a subsurface body from the residual profiles obtained using these multisystem combinations is that while different electrode spacings produce similar residual profiles, they may show different locations for the edges of the body. The residual profiles with large electrode spacings show large and wide responses so that the peaks of the residual profiles (indicating the lateral edges) either are removed (in the case of combination B) or occur beyond the lateral edges of the body (in the case of combination A). The residual response, in addition to the electrode spacings of the arrays used, depends on several other factors related to the body, the layers and the interaction between the body and the host medium. It would appear that for both combinations, the best estimate of the location of the edges of a body is from a residual profile, in which the ratio of electrode spacing to depth of body is between 0.1 to 1. This ratio, which is just nominal, is based on the limited number of examples tested for this purpose and it does differ in this range from one model to another.

The centre of the top section of an anomalous body is indicated by a zero crossover in the residual profile obtained using combination A, and by a peak in the residual profile obtained using combination B.

The height of a residual anomaly depends on the resistivity contrast between the body and the host medium as well as the array type and electrode spacings. We see that higher resistivity contrasts (between the body and the host environment), and

shallower and larger bodies produce the larger residual anomalies. Multisystem combination B produces a larger residual anomaly than that produced by the multisystem combination A for the same model and electrode spacing.

It would appear that the apparent resistivity residual technique could be quite successful for simple geological model environments free of noise (or with minimum noise). For the noise free environments, the residual profiles obtained by the multisystem combination A are better than those obtained by the multisystem combination B for resolving the body in the subsurface.

The apparent resistivity residual can be obtained from any multisystem combination for which we can establish a mathematical relationship between the apparent resistivities of the systems used in the combination for a layered earth (free of any anomalous body). The apparent resistivity residual quantities obtained by other multisystem combinations are expected to be different, and thus, may indicate a body in the subsurface differently. In this thesis, only multisystem combinations A and B were considered for obtaining the apparent resistivity residual just because of the simplicity of the mathematical relationships which exist between the apparent resistivities given by those systems for a layered earth, in order to illustrate the principle of the method.

In all cases, the computed apparent resistivity residual values will go to zero where no 3-D anomalous zones exist.

The most significant and common aspect of the apparent resistivity residual data (obtained by any multisystem combination) is that they greatly enhance the anomalous 3-D effects and they considerably reduce the effects of layered structures in the apparent resistivity residual computations. The apparent resistivity residual data mainly contain the resistivity information from the anomalous regions. Hence, the apparent resistivity residual improves the target detectability of DC resistivity methods for subsurface anomalous targets.

3.3 Case study: Application of the apparent resistivity residual technique to field data recorded in an area in Western Australia

In this section, we present the results of resistivity profiling surveys carried out in an area in Western Australia. We also test the corresponding apparent resistivity residual results for their effectiveness in detecting subsurface conductive anomalies in that area. Furthermore, interpretation of the field data using numerically simulated synthetic data is presented.

3.3.1 Geology and hydrogeology of the survey area

The survey area is located in the coastal plain, which is underlain by the sedimentary rocks of the Perth Basin (Figure 3.18). The area has been drilled extensively for the installation of ground water bores and water supply bores, and therefore the near-surface geology of the area is well established. The Yilgarn Craton, which consists of igneous and metamorphic rocks, bounds the Perth Basin in the east. The boundary is defined by the Darling Fault, a major regional north-south striking structure (Figure 3.18). In the survey area, a sequence of sediments comprising sandy clay, sand and sandy gravel unconformably overlie mottled red and grey silty clay at approximately 15 metres depth. The sequence of sandy clay, sand and sandy gravel sediments, which are known as a member of late Tertiary to Quaternary geological units, lies beneath the coastal plain and is informally termed the superficial formations. An east-west schematic section of the subsurface geology of the survey area is shown in Figure 3.19.

Regional hydrogeology of the survey area indicates that groundwater in the region occurs in three main aquifers: the superficial formations, the silty clay sediments beneath the superficial formations, and fractures in the granitic bedrock. The superficial formations, which comprise the early and middle Pleistocene geological formations, are up to 25 metres thick and consist of quartzose sandy to clayey

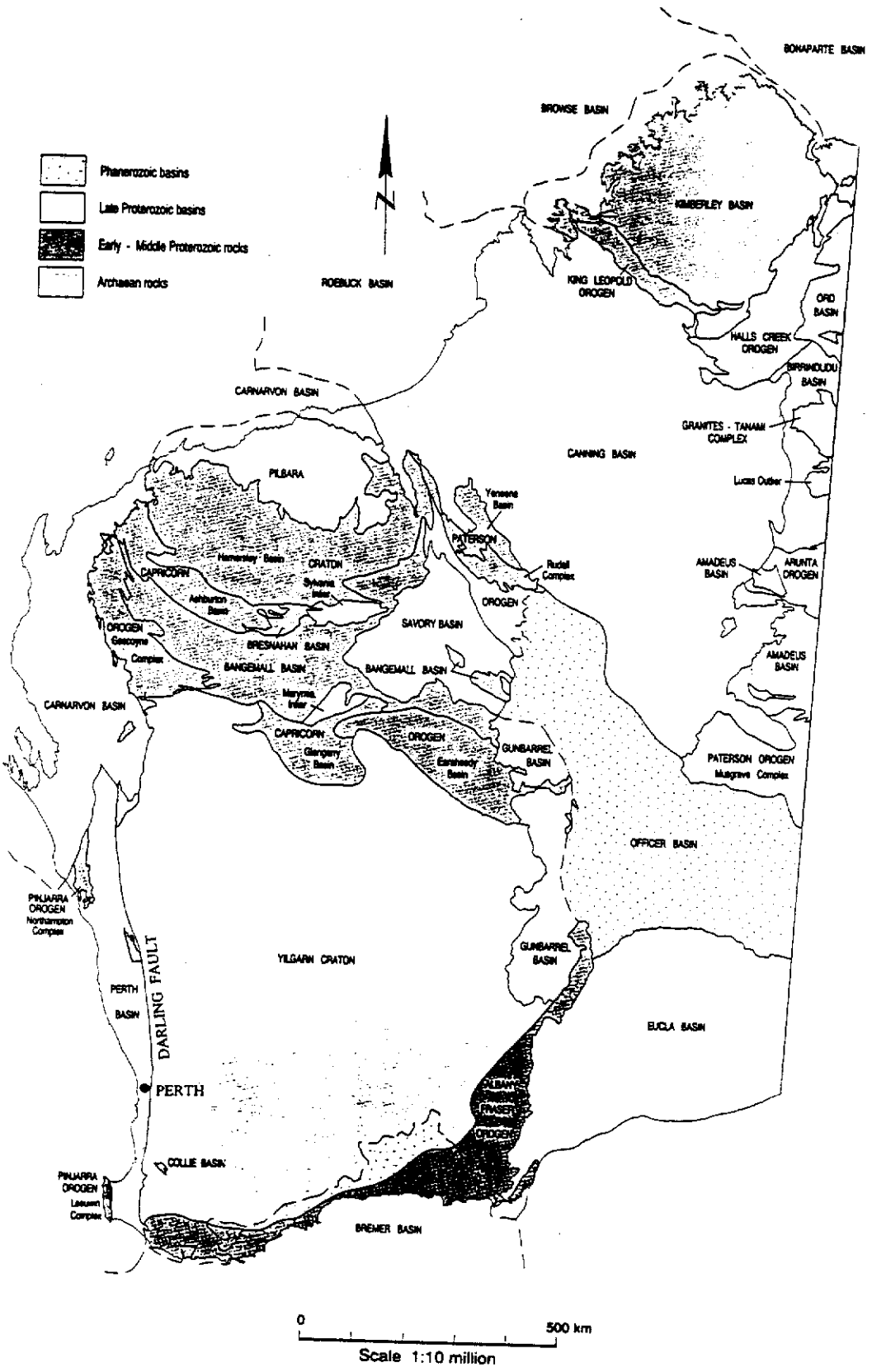

Figure 3.18. Main geological divisions in Western Australia. The survey area is located in the Perth Basin (Geological Survey of Western Australia, 1996).

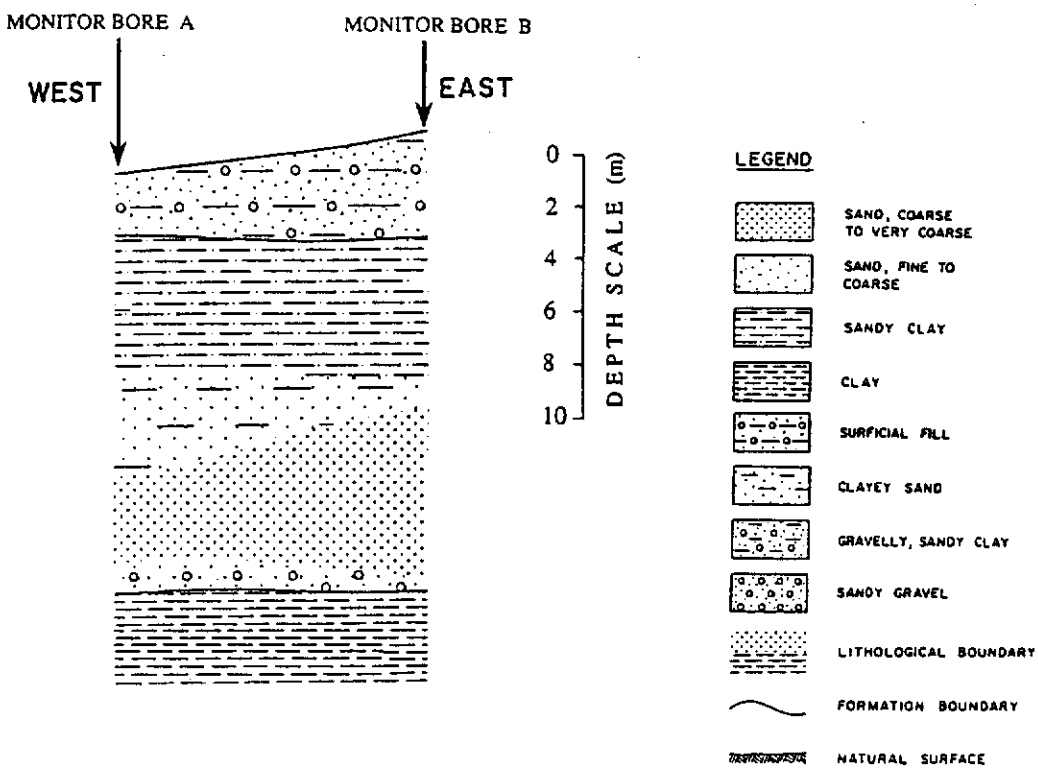

Figure 3.19. An east-west schematic section of the subsurface geology of the survey area.

deposits. The superficial formations unconformably overlie a Jurassic geological unit which is comprised of clay, siltstone and shale interbedded with sandstone, and which, in turn unconformably overlies Archaean granitic basement. The superficial formations form an unconfined aquifer system. Within the survey area only the early Pleistocene formation is represented in the superficial formations. The formation may be further subdivided into an upper, largely unsaturated sandy-clay member (approximately 8 metres thick) and a lower, saturated, clayey-sand member, which extends to depths of approximately 15 metres below ground level. The saturated portions of the sandy clay member of this formation are termed the shallow aquitard (a low permeability unit that can store and transmit groundwater slowly to adjacent aquifers) while the saturated clayey sand member comprises the main regional aquifer.

Recharge to the superficial formation aquifers is expected to occur directly from rainfall where sandy strata are exposed at the surface. Groundwater flow in the region is westerly, towards the coast, and locally towards natural surface water bodies and man-made surface features. Discharge occurs by seepage to the surface and by evapotranspiration.

Lateral advection and dispersion is likely to be greater than vertical movement and lateral advection will be increased where the formation has a higher permeability.

The rate of the westward groundwater flow is up to 100 metre per year. The water table in the upper part of the superficial formations in the study area occurs at between 5 to 7 metres below surface.

3.3.2 Resistivity profiling at the survey area

The DC resistivity method was selected to locate anomalous conductive zones in the survey area. Since the area is full of cultural features such as buildings, power lines,

and topographic variations, it was considered that the DC resistivity methods would give better results than electromagnetic surveys.

3.3.2.1 Resistivity data acquisition

The resistivity equipment, which was used in the field, consisted of a TSQ-3/3000 W IP/Resistivity transmitter and a IPR-10A IP receiver, both produced by the Scintrex company. In addition, a generator was used in connection with the transmitter for injecting the electric current into ground through steel spike electrodes. The amount of the current injected into ground was read from the transmitter, and the potential difference created between the potential electrodes was measured by the receiver.

The survey area (shown in Figure 3.20) is located to the west of building A. The resistivity profiling surveys were carried out along lines 1 and 2 (Figure 3.20) which run north-south and east-west respectively. The approximate length of each line was 150 m. Since the main aim was to locate anomalous conductive zones in the subsurface along lines 1 and 2, the resistivity profiling survey was extensively applied along these two lines using a range of electrode spacings.

The apparent resistivity residual, which was successful for detecting subsurface anomalous bodies on synthetic data, was computed for each profiling case. Since the apparent resistivity residual obtained by the multisystem combination A (Figure 3.2) gives more accurate positioning of the extent of anomalous zones than that by the multisystem combination B (Figure 3.2), we chose combination A, although it is more susceptible to noise. Hence the resistivity profiling survey was carried out along lines 1 and 2 using the Wenner and two-electrode arrays, from which the corresponding apparent resistivity residual results were obtained. Because we were looking for low resistivity anomalies (indicating the subsurface conductive zones), we expected them to be indicated by residual signatures like the one shown in Figure 3.3.

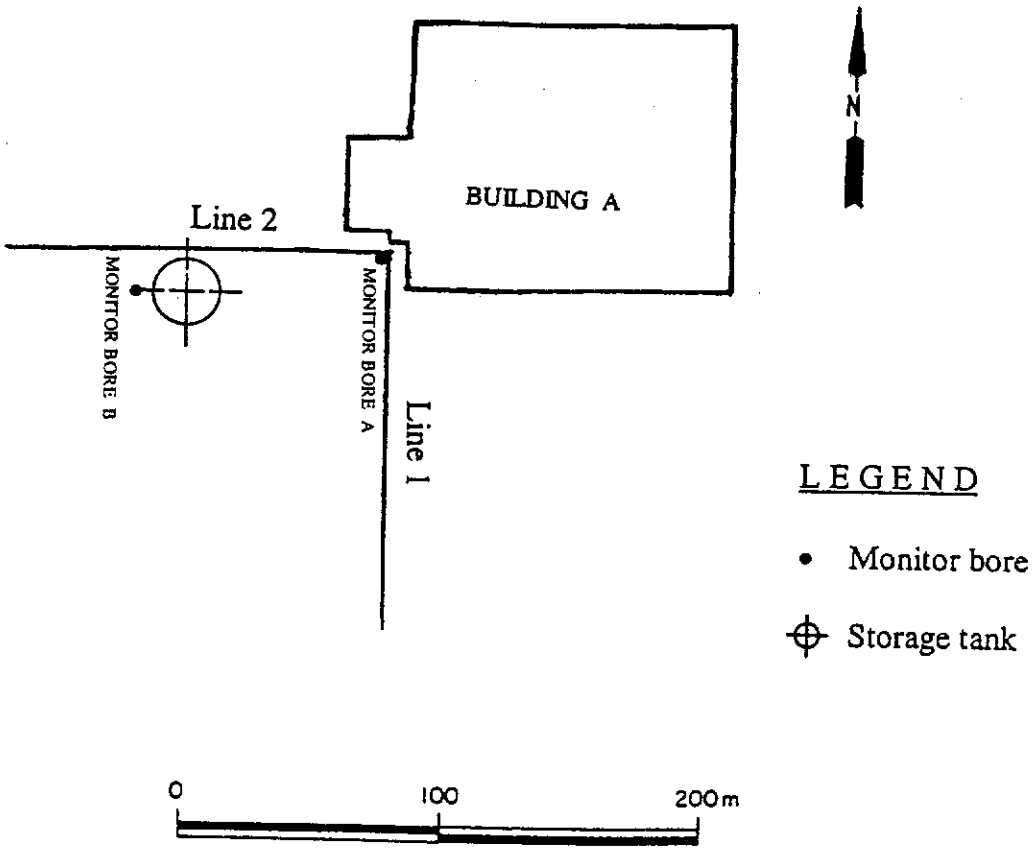

Figure 3.20. The survey area and traverse locations. The DC resistivity profiling surveys were carried out along traverse lines 1 and 2.

3.3.2.2 Processing and interpretation of the results

Resistivity profiling was carried out along lines 1 and 2. Each profile commenced 3.5 m from building A. We designated this end of both lines as the origin. Hydrogeological data from the monitor bores in the area indicate that the subsurface conductive anomaly is relatively shallow, generally at a depth of less than 7 m, but it may extend to 15 m below ground level. In the resistivity profiling survey, electrode spacings of 2, 4, 8, 12 and 16 m were used with the Wenner array while with the two-electrode array we used the electrode spacings 24 and 32 m as well. Consequently, we obtained the apparent resistivity values for a range of electrode spacings along these two lines. The above-mentioned electrode spacings were considered to be sufficient for investigating the shallow subsurface conductive anomalies expected within the survey area, based on conventional profiling practice.

From profiling data obtained with the Wenner and two-electrode configurations, an apparent resistivity residual profile was produced for each electrode separation. Then the apparent resistivity residual profiles were examined for possible anomalous conductive zones.

Interpretation

Line 1

Figure 3.21 shows the Wenner apparent resistivity profiles and the corresponding apparent resistivity residual responses for different electrode spacings of 2, 4, 8, 12 and 16 m along the north-south line 1. The Wenner apparent resistivity profiles indicate two regions of low resistivity. The first region is from 0 m to 25 m from the start of the line (adjacent to building A), and the other region is at 30-55 m from the start of the line. Beyond 60 m there is no indication of anomalous conductive zones, and the noisy character is attributed to cultural origins. The two-electrode apparent

a)

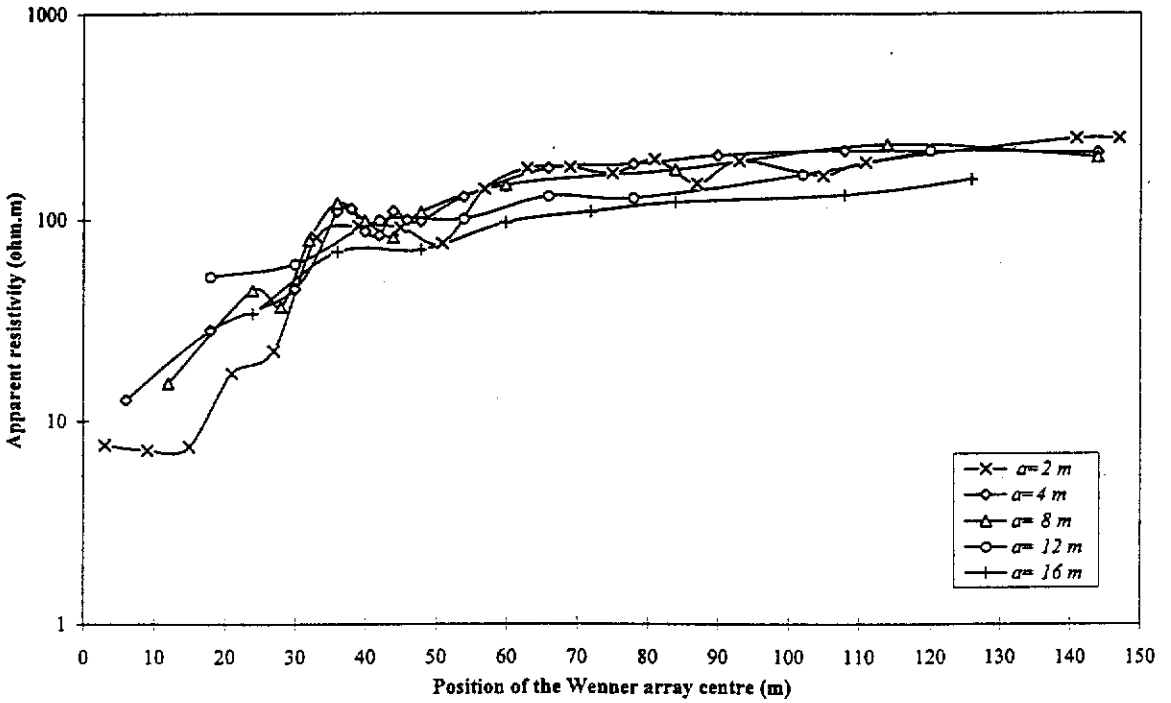

b)

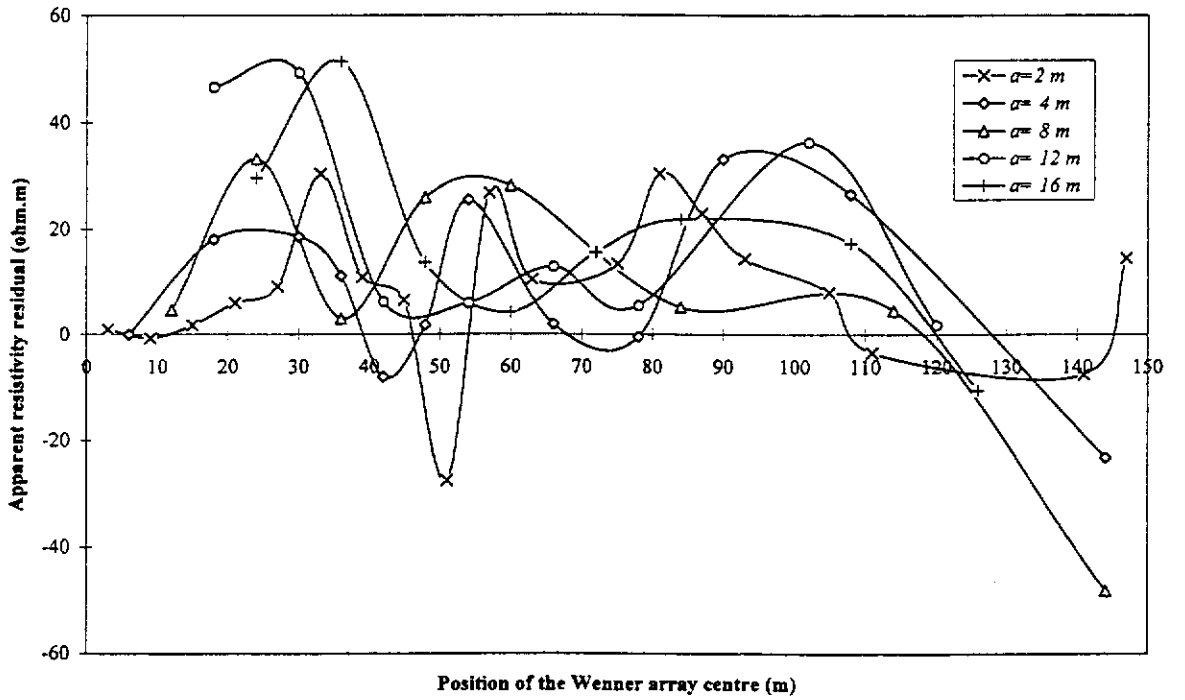

Figure 3.21. Results of the resistivity profiling survey using the multisystem combination A along line 1 at the survey area. (a) Wenner apparent resistivity profiles, and (b) corresponding apparent resistivity residual profiles.

resistivity profiles, shown in Figure 3.22, indicate the anomalous conductive zone at the beginning of the line, but the zone at 30-55 m is not detected (except for electrode spacing $a=8\ m$).

The apparent resistivity residual profiles (Figure 3.21b) at first glance seem to lack consistency, but this is not unexpected due to the noisy nature of the data. Furthermore, from the modelling studies discussed in section 3.2, we see that the residual response depends on the depth of the anomalous zone and the array dimensions. The apparent resistivity residual profiles, for electrode spacings 8, 12 and 16 m, show that a relatively deep conductive anomaly zone exists at the beginning of the line, while the residual profiles for electrode spacings 2 and 4 m indicate a relatively shallow conductive anomaly in the 35-55 m region as well as at the beginning of the line. The high positive residuals at the beginning of the line show a good correlation with the "right-hand side" of a synthetically generated residual profile (Figure 3.3) from a subsurface anomalous conductive zone, which is considered to extend under building A to the north. The negative response region of the residual ("left-hand side" of Figure 3.3), though not measured, would have been located also to the left of the profile origin in Figure 3.21b, had measurements been possible to the north beneath building A (Figure 3.20).

No consistency can be found in the noisy residual data beyond 60 m. In this region, no anomalous features are observed, and no anomalous conductive zones are interpreted as being within that region.

The hydrogeological data from monitor bore A, which is located in the close vicinity of building A (Figure 3.20), indicate high conductivity in the subsurface in this part of the survey area. However there is no other monitor bore close to line 1 for direct confirmation.

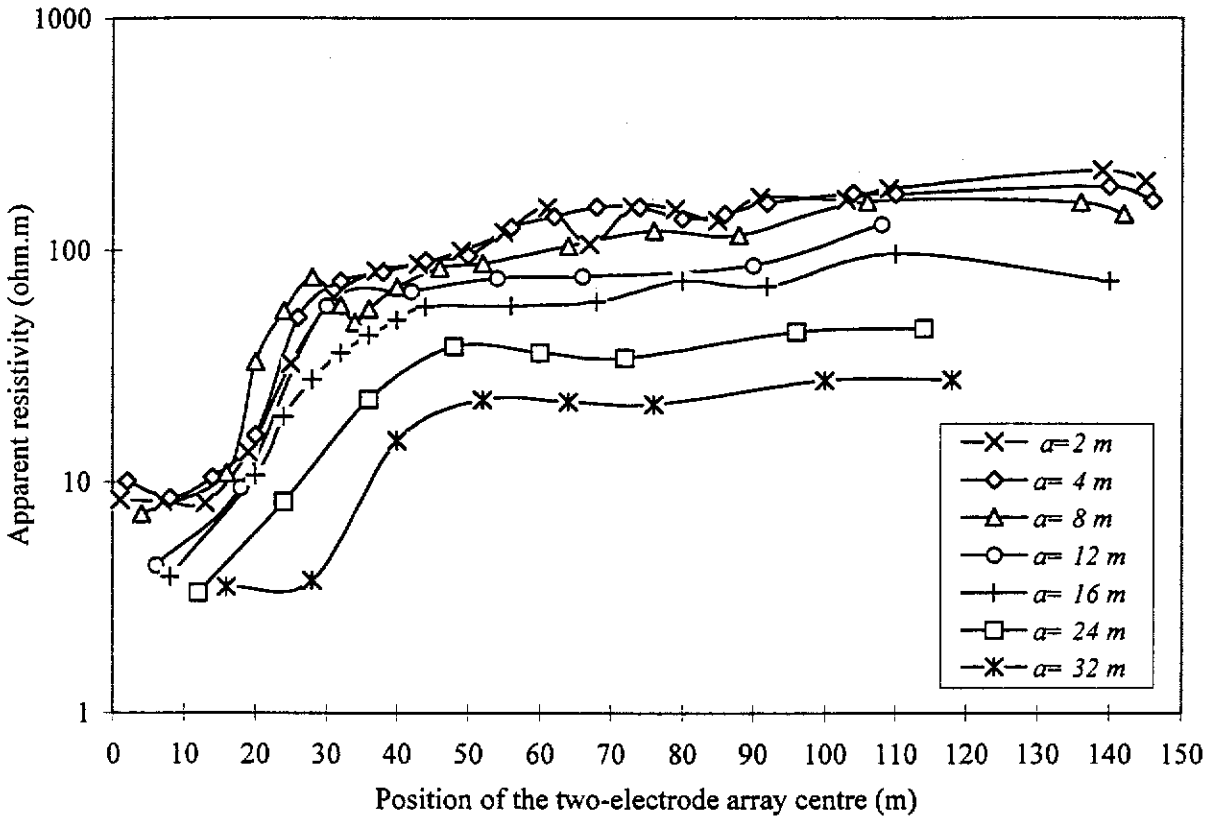

Figure 3.22. Results of the resistivity profiling survey using the two-electrode array along line 1 at the survey area. Different electrode spacings of 2, 4, 8, 12, 16, 24 and 32 m in this survey were used.

Noise reduction

The apparent resistivity residual profiles (Figure 3.21b) are very noisy, which makes the distinction between variations due to anomalous conductive zones and irregularities due to noise very difficult. To reduce the effect of noise in the apparent resistivity residuals, we normalise them. For this, we divide the apparent resistivity residual by an apparent resistivity.

A brief study of normalisation on the synthetic apparent resistivity residual data obtained from numerical modelling showed that normalisation does not change the basic shape of the apparent resistivity residual anomaly, but it does change the height of anomalies. For a particular model and array combination type, one particular normalisation method may give larger anomaly heights compared to other normalisation methods for detecting an anomalous surface zone. However, there is no one particular normalisation method, which can be used for all situations. It varies with the array combination and the geoelectrical structure. Generally though, the normalisation studies on the synthetic apparent resistivity residual data for a limited number of models indicated that normalisation would not add any new information to that obtained from the apparent resistivity residual profiles. More work on normalisation for further field studies needs to be carried out.

Normalisation was found to be very helpful for reducing the effect of noise on the apparent resistivity residual profiles, which we obtained from the field data. The reason is that by dividing the residual noisy data by the corresponding noisy apparent resistivity, the effect of noise is reduced. Figure 3.23 shows normalised apparent resistivity residual profiles along line 1 for different electrode spacings shown in the figure. The normalisation in this case has been carried out using the weighted average of the Wenner and two-electrode apparent resistivities in the following way:

$$\rho_{aAv}(a) = \frac{\rho_{aW}(a) + 2\rho_{aT}(a) + \rho_{aT}(2a)}{4}, \tag{3.38}$$

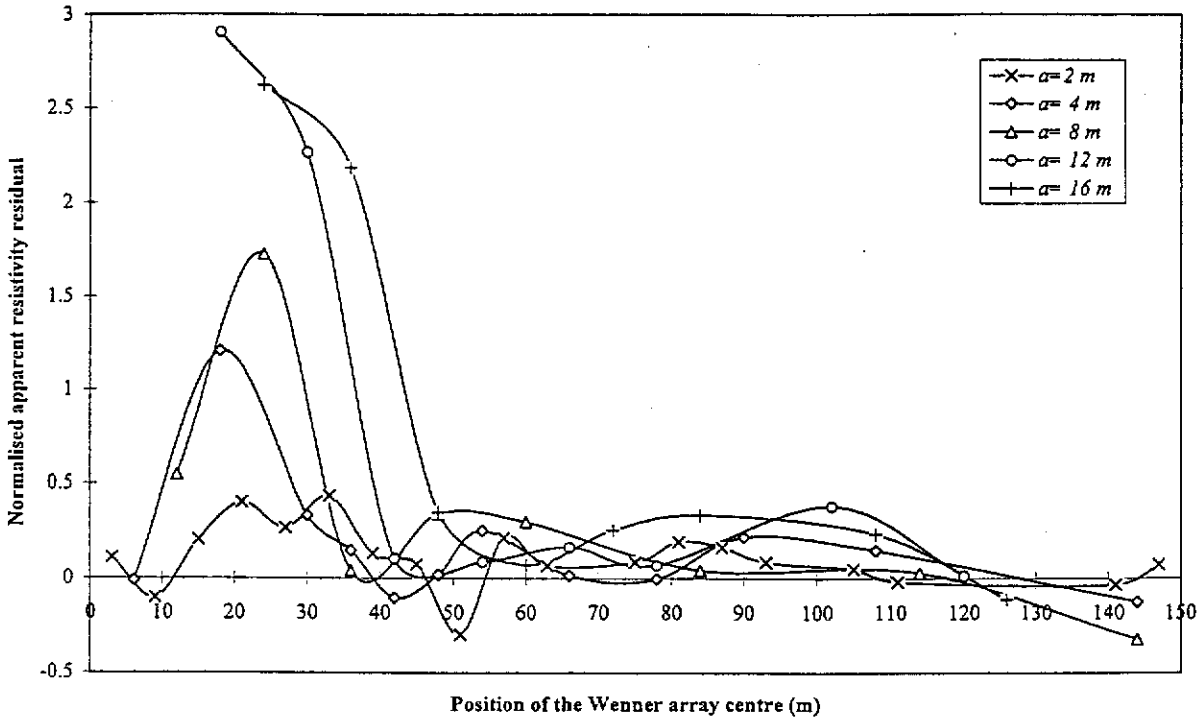

Figure 3.23. Normalised apparent resistivity residual profiles along line 1 at the survey area. The profiles with different electrode spacings of 2, 4, 8, 12 and 16 m are shown in this figure.

where $\rho_{aAv}(a)$ is the weighted apparent resistivity average for electrode spacing a, and ρ_{aW} and ρ_{aT} are, respectively, the measured Wenner and two-electrode apparent resistivities in the field. Then, we obtain the normalised apparent resistivity residual $NR(a)$ as

$$NR(a) = \frac{R(a)}{\rho_{aAv}(a)}, \tag{3.39}$$

where $R(a)$ is the apparent resistivity residual given by equation (3.19).

As can be seen from the normalised apparent resistivity residual profiles (Figure 3.23), they have basically similar shapes to the un-scaled apparent resistivity residual profiles (Figure 3.21b). However, the subsurface anomalous conductive zone at the beginning of the line can be seen more clearly in the normalised residual profiles than in the residual profiles. Furthermore, the large variations due to noise (irregularities), that are seen in the region beyond 60 m on the residual profiles along the line, are considerably reduced in the normalised residual profiles, as the normalisation significantly reduces the effect of noise.

Line 2

Wenner apparent apparent resistivity profiles and the corresponding apparent resistivity residual responses are presented in Figures 3.24a and 3.24b for different electrode spacings of 2, 4, 8 and 16 m along the east-west line 2. Also, we present in Figure 3.25 the two-electrode apparent resistivity profiles for different electrode spacings of 2, 4, 8, 16 and 32 m along line 2. As can be seen from the Wenner and two-electrode profiles along this line, a zone with a very low resistivity occurs at the beginning of the line. This low resistivity zone is assumed to be due to the subsurface conductive anomaly in the area since we do not see any considerable lateral changes in the stratigraphy of the area to relate to this low resistivity zone. Also, as can be seen from the Wenner and two-electrode profiles, especially with small electrode

a)

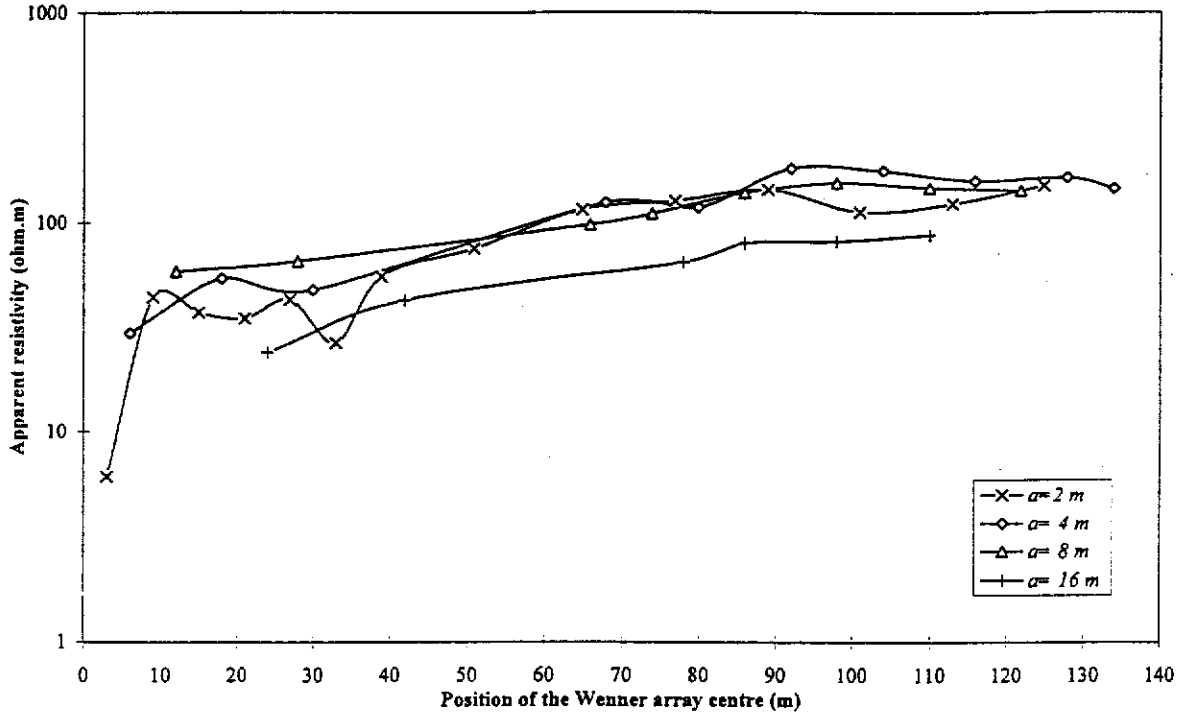

b)

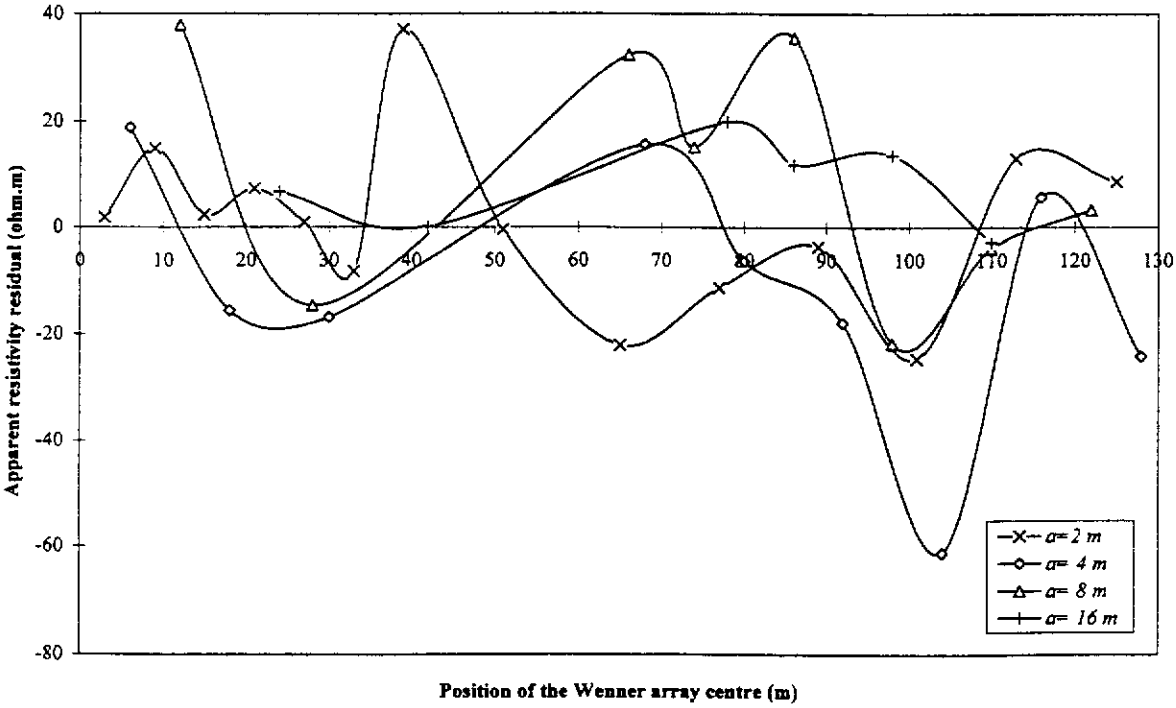

Figure 3.24. Results of the resistivity profiling survey using the multisystem combination A along line 2 at the survey area. (a) Wenner apparent resistivity profiles, and (b) corresponding apparent resistivity residual profiles.

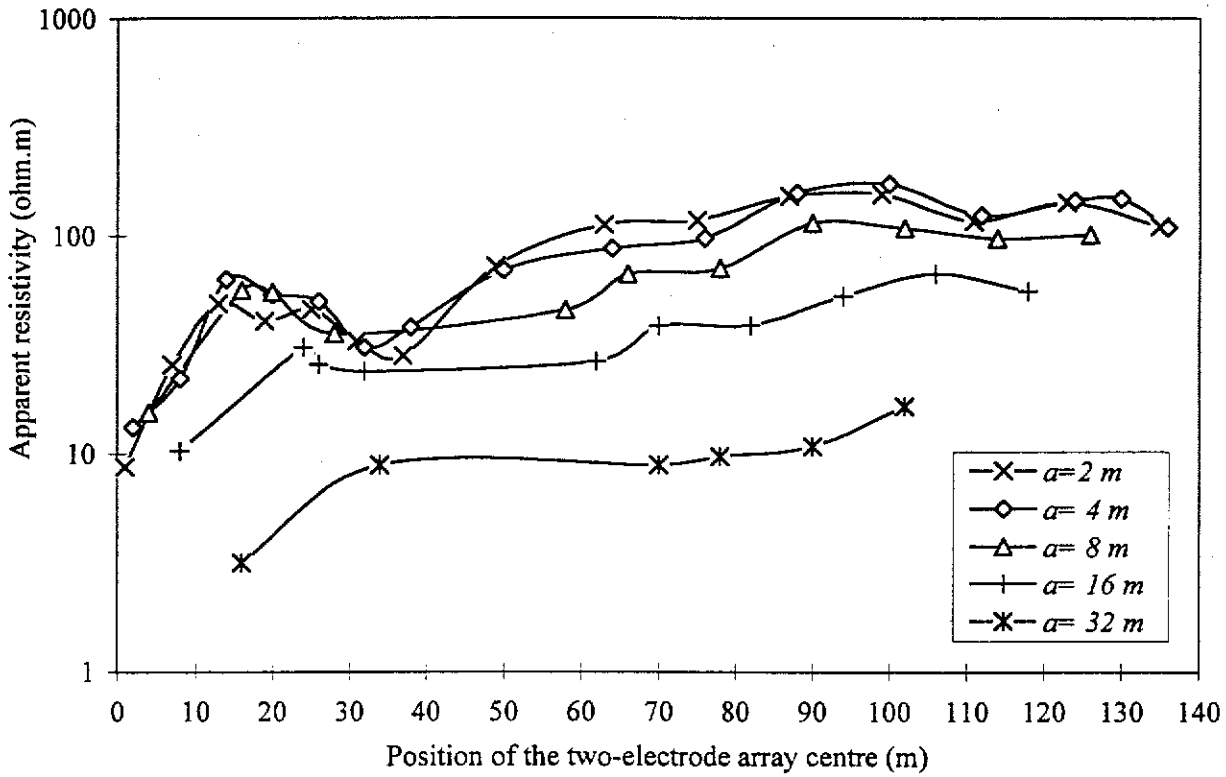

Figure 3.25. Results of the resistivity profiling survey using the two-electrode array along line 2 at the survey area. Electrode spacings of 2, 4, 8, 16 and 32 m were used.

spacings, another relatively low resistivity zone appears at 25-40 m west of the origin of the line. Beyond 60-70 m no significant changes are seen in the resistivity values of the profiles. The relatively low resistivity zone at the 95-120 m region along this line can be attributed to the presence of noise in the survey area. Likely noise sources are a large steel tank and sudden breaks in topography, which are located close to this part of the line.

As in the case of line 1, the apparent resistivity residual profiles along line 2, shown in Figure 3.24b, are also very irregular, which may possibly indicate they are influenced by noise. This makes the distinction between variations due to anomalous conductive zones and irregularities due to noise very difficult. In this case, the residual profiles corresponding to different electrode spacings have similar forms along some parts of the profile. The high positive residuals at the beginning of the line can be correlated with the "right-hand side" of the synthetically generated residual profile (Figure 3.3) from a subsurface anomalous conductive zone, which is considered to extend under building A to the east. The negative response region of the residual ("left-hand side" of Figure 3.3), though not measured, would have been located also to the left of the profile origin in Figure 3.24b, had measurements been possible to the east beneath building A (Figure 3.20). At a distance of between 25 to 70 m west of the origin of the line another conductive anomaly can be recognised as the residual profiles show for short offsets, first, a negative peak and then a positive peak in the profiling direction. Beyond 70 m the residual profiles are very noisy presumably due to noise sources such as a large steel tank and sudden breaks in the topography, which are located close to this part of line 2. The hydrogeological information along this line is available only from monitor bore A (Figure 3.20) located close to the origin of the line and monitor bore B located close to the other end of the line. The hydrogeological data from monitor bore A indicate the existence of a highly conductive anomaly in the subsurface while the hydrogeological data for monitor bore B indicate no subsurface conductive anomaly at this bore location.

For this line, normalised apparent resistivity residual profiles are shown in Figure 3.26. The normalisation in this case also has been carried out as for line 1. We see

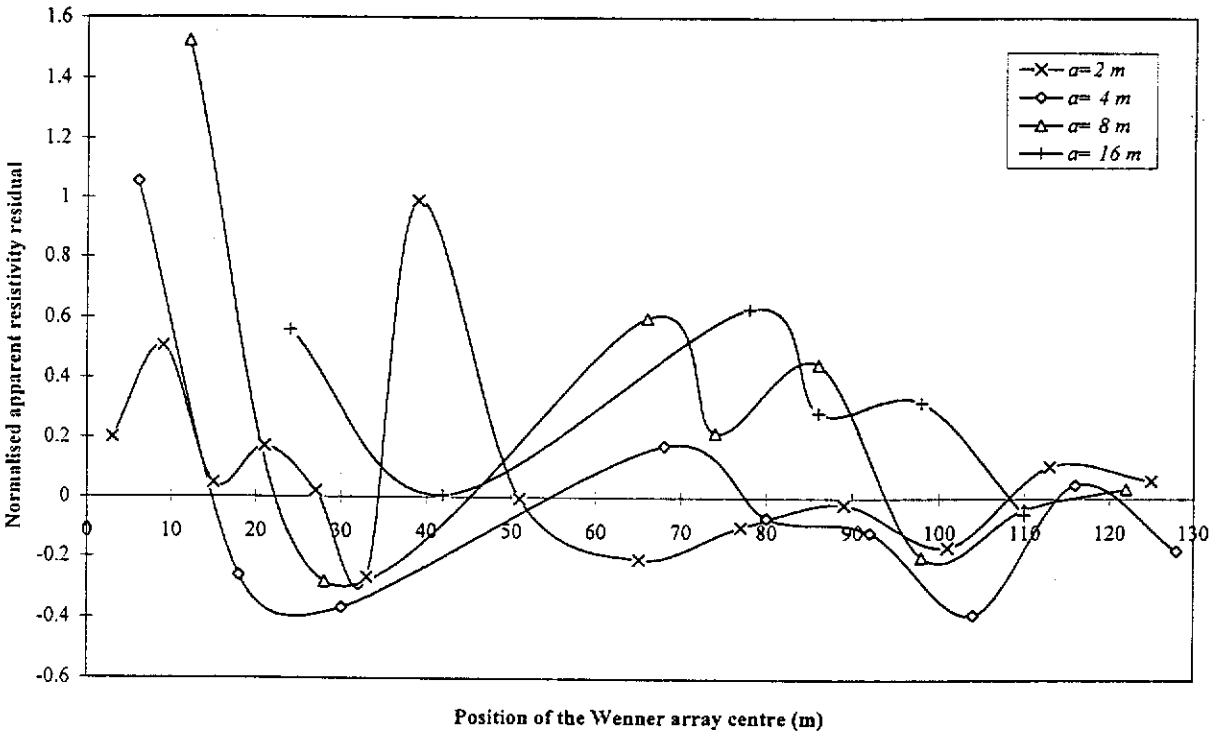

Figure 3.26. Normalised apparent resistivity residual profiles along line 2 at the survey area. The profiles with different electrode spacings of 2, 4, 8 and 16 m are shown in this figure.

that the normalised apparent resistivity residual profile displays quite similar anomaly shapes to those on the un-normalised apparent resistivity residual profile (Figure 3.24b). However, the effect of noise is considerably reduced by normalisation. Thus, as the normalised apparent resistivity residual profiles indicate, a large conductive anomaly is seen at the beginning of the line. Large variations on the residual profiles beyond 60-70 m can be seen. However, after normalising these variations significantly become small, indicating that they are mainly due to noise.

3.3.3 Discussion

The apparent resistivity residual method, which was developed as a result of modelling studies in this research work, was tested in the field. The field data obtained were quite noisy. The effect of noise in the data is considerable since the resistivity measurements were carried out along lines, which were unavoidably located in the vicinity of noise sources. This noise made the interpretation of the data very difficult. For this reason, some noise reduction procedure was called for. For this purpose, the apparent resistivity residual data were normalised. Although the normalisation of the apparent resistivity residual data greatly helped in reducing the noise on the normalised residual profiles, noise still was an impediment to the interpretation of the data.

From the application of the apparent resistivity residual method using the multisystem combination A at the survey area, we can see that the method is capable of successfuly locating the subsurface anomalous zones in the area. However, since the residual profiles obtained by the multisystem combination A are greatly influenced by noise, interpretation of the results is difficult. Using the normalisation method for reducing the effect of noise, the apparent resistivity residual data along lines 1 and 2 clearly indicated on both lines a subsurface conductive anomaly adjacent to building A as had been previously observed from the hydrogeological data for monitor bore A. One other shallow anomaly was suggested on line 1.

Chapter 4

STUDY OF TRANSITIONAL LAYERING EFFECTS ON RESISTIVITY AND APPARENT RESISTIVITY RESIDUAL MEASUREMENTS OVER A 3-D BODY

4.1 Introduction

One of the simplest model assumptions, for the interpretation of resistivity profiling data for mineral exploration, is a three dimensional deposit in a layered structure with each layer having a constant resistivity. However, in reality, resistivities of the layers may vary continuously with depth. This may be due to differential weathering of the surface layer especially in areas subjected to tropical and subtropical conditions. A layer, in which resistivity (or conductivity) changes with depth in some continuous fashion, is called a *transitional layer.*

A typical example of a transitional layer is a weathered granite or basalt layer of gradually increasing freshness with depth. In general, any weathered zone in hard rock areas, where the degree of weathering diminishes with depth, represents a transitional layer. Transitional cases can also be seen in variable permeability and salinity of overburden as well as groundwater situations (Unz, 1968). Often where the geological section is approximated by horizontal layers, the boundaries between the layers are commonly assumed to be sharp. However, in reality these boundaries are not sharp but are mostly transitional in nature.

A geological section in much of Peninsular India containing such transitional layers has been reported by Mallick and Roy (1968). In these areas hard granitic and basaltic rocks occur either as exposures or concealed under a thin cover of soil and weathered in-situ material. A typical section in these areas consists of a transported soil cover of a few metres thickness, underlain by a transitional layer of weathered granite or basalt of gradually increasing freshness, and finally at the bottom the

unaltered highly resistive bedrock occurs. The top soil cover is more or less uniform with a resistivity of a few ohm-metres. The resistivity of the weathered layer increases, approximately in a linear pattern with depth, until the unweathered resistive bedrock is reached. The transitional layer in such areas can be an issue in the determination of depths to fresh bedrock for foundation purposes in engineering when the bedrock is concealed by river sands, alluvium, or other sediments.

Lee and Ignetik (1994) have presented some soil salinity depth profiles from an area in Queensland, Australia, in which salt concentration varies continuously with depth. This salt concentration is strongly correlated with the conductivity or resistivity of the ground. This salt concentration variation is quite evident in the top layer of the subsurface, and therefore, this layer may also be classified as a transitional layer. Plotting the salt concentration against depth for the first 10 or 20 m shows that the curve of best fit in the regression analysis sense is an exponential function, and as a result, the conductivity or resistivity of the top layer can be represented as an exponential function of depth. This region is important because the first 10 m or so is of interest to agriculture. In some areas, a transitional layer situation appears where the salinity of the pore water increases gradually with depth (Kim and Lee, 1996).

A particularly interesting transitional case occurs in deep basement layers of the Earth's crust, where increasing temperature can be associated with continuously increasing conductivity (Wait, 1982). Another field example, presented by Patella (1978), is a fissured geological formation (e.g. limestone) which forms a transitional layer due to any phenomenon that alters continuously the physical status of the fissures. In this case, the increasing pressure in the deeper zones because of the increasing load and the gradual filling of fissures with other materials such as clay, loam, sand and water can be two important reasons for this continuous variation of the resistivity with depth.

Transitional layers can also be seen in coastal areas where the diffusion of saline water from the sea into fresh water produces a region with continuously variable salinity in the vertical direction. In this regard, Patella (1978) has presented a typical

stratigraphic column of coastal areas, in which the upper dry layer is followed by the capillary zone, then rock saturated with water and finally is ended with the impermeable basement. The capillary and diffusion zones form transitional layers as salinity concentration in these zones continuously varies with depth. Besides, in many areas with environmental problems the resistivity of the surficial layer may vary with depth due to seepage of chemicals spilled on the surface, or any other contaminants percolating through the subsurface with gradually decreasing concentration with depth.

The theoretical formulation of the resistivity problem in a layered earth with transitional layers has been presented in a number of publications. This problem was first treated by Mallick and Roy (1968). In general, the authors of these publications have used mathematical relations and boundary conditions to obtain a rigorous solution for the electrical potential in a transitional zone in which the resistivity (or conductivity) varies with depth in accordance with a specific function. This resistivity (or conductivity) function has been considered mainly to be of exponential, linear, or generalised power n variation with depth. Mallick and Roy (1968) obtained a theoretical solution to the problem of a three-layered earth in which the second layer is a transitional layer with a linear change in the conductivity with depth. They considered the three-layered model without conductivity jumps at the boundaries, and derived the expressions for the electric potential and apparent resistivity functions for the model.

Jain (1972) obtained expressions for the electric potential and apparent resistivity in the case of a three-layered model in which the conductivity in the second layer varies linearly with depth and changes abruptly at the boundaries. Paul and Banerjee (1970) obtained solutions for the apparent resistivity functions for the cases of a half-space and a two-layered earth in which the conductivity of the half-space or the first layer varies either exponentially with depth or is proportional to $(1+z/a)^n$, where z is the depth from the surface, a and n are constants, a with the dimension L^{-1} and n is the dimensionless power of the above term. Lal (1970) considered a three-layered model with continuous conductivity at the boundaries and variable conductivity in the

second layer in which the conductivity either changes exponentially with depth or follows the generalised power law variation (i.e. $\sigma(z) = \sigma_1[1 + a(z - h_1)]^n$ where σ_1 and h_1 are the conductivity and thickness of the first layer, respectively, a and n, as described in the former relation presented by Paul and Banerjee (1970), are constants).

Unlike many authors who considered a type of change with depth for the *conductivity* of a transitional layer in a layered earth, Koefoed (1979b) considered a layered earth model with a transitional layer in which the *resistivity* changes linearly with depth. The reason, as he claimed, is that the linear change of the resistivity with depth seems to be a far more common occurrence than the linear change of the conductivity with depth. Also, the layered earth model, which he considered, contained an arbitrary number of homogeneous layers and transitional layers. Nevertheless, the solution of the problem for the case of resistivity variation with depth is the same as for the case of conductivity variation with depth. Banerjee et al. (1980) also gave apparent resistivity expressions for a multi-layered earth with an arbitrary transitional layer having exponentially varying conductivity.

Inclusion of a 3-D body

Previous publications concerning transitional layers have investigated the problem of a layered earth model without considering a 3-D body embedded in it. In this regard, an interest from the detectability point of view of the resistivity profiling method is to consider a mineral deposit or a 3-D body under a transitional cover. In this chapter, we discuss such a problem. In the following, first we derive relevant mathematics for a 3-D body embedded in a layered earth with a transitional layer, and then we present some numerical examples. In this chapter, we examine one model of a transitional layer in which resistivity or conductivity varies exponentially with depth. In numerical examples, we are going to investigate the effect of transitional overburden layers on the detectability of 3-D bodies from the apparent resistivity profiles and

residual profiles using different electrode configurations such as the Wenner and Schlumberger arrays.

Appendix B, in addition, gives the mathematics for a 3-D body in a homogeneous layer beneath a transitional layer having a linear variation of resistivity or conductivity with depth.

4.2 Mathematical formulation of the problem

Consider the general case of an arbitrarily shaped 3-D body, as shown in Figure 2.1, in an M-layered earth, in which one or more layers are transitional, i.e. the resistivity or conductivity in these layers varies exponentially with depth. A constant electric current is injected into the ground at a point located on the ground surface. The problem is to obtain the potential at any point in the layered earth. We use a cylindrical coordinate system (r, θ, z) with its origin at the current source point. We also consider the z-axis to be vertically downward with $z = 0$ at the ground surface. The half-space $(z < 0)$ above the surface is infinitely resistive, whereas the half-space $(z > 0)$ below the surface is a horizontally stratified earth containing M layers with conductivities and thicknesses σ_j and h_j, respectively, where $j = 1, 2, 3, ..., M$ and $h_M = \infty$. For circular symmetry, the cylindrical coordinate system (r, θ, z) can be replaced by (r, z) (Paul and Banerjee, 1970; Koefoed, 1979a; Banerjee et al., 1980).

For simplicity we assume that the *conductivity* (rather than the *resistivity*) of the transitional layer is an exponential function of depth. Since the resistivity ρ and the conductivity σ are two different physical properties with a simple inverse relation $\rho = \frac{1}{\sigma}$, we can convert one to the other at any stage of the formulation or computation. If the conductivity of a transitional layer varies exponentially with depth, then the resistivity of the transitional layer also varies exponentially with depth but the exponent will have a different sign.

4.2.1 Computation of the primary layered-earth potential

The mathematical expressions for the primary layered-earth potential due to an electric current point source on the ground surface are given by Paul and Banerjee (1970), and Banerjee et al. (1980). However, their papers contain some typographical errors. The following is a mathematical summary to correct their papers and provide a convenient reference for the reader.

For a layered earth, equation (2.6) can be written in the following form for any points excluding the source point:

$$\nabla\sigma.\nabla V + \sigma\nabla^2 V = 0. \tag{4.1}$$

When the conductivity σ (or resistivity ρ) in a medium is constant, equation (4.1) reduces to

$$\nabla^2 V = 0, \tag{4.2}$$

or

$$\frac{\partial^2 V}{\partial r^2} + \frac{1}{r}\frac{\partial V}{\partial r} + \frac{\partial^2 V}{\partial z^2} = 0. \tag{4.3}$$

If the conductivity σ (or resistivity ρ) is not a constant but varies with depth only (i.e. in the z-direction), as we have in a transitional layer, then equation (4.1) becomes

$$\frac{\partial\sigma}{\partial z}\frac{\partial V}{\partial z} + \sigma\nabla^2 V = 0. \tag{4.4}$$

Dividing equation (4.4) by σ, we can write this equation in the following form:

$$\nabla^2 V + \frac{1}{\sigma}\frac{\partial \sigma}{\partial z}\frac{\partial V}{\partial z} = 0. \tag{4.5}$$

Considering $\sigma = \frac{1}{\rho}$, equation (4.5) can also be written as

$$\nabla^2 V - \frac{1}{\rho}\frac{\partial \rho}{\partial z}\frac{\partial V}{\partial z} = 0. \tag{4.6}$$

For the solutions of the differential equations (4.2) and (4.5) let us assume

$$V(r, z) = \int_0^\infty f(\lambda, z) J_0(\lambda r) d\lambda, \tag{4.7}$$

where λ is the integration variable. Substituting equation (4.7) in equation (4.2), we finally obtain

$$\frac{\partial^2 f}{\partial z^2} - \lambda^2 f = 0. \tag{4.8}$$

Similarly, substituting equation (4.7) in equation (4.5) yields

$$\frac{\partial^2 f}{\partial z^2} + \frac{1}{\sigma}\frac{\partial \sigma}{\partial z}\frac{\partial f}{\partial z} - \lambda^2 f = 0. \tag{4.9}$$

The solution for $f(r, z)$ can be obtained from equation (4.8) for the layers having constant conductivities, while from equation (4.9) the solution of $f(r, z)$ is obtained for the layer(s) having a varying conductivity with depth. Considering σ as a function of z in a transitional layer, equation (4.9) can be written as

$$\frac{\partial^2 f}{\partial z^2} + \frac{\partial(\log \sigma)}{\partial z}\frac{\partial f}{\partial z} - \lambda^2 f = 0. \tag{4.10}$$

Equations (4.4)-(4.6), (4.9) and (4.10) hold for a transitional layer in which the conductivity (or resistivity) varies only with depth, whether exponentially or any other type of variation.

The solution of differential equation (4.8) is given by (Koefoed, 1979a)

$$f(\lambda, z) = A(\lambda)e^{\lambda z} + B(\lambda)e^{-\lambda z}, \tag{4.11}$$

where $A(\lambda)$ and $B(\lambda)$ are coefficients. Substituting equation (4.11) in equation (4.7), we obtain the primary layered-earth potential $V_i(r,z)$ for the ith layer, which has a constant conductivity σ_i, in the following form:

$$V_i(r,z) = \int_0^\infty [A_i(\lambda)e^{\lambda z} + B_i(\lambda)e^{-\lambda z}]J_0(\lambda r)d\lambda, \quad \text{for} \quad z_{i-1} \le z \le z_i; \quad i = 1, 2, ..., M-1. \tag{4.12}$$

Here z is the depth from the ground surface, z_{i-1} and z_i are the *depths* to the ith layer and the $(i+1)$th layer, respectively. For the lowermost layer M, with constant conductivity σ_M, $A_M(\lambda) = 0$ and thus the layered earth potential $V_M(r,z)$ is given by

$$V_M(r,z) = \int_0^\infty B_M(\lambda)e^{-\lambda z}J_0(\lambda r)d\lambda, \quad \text{for} \quad z_{M-1} \le z < \infty, \tag{4.13}$$

where z_{M-1} is the depth to the lowermost layer M.

Exponential variation of resistivity or conductivity with depth

If the ith layer in the M-layered earth, shown in Figure 2.1, is transitional and has a conductivity σ_i or resistivity ρ_i, which varies exponentially with depth, we can write

$$\sigma_i(z) = c\sigma_{i-1}e^{\beta(z-z_{i-1})}, \quad \text{for} \quad z_{i-1} \le z \le z_i; \quad i = 1, 2, ..., M-1, \tag{4.14}$$

or

$$\rho_i(z) = \frac{1}{c}\rho_{i-1}e^{-\beta(z-z_{i-1})}, \quad \text{for} \quad z_{i-1} \le z \le z_i; \quad i = 1, 2, ..., M-1, \tag{4.15}$$

where β is a constant with a dimension of L^{-1}, σ_{i-1} and ρ_{i-1} are the conductivity and resistivity of the $(i-1)$th layer, respectively, and c is a dimensionless constant. For $c = 1$ the conductivity or resistivity is continuous at the interface between the $(i-1)$th and ith layers, otherwise there is a discontinuity at the interface. Using equation (4.14), we can write equation (4.9) for the ith layer in the following form:

$$(\frac{\partial^2}{\partial z^2} + \beta\frac{\partial}{\partial z} - \lambda^2)f = 0. \tag{4.16}$$

The solution of differential equation (4.16) is given by (Lal, 1970; Wait, 1982)

$$f(\lambda, z) = A(\lambda)e^{\alpha_1 z} + B(\lambda)e^{\alpha_2 z}, \tag{4.17}$$

where $A(\lambda)$ and $B(\lambda)$ are coefficients, and α_1 and α_2 are the roots of the following quadratic equation:

$$\alpha^2 + \beta\alpha - \lambda^2 = 0. \tag{4.18}$$

Thus, α_1 and α_2 are given by

$$\alpha_1 = \frac{-\beta + \sqrt{\beta^2 + 4\lambda^2}}{2}, \tag{4.19}$$

and

$$\alpha_2 = \frac{-\beta - \sqrt{\beta^2 + 4\lambda^2}}{2}. \tag{4.20}$$

Substituting equation (4.17) in equation (4.7), we obtain the primary layered-earth potential $V_i(r,z)$ for the ith layer, which has an exponentially varying conductivity with depth, in the following form:

$$V_i(r,z) = \int_0^\infty [A_i(\lambda)e^{\alpha_1 z} + B_i(\lambda)e^{\alpha_2 z}]J_0(\lambda r)d\lambda, \quad \text{for } z_{i-1} \le z \le z_i; \quad i = 1, 2, ..., M-1. \tag{4.21}$$

If the lowermost layer M is transitional and its conductivity varies exponentially with depth, $A_M(\lambda) = 0$, and thus, the layered earth potential $V_M(r,z)$ for the transitional layer M is given by

$$V_M(r,z) = \int_0^\infty B_M(\lambda)e^{\alpha_2 z}J_0(\lambda r)d\lambda, \quad \text{for } z_{M-1} \le z < \infty. \tag{4.22}$$

The coefficients $A_i(\lambda)$, $B_i(\lambda)$ [where $i = 1, 2, ..., M-1$], and $B_M(\lambda)$ are to be determined from boundary conditions.

Two-layered case

For simplicity, we consider a simple two-layered case, as shown in Figure 4.1, in which the overburden layer is transitional, and the isotropic homogeneous lower half-space of the two-layered earth hosts a 3-D body. The overburden layer has a conductivity σ_1 which varies exponentially with depth, i.e.

$$\sigma_1(z) = \sigma_0 e^{\beta z}, \quad \text{for } 0 \le z \le z_1, \tag{4.23}$$

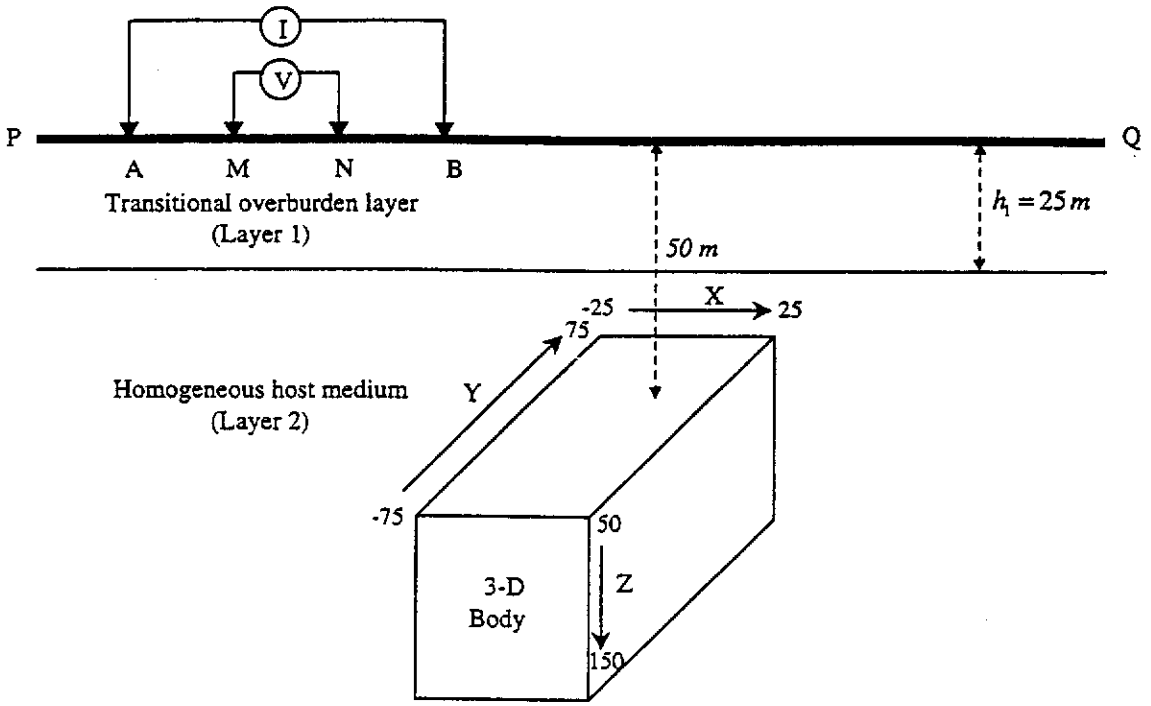

Figure 4.1. A 3-D body embedded in an isotropic, homogeneous lower half-space of a two-layer earth with transitional overburden. The thickness of the transitional overburden layer is denoted by h_1.

where z is the depth from the ground surface, z_1 is the depth to the homogeneous lower half-space or second layer (host medium), β is a constant, and σ_0 is the conductivity of the transitional overburden at the ground surface (where $z=0$). Considering $z=0$ at the ground surface, we can write $z_1 = h_1$ (Figure 4.1) where h_1 is the thickness of the transitional overburden layer. In this case, the layered earth potential for the transitional overburden and the second layer (host medium) is written as

$$V_1(r,z) = \int_0^\infty [A_1(\lambda)e^{\alpha_1 z} + B_1(\lambda)e^{\alpha_2 z}]J_0(\lambda r)d\lambda, \quad \text{for } 0 \le z \le h_1, \tag{4.24}$$

and

$$V_2(r,z) = \int_0^\infty B_2(\lambda)e^{-\lambda z}J_0(\lambda r)d\lambda, \quad \text{for } h_1 \le z < \infty, \tag{4.25}$$

respectively. α_1 and α_2 are given by equations (4.19) and (4.20), respectively. The coefficients $A_1(\lambda)$, $B_1(\lambda)$, and $B_2(\lambda)$ are determined from the following boundary conditions:

1) The normal current density at the surface ($z=0$) is satisfied by the following expression:

$$J_z\Big|_{z=0} = -\sigma_1 \frac{\partial V_1}{\partial z}\Big|_{z=0} = \frac{I}{2\pi r}\delta(r), \tag{4.26}$$

where I is the electric current, r is the distance between the current source point and the potential measuring location, and $\delta(r)$ is the Dirac delta function. Differentiating the potential V_1, defined in equation (4.24), with respect to z and substituting it in equation (4.26) yields

$$-\sigma_0 \int_0^\infty [A_1(\lambda)\alpha_1 + B_1(\lambda)\alpha_2]J_0(\lambda r)d\lambda = \frac{I}{2\pi r}\delta(r). \tag{4.27}$$

Note that σ_1 at $z=0$ is equal to σ_0 [see equation (4.23)]. Equation (4.27) can be written in the following form:

$$\int_0^\infty [A_1(\lambda)\frac{\alpha_1}{\lambda} + B_1(\lambda)\frac{\alpha_2}{\lambda}]\lambda J_0(\lambda r)d\lambda = \frac{-I}{2\pi\sigma_0}\frac{\delta(r)}{r}\,, \tag{4.28}$$

which, when inverted with the help of the Fourier Bessel integral (Watson, 1958), yields

$$A_1(\lambda)\frac{\alpha_1}{\lambda} + B_1(\lambda)\frac{\alpha_2}{\lambda} = \frac{-I}{2\pi\sigma_0} \tag{4.29}$$

2) Continuity of the potential at the interface between the first (overburden) and second (host medium) layers, i.e. $V_1 = V_2$ at $z = h_1$. Thus, using equations (4.24) and (4.25), we obtain

$$A_1(\lambda)e^{\alpha_1 h_1} + B_1(\lambda)e^{\alpha_2 h_1} - B_2(\lambda)e^{-\lambda h_1} = 0\,. \tag{4.30}$$

3) Continuity of the normal current density at the interface between the first and second layers i.e. $\sigma_1 \left.\frac{\partial V_1}{\partial z}\right|_{z=h_1} = \sigma_2 \left.\frac{\partial V_2}{\partial z}\right|_{z=h_1}$. Thus, differentiating equations (4.24) and (4.25) with respect to z, we have

$$\sigma_1\int_0^\infty [\alpha_1 A_1(\lambda)e^{\alpha_1 h_1} + \alpha_2 B_1(\lambda)e^{\alpha_2 h_1}]J_0(\lambda r)d\lambda = \sigma_2\int_0^\infty [-\lambda B_2(\lambda)e^{-\lambda h_1}]J_0(\lambda r)d\lambda\,. \tag{4.31}$$

Considering σ_1 at the interface between the first and second layers (i.e. $z = z_1 = h_1$) is equal to $\sigma_0 e^{\beta h_1}$, we obtain the following expression from equation (4.31):

$$\sigma_0 e^{\beta h_1}\alpha_1 A_1(\lambda)e^{\alpha_1 h_1} + \sigma_0 e^{\beta h_1}\alpha_2 B_1(\lambda)e^{\alpha_2 h_1} + \sigma_2\lambda B_2(\lambda)e^{-\lambda h_1} = 0\,. \tag{4.32}$$

Defining

$$\sigma^* = \sigma_0 e^{\beta h_1}, \tag{4.33}$$

we can write equation (4.32) in the following form:

$$\sigma^* \alpha_1 A_1(\lambda) e^{\alpha_1 h_1} + \sigma^* \alpha_2 B_1(\lambda) e^{\alpha_2 h_1} + \sigma_2 \lambda B_2(\lambda) e^{-\lambda h_1} = 0. \tag{4.34}$$

$A_1(\lambda)$, $B_1(\lambda)$, and $B_2(\lambda)$ are evaluated from the set of equations (4.29), (4.30), and (4.34). This set of equations can be written in the form of a matrix equation, and the values $A_1(\lambda)$, $B_1(\lambda)$, and $B_2(\lambda)$ can be obtained using Cramer's rule. Therefore, we obtain

$$A_1(\lambda) = \frac{-\frac{I}{2\pi\sigma_0}[(\lambda\sigma_2 + \sigma^*\alpha_2)e^{h_1(\alpha_2-\lambda)}]}{(\alpha_1\sigma_2 + \frac{\alpha_1\alpha_2}{\lambda}\sigma^*)e^{h_1(\alpha_2-\lambda)} - (\alpha_2\sigma_2 + \frac{\alpha_1\alpha_2}{\lambda}\sigma^*)e^{h_1(\alpha_1-\lambda)}}, \tag{4.35}$$

$$B_1(\lambda) = \frac{\frac{I}{2\pi\sigma_0}[(\lambda\sigma_2 + \sigma^*\alpha_1)e^{h_1(\alpha_1-\lambda)}]}{(\alpha_1\sigma_2 + \frac{\alpha_1\alpha_2}{\lambda}\sigma^*)e^{h_1(\alpha_2-\lambda)} - (\alpha_2\sigma_2 + \frac{\alpha_1\alpha_2}{\lambda}\sigma^*)e^{h_1(\alpha_1-\lambda)}}, \tag{4.36}$$

$$B_2(\lambda) = \frac{-\frac{I}{2\pi\sigma_0}(\alpha_2 - \alpha_1)\sigma^* e^{h_1(\alpha_1+\alpha_2)}}{(\alpha_1\sigma_2 + \frac{\alpha_1\alpha_2}{\lambda}\sigma^*)e^{h_1(\alpha_2-\lambda)} - (\alpha_2\sigma_2 + \frac{\alpha_1\alpha_2}{\lambda}\sigma^*)e^{h_1(\alpha_1-\lambda)}}, \tag{4.37}$$

where σ^* is given by equation (4.33). Substituting equations (4.35) and (4.36) in equation (4.24), we obtain the layered earth potential. Therefore, the layered earth potential at the ground surface ($z = 0$), represented by $V_l(r,0)$, is given by

$$V_l(r,0)=\frac{I}{2\pi\sigma_0}\int_0^\infty[\frac{-(\lambda\sigma_2+\sigma_0e^{\beta h_1}\alpha_2)e^{h_1\alpha_2}+(\lambda\sigma_2+\sigma_0e^{\beta h_1}\alpha_1)e^{h_1\alpha_1}}{(\alpha_1\sigma_2+\frac{\alpha_1\alpha_2}{\lambda}\sigma_0e^{\beta h_1})e^{h_1\alpha_2}-(\alpha_2\sigma_2+\frac{\alpha_1\alpha_2}{\lambda}\sigma_0e^{\beta h_1})e^{h_1\alpha_1}}]J_0(\lambda r)d\lambda\,. \tag{4.38}$$

Dividing the numerator and denominator of the kernel function in equation (4.38) by $(\lambda\sigma_2+\sigma_0e^{\beta h_1}\alpha_1)e^{h_1\alpha_1}$, we can write equation (4.38) after simplification in the following form:

$$V_l(r,0)=\frac{I}{2\pi\sigma_0}\int_0^\infty\{-\frac{\lambda}{\alpha_2}+(1-\frac{\alpha_1}{\alpha_2})\frac{(\frac{\lambda\sigma_2+\sigma_0e^{\beta h_1}\alpha_2}{\lambda\sigma_2+\sigma_0e^{\beta h_1}\alpha_1})e^{h_1(\alpha_2-\alpha_1)}}{\frac{\alpha_2}{\lambda}[1-\frac{\alpha_1}{\alpha_2}(\frac{\lambda\sigma_2+\sigma_0e^{\beta h_1}\alpha_2}{\lambda\sigma_2+\sigma_0e^{\beta h_1}\alpha_1})e^{h_1(\alpha_2-\alpha_1)}]}\}J_0(\lambda r)d\lambda\,, \tag{4.39}$$

where α_1 and α_2 are given by equations (4.19) and (4.20) respectively.

4.2.2 Computation of Green's functions, electric field, anomalous potential and other parameters involved in the integral equation approach

Our aim is to compute numerically the effect of the 3-D body in the homogeneous lower half-space of a two-layered earth under a transitional overburden. For this, as discussed in Chapter 2, we apply the integral equation method of numerical modelling to obtain the effect of the body. We discretise the surface S of the body into N small elementary cells (as shown in Figure 4.2) for use of the moment method. Application of the relevant integral equation requires computation of the unknown charges Q^n on the surface of the elementary cells via equation (2.50), mentioned in Chapter 2. We repeat equation (2.50) for convenience

$$\hat{n}.\overline{E}_m^i=\sum_{n=1}^{N}K^{mn}Q^n\,. \tag{4.40}$$

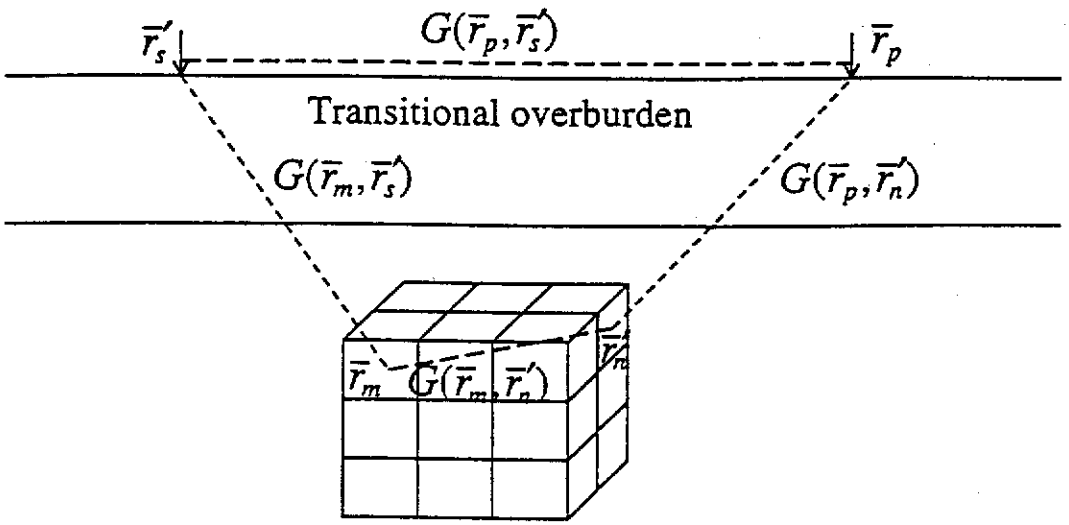

Figure 4.2. The Green's functions required for computation of the body response with a transitional overburden. $G(\bar{r}_p, \bar{r}_s')$ is the Green's function for the layered earth potential at the potential point $\bar{r}_p$ due to the current point source at $\bar{r}_s'$, $G(\bar{r}_m, \bar{r}_s')$ is the Green's function for the electric field at the centre of a surface cell ($\bar{r}_m$) due to the current point source at $\bar{r}_s'$, $G(\bar{r}_m, \bar{r}_n')$ is the Green's function for the interaction between the cells, and $G(\bar{r}_p, \bar{r}_n')$ is the Green's function for the anomalous potential at $\bar{r}_p$ due to the surface charge density at $\bar{r}_n'$. These Green's functions account for the effects of the transitional overburden.

Here, $\hat{n}$ is the outward normal unit vector of each surface cell, $\overline{E}_m^i$ is the electric field at the centre of a surface cell as a result of an electric current injected into the ground, and K^{mn} is the matrix which represents the interaction between the cells. m represents the field point at the centre of a surface cell and n represents the source cell (or point) based on the moment method. In equation (4.40), computations of both the electric field $\overline{E}_m^i$ and the elements of the matrix K^{mn} involve the evaluation of the Green's functions $G(\overline{r}_m, \overline{r}_s')$ and $G(\overline{r}_m, \overline{r}_n')$, respectively (Figure 4.2). These Green's functions, as shown in Figure 4.2, account for the effect of the transitional overburden. Here, we use a primed quantity for a source point location and unprimed one for a field point location. In this case (i.e. a 3-D body under a transitional layer), the electric field $\overline{E}^i$ at the centre of each surface cell, the elements of the matrix K^{mn}, and the charges Q^n developed on the surface of each cell, are computed in the same way as discussed in Chapter 2. Knowing the surface charges Q^n, the total electric potential V, measured by a potential electrode at a point $\overline{r}_p$ other than the location $\overline{r}_s'$ of the current electrode (Figure 4.2), may be expressed as the sum of the layered earth potential V_l (in the absence of the anomalous 3-D body) and the anomalous electric potential V_a due to the surface charges Q^n, i.e.

$$V(\overline{r}_p) = V_l(\overline{r}_p) + V_a(\overline{r}_p), \tag{4.41}$$

where

$$V_l(\overline{r}_p) = \frac{I}{2\pi\sigma_s} G(\overline{r}_p, \overline{r}_s'), \tag{4.42}$$

and

$$V_a(\overline{r}_p) = \frac{1}{4\pi} \sum_{n=1}^{N} \int_S G(\overline{r}_p, \overline{r}_n') Q(\overline{r}_n') dS'. \tag{4.43}$$

Equations (4.41), (4.42), and (4.43) are the same equations (2.21), (2.22), and (2.23) [also see equation (2.52)] given in Chapter 2 for the case of a 3-D body embedded in the lower half-space of a two-layered earth with a homogeneous overburden. The difference appears only in the expressions for the relevant Green's functions $G(\bar{r}_p, \bar{r}_s')$ and $G(\bar{r}_p, \bar{r}_n')$, which again account for the effect of the transitional overburden (Kamkar-Rouhani and Das, 1998). In equation (4.42), σ_s is the conductivity at the place where the current source is located. In this case, as shown in Figure 4.2, the current electrode is located at point $\bar{r}_s'$ on the ground surface of the transitional overburden, thus $\sigma_s = \sigma_0$. Considering equations (4.39) and (4.42), we can express the Green's function $G(\bar{r}_p, \bar{r}_s')$ for the case of the transitional overburden in the following form:

$$G(\bar{r}_p, \bar{r}_s') = \int_0^\infty \left\{ -\frac{\lambda}{\alpha_2} + \left(1 - \frac{\alpha_1}{\alpha_2}\right) \frac{\left(\frac{\lambda\sigma_2 + \sigma_0 e^{\beta h_1}\alpha_2}{\lambda\sigma_2 + \sigma_0 e^{\beta h_1}\alpha_1}\right) e^{h_1(\alpha_2 - \alpha_1)}}{\frac{\alpha_2}{\lambda}\left[1 - \frac{\alpha_1}{\alpha_2}\left(\frac{\lambda\sigma_2 + \sigma_0 e^{\beta h_1}\alpha_2}{\lambda\sigma_2 + \sigma_0 e^{\beta h_1}\alpha_1}\right) e^{h_1(\alpha_2 - \alpha_1)}\right]} \right\} J_0(\lambda r_p) d\lambda , \tag{4.44}$$

which is quite different from the Green's function $G(\bar{r}_p, \bar{r}_s')$ for the case of a homogeneous two-layered earth given by equation (2.75) in Chapter 2. If $\beta = 0$, then the two-layered case reverts to the simple case of a two-layered earth with homogeneous overburden. In this case, considering equations (4.23), (4.19) and (4.20), we obtain $\sigma_0 = \sigma_1$, $\alpha_1 = \lambda$ and $\alpha_2 = -\lambda$. Substituting these values in equation (4.44), we obtain the same expression for the Green's function $G(\bar{r}_p, \bar{r}_s')$ as in equation (2.75). Note that we have also included the source term $\frac{I}{2\pi\sigma_1}$ (which is constant) in equation (2.75), but in equation (4.44) we have not included the source term, which in this case is $\frac{I}{2\pi\sigma_0}$.

Alternatively, we can obtain the expression for the Green's function $G(\bar{r}_p, \bar{r}_s')$, and also expressions for other required Green's functions, which are followed, using the spectral formalism in the same way as shown in Chapter 2.

For computation of the electric field $\bar{E}$, the following expression is used (see equation (2.44) in Chapter 2):

$$\hat{n}.\bar{E}_m^i = \frac{-\hat{n}.\nabla G(\bar{r}_m, \bar{r}_s')}{\sigma_s} I . \tag{4.45}$$

The current point source is located at $\bar{r}_s'$ where the conductivity at the point is σ_0. Equation (4.45) can be written in the following form:

$$\left|E^i\right| = -\frac{I}{\sigma_0}\frac{\partial}{\partial \hat{n}} G(\bar{r}_m, \bar{r}_s') , \tag{4.46}$$

where $\left|E^i\right|$ is the electric field vector matrix. As we said earlier $\hat{n}$ is the outward normal unit vector of each surface cell. Each element of matrix $\left|E^i\right|$ represents the electric field at the centre $\bar{r}_m$ of each elementary cell on the surface of the body due to the current point source at $\bar{r}_s'$.

The Green's function $G(\bar{r}_m, \bar{r}_s')$ can be written as a sum of the whole space term $G^W(\bar{r}, \bar{r}_s')$ and the reflected term $G^R(\bar{r}, \bar{r}_s')$, i.e.

$$G(\bar{r}_m, \bar{r}_s') = G^W(\bar{r}_m, \bar{r}_s') + G^R(\bar{r}_m, \bar{r}_s') . \tag{4.47}$$

Thus, equation (4.46) can be written as

$$\left|E^i\right| = -\frac{I}{\sigma_0}\frac{\partial}{\partial \hat{n}} [G^W(\bar{r}_m, \bar{r}_s') + G^R(\bar{r}_m, \bar{r}_s')] . \tag{4.48}$$

To obtain the Green's function $G(\bar{r}_m,\bar{r}_s')$, we consider the situation shown in Figure 4.3, in which the electric field $\bar{E}$ is shown at the centre of a surface cell $\bar{r}_m$ in the homogeneous lower half-space of a two-layered earth under a transitional layer. The electric current is injected into the ground by an electrode at a point $\bar{r}_s'$ on the surface. The conductivity at the surface and in the second layer (host medium) is represented by σ_0 and σ_2 $(=\sigma_H)$, respectively. In this case, the Green's function $G(\bar{r}_m,\bar{r}_s')$, which represents the potential at point $\bar{r}_m$ due to the current point source at $\bar{r}_s'$, is defined as

$$G(\bar{r}_m,\bar{r}_s') = \int_0^\infty B_2(\lambda)e^{-\lambda z}J_0(\lambda r_m)d\lambda, \tag{4.49}$$

where $B_2(\lambda)$ is given by equation (4.37). Using equation (4.37) and also equation (4.33), we can write equation (4.49) in the following form:

$$G(\bar{r}_m,\bar{r}_s') = \frac{I}{2\pi\sigma_0}\int_0^\infty \frac{(\alpha_1-\alpha_2)\sigma_0 e^{\beta h_1}e^{h_1(\alpha_1+\alpha_2)}}{(\alpha_1\sigma_2+\frac{\alpha_1\alpha_2}{\lambda}\sigma_0 e^{\beta h_1})e^{h_1(\alpha_2-\lambda)}-(\alpha_2\sigma_2+\frac{\alpha_1\alpha_2}{\lambda}\sigma_0 e^{\beta h_1})e^{h_1(\alpha_1-\lambda)}}e^{-\lambda z}$$
$$J_0(\lambda r_m)d\lambda. \tag{4.50}$$

After simplification, we obtain

$$G(\bar{r}_m,\bar{r}_s') = \frac{I}{2\pi\sigma_0}\int_0^\infty \frac{\lambda(\alpha_1-\alpha_2)\sigma_0 e^{\beta h_1}e^{h_1(\alpha_1+\alpha_2+\lambda)}}{(\lambda\alpha_1\sigma_2+\alpha_1\alpha_2\sigma_0 e^{\beta h_1})e^{h_1\alpha_2}-(\lambda\alpha_2\sigma_2+\alpha_1\alpha_2\sigma_0 e^{\beta h_1})e^{h_1\alpha_1}}e^{-\lambda z}$$
$$J_0(\lambda r_m)d\lambda. \tag{4.51}$$

We can write the integral in the following form:

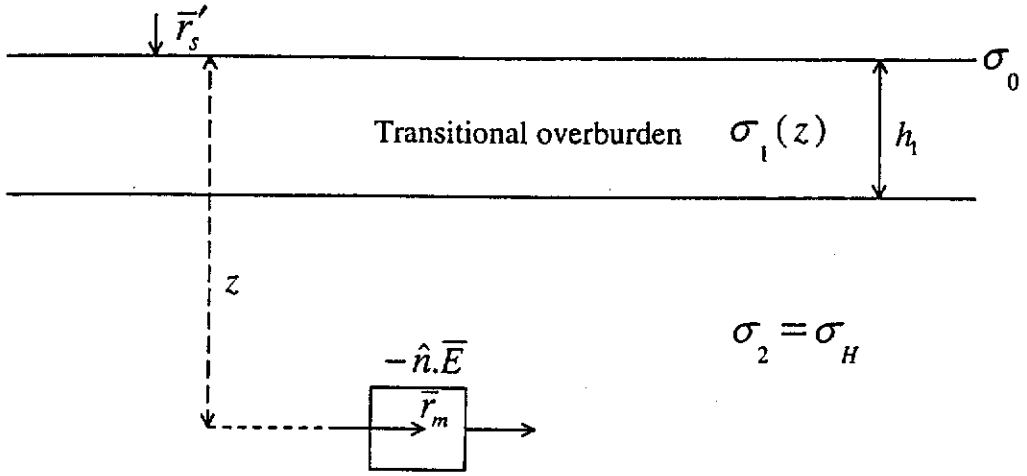

Figure 4.3. An electric field $\bar{E}$ at the centre of a surface cell as a result of an electric current point injection into the ground. The electric current is injected into the ground at a point $\bar{r}_s'$ on the surface. $\bar{r}_m$ is a field point at the centre of a surface cell. The conductivity of the first layer, represented by σ_1, varies exponentially with depth (z). σ_0 is the conductivity at the ground surface (where $z = 0$), $\sigma_2 = \sigma_H$ is the conductivity of the second layer (host medium). h_1 is the thickness of the transitional overburden layer.

$$G(\bar{r}_m,\bar{r}_s')=\frac{I}{2\pi\sigma_0}\int_0^\infty[1+\frac{\lambda(\alpha_1-\alpha_2)\sigma_0 e^{\beta h_1}e^{h_1(\alpha_1+\alpha_2+\lambda)}-(\lambda\alpha_1\sigma_2+\alpha_1\alpha_2\sigma_0 e^{\beta h_1})e^{h_1\alpha_2}}{(\lambda\alpha_1\sigma_2+\alpha_1\alpha_2\sigma_0 e^{\beta h_1})e^{h_1\alpha_2}-(\lambda\alpha_2\sigma_2+\alpha_1\alpha_2\sigma_0 e^{\beta h_1})e^{h_1\alpha_1}}$$
$$\underline{+(\lambda\alpha_2\sigma_2+\alpha_1\alpha_2\sigma_0 e^{\beta h_1})e^{h_1\alpha_1}}]e^{-\lambda z}J_0(\lambda r_m)d\lambda,$$

(4.52)

or

$$G(\bar{r}_m,\bar{r}_s')=\frac{I}{4\pi\sigma_0}\int_0^\infty[e^{-\lambda z}+\frac{2\lambda(\alpha_1-\alpha_2)\sigma_0 e^{\beta h_1}e^{h_1(\alpha_1+\alpha_2+\lambda)}e^{-\lambda z}-(\lambda\alpha_1\sigma_2+\alpha_1\alpha_2\sigma_0 e^{\beta h_1})e^{h_1\alpha_2}e^{-\lambda z}}{(\lambda\alpha_1\sigma_2+\alpha_1\alpha_2\sigma_0 e^{\beta h_1})e^{h_1\alpha_2}-(\lambda\alpha_2\sigma_2+\alpha_1\alpha_2\sigma_0 e^{\beta h_1})e^{h_1\alpha_1}}$$
$$\underline{+(\lambda\alpha_2\sigma_2+\alpha_1\alpha_2\sigma_0 e^{\beta h_1})e^{h_1\alpha_1}e^{-\lambda z}}]J_0(\lambda r_m)d\lambda.$$

(4.53)

The first term inside the integral represents the whole space term $G^W(\bar{r}_m,\bar{r}_s')$, and the second term inside the integral represents the reflected term $G^R(\bar{r}_m,\bar{r}_s')$ (note that $\frac{I}{4\pi\sigma_0}$ is the constant source term), i.e.

$$G^W(\bar{r}_m,\bar{r}_s')=\int_0^\infty e^{-\lambda z}J_0(\lambda r_m)d\lambda, \tag{4.54}$$

and

$$G^R(\bar{r}_m,\bar{r}_s')=\int_0^\infty\frac{2\lambda(\alpha_1-\alpha_2)\sigma_0 e^{\beta h_1}e^{h_1(\alpha_1+\alpha_2+\lambda)}e^{-\lambda z}-(\lambda\alpha_1\sigma_2+\alpha_1\alpha_2\sigma_0 e^{\beta h_1})e^{h_1\alpha_2}e^{-\lambda z}}{(\lambda\alpha_1\sigma_2+\alpha_1\alpha_2\sigma_0 e^{\beta h_1})e^{h_1\alpha_2}-(\lambda\alpha_2\sigma_2+\alpha_1\alpha_2\sigma_0 e^{\beta h_1})e^{h_1\alpha_1}}$$
$$\underline{+(\lambda\alpha_2\sigma_2+\alpha_1\alpha_2\sigma_0 e^{\beta h_1})e^{h_1\alpha_1}e^{-\lambda z}}J_0(\lambda r_m)d\lambda.$$

(4.55)

Since the integral in equation (4.54) is in the form of the Lipschitz integral, we can write this equation in the following form:

$$G^W(\bar{r}_m,\bar{r}_s') = \int_0^\infty e^{-\lambda z} J_0(\lambda r_m) d\lambda = \frac{1}{\sqrt{r_m^{\,2} + z^2}}. \tag{4.56}$$

Using a Cartesian coordinate system with the same origin and z-axis as those of the cylindrical coordinate system used earlier, we specify the coordinates of $\bar{r}_m$ and $\bar{r}_s'$ in the Cartesian coordinate system by (x, y, z) and (x', y', z'), respectively. In this case, the current source point $\bar{r}_s'$ is located on the surface, thus $z' = 0$. Hence, equation (4.56) can be written as

$$G^W(\bar{r}_m,\bar{r}_s') = \frac{1}{R}, \tag{4.57}$$

where

$$R = \sqrt{(x-x')^2 + (y-y')^2 + (z-z')^2}\,. \tag{4.58}$$

Using equations (4.55), (4.57) and (4.58), we can write equation (4.48) in the following form:

$$\left|E^i\right| = -\frac{I}{\sigma_0}\Big[\frac{\partial}{\partial \hat{n}}\Big(\frac{1}{\sqrt{(x-x')^2 + (y-y')^2 + (z-z')^2}}\Big) + \frac{\partial}{\partial \hat{n}}\int_0^\infty \frac{2\lambda(\alpha_1 - \alpha_2)\sigma_0 e^{\beta h_1} e^{h_1(\alpha_1+\alpha_2+\lambda)} e^{-\lambda z} - (\lambda\alpha_1\sigma_2 + \alpha_1\alpha_2\sigma_0 e^{\beta h_1}) e^{h_1\alpha_2} e^{-\lambda z}}{(\lambda\alpha_1\sigma_2 + \alpha_1\alpha_2\sigma_0 e^{\beta h_1}) e^{h_1\alpha_2} - (\lambda\alpha_2\sigma_2 + \alpha_1\alpha_2\sigma_0 e^{\beta h_1}) e^{h_1\alpha_1}} + (\lambda\alpha_2\sigma_2 + \alpha_1\alpha_2\sigma_0 e^{\beta h_1}) e^{h_1\alpha_1} e^{-\lambda z} J_0(\lambda r) d\lambda\Big]. \tag{4.59}$$

Thus, the normal components of the electric field at the centre of each elementary surface cell are given by

$$E_x^i = \frac{I}{\sigma_0}\Big[\frac{(x-x')}{R^3} + \frac{(x-x')}{r}\int_0^\infty \frac{2\lambda(\alpha_1-\alpha_2)\sigma_0 e^{\beta h_1} e^{h_1(\alpha_1+\alpha_2+\lambda)} e^{-\lambda z} - (\lambda\alpha_1\sigma_2 + \alpha_1\alpha_2\sigma_0 e^{\beta h_1}) e^{h_1\alpha_2} e^{-\lambda z}}{(\lambda\alpha_1\sigma_2 + \alpha_1\alpha_2\sigma_0 e^{\beta h_1}) e^{h_1\alpha_2} - (\lambda\alpha_2\sigma_2 + \alpha_1\alpha_2\sigma_0 e^{\beta h_1}) e^{h_1\alpha_1} + (\lambda\alpha_2\sigma_2 + \alpha_1\alpha_2\sigma_0 e^{\beta h_1}) e^{h_1\alpha_1} e^{-\lambda z}} \lambda J_1(\lambda r) d\lambda\Big], \tag{4.60}$$

with a similar equation for the $y-$component with y and y' replacing, respectively, x and x' i.e.

$$E_y^i = \frac{I}{\sigma_0}\Big[\frac{(y-y')}{R^3} + \frac{(y-y')}{r}\int_0^\infty \frac{2\lambda(\alpha_1-\alpha_2)\sigma_0 e^{\beta h_1} e^{h_1(\alpha_1+\alpha_2+\lambda)} e^{-\lambda z} - (\lambda\alpha_1\sigma_2 + \alpha_1\alpha_2\sigma_0 e^{\beta h_1}) e^{h_1\alpha_2} e^{-\lambda z}}{(\lambda\alpha_1\sigma_2 + \alpha_1\alpha_2\sigma_0 e^{\beta h_1}) e^{h_1\alpha_2} - (\lambda\alpha_2\sigma_2 + \alpha_1\alpha_2\sigma_0 e^{\beta h_1}) e^{h_1\alpha_1} + (\lambda\alpha_2\sigma_2 + \alpha_1\alpha_2\sigma_0 e^{\beta h_1}) e^{h_1\alpha_1} e^{-\lambda z}} \lambda J_1(\lambda r) d\lambda\Big], \tag{4.61}$$

and finally

$$E_z^i = \frac{I}{\sigma_0}\Big[\frac{(z-z')}{R^3} + \int_0^\infty \frac{2\lambda(\alpha_1-\alpha_2)\sigma_0 e^{\beta h_1} e^{h_1(\alpha_1+\alpha_2+\lambda)} e^{-\lambda z} - (\lambda\alpha_1\sigma_2 + \alpha_1\alpha_2\sigma_0 e^{\beta h_1}) e^{h_1\alpha_2} e^{-\lambda z}}{(\lambda\alpha_1\sigma_2 + \alpha_1\alpha_2\sigma_0 e^{\beta h_1}) e^{h_1\alpha_2} - (\lambda\alpha_2\sigma_2 + \alpha_1\alpha_2\sigma_0 e^{\beta h_1}) e^{h_1\alpha_1} + (\lambda\alpha_2\sigma_2 + \alpha_1\alpha_2\sigma_0 e^{\beta h_1}) e^{h_1\alpha_1} e^{-\lambda z}} \lambda J_0(\lambda r) d\lambda\Big]. \tag{4.62}$$

The integrals in equations (4.60), (4.61), and (4.62) are solved using digital linear filters designed for Hankel J_0 and J_1 transforms, which were briefly discussed in Chapter 2. If $\beta = 0$, then considering equation (4.23), $\sigma_1(z) = \sigma_0$, the case will revert to the case of a homogeneous overburden. Thus, from equations (4.19) and (4.20), we obtain $\alpha_1 = \lambda$ and $\alpha_2 = -\lambda$. Substituting these values in equations

(4.60), (4.61), and (4.62), we obtain the expressions for E_x^i, E_y^i, and E_z^i quite similar to those given by Das and Paranis (1987) for the homogeneous overburden case.

To obtain the expression for the Green's function $G(\bar{r}_m, \bar{r}_n')$, used in the computation of the elements of matrix K^{mn}, and also the expression for the Green's function $G(\bar{r}_p, \bar{r}_n')$, used in the computation of the anomalous potential $V_a(\bar{r}_p)$ due to the charges Q^n developed on the surface of each cell, we consider the situation shown in Figure 4.4. Both the field point $\bar{r}_m$ and the source at $\bar{r}_n'$ are located in the lower half-space of the two-layered earth shown in Figure 4.4, while the potential point $\bar{r}_p$ is located on the ground surface. The conductivity at the surface and the second layer (host medium) is represented by σ_0 and $\sigma_2 (= \sigma_H)$, respectively. The source at $\bar{r}_n'$ is located at a depth of z' (Figure 4.4). The Green's function $G(\bar{r}_p, \bar{r}_n')$ represents the potential at point $\bar{r}_p$ due to source at $\bar{r}_n'$, thus it can be defined as the potential V_1 of the first layer at point $\bar{r}_p$ on the ground surface (where $z = 0$) due to source at $\bar{r}_n'$. Also, the Green's function $G(\bar{r}_m, \bar{r}_n')$ represents the potential at field point $\bar{r}_m$ due to source at $\bar{r}_n'$, thus it can be defined as the potential V_2 of the second layer at point $\bar{r}_m$ due to source at $\bar{r}_n'$. Therefore, we can write

$$G(\bar{r}_p, \bar{r}_n') = V_1\Big|_{z=0} = c\int_0^\infty [A_1(\lambda)e^{\alpha_1 z} + B_1(\lambda)e^{\alpha_2 z}]J_0(\lambda r_p)d\lambda\Big|_{z=0}, \tag{4.63}$$

and

$$G(\bar{r}_m, \bar{r}_n') = V_2 = c\int_0^\infty [e^{-\lambda|z-z'|} + B_2(\lambda)e^{-\lambda z}]J_0(\lambda r_m)d\lambda, \tag{4.64}$$

where, for a current I injected into the ground by an electrode in the second layer $c = \dfrac{I}{4\pi\sigma_2}$, and for a unit charge $c = 1$. For the situation shown in Figure 4.4, $c = 1$.

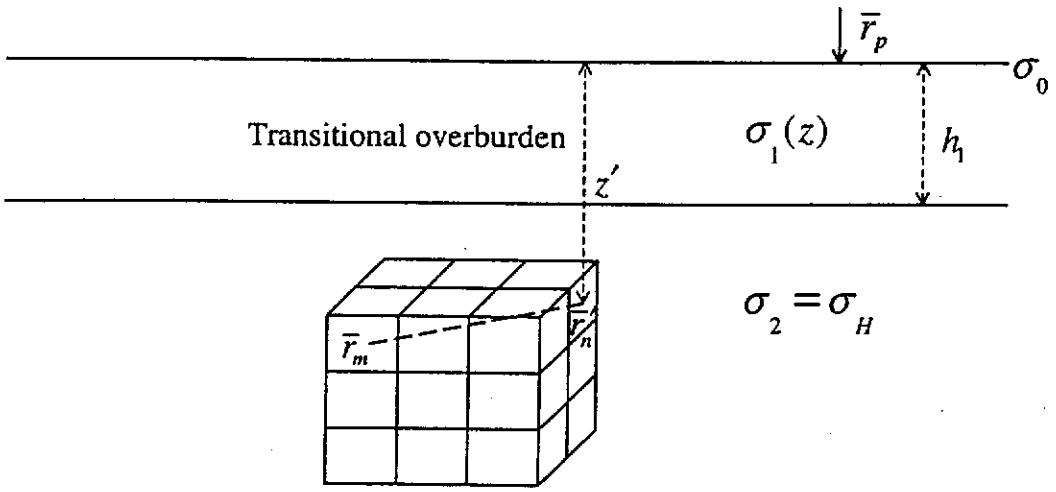

Figure 4.4. A source located in the lower half-space of a two-layered earth. In this figure, both the source at $\bar{r}_n'$ and the field point $\bar{r}_m$ at the centre of a surface cell are located in the lower half-space of the two-layered earth, while the potential point $\bar{r}_p$ is located on the ground surface. σ_1 is the conductivity of the first layer, which changes exponentially with depth (z), σ_0 is the conductivity at the ground surface (where $z = 0$), and $\sigma_2 = \sigma_H$ is the conductivity of the second layer (host medium). h_1 is the thickness of the transitional overburden layer.

α_1 and α_2 are given by equations (4.19) and (4.20), respectively. Applying the following boundary conditions, we obtain the coefficients $A_1(\lambda)$, $B_1(\lambda)$, and $B_2(\lambda)$:

1) The normal current density at the surface ($z = 0$):

$$J_z\Big|_{z=0} = -\sigma_1 \frac{\partial V_1}{\partial z}\Big|_{z=0} = 0. \tag{4.65}$$

Note that in this case, the source is located in the second layer. Differentiating V_1, given by equation (4.63), with respect to z and substituting it in equation (4.65) yields

$$\int_0^\infty [A_1(\lambda)\alpha_1 + B_1(\lambda)\alpha_2] J_0(\lambda r) d\lambda = 0. \tag{4.66}$$

From this equation, we can conclude

$$A_1(\lambda)\alpha_1 + B_1(\lambda)\alpha_2 = 0. \tag{4.67}$$

Then,

$$B_1(\lambda) = -\frac{\alpha_1}{\alpha_2} A_1(\lambda). \tag{4.68}$$

2) $V_1 = V_2$ at the interface between the first and second layers (i.e. at $z = h_1$). Thus, using equations (4.63) and (4.64), we obtain

$$A_1(\lambda)e^{\alpha_1 h_1} + B_1(\lambda)e^{\alpha_2 h_1} = e^{-\lambda(z'-h_1)} + B_2(\lambda)e^{-\lambda h_1}. \tag{4.69}$$

Substituting equation (4.68) in equation (4.69), we obtain

$$B_2(\lambda) = A_1(\lambda)[e^{h_1(\alpha_1+\lambda)} - \frac{\alpha_1}{\alpha_2} e^{h_1(\alpha_2+\lambda)}] - e^{-\lambda(z'-2h_1)}. \quad (4.70)$$

3) $\sigma_1 \frac{\partial V_1}{\partial z} = \sigma_2 \frac{\partial V_2}{\partial z}$ at the interface between the first and second layers (i.e. at $z = h_1$). Thus, differentiating equations (4.63) and (4.64) with respect to z, we obtain

$$\sigma_0 e^{\beta h_1}[\alpha_1 A_1(\lambda) e^{\alpha_1 h_1} + \alpha_2 B_1(\lambda) e^{\alpha_2 h_1}] = \sigma_2[\lambda e^{-\lambda(z'-h_1)} - \lambda B_2(\lambda) e^{-\lambda h_1}]. \quad (4.71)$$

Substituting equations (4.68) and (4.70) in equation (4.71), we finally have

$$A_1(\lambda) = \frac{2\alpha_2\sigma_2\lambda e^{-\lambda(z'-h_1)}}{\sigma_0 e^{\beta h_1}\alpha_1\alpha_2(e^{\alpha_1 h_1} - e^{\alpha_2 h_1}) + \sigma_2\lambda(\alpha_2 e^{\alpha_1 h_1} - \alpha_1 e^{\alpha_2 h_1})}. \quad (4.72)$$

Substituting (4.72) in (4.68), we obtain

$$B_1(\lambda) = \frac{-2\alpha_1\sigma_2\lambda e^{-\lambda(z'-h_1)}}{\sigma_0 e^{\beta h_1}\alpha_1\alpha_2(e^{\alpha_1 h_1} - e^{\alpha_2 h_1}) + \sigma_2\lambda(\alpha_2 e^{\alpha_1 h_1} - \alpha_1 e^{\alpha_2 h_1})}. \quad (4.73)$$

Similarly, substituting (4.72) in (4.70), we obtain

$$B_2(\lambda) = \frac{(\lambda\sigma_2 - \alpha_1\sigma_0 e^{\beta h_1})\alpha_2 e^{-\lambda(z'-2h_1)+\alpha_1 h_1} - (\lambda\sigma_2 - \alpha_2\sigma_0 e^{\beta h_1})\alpha_1 e^{-\lambda(z'-2h_1)+\alpha_2 h_1}}{(\lambda\sigma_2 + \alpha_1\sigma_0 e^{\beta h_1})\alpha_2 e^{\alpha_1 h_1} - (\lambda\sigma_2 + \alpha_2\sigma_0 e^{\beta h_1})\alpha_1 e^{\alpha_2 h_1}}. \quad (4.74)$$

Substituting equation (4.74) in equation (4.64), we obtain the expression for the Green's function $G(\bar{r}_m, \bar{r}_n')$ in the following form:

$$G(\bar{r}_m,\bar{r}_n') = \int_0^\infty [e^{-\lambda|z-z'|} + \frac{(\lambda\sigma_2 - \alpha_1\sigma_0 e^{\beta h_1})\alpha_2 e^{-\lambda(z+z'-2h_1)+\alpha_1 h_1} - (\lambda\sigma_2 - \alpha_2\sigma_0 e^{\beta h_1})\alpha_1 e^{-\lambda(z+z'-2h_1)+\alpha_2 h_1}}{(\lambda\sigma_2 + \alpha_1\sigma_0 e^{\beta h_1})\alpha_2 e^{\alpha_1 h_1} - (\lambda\sigma_2 + \alpha_2\sigma_0 e^{\beta h_1})\alpha_1 e^{\alpha_2 h_1}}] J_0(\lambda r_m)d\lambda. \quad (4.75)$$

The first exponential term inside the integral represents the whole space term $G^W(\bar{r}_m,\bar{r}_n')$, i.e.

$$G^W(\bar{r}_m,\bar{r}_n') = \int_0^\infty e^{-\lambda|z-z'|} J_0(\lambda r_m)d\lambda. \quad (4.76)$$

Considering that the integral in equation (4.76) is in the form of the Lipschitz integral and also defining the coordinates of $\bar{r}_m$ and $\bar{r}_n'$ respectively by (x,y,z) and (x',y',z') in the Cartesian coordinate system used, we can write equation (4.76) as

$$G^W(\bar{r}_m,\bar{r}_n') = \int_0^\infty e^{-\lambda|z-z'|} J_0(\lambda r_m)d\lambda = \frac{1}{R}, \quad (4.77)$$

where R is given by equation (4.58). The second term inside the integral in equation (4.75) includes the reflection contribution to the Green's function $G(\bar{r}_m,\bar{r}_n')$, represented by $G^R(\bar{r}_m,\bar{r}_n')$, i.e.

$$G^R(\bar{r}_m,\bar{r}_n') = \int_0^\infty \frac{(\lambda\sigma_2 - \alpha_1\sigma_0 e^{\beta h_1})\alpha_2 e^{-\lambda(z+z'-2h_1)+\alpha_1 h_1} - (\lambda\sigma_2 - \alpha_2\sigma_0 e^{\beta h_1})\alpha_1 e^{-\lambda(z+z'-2h_1)+\alpha_2 h_1}}{(\lambda\sigma_2 + \alpha_1\sigma_0 e^{\beta h_1})\alpha_2 e^{\alpha_1 h_1} - (\lambda\sigma_2 + \alpha_2\sigma_0 e^{\beta h_1})\alpha_1 e^{\alpha_2 h_1}} J_0(\lambda r_m)d\lambda. \quad (4.78)$$

For computation of the elements of matrix K^{mn}, as in Chapter 2, we use the following equation

$$K^{mn} = \Gamma^{mn} - \delta^{mn}, \quad (4.79)$$

where

$$\Gamma^{mn} = \int_S \hat{n}.\nabla G(\bar{r}_m, \bar{r}_n')ds', \quad \text{and} \quad \delta^{mn} = 0 \qquad \text{if} \quad m \neq n, \tag{4.80}$$

and

$$\Gamma^{mn} = \int_S \hat{n}.\nabla G^R(\bar{r}_m, \bar{r}_n')ds', \text{ and } \delta^{mn} = C = \frac{2\pi(\sigma_H + \sigma_B)}{\sigma_H - \sigma_B} \text{ if } m = n. \tag{4.81}$$

In the above equations, as before, m represents a field point at the centre of a surface cell and n represents a source cell. In equation (4.81), $\sigma_H = \sigma_2$ is the conductivity of the second layer or host medium and σ_B is the conductivity of the body. Separating the Green's function in equation (4.80) into its whole-space and reflected parts, we can write

$$\Gamma^{mn} = \int_S \hat{n}.\nabla G^W(\bar{r}_m, \bar{r}_n')ds' + \int_S \hat{n}.\nabla G^R(\bar{r}_m, \bar{r}_n')ds', \qquad \text{for} \quad m \neq n. \tag{4.82}$$

We can write equation (4.82) in the following form:

$$\Gamma^{mn} = \Gamma_W^{mn} + \Gamma_R^{mn}, \qquad \text{for} \quad m \neq n, \tag{4.83}$$

where

$$\Gamma_W^{mn} = \int_S \hat{n}.\nabla G^W(\bar{r}_m, \bar{r}_n')ds', \tag{4.84}$$

and

$$\Gamma_R^{mn} = \int_S \hat{n}.\nabla G^R(\bar{r}_m, \bar{r}_n')ds'. \tag{4.85}$$

Thus, for equation (4.81) we can write

$$\Gamma^{mn} = \Gamma_R^{mn}, \qquad \text{for} \qquad m = n. \tag{4.86}$$

Using equations (4.77) and (4.58), we can evaluate equation (4.84) exactly over the surface of the body. The surface integral equation (4.85) is evaluated by assuming the integrand to be constant over each surface cell. This approximation is justified since the image sources are far from the field point. Differentiating equation (4.78) with respect to x, y and z, and substituting it in equation (4.85), we obtain the various components of Γ_R^{mn} as follows:

$$\Gamma_{R,x}^{mn} = -\frac{\Delta S(x-x')}{r}\int_0^\infty \frac{(\lambda\sigma_2 - \alpha_1\sigma_0 e^{\beta h_1})\alpha_2 e^{-\lambda(z+z'-2h_1)+\alpha_1 h_1} - (\lambda\sigma_2 - \alpha_2\sigma_0 e^{\beta h_1})\alpha_1 e^{-\lambda(z+z'-2h_1)+\alpha_2 h_1}}{(\lambda\sigma_2 + \alpha_1\sigma_0 e^{\beta h_1})\alpha_2 e^{\alpha_1 h_1} - (\lambda\sigma_2 + \alpha_2\sigma_0 e^{\beta h_1})\alpha_1 e^{\alpha_2 h_1}} \lambda J_1(\lambda r)d\lambda, \tag{4.87}$$

with a similar equation for the $y-$component with y and y' replacing, respectively, x and x', and finally

$$\Gamma_{R,z}^{mn} = -\Delta S\int_0^\infty \frac{(\lambda\sigma_2 - \alpha_1\sigma_0 e^{\beta h_1})\alpha_2 e^{-\lambda(z+z'-2h_1)+\alpha_1 h_1} - (\lambda\sigma_2 - \alpha_2\sigma_0 e^{\beta h_1})\alpha_1 e^{-\lambda(z+z'-2h_1)+\alpha_2 h_1}}{(\lambda\sigma_2 + \alpha_1\sigma_0 e^{\beta h_1})\alpha_2 e^{\alpha_1 h_1} - (\lambda\sigma_2 + \alpha_2\sigma_0 e^{\beta h_1})\alpha_1 e^{\alpha_2 h_1}} \lambda J_0(\lambda r)d\lambda. \tag{4.88}$$

The above integrals are solved using digital linear filters designed for Hankel J_0 and J_1 transforms (see Chapter 2). By putting $\beta = 0$ in equation (4.23), it gives us the case of a homogeneous overburden. In this case, from equations (4.19) and (4.20), we obtain $\alpha_1 = \lambda$ and $\alpha_2 = -\lambda$. Substituting these values in equations (4.87) and (4.88), we obtain the same expressions as obtained by Das and Parasnis (1987) for different components of Γ_R^{mn} in the case of a 3-D body embedded in the lower half-space of a two-layered earth with a homogeneous overburden.

The expression for the Green's function $G(\bar{r}_p, \bar{r}_n')$, used in the computation of the anomalous electric potential V_a at $\bar{r}_p$ on the ground surface due to the surface charge density at $\bar{r}_n'$, is obtained by substituting equations (4.72) and (4.73) in equation (4.63). Then after simplification, we finally obtain

$$G(\bar{r}_p, \bar{r}_n') = (1-k)\left\{\frac{1}{R} + \int_0^\infty \frac{2(\alpha_2 - \alpha_1)\lambda e^{-\lambda(z'-h_1)} - e^{-\lambda z'}[(1+k)e^{\beta h_1}\alpha_1\alpha_2(e^{\alpha_1 h_1} - e^{\alpha_2 h_1}) + \lambda(1-k)(\alpha_2 e^{\alpha_1 h_1} - \alpha_1 e^{\alpha_2 h_1}) + \lambda(1-k)(\alpha_2 e^{\alpha_1 h_1} - \alpha_1 e^{\alpha_2 h_1})]}{(1+k)e^{\beta h_1}\alpha_1\alpha_2(e^{\alpha_1 h_1} - e^{\alpha_2 h_1}) + \lambda(1-k)(\alpha_2 e^{\alpha_1 h_1} - \alpha_1 e^{\alpha_2 h_1})} J_0(\lambda r_p) d\lambda\right\}. \tag{4.89}$$

In equation (4.90),

$$k = \frac{\sigma_0 - \sigma_2}{\sigma_0 + \sigma_2}, \tag{4.90}$$

and R is given by equation (4.58) considering the coordinates of $\bar{r}_p$ and $\bar{r}_n'$ in the Cartesian coordinate system to be respectively (x, y, z) and (x', y', z'). Note that in this case the potential point $\bar{r}_p$ is located on the surface, thus $z = 0$. Also, as for the other Green's functions, the Green's function $G(\bar{r}_p, \bar{r}_n')$, given by equation (4.89) can be shown in two parts: whole space part $G^W(\bar{r}_p, \bar{r}_n')$ and reflected part $G^R(\bar{r}_p, \bar{r}_n')$. The term $\frac{1}{R}$ in equation (4.89) represents the whole space part $G^W(\bar{r}_p, \bar{r}_n')$, while the integral in equation (4.89) represents the reflected part $G^R(\bar{r}_p, \bar{r}_n')$. Substituting equation (4.89) in equation (4.43) yields

$$V_a(\bar{r}_p) = V_a^W(\bar{r}_p) + V_a^R(\bar{r}_p), \tag{4.91}$$

where the whole space contribution $V_a^W(\bar{r}_p)$ [which includes whole space term $G^W(\bar{r}_p,\bar{r}_n')$] and the reflection contribution $V_a^R(\bar{r}_p)$ [which includes reflected term $G^R(\bar{r}_p,\bar{r}_n')$] to the anomalous potential are given by

$$V_a^W(\bar{r}_p)=\frac{1}{4\pi}(1-k)\sum_{n=1}^{N}Q(\bar{r}_n')\int_S\frac{dS'}{\sqrt{(x-x')^2+(y-y')^2+(z-z')^2}}, \qquad (4.92)$$

and

$$V_a^R(\bar{r}_p)=\frac{1}{4\pi}(1-k)\sum_{n=1}^{N}Q(\bar{r}_n').\Delta S.\int_0^\infty\frac{2(\alpha_2-\alpha_1)\lambda e^{-\lambda(z'-h_1)}-e^{-\lambda z'}[(1+k)e^{\beta h_1}\alpha_1\alpha_2(e^{\alpha_1 h_1}-e^{\alpha_2 h_1})}{(1+k)e^{\beta h_1}\alpha_1\alpha_2(e^{\alpha_1 h_1}-e^{\alpha_2 h_1})+\lambda(1-k)(\alpha_2 e^{\alpha_1 h_1}-\alpha_1 e^{\alpha_2 h_1})}$$
$$\frac{+\lambda(1-k)(\alpha_2 e^{\alpha_1 h_1}-\alpha_1 e^{\alpha_2 h_1})]}{}J_0(\lambda r_p)d\lambda. \qquad (4.93)$$

The integral in equation (4.92) is evaluated analytically, while the integral in equation (4.93) is solved using a digital linear filter for Hankel J_0 transforms. If $\beta=0$ then $\sigma_1(z)=\sigma_0$, which makes it a homogeneous overburden. In this case, considering equations (4.19) and (4.20), $\alpha_1=\lambda$ and $\alpha_2=-\lambda$. Substituting these values in the above equations, we obtain the same expression as obtained by Das and Parasnis (1987) for the anomalous potential V_a in the case of a 3-D body embedded in the lower half-space of a two-layered earth with a homogeneous overburden.

Applications of this theory for the two-layered case were implemented in a 3-D Fortran program. The numerical modelling results for various models will be presented in the next section.

4.3 Numerical examples – exponentially varying transitional overburden

The models studied here consist of a 3-D body in the lower half-space of a two-layered earth with an overburden layer of exponentially varying resistivity with depth. Although the resistivity response was computed for a large number of models, we present a representative selection of them in this section.

Consider a prismatic body with dimensions $50\times150\times100$ m located at depth of 50 m below the ground surface as shown in Figure 4.1. We place the model in a Cartesian coordinate system with its origin on the surface of the ground at a point vertically above the centre of the body. The body is placed symmetrically below the origin between –25 to 25 m in the x-direction, -75 to 75 m in the y-direction and 50 to 150 m in the z-direction (Figure 4.1).

Isotropic case for future comparisons

We first compute apparent resistivity profiles using the electrode arrays of multisystem combinations A and B (see Figure 3.2), over the body (Figure 4.1) in a layered earth with an isotropic homogeneous overburden. This will then be used for comparison with the subsequent transitional layer examples in which resistivity varies exponentially with depth. Then later we present and compare the apparent resistivity residual profiles with those of the case of transitional layers. These profiles are computed with different electrode spacings along a profile line PQ (Figure 4.1) on the surface passing through the origin of the Cartesian coordinate system. Thus, in this coordinate system the line PQ is at $y = 0$.

Figures 4.5a and 4.5b show, respectively, Wenner and Schlumberger apparent resistivity profiles with different electrode separations of 5, 10, 20 and 30 m along the line PQ over the 3-D body (Figure 4.1) embedded in an isotropic homogeneous half-space with resistivity $\rho_1 = \rho_2 = 100$ ohm.m. The resistivity of the body is $\rho_B = 5$ ohm.m. In these figures and also in the other figures presented in this section, we

a)

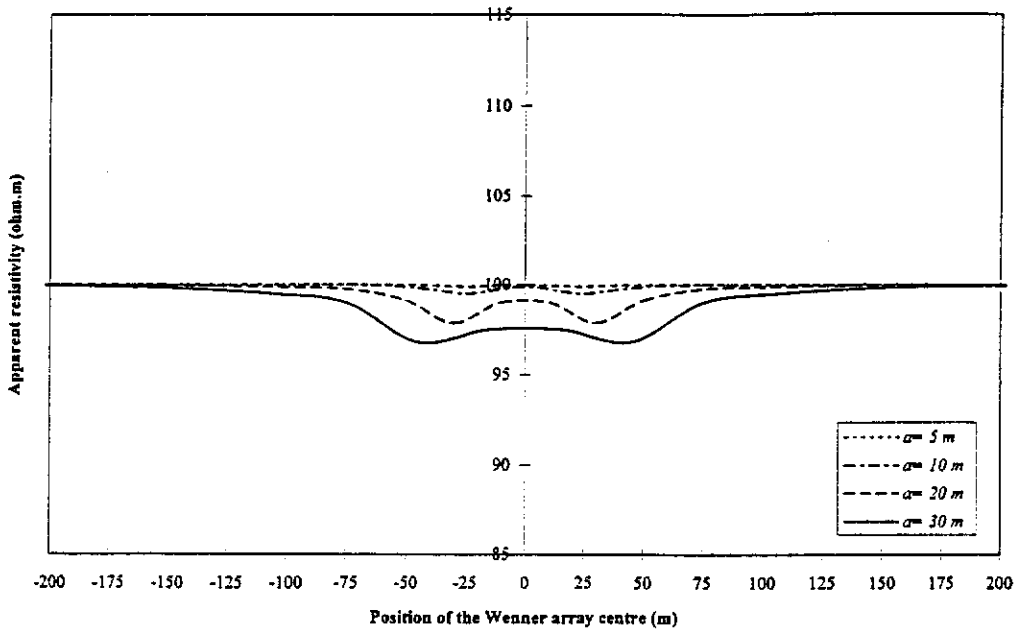

b)

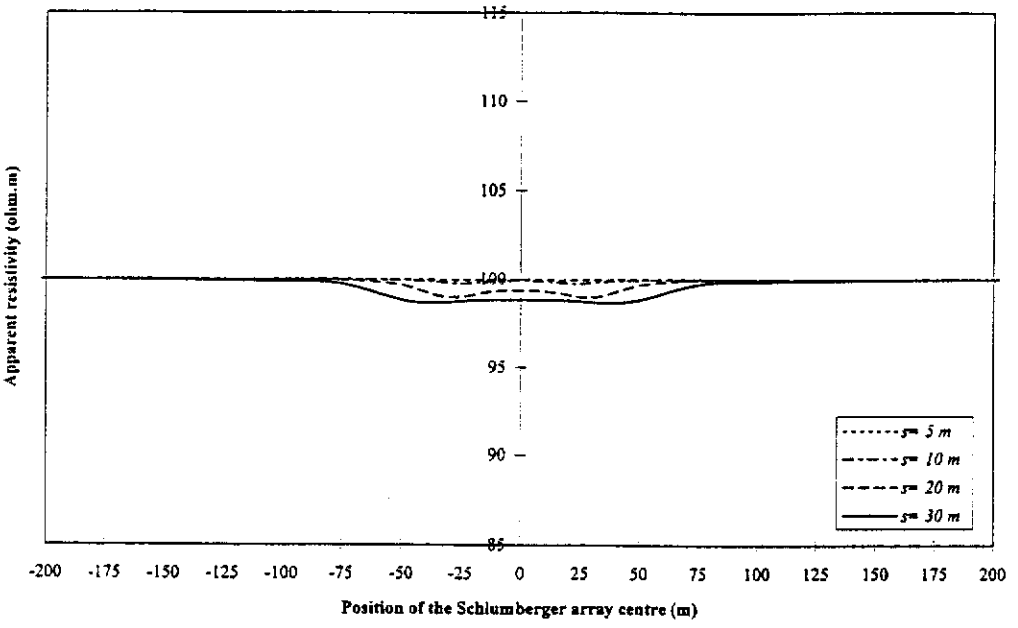

Figure 4.5. Apparent resistivity profiles over a conductive body embedded in an isotropic, homogeneous half-space. (a) Wenner profiles and (b) Schlumberger profiles along PQ (Figure 4.1). The body with resistivity $\rho_B = 5$ ohm.m is located in the homogeneous half-space with resistivity $\rho_1 = \rho_2 = 100$ ohm.m at a depth of 50 m.

refer to an electrode separation $a=AM$ for the Wenner profiles and $s=AB/2$ for the Schlumberger profiles (see Figure 3.2).

As can be seen from Figures 4.5a and 4.5b, the anomalous body can be detected with the Wenner and Schlumberger apparent resistivity profiles with larger electrode separations although the resolution is low. The relatively resistive half-space above and surrounding the body does not totally smear the response of the body. It does allow some electric current to flow through the conductive anomalous body.

Transitional layer examples

Figure 4.6a indicates a resistivity depth profile for a two-layered earth in which the overburden layer, with a thickness of $h_1 = 25$ m, has an exponentially varying resistivity with depth given by $\rho_1(z) = 100e^{0.083z}$. It starts at $\rho_0 = 100$ ohm.m at the surface ($z = 0$ m) and goes to about 800 ohm.m at the bottom of the overburden layer ($z = 25$ m). The lower half-space (second layer) has a constant resistivity of $\rho_2 = 100$ ohm.m.

Figures 4.6b and 4.6c indicate, respectively, Wenner and Schlumberger apparent resistivity profiles along the line PQ over a body, with resistivity of $\rho_B = 5$ ohm.m, embedded in the lower-half-space of a two-layered earth (Figure 4.1), having resistivity depth profile shown in Figure 4.6a. Different electrode separations of 20 and 30 m are used with these apparent resistivity profiles. In this example and other examples presented in this section, the body geometry and depth are the same as shown in Figure 4.1. In order to make comparison between the resistivity profiles, shown in Figures 4.5 and 4.6, we have chosen the same axis scale in both figures. Comparing these profiles we see that larger resistivity anomalies over the 3-D anomalous body are seen in the profiles shown in Figure 4.6.

In Figure 4.7a, we present a resistivity depth profile for a two-layered earth in which the overburden, with a thickness of $h_1 = 25$ m, has an exponentially varying

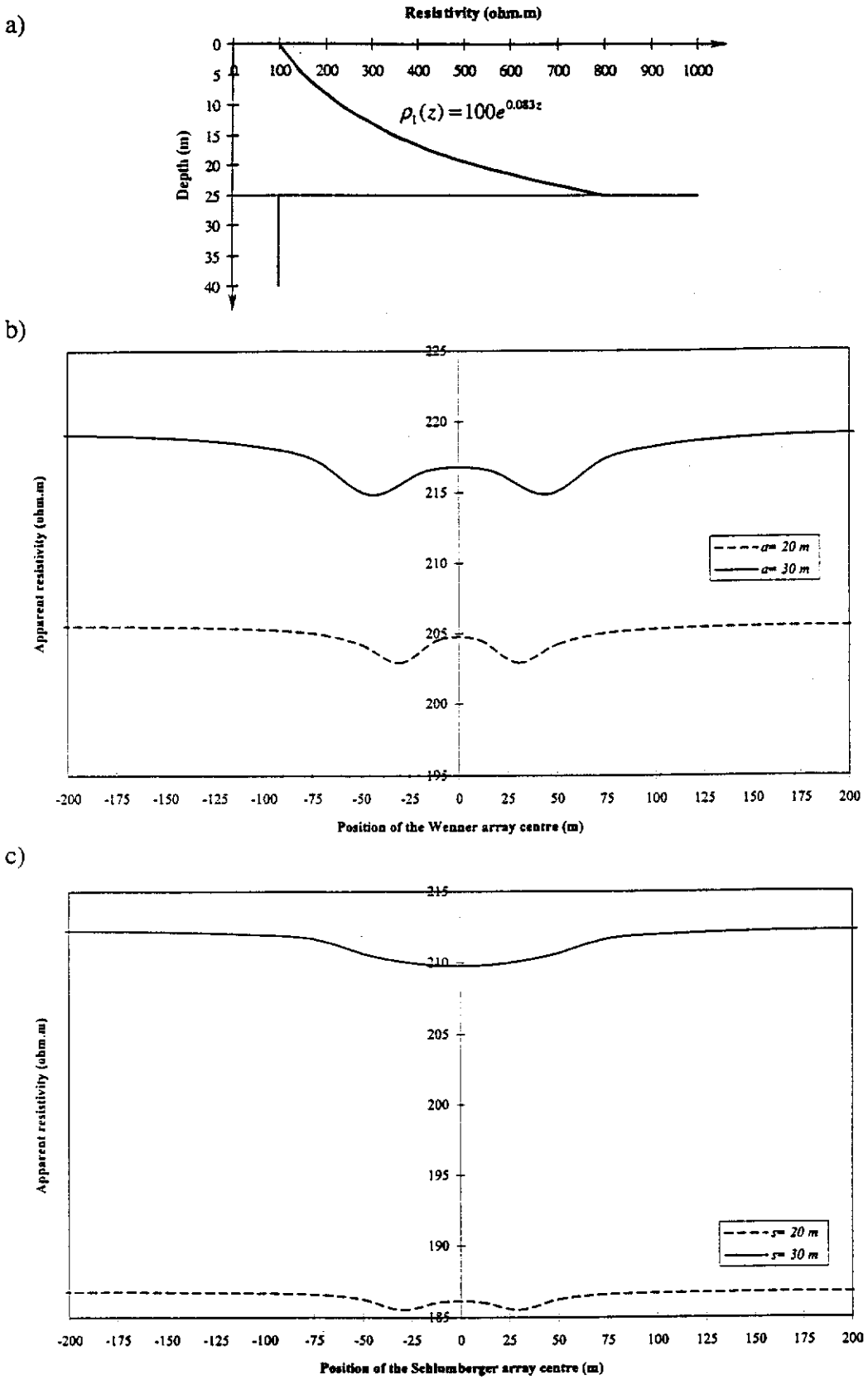

Figure 4.6. Apparent resistivity profiles over a conductive body with an overburden in which resistivity exponentially increases with depth from 100 to 800 ohm.m. (a) Resistivity depth profile, (b) Wenner profiles and (c) Schlumberger profiles along PQ (Figure 4.1). The second layer (host medium) has a constant resistivity of $\rho_2 = 100$ ohm.m. The resistivity of the body is $\rho_B = 5$ ohm.m.

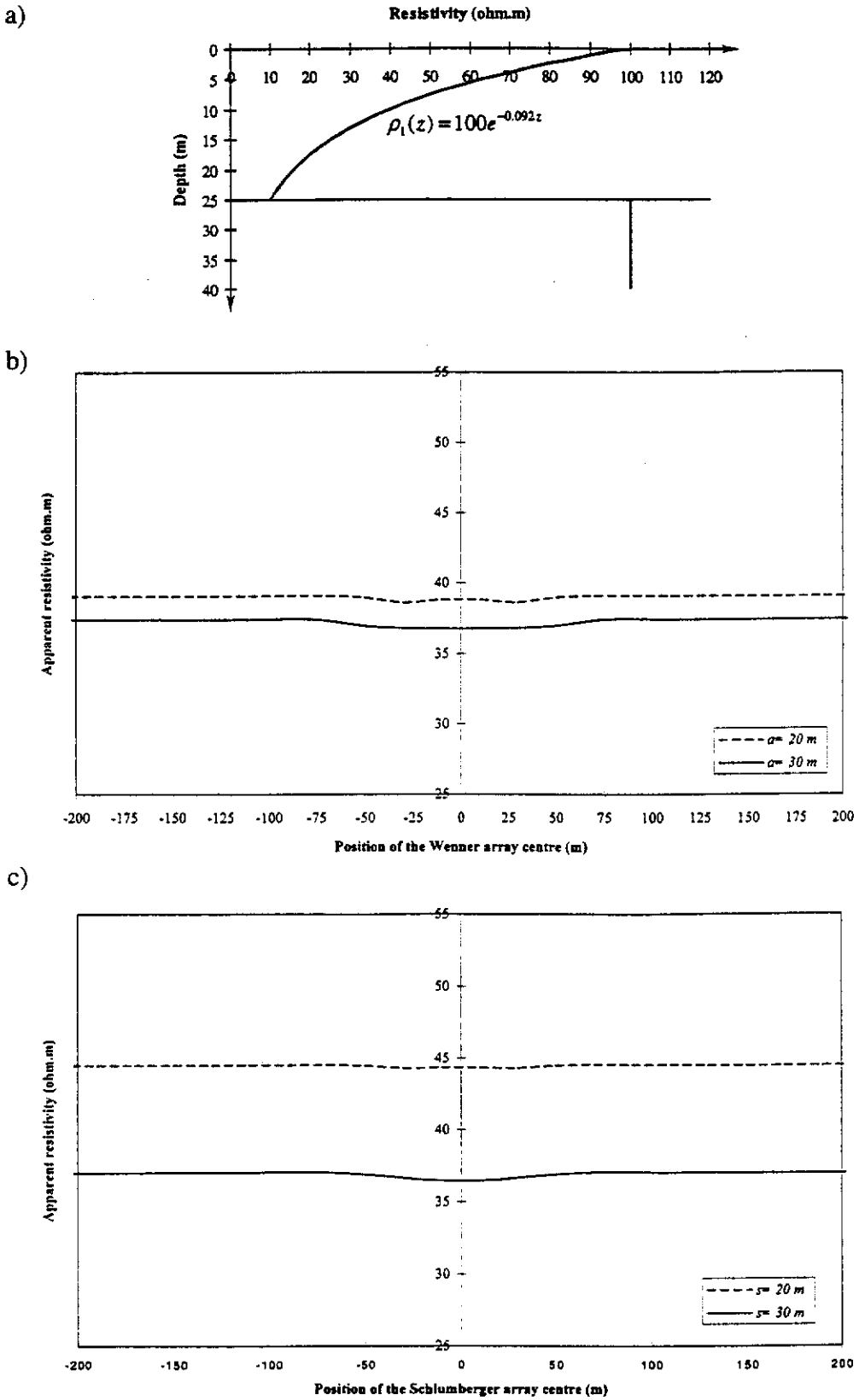

Figure 4.7. Apparent resistivity profiles over a conductive body with an overburden in which resistivity exponentially decreases with depth from 100 to 10 ohm.m. (a) Resistivity depth profile, (b) Wenner profiles and (c) Schlumberger profiles along PQ (Figure 4.1). The second layer (host medium) has a constant resistivity of $\rho_2 = 100$ ohm.m. The resistivity of the body is $\rho_B = 5$ ohm.m.

resistivity with depth given by $\rho_1(z) = 100e^{-0.092z}$. The resistivity goes from $\rho_0 = 100$ ohm.m at the surface ($z = 0$ m) to about 10 ohm.m at the bottom of the overburden layer ($z = 25$ m). The lower half-space (second layer), as in Figure 4.6a, has a constant resistivity of $\rho_2 = 100$ ohm.m, and contains an anomalous body with a resistivity of $\rho_B = 5$ ohm.m.

As can be seen from the Wenner and Schlumberger apparent resistivity profiles, in Figures 4.7b and 4.7c, the resistivity anomalies over the 3-D anomalous body are relatively small.

A comparison between the apparent resistivity profiles shown in Figures 4.5, 4.6, and 4.7 indicates that the resistivity anomaly response over the body in Figure 4.6 is larger than that in Figures 4.5 and 4.7. This is because the resistivity of the overburden layer in the case of Figure 4.6 increases with depth, which results in more resistive levels in lower parts of the overburden layer than in the second layer (host medium). Thus, less electric current channelling occurs in the resistive overburden, which results in more current travelling in the host medium. It can also be noted that the resistivity anomaly response over the body in Figure 4.7 is smaller than that in Figure 4.5. The resistivity of the overburden in the case of Figure 4.7 decreases with depth, making the overburden at lower levels even more conductive. Consequently, more electric current channelling occurs in the overburden, resulting in smaller electric current in the lower layer. Thus, the transitional overburden affects the resistivity anomaly response of a 3-D body compared to a homogeneous overburden (which has a constant resistivity). It is concluded from resistivity profiling that the detection of a conductive body under an overburden of increasing resistivity with depth is better than the case of a homogeneous overburden or an overburden of decreasing resistivity with depth. An overburden of decreasing resistivity with depth may cause more difficulty in detection of a conductive body below it compared to the case of a homogeneous overburden.

Apparent resistivity residual profiles

To enhance the anomalous body response, we apply the apparent resistivity residual technique. Figures 4.8a, 4.8b, and 4.8c show the apparent resistivity residual profiles using multisystem combination A (i.e. Wenner and two-electrode resistivity measurements) for the cases in which the Wenner apparent resistivity profiles are given in Figures 4.5a, 4.6b and 4.7b, respectively. Likewise, we have shown the apparent resistivity residual profiles using multisystem combination B (i.e. Schlumberger and equatorial dipole-dipole resistivity measurements) in Figures 4.9a, 4.9b, and 4.9c for the cases in which the Schlumberger apparent resistivity profiles are shown in Figures 4.5b, 4.6c and 4.7c, respectively. Electrode separations of 20 and 30 m are used for these apparent resistivity residual profiles.

A comparison of these residual profiles with the Wenner and Schlumberger apparent resistivity profiles indicates that the residual profiles greatly enhance the anomalous body response. It is noticed that the signature of the residual profiles for the case of transitional overburden is of the same form as the signature of residual profiles for the case of homogeneous overburden. This is not unexpected since a transitional layer, as indicated by Unz (1968), can be replaced by an equivalent layered system composed of a number of layers having constant resistivity in each layer.

Also, it is clearly seen from Figures 4.8 and 4.9 that the residual profile for the case of an overburden with exponentially increasing resistivity shows a larger anomaly compared to the case of homogeneous overburden or the case of an overburden with exponentially decreasing resistivity. For the latter case, as the figures show, the residual anomaly response is smaller than the case of a homogeneous overburden. We see that the detection of a conductive body beneath an overburden of increasing resistivity with depth is better than under a homogeneous overburden or an overburden of decreasing resistivity with depth. Also the residual profiles over a conductive body with an overburden of decreasing resistivity with depth (e.g. Figures 4.8c and 4.9c), do not show such large anomalies as in the other cases, and thus,

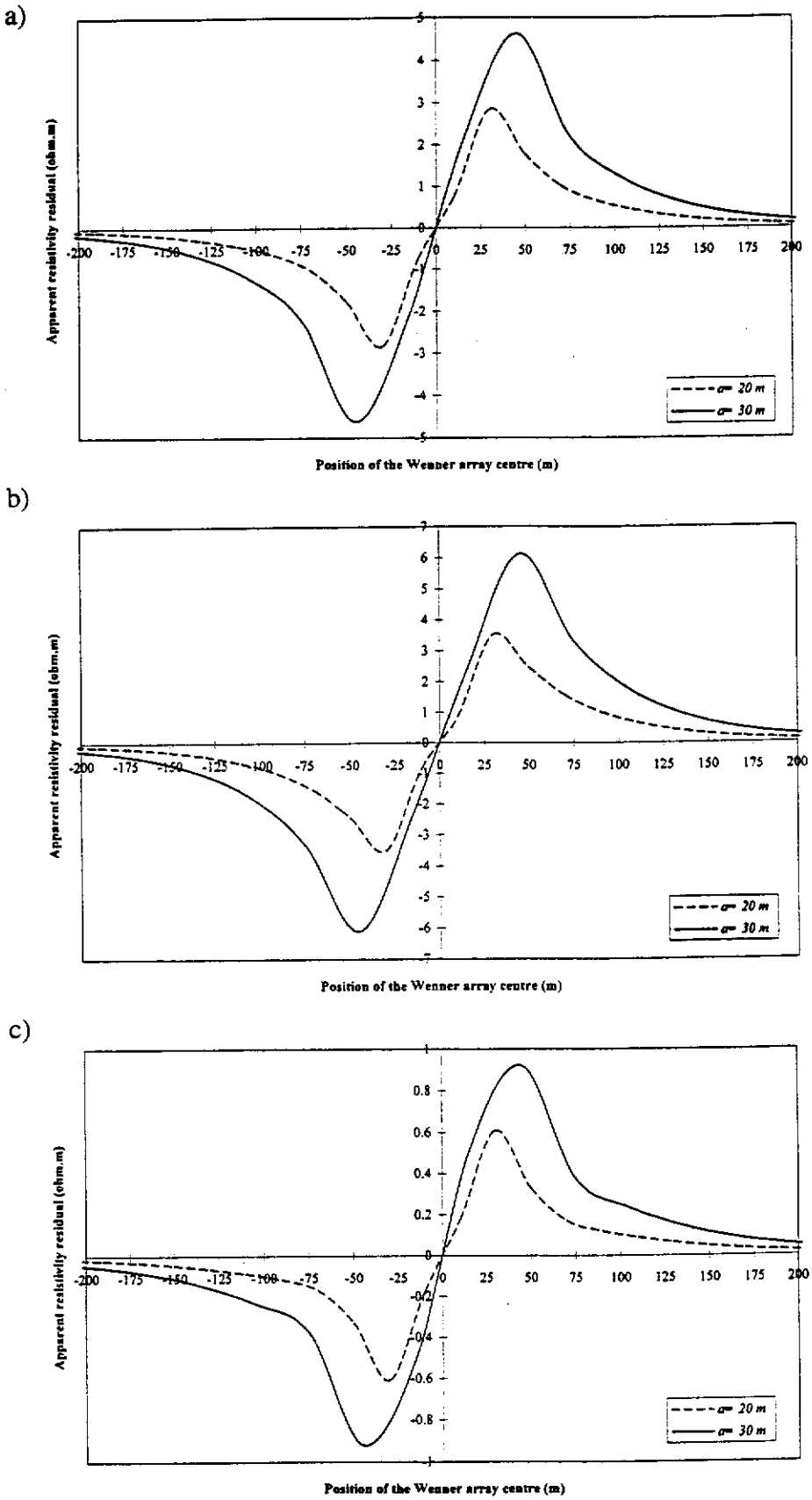

Figure 4.8. Apparent resistivity residual profiles obtained using multisystem combination A over a conductive body examined in Figures 4.5 to 4.7. (a) Residual profiles corresponding to the Wenner profiles shown in Figure 4.5a, (b) Residual profiles corresponding to the Wenner profiles shown in Figure 4.6b, and (c) Residual profiles corresponding to the Wenner profiles shown in Figure 4.7b.

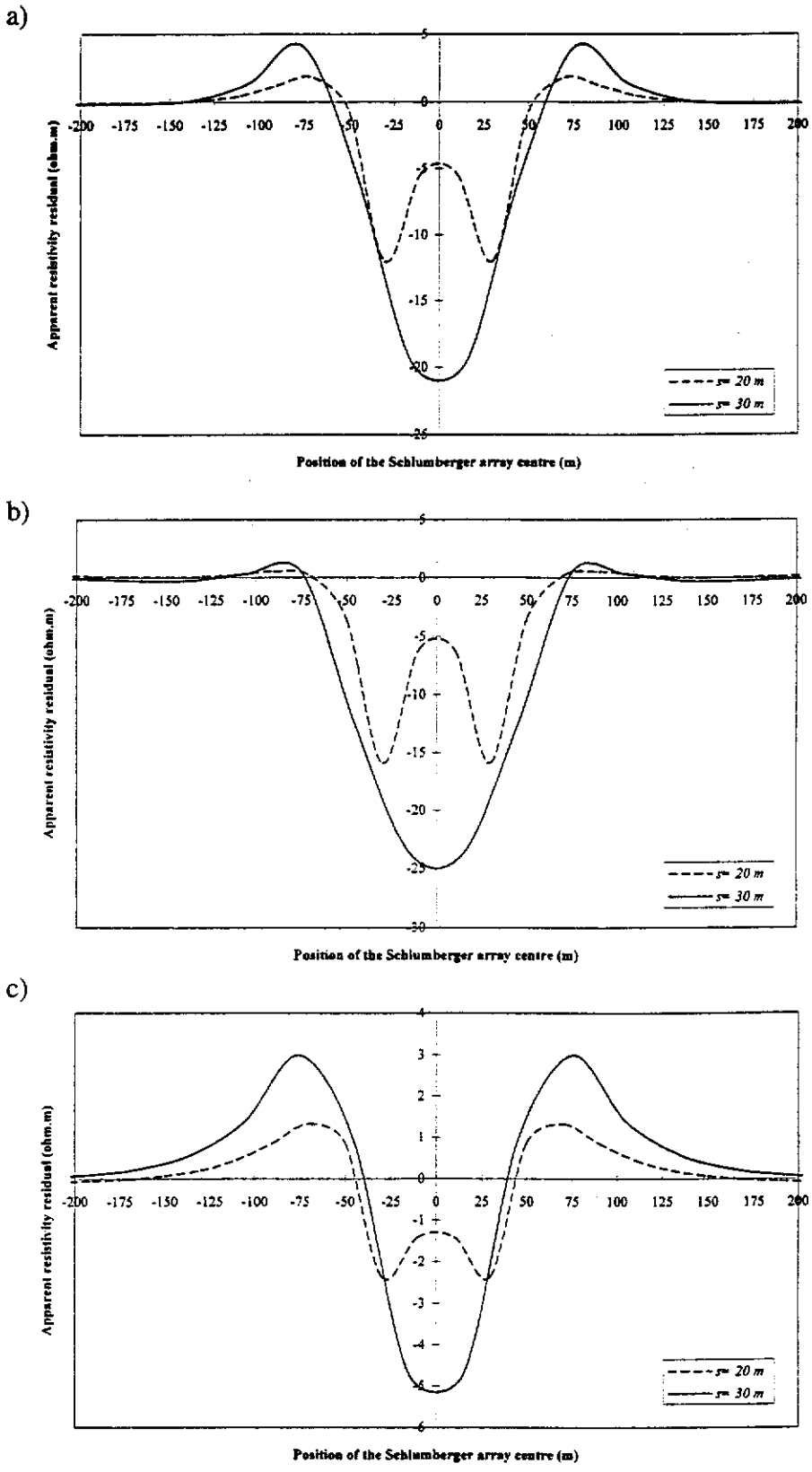

Figure 4.9. Apparent resistivity residual profiles obtained using multisystem combination B over a conductive body examined in Figures 4.5 to 4.7. (a) Residual profiles corresponding to the Schlumberger profiles shown in Figure 4.5b, (b) Residual profiles corresponding to the Schlumberger profiles shown in Figure 4.6c, and (c) Residual profiles corresponding to the Schlumberger profiles shown in Figure 4.7c.

detectability of a conductive target in this case is not as good as in the other cases. Hence, the transitional overburden affects the *apparent resistivity residual* response in a similar way to the Wenner and Schlumberger apparent resistivity responses.

Further examples

In the following examples, we see how the apparent resistivity residual technique enhances even more, the detection of buried anomalous bodies under an overburden of exponentially varying resistivity with depth.

In Figure 4.10, we show another example of the transitional overburden case. Figure 4.10a shows a resistivity depth profile for a two-layered earth in which the overburden, with a thickness of $h_1 = 25$ m, is transitional. The resistivity of the overburden varies exponentially with depth according to the function $\rho_1(z) = 200e^{0.1z}$. Therefore, the resistivity of the overburden, which is 200 ohm.m at the surface ($z = 0$ m) increases exponentially with depth so that it will be about 2440 ohm.m at the bottom of the overburden layer ($z = 25$ m). The lower half-space (second layer) has a constant resistivity of $\rho_2 = 800$ ohm.m.

In Figures 4.10b and 4.10c we show, respectively, Wenner and Schlumberger apparent resistivity profiles with electrode separations of 5, 10, 20 and 30 m along the line PQ over a body of resistivity $\rho_B = 5$ ohm.m in the lower-half-space of a two-layered earth (Figure 4.1) with resistivity depth profile shown in Figure 4.10a.

In Figure 4.11a, we present a resistivity depth profile for a two-layered earth in which the overburden, with a thickness of $h_1 = 25$ m, has an exponentially varying resistivity with depth $\rho_1(z) = 200e^{-0.1z}$. It starts from 200 ohm.m at the surface ($z = 0$ m) and goes to about 16 ohm.m at the bottom of the overburden layer ($z = 25$ m). The lower half-space (second layer), as in Figure 4.10a, has a constant resistivity of $\rho_2 = 800$ ohm.m.

a)

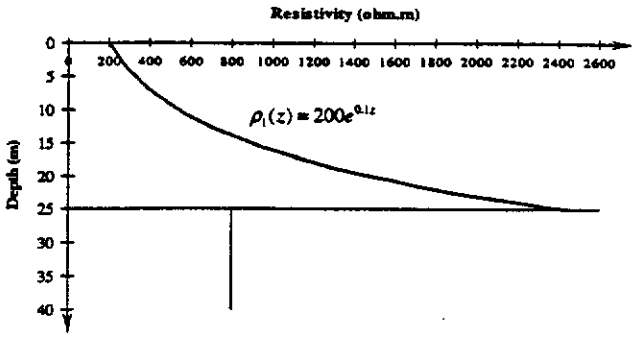

b)

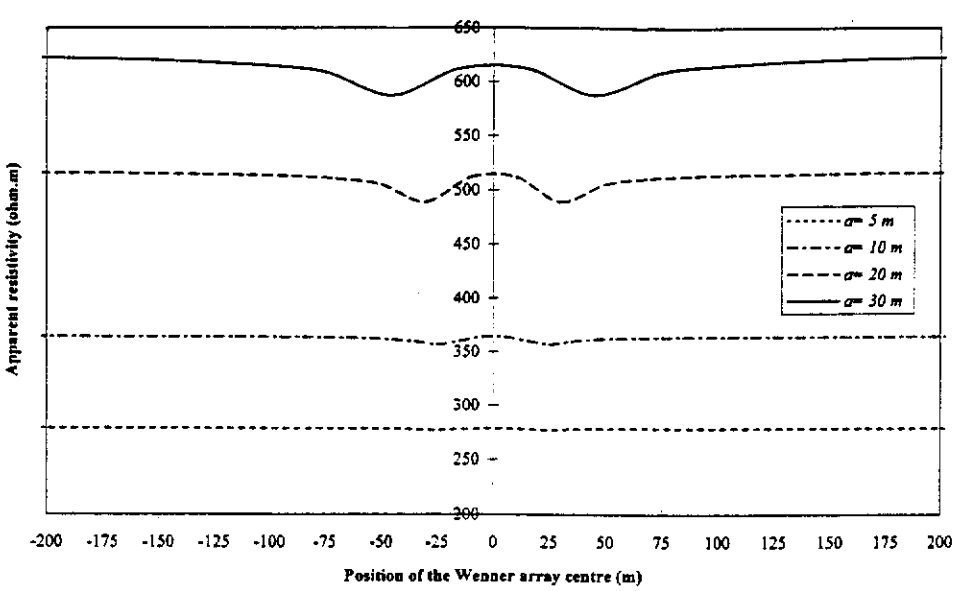

c)

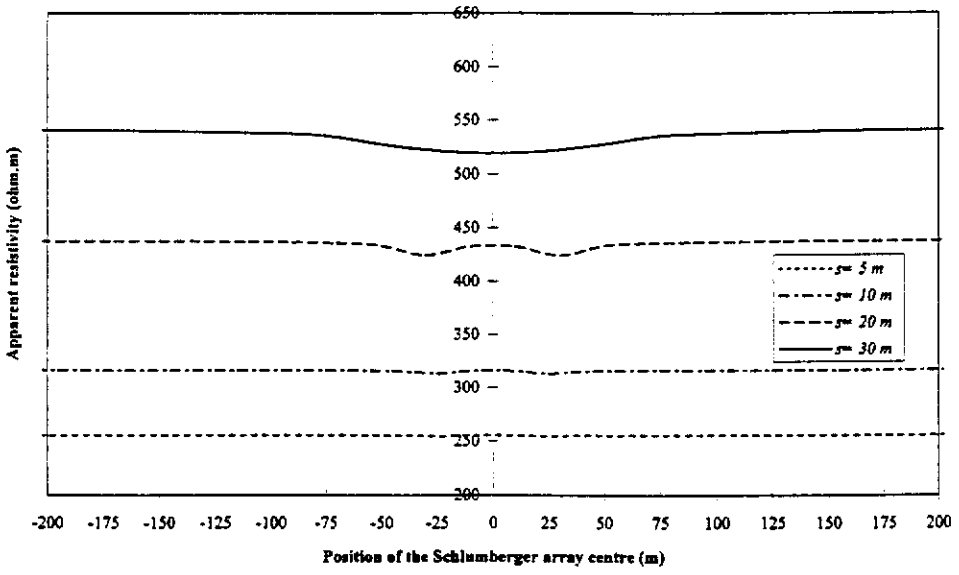

Figure 4.10. Apparent resistivity profiles over a conductive body with an overburden in which resistivity exponentially increases with depth from 200 to 2440 ohm.m. (a) Resistivity depth profile, (b) Wenner profiles and (c) Schlumberger profiles along PQ (Figure 4.1). The second layer (host medium) has a constant resistivity of $\rho_2 = 800$ ohm.m. The resistivity of the body is $\rho_B = 5$ ohm.m.

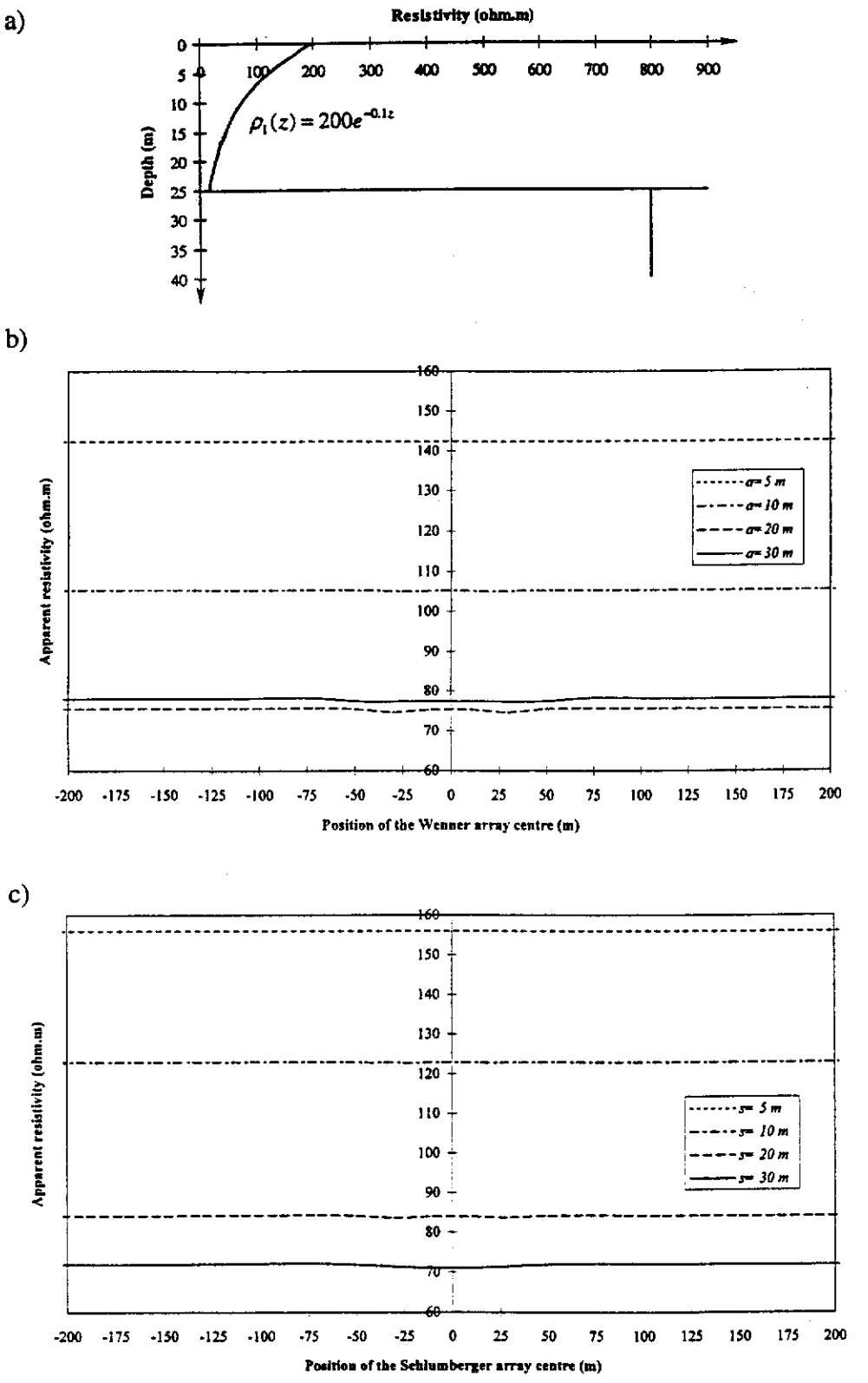

Figure 4.11. Apparent resistivity profiles over a conductive body with an overburden in which resistivity exponentially decreases with depth from 200 to 16 ohm.m. (a) Resistivity depth profile, (b) Wenner profiles and (c) Schlumberger profiles along PQ (Figure 4.1). The second layer (host medium) has a constant resistivity of $\rho_2 = 800$ ohm.m. The resistivity of the body is $\rho_B = 5$ ohm.m.

For this resistivity depth profile, we show in Figures 4.11b and 4.11c, respectively, Wenner and Schlumberger apparent resistivity profiles with electrode spacings of 5, 10, 20 and 30 m along the line PQ over a 3-D body, which is embedded in the second layer (Figure 4.1). The resistivity of the body is the same as in Figure 4.10 (i.e. $\rho_B = 5$ ohm.m). These profiles indicate that the resistivity anomalies over the 3-D anomalous body are relatively small. Generally, the values of apparent resistivity on the Wenner or Schlumberger profiles over the line PQ decrease with increasing electrode spacing up to 30 m due to decreasing the resistivity of the overburden. However, as can be seen from Figure 4.11b, the values of apparent resistivity on the Wenner profile with electrode spacing a=30 m are higher than those on the Wenner profile with electrode spacing a=20 m. This can be explained by noting that a larger portion of the electric current flows in the second layer in the case of the electrode spacing a=30 m than in the case of the electrode spacing a=20 m. Since the second layer has a higher resistivity than that of the overburden, it is expected that we have higher apparent resistivity values in the case of the Wenner profile with a=30 m (or larger electrode spacings) than the Wenner profile with a=20 m. For the Schlumberger profiles, shown in Figure 4.11c, it appears that the apparent resistivity values tend to increase with electrode spacings larger than s=30 m. Note that the distance between the current electrodes in a Wenner profile with an electrode spacing a is greater than that in a Schlumberger profile with electrode spacing s=a (see Figure 3.2).

A comparison of the apparent resistivity profiles in Figures 4.10 and 4.11 indicates that the resistivity anomaly response over the body in Figure 4.10 is larger. The reason is the same as that given earlier when comparing the profiles in Figure 4.6 with those in Figures 4.5 and 4.7. We can also compare these Wenner and Schlumberger profiles, shown in Figures 4.10 and 4.11, with the profiles for a similar case having a homogeneous overburden with a resistivity of $\rho_1 = 200$ ohm.m, which were shown in Figures 3.4 and 3.12. The comparison, from detectability point of view, indicates that detection of a conductive body under an overburden of increasing resistivity with depth is better than under a homogeneous overburden or an

overburden of decreasing resistivity with depth. An overburden, in which resistivity decreases with depth, makes detection of a body underneath difficult.

The corresponding apparent resistivity residual profiles are shown in Figures 4.12 and 4.13. Figures 4.12a and 4.12b indicate the apparent resistivity residual profiles using multisystem combination A for the cases in which the Wenner apparent resistivity profiles are given in Figures 4.10b and 4.11b, respectively. Also, Figures 4.13a and 4.13b show the apparent resistivity residual profiles using multisystem combination B corresponding to the apparent resistivity profiles shown in Figures 4.10c and 4.11c.

The residual profiles, compared to the resistivity profiles, clearly indicate the enhancement of the signal from the body, and thus, they improve the detectability of the body. Although the residual anomalies for the case of overburden with exponentially increasing resistivity (Figures 4.12a and 4.13a) are much larger than the anomalies for the case of overburden with exponentially decreasing resistivity (Figures 4.12b and 4.13b), the latter residual anomalies are also capable of locating the body. However, for this case, it is quite difficult to locate the body from the resistivity profiles shown in Figure 4.11 without the residual computation.

We have also computed the resistivity and residual responses for models containing a resistive body and models having a body in a two-layered earth with continuous resistivity at the interface between the transitional overburden and homogeneous second layer. To avoid a lengthy section here, we have not presented the results for these models. Comparing the residual profiles with the Wenner and Schlumberger apparent resistivity profiles for these models also indicates that the residual profiles significantly enhance the anomalous resistive body response.

4.4 Discussion

In this chapter, we have considered the effect of transitional layers on resistivity and apparent resistivity residual responses over a 3-D body. The case of an exponentially

a)

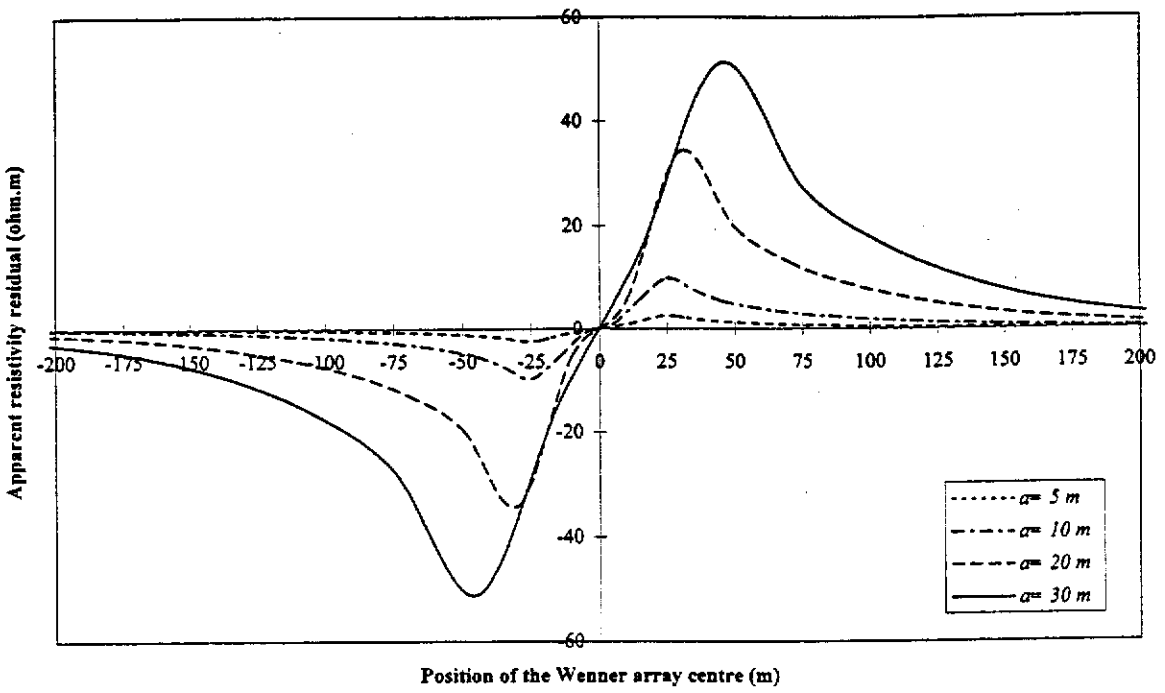

b)

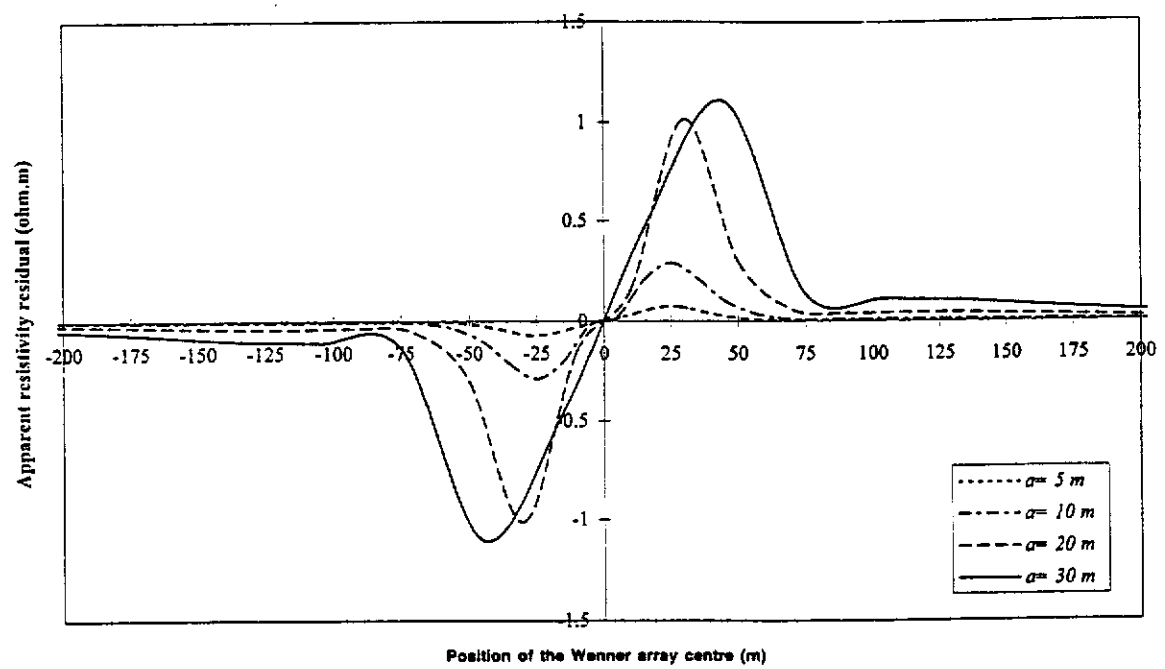

Figure 4.12. Apparent resistivity residual profiles obtained using multisystem combination A over a conductive body examined in Figures 4.10 and 4.11. (a) Residual profiles corresponding to the Wenner profiles shown in Figure 4.10b, and (b) Residual profiles corresponding to the Wenner profiles shown in Figure 4.11b.

a)

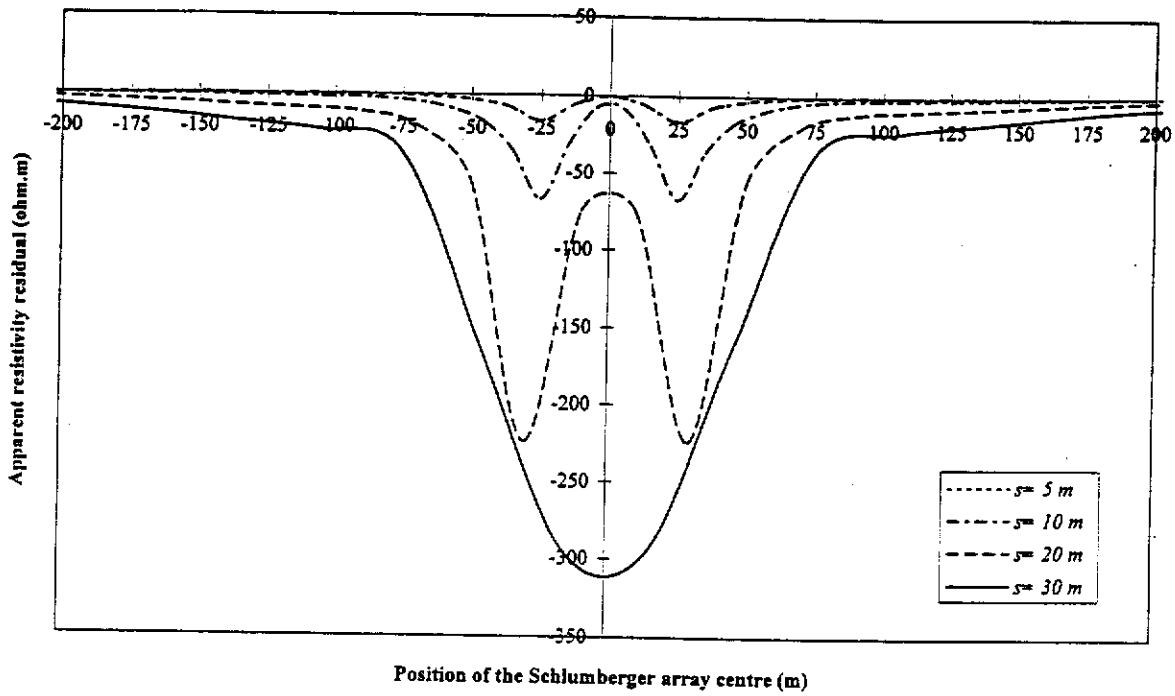

b)

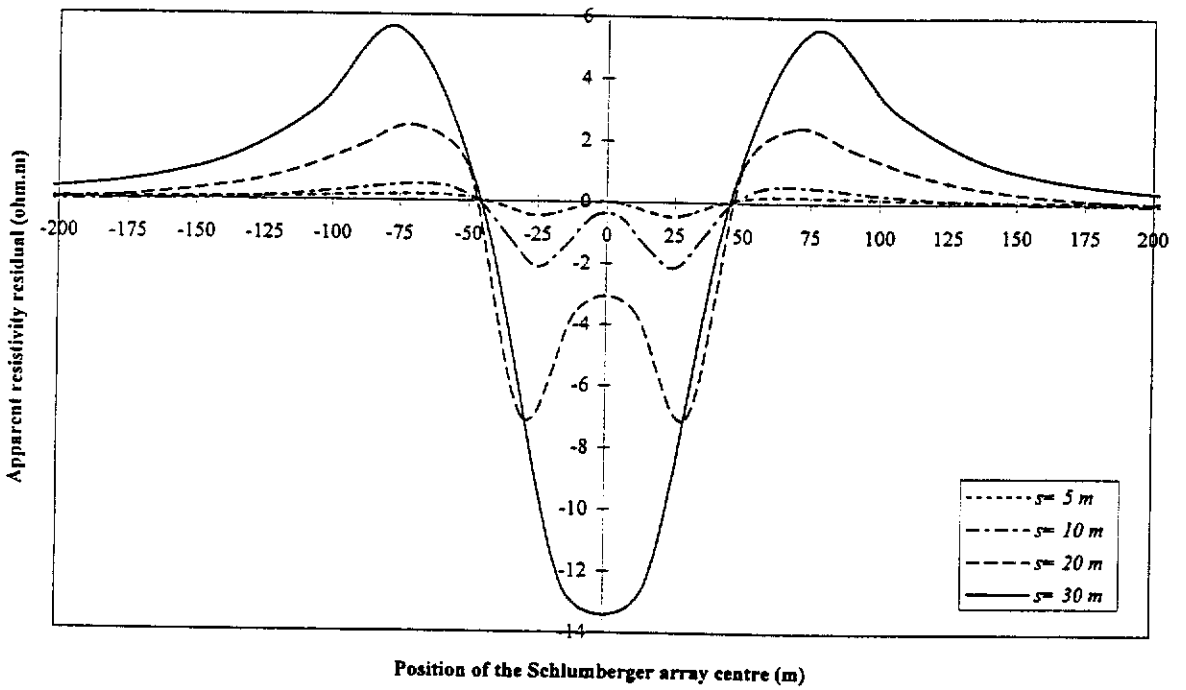

Figure 4.13. Apparent resistivity residual profiles obtained using multisystem combination B over a conductive body examined in Figures 4.10 and 4.11. (a) Residual profiles corresponding to the Schlumberger profiles shown in Figure 4.10c, and (b) Residual profiles corresponding to the Schlumberger profiles shown in Figure 4.11c.

varying transitional overburden has just been chosen as a specific transitional example. Through numerical examples we have shown that the apparent resistivity residual technique is capable of detecting anomalous bodies which are difficult to detect by conventional resistivity methods. We have demonstrated that the detectability of a 3-D body under a transitional overburden layer in some layered earth situations (e.g. a conductive body under a transitional overburden of decreasing resistivity with depth) using the conventional apparent resistivity profiles is worse than under a homogeneous overburden layer. However, using the apparent resistivity residual profiles the anomalous body response is significantly enhanced. The residual profiles clearly indicate the location of lateral edges of the body.

The effect of noise on the case of a transitional layer has not been studied. However, it is expected that noise in this case will affect the resistivity and residual profiles in a similar way to the effect of noise on these profiles for the homogeneous layer case, investigated in Chapter 3. This is because a transitional layer can be replaced by a number of homogeneous layers with a good approximation.

Chapter 5

CONCLUSIONS AND RECOMMENDATIONS

5.1 Conclusions

In geophysical exploration one is often faced with the problem of locating anomalous bodies situated in a layered host environment. The electrical response in these situations is often dominated by the layered environment, and consequently, the detection of the target anomaly electrically is often quite difficult.

The exploration industry is currently developing new resistivity field data acquisition systems, which facilitate the recording of electrical survey data from multiple electrode array geometries. In this thesis, based on multisystem resistivity survey data, new processing techniques have been developed to minimise the electrical effects of layered host environments, and enhance the effect of anomalous conductivity zones within them. *Apparent resistivity residual* is a new concept or technique introduced and developed in this work. This technique has been shown to enhance the presence of anomalous zones, which with conventional apparent resistivity profiling would not be otherwise detected.

The new procedures were first tested on numerically modelled data, followed by limited testing on field data. In order to develop and test these methods for enhancing the electrical response of 3-D bodies in layered environments, recent developments in numerical modelling techniques were employed in new applications. The biconjugate gradient method, which provided higher accuracy than the LU decomposition method, was used to solve the partitioned matrix equation for the electric charge density column vector. Also, applying new digital linear filters for computation of Hankel J_0 and J_1 transforms resulted in improvement in the accuracy of the computations as these filters produced much smaller errors than those made by all other filters available for these transforms at this time. The recently

developed spectral formalism, which is quite versatile, was shown to have distinct advantages over the classical propagator matrix formalism, when used for computations of the required Green's functions involving 3-D anomalous bodies in layered environments.

Using results from the improvements made to numerical modelling software, procedures were developed for computing *apparent resistivity residual* data from the following composite surveys:

(a) Wenner and two-electrode surveys
(b) Schlumberger and equatorial dipole-dipole surveys.

Tests on numerical data showed that the detection of anomalous zones could be significantly enhanced by the computation of apparent resistivity residual. By addition of random noise to model data, it was shown that the procedure is somewhat sensitive to noise. This sensitivity may be reduced by the use of a normalisation procedure.

Following successful theoretical testing, preliminary field tests were conducted on a survey site to explore for subsurface conductive anomalies. Because the survey area contained a number of cultural features such as buildings, power lines, and topographic variations, it was considered that the DC resistivity methods would provide superior field data to electromagnetic techniques. Even though it was recognised that such cultural features would probably influence the results of the resistivity surveys also, it was considered that the extent of any influence would be less. The apparent resistivity residual profiles obtained indicated the presence of conductive anomalies. Further field testing at that site is required to confirm the nature of their source. It was concluded that extensive testing generally under a range of conditions should be conducted, but that was beyond the scope and time provisions of the current research program.

The *apparent resistivity residual* computed using the multisystem resistivity measurements enhances any non-layered response. Where multiple bodies or geological and cultural noise are present, the sensitivity of the procedure enhances these "non layered" features as well. Thus, it is recommended that this new procedure is best applied (as with all resistivity survey techniques) in electrically quiet and undisturbed areas, but where electrical contrasts obscure any anomalous non-layered response.

It was found that the anomalous apparent resistivity residual was as much as characteristic of the survey combinations used, as it was of the anomalous body itself. For the case of the Wenner and two-electrode combination system, positive and negative peaks are produced depending on the direction of profiling. These extrema indicate edges of the body, while the intermediate zero crossover point is generally indicative of the centre of the body. For the apparent resistivity residual profile obtained using the Schlumberger and equatorial dipole-dipole profiling measurements, the lateral edges of the body are recognised from the large negative peaks (for the case of a conductive body) and positive peaks (for the case of a resistive body). The apparent resistivity residual should be regarded principally as an anomaly indicator rather than an absolute quantity. Because its signature depends on a combination of electrode configurations, electrode spacings related to the electrical contrasts and dimensions and depth of the anomalous zone, a fair degree of skill and experience is needed in the interpretation of apparent resistivity residuals computed from field data.

In addition, in the research work on layers of fixed resistivity, for the first time, the electrical response of a 3-D body embedded in a layered earth with a transitional overburden layer was derived. All of the previously published work involving transitional layers investigated the problem of a layered earth model without considering a 3-D body embedded in it. Computer software was written based on the development in this thesis for a 3-D body embedded in a layered earth containing a transitional overburden layer. For a transitional layer, the case where resistivity or conductivity varies exponentially with depth was implemented in modelling software.

The significance of this development for the transitional layer case is quite clear as there are many instances in nature, in which the resistivities (or conductivities) of the layers vary continuously with depth.

5.2 Recommendations

As with any new geophysical technique, further developments in the interpretation of these new apparent resistivity residual techniques are required. These are not necessarily independent of additional field survey procedures likely to be developed in the future. Areal coverage by multiple profiling could result in a type of apparent resistivity residual mapping. Furthermore, the concept of apparent resistivity residual computation should be considered for development with electromagnetic surveys as well.

One of the spin-offs from the research was the improvement in 3-D simulation of resistivity surveys by numerical modelling. Further improvements could be made following the developments introduced in this thesis:

(a) The moment method with pulse basis functions and point collocation, and also the method of weighted residuals were used for the distribution of the unknown electric charge density on the surface of a body. These methods approximate the electric charge density on each surface cell of the body. The use of a different method for this purpose, that could approximate the electric charge density better, may improve the computation of the resistivity response of the body. In this regard, the multidomain Chebyshev spectral method should be investigated.

(b) In this PhD research work, a single 3-D body (or multiple bodies) was considered in the lower half-space of a two-layered earth under a homogeneous or transitional overburden. However, if the body is considered in the first layer of the two-layered earth or in any layer of an N-layered earth, the method of the computations for the resistivity response of the body is the same, only the

Green's functions will be different. Using the spectral formalism, which is quite versatile and convenient, the required Green's functions could be computed easily for these other cases.

(c) Using this spectral formalism, the problem of computing the electric potential for the borehole case is also simplified. Thus, the electric potential (and subsequently the resistivity response) of a 3-D body in a borehole, whether the source is located in the same borehole (i.e. single-borehole) or different borehole (i.e. cross-borehole) could be computed in future work.

REFERENCES

Annan, A. P., Brewster, M. L., Greenhouse, J. P., Redman, J. D., Schneider, G. W., Olhoeft, G. R., and Sander, K. A., 1992, Geophysical monitoring of DNAPL migration in a sandy aquifer: 62nd Ann. Internat. Mtg., Soc. Expl. Geophys., Expanded Abstracts, 344-347.

Banerjee, B., Sengupta, B. J., and Pal, B. P., 1980, Apparent resistivity of a multilayered earth with a layer having exponentiality varying conductivity: Geophys. Prosp., **28**, 435-452.

Barker, R. D., 1981, The offset system of electrical resistivity sounding and its use with a multicore cable: Geophys. Prosp., **29**, 128-143.

Barker, R. D., 1990, investigation of groundwater salinity by geophysical methods, *in* Ward, S. H., Ed., Geotechnical and environmental geophysics: Soc. Explor. Geophys., **2**, 201-211.

Benson, A. K., Payne, K. L., and Stubben, M. A., 1997, Mapping groundwater contamination using dc resistivity and VLF geophysical methods - A case study: Geophysics, **62**, 80-86.

Best, M. E., Duncan, P., Jacobs, F. J., and Scheen, W. L., 1985, Numerical modelling of the electromagnetic response of three-dimensional conductors in a layered earth: Geophysics, **50**, 665-676.

Bhattacharya, P. K. and Patra, H. P., 1968, Direct current geoelectric sounding, principles and interpretation: Elsevier Scientific Publishing Co.

Brizzolari, E., and Bernabini, M., 1979, Comparison between Schlumberger electrode arrangement and some focussed electrode arrangements in resistivity profiles: Geophys. Prosp., **27**, 233-244.

Buselli, G., Barber, C., Davis, G. B., and Salama, R. B., 1990, Detection of groundwater contamination near waste disposal sites with transient electromagnetic and electrical methods, *in* Ward, S. H., Ed., Geotechnical and environmental geophysics: Soc. Explor. Geophys., **2**, 27-38.

Coggon, J. H., 1971, Electromagnetic and electrical modeling by the finite-element method: Geophysics, **36**, 132-155.

Dahlin, T., 1996, 2D resistivity surveying for environmental and engineering applications: First Break, **14**, No. 7, 275-283.

Das, U. C., 1982, Designing digital linear filters for computing resistivity and electromagnetic sounding curves: Geophysics, **47**, 1456-1459.

Das, U. C., 1995, Apparent resistivity curves in controlled-source electromagnetic sounding directly reflecting true resistivities in a layered earth: Geophysics, **60,** 53-60.

Das, U. C., and de Hoop, A. T., 1995, Efficient computation of apparent resistivity curves for depth profiling of a layered earth: Geophysics, **60**, 1691-1697.

Das, U. C., and Parasnis, D. S., 1987, Resistivity and induced polarization responses of arbitrarily shaped 3-D bodies in a two-layered earth: Geophys. Prosp., **35**, 98-109.

Das, U. C., and Verma, S. K., 1980, Digital linear filter for computing type curves for the two-electrode system of resistivity sounding: Geophys. Prosp., **28**, 610-619.

Dey, A., and Morrison, H. F., 1979, Resistivity modeling for arbitrarily shaped three-dimensional structures: Geophysics, **44**, 753-780.

Dieter, K., Paterson, N. R., and Grant, F. S., 1969, IP and resistivity type curves for three-dimensional bodies: Geophysics, **34**, 615-632.

Eskola, L., 1992, Geophysical interpretation using integral equations: Chapman & Hall.

Frohlich, R. K., Urish, D. W., Fuller, J., and O'Reilly, M., 1994, Use of geoelectrical methods in groundwater pollution surveys in a coastal environment: Applied Geophysics, **32**, 139-154.

Geological Survey of Western Australia, 1996, Atlas of Western Australian mineral deposits and petroleum fields.

Griffiths, D. H., and Turnbull, J., 1985, A multi-electrode array for resistivity surveying: First Break, **3**, No. 7, 16-20.

Guptasarma, D., and Singh, B., 1997, New digital linear filters for Hankel J_0 and J_1 transforms: Geophys. Prosp., **45**, 745-762.

Hohmann, G. W., 1987, Numerical modeling for electromagnetic methods of geophysics, *in* Nabighian, M. N., Ed., Electromagnetic methods in applied geophysics: Soc. Explor. Geophys., **1**, 313-363.

Holcombe, H. T., and Jiracek, G. R., 1984, Three-dimensional terrain corrections in resistivity surveys: Geophysics, **49**, 439-452.

Jain, S. C., 1972, Resistivity sounding on a three-layer transitional model: Geophys. Prosp., **20**, 283-292.

Jain, S. C., Kumar, R., and Roy, A., 1973, Some results of experimental geophysical surveys for location of ancient gold workings, Kolar, India: Geophys. Prosp., **21**, 229-242.

James, B. A., 1985, Efficient microcomputer-based finite difference resistivity modeling via Polozhii decomposition: Geophysics, **50**, 443-465.

Kamkar-Rouhani, A., 1997, Using multisystem surveys to differentiate the resistivity responses of multiple three dimensional subsurface bodies: Moscow '97 Internat. Geosci. Conf., Abstracts, B1.3 (EAGO/EAGE/SEG).

Kamkar-Rouhani, A., and Das, U. C., 1996a, A new processing technique in reducing (sub)horizontal layering effects in 3-D measurements: 58th Ann. Internat. Mtg., Eur. Assn. Geosci. & Eng., Extended Abstracts, M003.

Kamkar-Rouhani, A., and Das, U. C., 1996b, Surface and borehole resistivity measurements using the two-electrode system in a layered earth: Jakarta '96 Internat. Geophys. Conf., Expanded Abstracts, 34-43 (SEG/EAGE/HAGI).

Kamkar-Rouhani, A., and Das, U. C., 1997, A new method for processing direct current resistivity data to enhance the detection of 3-D subsurface targets: 67th Ann. Internat. Mtg., Soc. Expl. Geophys., Expanded Abstracts, 391-394.

Kamkar-Rouhani, A., and Das, U. C., 1998, Resistivity responses of mineral deposits under a transitional overburden: 60th Ann. Internat. Mtg., Eur. Assn. Geosci. & Eng., Extended Abstracts, P148.

Kaufman, A. A., and Keller, G. V., 1983, Frequency and transient soundings: Elsevier Scientific Publishing Co.

Keller, G. V., and Frischkecht, F. C., 1966, Electrical methods in geophysical prospecting: Pergamon Press Inc.

Kellogg, O. D., 1953, Foundations of potential theory: Dover Publications, Inc.

Kim, H. S., and Lee, K., 1996, Response of a multilayered earth with layers having exponentially varying resistivities: Geophysics, **61**, 180-191.

Koefoed, O., 1979a, Geosounding principles 1, Resistivity sounding measurements: Elsevier Scientific Publishing Co.

Koefoed, O., 1979b, Resistivity sounding on earth model containing transitional layers with linear change of resistivity with depth: Geophys. Prosp., **27**, 862-868.

Koefoed, O., Ghosh, D. P., and Polman, G. J., 1972, Computation of type curves for electromagnetic depth sounding with a horizontal transmitting coil by means of a digital linear filter: Geophys. Prosp., **20**, 406-420.

Lal, T., 1970, Apparent resistivity over a three-layer earth with an inhomogeneous interstratum: Pure and Applied Geophysics, **82**, 259-269.

Lee, T., 1975, An integral equation and its solution for some two and three-dimensional problems in resistivity aqnd induced polarization: Geophys. J. Roy. Astr. Soc., **42**, 81-95.

Lee, T. J., and Ignetik, R., 1994, Transient electromagnetic response of a half-space with exponential conductivity profile and its applications to salinity mapping: Exploration Geophysics, **25**, No. 1, 39-51.

Liu, E. H., and Lamontagne, Y., 1998, Geophysical application of a new surface integral equation method for EM modeling: Geophysics, **63**, 411-423.

Lowry, T., Allen, M. B., and Shive, P. N., 1989, Singularity removal: A refinement of resistivity modeling techniques: Geophysics, **54**, 766-774.

Mallick, K., and Roy, A., 1968, Resistivity sounding on a two-layer earth model with transitional boundary: Geophys. Prosp., **16**, 436-446.

Mooney, H. M., 1980, Handbook of engineering geophysics: Bison Instruments, Inc.

Overmeeren, R. A. van, and Ritsema, I. L., 1988, Continuous vertical electrical sounding: First Break, **6**, No. 10, 313-324.

Patella, D., 1978, Resistivity sounding on a multi-layered earth with transitional layers - Part II: Theoretical and field examples: Geophys. Prosp., **26**, 130-156.

Paul, M. K., and Banerjee, B., 1970, Electrical potentials due to a point source upon models of continuously varying conductivity: Pure and Applied Geophysics, **80**, 218-237.

Pazdirek, O., and Blaha, V., 1996, Examples of resistivity imaging using ME-100 resistivity field acquisition system: 58th Ann. Internat. Mtg., Eur. Assn. Geosci. & Eng., Extended Abstracts, P050.

Pekris, C. L., 1940, Direct method of interpretation in resistivity prospecting: Geophysics, **5**, 31-42.

Press, W. H., Teukolsky, S. A., Vetterling, W. T., and Flannery, B. P., 1992, Numerical recipes in Fortran, The art of scientific computing: Cambridge Univ. Press.

Pridmore, D. F., Hohmann, G. W., Ward, S. H., and Sill, W. R., 1981, An investigation of finite-element modeling for electrical and electromagnetic data in three dimensions: Geophysics, **46**, 1009-1024.

Raiche, A., 1994, Modelling and inversion - Progress, problems, and challenges: Surveys in Geophysics, **15**, 159-207.

Sarkar, T. K., Yang, X., and Arvas, E., 1988, A limited survey of various conjugate gradient methods for solving complex matrix equations arising in electromagnetic wave interactions: Wave Motion, **10**, 527-546.

Schulz, R., 1985, The method of integral equation in the direct current resistivity method and its accuracy: Journal of Geophysics, **56**, 192-200.

Sheriff, R. E., 1991, Encyclopedic dictionary of exploration geophysics: Soc. Expl. Geophys.

Shi, W., and Morgan, D., 1997, Application of electrical resistivity tomography to image Harrison Caves in Barbados, West Indies: 67th Ann. Internat. Mtg., Soc. Expl. Geophys., Expanded Abstracts, 350-353.

Smith, D. L., 1986, Application of the pole-dipole resistivity technique to the detection of solution cavities beneath highways: Geophysics, **51,** 833-837.

Snyder, D. D., 1976, A method for modeling the resistivity and IP response of two-dimensional bodies: Geophysics, **41,** 997-1015.

Spitzer, K., and Wurmstich, B., 1995, Speed and accuracy in 3D resistivity modeling: Proceedings of Internat. Symp. on Three-Dimensional electromagnetics, Schlumberger-Doll Research, 167-180.

Stierman, D. J., and Ruedisili, L. C., 1988, Integrating geophysical and hydrogeological data: An efficient approach to remedial investigations of contaminated ground water, *in* Collins, A. G., and Johnson, A. I., Eds., Ground-water contamination: Field methods: ASTM Special Technical Publication, **963**, 43-57.

Szaraniec, E., 1980, Direct resistivity interpretation by accumulation of layers: Geophys. Prosp., **28**, 257-268.

Unz, M., 1968, Vertical profiling over a medium of continuously varying resistivity: Geophys. Prosp., **16**, 427-435.

Van Nostrand, R. G., and Cook, K. L., 1966, Interpretation of resistivity data: U.S. Geol. Survey, Prof. Paper 499.

Vogelsang, D., 1995, Environmental geophysics: Springer-Verlag.

Wait, J. R., 1982, Geo-electromagnetism: Academic Press, Inc.

Ward, S. H., 1980, History of geophysical exploration – Electrical, electromagnetic, and magnetotelluric methods: Geophysics, **45**, 1659-1666.

Ward, S. H., 1990, Resistivity and induced polarization methods, *in* Ward, S. H., Ed., Geotechnical and environmental geophysics: Soc. Explor. Geophys., **1**, 147-189.

Watson, G. N., 1958, A treatise on the theory of Bessel functions: Cambridge Univ. Press.

White, P. A., 1994, Electrode arrays for measuring groundwater flow direction and velocity: Geophysics, **59**, 192-201.

Xu, S. Z., Gao, Z. C., and Zhao, S. K., 1988, An integral formulation for three-dimensional terrain modeling for resistivity surveys: Geophysics, **53**, 546-552.

Zhao, S., and Yedlin, M. J., 1996a, Multi-domain chebyshev spectral method for 3-D dc resistivity modeling: Geophysics, **61**, 1616-1623.

Zhao, S., and Yedlin, M. J., 1996b, Some refinements on the finite-difference method for 3-D dc resistivity modeling: Geophysics, **61**, 1301-1307.

Zhdanov, M. S., and Keller, G. V., 1994, The geoelectrical methods in geophysical exploration: Elsevier Scientific Publishing Co.

Zohdy, A. A. R., 1989, A new method for the automatic interpretation of Schlumberger and Wenner sounding curves: Geophysics, **54**, 245-253.

APPENDICES

Appendix A

SPECTRAL FORMALISM AND ITS USE IN GREEN'S FUNCTIONS COMPUTATIONS

In this Appendix, first we present a review of the spectral formalism for computing the electrical potential due to a direct current source in a layered earth, and then, we apply this formalism to computation of various Green's functions used in the research work.

A.1 Spectral formalism

We consider a piece-wise homogeneous layered earth as shown in Figure A.1. The layered earth consists of an upper half-space D(0) in which $-\infty < z < z(1)$, a stack of (ND-1) layers D(ID) [where ID=1, 2, ..., ND-1] in which $z(ID) < z < z(ID+1)$, and a lower half-space D(ND) in which $z(ID) < z < \infty$. The conductivity D(ID) is shown by $\sigma(ID)$ [where ID=0, 1, 2, ..., ND-1, ND]. In a circularly cylindrical coordinate system, the layered earth electric potential V due to a direct current electric source is represented as the inverse Fourier-Bessel integral

$$V(r,z) = \frac{1}{2\pi}\int_0^\infty \tilde{V}(\lambda,z) J_0(\lambda r)\lambda d\lambda\,, \tag{A.1}$$

in which, in any homogeneous and source-free domain, $\tilde{V} = \tilde{V}(\lambda, z)$ has to satisfy the following differential equation:

$$\partial_z^2 \tilde{V} - \lambda^2 \tilde{V} = 0\,. \tag{A.2}$$

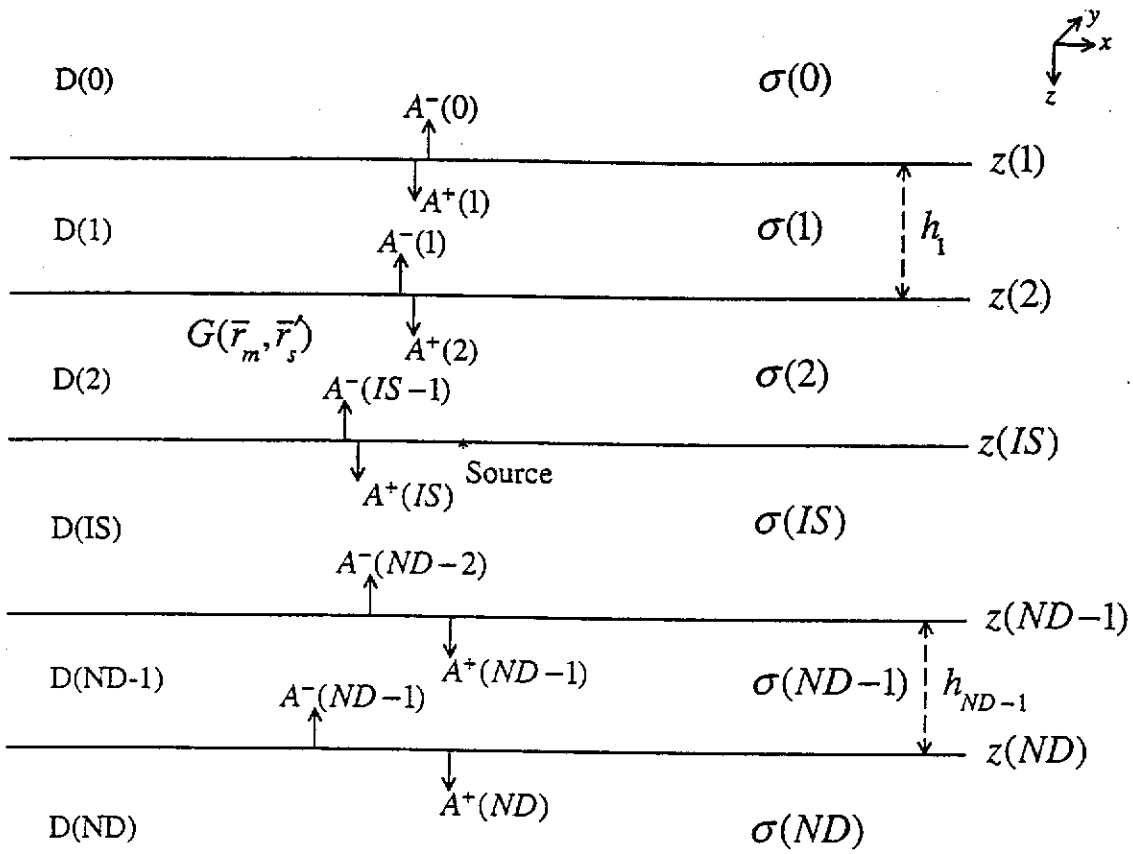

Figure A.1. A layered earth with a buried point electric source. Each layer is a domain D(ID) where ID = 0, 1, ..., ND-1, ND. Two adjacent domains D(ID) and D(ID+1) are separated by interface z(ID+1). The thickness for domain D(ID) is shown by h_{ID}.

where ∂_z denotes differentiation with respect to z. In equation (A.1), J_0 is the Bessel function of the first kind and order zero. The vertical component of the volume density of electric current J_z is expressed as

$$J_z = -\sigma \partial_z V . \tag{A.3}$$

The expression for $\tilde{V}$, and correspondingly for $\tilde{J}_z$ (defined by $\tilde{J}_z = -\sigma \partial_z \tilde{V}$) in a domain $D(ID)$ [Figure A.1] can be written in the following form (omitting the variable λ and including the domain indication ID in the argument list of $\tilde{V}$):

$$\tilde{V}(ID,z) = A^+(ID)e^{-\lambda(z-z(ID))} + A^-(ID)e^{-\lambda(z(ID+1)-z)},$$
$$\text{for } z(ID) < z < z(ID+1); \quad ID = 1,\ldots,ND-1 , \tag{A.4}$$

$$\tilde{J}_z(ID,z) = \lambda\sigma(ID)[A^+(ID)e^{-\lambda(z-z(ID))} - A^-(ID)e^{-\lambda(z(ID+1)-z)}] ,$$
$$\text{for } z(ID) < z < z(ID+1); \quad ID = 1,\ldots,ND-1 . \tag{A.5}$$

The coefficients A^+ and A^- are to be determined from the jump condition at source level and the boundary conditions at the interface levels. In the two outer half-spaces $A^+(0) = 0$ and $A^-(ND) = 0$. Thus, in the upper half-space, we have

$$\tilde{V}(0,z) = A^-(0)e^{-\lambda(z(1)-z)} \qquad \text{for } -\infty < z < z(1), \tag{A.6}$$

$$\tilde{J}_z(0,z) = -\lambda\sigma(0)A^-(0)e^{-\lambda(z(1)-z)} \qquad \text{for } -\infty < z < z(1), \tag{A.7}$$

and in the lower half-space,

$$\tilde{V}(ND,z) = A^+(ND)e^{-\lambda(z-z(ND))} \qquad \text{for } z(ND) < z < \infty, \tag{A.8}$$

$$\tilde{J}_z(ND,z) = \lambda\sigma(ND)A^+(ND)e^{-\lambda(z-z(ND))} \qquad \text{for } z(ND) < z < \infty . \tag{A.9}$$

Note that the exponential functions in equations (A.4) to (A.9) have been chosen such that their arguments are nonpositive. The problem for computing the electric potential at an arbitrary depth is the coefficients A^+ and A^-. To obtain these coefficients, we use a recurrence scheme (explained in the following). Using the electric potential $\tilde{V}$ and vertical volume density of electric current $\tilde{J}_z$, we define an input admittance at an arbitrary level z [up to the source level *z(IS)*] as (omitting the domain indication):

$$Y^-(z) = -\frac{\tilde{J}_z(z)}{\tilde{V}(z)} \qquad \text{for} \quad -\infty < z \le z(IS), \tag{A.10}$$

$$Y^+(z) = \frac{\tilde{J}_z(z)}{\tilde{V}(z)} \qquad \text{for} \quad z(IS) \le z < \infty. \tag{A.11}$$

Using Y^- and Y^+ in the following recurrence scheme, we can directly determine the electric potential, uniquely, from the input admittances at the source level. The electric potential, in turn, leads to the computation of the coefficients on the source level. Starting from these known coefficients at the source level, we can easily obtain the coefficients at other interfaces (as discussed below). Before dealing with the recurrence scheme, we present the following boundary conditions, which are mainly used.

Boundary conditions

In the spectral formalism to develop the computational scheme, we introduce a possibly fictitious horizontal interface at the source level, *z(IS)*, where the point source of current injection or extraction of magnitude *I(IS)* is located. For this type of excitation, the electric potential is continuous across the interfaces, while the vertical component of the volume density of electric current makes a nonzero jump at the source interface. Thus, we have

$$\lim_{z \downarrow z(ID)} \tilde{V}(ID,z) = \lim_{z \uparrow z(ID)} \tilde{V}(ID-1,z) \qquad \text{for } ID = 1,2,...,IS,...,ND, \qquad \text{(A.12)}$$

and

$$\lim_{z \downarrow z(ID)} \tilde{J}_z(ID,z) - \lim_{z \uparrow z(ID)} \tilde{J}_z(ID-1,z) = I(ID)\delta(ID,IS)$$

$$\text{for } ID = 1,2,...,IS,...,ND, \quad \text{(A.13)}$$

where

$$\delta(ID,IS) = \begin{cases} 0 & \text{if ID} \neq IS \\ 1 & \text{if ID} = IS \end{cases}. \qquad \text{(A.14)}$$

Introducing these boundary conditions given by equations (A.12) and (A.13), we note that the admittances $Y^-(z)$ and $Y^+(z)$ are continuous across any source-free interface.

From equations (A.4) to (A.7) and equation (A.10), we obtain the admittances at two consecutive interfaces *z(ID)* and *z(ID+1)* of any layer above and including the source level in terms of the coefficients $A^+(ID)$ and $A^-(ID)$, i.e.

$$Y^-(z(ID)) = -\lambda\sigma(ID)\frac{A^+(ID) - A^-(ID)e^{-\lambda h(ID))}}{A^+(ID) + A^-(ID)e^{-\lambda h(ID))}} \qquad \text{for } ID = 1,2,...,IS-1, \quad \text{(A.15)}$$

and

$$Y^-(z(ID+1)) = -\lambda\sigma(ID)\frac{A^+(ID)e^{-\lambda h(ID))} - A^-(ID)}{A^+(ID)e^{-\lambda h(ID))} + A^-(ID)} \quad \text{for } ID = 1,2,...,IS-1. \quad \text{(A.16)}$$

Here, $h(ID) = h_{ID}$ is the thickness of the layer *D(ID)*. Also, from equations (A.6), (A.7) and (A.10), we obtain the admittance at any level above the uppermost interface, i.e.

$$Y^{-}(z) = \lambda\sigma(0) \quad \text{for} \quad -\infty < z < z(1). \tag{A.17}$$

In particular, the admittance at the uppermost interface *z(1)* is

$$Y^{-}(z(1)) = \lambda\sigma(0). \tag{A.18}$$

Similarly, the admittance at any level below the lowermost interface *z(ND)* is obtained using equations (A.8), (A.9) and (A.11) as

$$Y^{+}(z) = \lambda\sigma(ND) \quad \text{for} \quad z(ND) < z < \infty. \tag{A.19}$$

In particular, the admittance at the lowermost interface *z(ND)* is

$$Y^{+}(z(ND)) = \lambda\sigma(ND). \tag{A.20}$$

A relationship between the coefficients of the interfaces enclosing a domain *D(ID)* is obtained from equation (A.15) as

$$A^{+}(ID) = \Gamma^{-}(ID)A^{-}(ID)e^{-\lambda h(ID)}, \tag{A.21}$$

where

$$\Gamma^{-}(ID) = \frac{\lambda\sigma(ID) - Y^{-}(z(ID))}{\lambda\sigma(ID) + Y^{-}(z(ID))}, \tag{A.22}$$

$$\text{for} \quad ID = 1, 2, ..., IS - 1.$$

Substituting equation (A.21) in equation (A.16), we obtain the following recurrence relation:

$$Y^{-}(z(ID+1)) = \lambda\sigma(ID)\frac{1-\Gamma^{-}(ID)e^{-2\lambda h(ID)}}{1+\Gamma^{-}(ID)e^{-2\lambda h(ID)}}, \quad \text{for} \quad ID = 1, 2, ..., IS-1. \quad \text{(A.23)}$$

Similarly, the admittances at two consecutive interfaces *z(ID)* and *z(ID+1)* of any layer below and including the source level in terms of the coefficients $A^{+}(ID)$ and $A^{-}(ID)$ are

$$Y^{+}(z(ID)) = \lambda\sigma(ID)\frac{A^{+}(ID)-A^{-}(ID)e^{-\lambda h(ID))}}{A^{+}(ID)+A^{-}(ID)e^{-\lambda h(ID))}}, \quad \text{(A.24)}$$

$$Y^{+}(z(ID+1)) = \lambda\sigma(ID)\frac{A^{+}(ID)e^{-\lambda h(ID))}-A^{-}(ID)}{A^{+}(ID)e^{-\lambda h(ID))}+A^{-}(ID)}, \quad \text{(A.25)}$$

$$\text{for } ID = IS, IS-1, ..., ND-1.$$

From equation (A.25), we obtain

$$A^{-}(ID) = \Gamma^{+}(ID)A^{+}(ID)e^{-\lambda h(ID)}, \quad \text{(A.26)}$$

where

$$\Gamma^{+}(ID) = \frac{\lambda\sigma(ID)-Y^{+}(z(ID+1))}{\lambda\sigma(ID)+Y^{+}(z(ID+1))}, \quad \text{(A.27)}$$

$$\text{for } ID = ND-1, ..., IS-1, IS.$$

Substituting equation (A.26) in equation (A.24), we obtain the following recurrence relation:

$$Y^{+}(z(ID)) = \lambda\sigma(ID)\frac{1-\Gamma^{+}(ID)e^{-2\lambda h(ID)}}{1+\Gamma^{+}(ID)e^{-2\lambda h(ID)}},$$

$$\text{for } ID = ND-1,...,IS-1,IS\,. \qquad \text{(A.28)}$$

Starting with the known initial values of $Y^{-}(z(1))$ and $Y^{+}(z(ND))$ given by equations (A.18) and (A.20), we use the equations (A.23) and (A.28) to obtain $Y^{-}(z(IS))$ and $Y^{+}(z(IS))$ at the source level, and then using equations (A.10) to (A.13) we obtain the potential at the source level as

$$\tilde{V}(z(IS)) = \frac{I(IS)}{Y^{-}(z(IS)) + Y^{+}(z(IS))}. \qquad \text{(A.29)}$$

We can write the following expressions using equations (A.4), (A.5) and (A.10) for *ID=IS-1*:

$$\tilde{V}(z(IS)) = A^{+}(IS-1)e^{-\lambda h(IS-1)} + A^{-}(IS-1)\,, \qquad \text{(A.30)}$$

$$Y^{-}(z(IS))\tilde{V}(z(IS)) = \lambda\sigma(IS-1)A^{-}(IS-1) - \lambda\sigma(IS-1)A^{+}(IS-1)e^{-\lambda h(IS-1)}\,. \qquad \text{(A.31)}$$

Similarly, using (A.4), (A.5) and (A.11) for *ID=IS*, we obtain

$$\tilde{V}(z(IS)) = A^{+}(IS) + A^{-}(IS)e^{-\lambda h(IS)}\,, \qquad \text{(A.32)}$$

$$Y^{+}(z(IS))\tilde{V}(z(IS)) = \lambda\sigma(IS)A^{+}(IS) - \lambda\sigma(IS)A^{-}(IS)e^{-\lambda h(IS)}\,. \qquad \text{(A.33)}$$

Solving equations (A.30) and (A.31) for $A^{-}(IS-1)$, we obtain

$$A^{-}(IS-1) = \tilde{V}(z(IS))\frac{\lambda\sigma(IS-1) + Y^{-}(z(IS))}{2\lambda\sigma(IS-1)}\,. \qquad \text{(A.34)}$$

Substituting equation (A.29) in equation (A.34), we obtain the coefficient $A^{-}(IS-1)$ as

$$A^{-}(IS-1)=\frac{I(IS)}{2\lambda\sigma(IS-1)}\frac{\lambda\sigma(IS-1)+Y^{-}(z(IS))}{Y^{-}(z(IS))+Y^{+}(z(IS))}. \tag{A.35}$$

Similarly, solving equations (A.32) and (A.33) for $A^{+}(IS)$, and using equation (A.29) yields

$$A^{+}(IS)=\frac{I(IS)}{2\lambda\sigma(IS)}\frac{\lambda\sigma(IS)+Y^{+}(z(IS))}{Y^{-}(z(IS))+Y^{+}(z(IS))}. \tag{A.36}$$

Now, having the coefficients $A^{-}(IS-1)$ and $A^{+}(IS)$ at the source level, we can obtain the coefficients at all the interfaces. Using equation (A.4), and the boundary condition given in equation (A.12), we can write

$$A^{+}(ID)+A^{-}(ID)e^{-\lambda h(ID)}=A^{+}(ID-1)e^{-\lambda h(ID-1)}+A^{-}(ID-1). \tag{A.37}$$

Substituting equation (A.21) in equation (A.37), we obtain

$$A^{-}(ID-1)=\frac{1+\Gamma^{-}(ID)}{1+\Gamma^{-}(ID-1)e^{-2\lambda h(ID-1)}}A^{-}(ID)e^{-\lambda h(ID)},$$

$$\text{for } ID=IS-1,\ldots,1. \tag{A.38}$$

Here, for convenience, we repeat equation (A.21):

$$A^{+}(ID)=\Gamma^{-}(ID)A^{-}(ID)e^{-\lambda h(ID)} \qquad \text{for } ID=IS-1,\ldots,1. \tag{A.39}$$

The left-hand sides of equations (A.38) and (A.39) are the coefficients on either side of an interface in terms the coefficient below it. Thus, having the known coefficient $A^{-}(IS-1)$ at the source level from equation (A.35), we can obtain all the coefficients at the interfaces above the source level by repeated use of equations (A.38) and (A.39).

Similarly, substituting equation (A.26) in equation (A.37) yields

$$A^{+}(ID+1)=\frac{1+\Gamma^{+}(ID)}{1+\Gamma^{+}(ID+1)e^{-2\lambda h(ID+1)}}A^{+}(ID)e^{-\lambda h(ID)}$$

$$\text{for } ID=IS,\ldots,ND-1. \qquad \text{(A.40)}$$

Repeating equation (A.26) for convenience,

$$A^{-}(ID)=\Gamma^{+}(ID)A^{+}(ID)e^{-\lambda h(ID)} \qquad \text{for } ID=IS,\ldots,ND-1. \qquad \text{(A.41)}$$

In this case, the left-hand sides of equations (A.40) and (A.41) are the coefficients on either side of an interface in terms the coefficient above it. Thus, having the known coefficient $A^{+}(IS)$ at the source level from equation (A.36), we can obtain all the coefficients at the interfaces below the source level by repeated use of equations (A.40) and (A.41). Knowing the coefficients at the interfaces, we use equations (A.1) and (A.4) to compute the potential at any point (excluding the source point) in the layered earth.

A.2 Application of spectral formalism for computations of Green's functions

Using the spectral formalism, we can obtain a Green's function since it represents an electric potential at a point due to a current point source. Here, expressions for different Green's functions for a two-layered earth, shown in Figure 2.5, are obtained. We use the suffixes *ab*, which indicate computation of the electric potential at *a* due to a unit current at *b*. For the Green's function $G(\bar{r}_p,\bar{r}_s')$, which represents the potential at the potential point $\bar{r}_p$ due to the unit current source at $\bar{r}_s'$ on the surface of the layered earth, we write using equations (A.1) and (A.4)

$$G(\bar{r}_p,\bar{r}_s') = \frac{1}{2\pi}\int_0^\infty [A_{ps}^+(1)e^{-\lambda(z_p - z(1))} + A_{ps}^-(1)e^{-\lambda(z(2)-z_p)}]J_0(\lambda r_p)\lambda d\lambda . \qquad (A.42)$$

Considering Figure 2.6, the field point at $\bar{r}_p$ is located on the surface where $z_p = z(1)$, and also we have $z(2) - z_p = h_1$ where h_1 is the thickness of the first layer. Thus, we can write equation (A.42) for this case as

$$G(\bar{r}_p,\bar{r}_s') = \frac{1}{2\pi}\int_0^\infty [A_{ps}^+(1) + A_{ps}^-(1)e^{-\lambda h_1}]J_0(\lambda r_p)\lambda d\lambda , \qquad (A.43)$$

For obtaining the coefficients $A_{ps}^+(1)$ and $A_{ps}^-(1)$, we use the relevant equations mentioned above. Using equation (A.41), we have

$$A_{ps}^-(1) = \Gamma_{ps}^+(1)A_{ps}^+(1)e^{-\lambda h_1}, \qquad (A.44)$$

and from equation (A.27) $\Gamma_{ps}^+(1)$ is obtained as

$$\Gamma_{ps}^+(1) = \frac{\lambda\sigma_1 - Y_{ps}^+(z(2))}{\lambda\sigma_1 + Y_{ps}^+(z(2))}, \qquad (A.45)$$

and using equation (A.20),

$$Y_{ps}^+(z(2)) = \lambda\sigma_H . \qquad (A.46)$$

Substituting equation (A.46) in equation (A.45), we obtain

$$\Gamma_{ps}^+(1) = \frac{\sigma_1 - \sigma_H}{\sigma_1 + \sigma_H}. \qquad (A.47)$$

$A_{ps}^+(1)$ is obtained using equation (A.36) as

$$A_{ps}^{+}(1)=\frac{I(1)}{2\lambda\sigma_1}\frac{\lambda\sigma_1+Y_{ps}^{+}(z(1))}{Y_{ps}^{-}(z(1))+Y_{ps}^{+}(z(1))}, \tag{A.48}$$

where $I(1)=I$ is the current injected into ground from the surface (source level), and the input admittances at the source level $Y_{ps}^{-}(z(1))$ and $Y_{ps}^{+}(z(1))$ are obtained using equations (A.18) and (A.28), respectively, i.e.

$$Y_{ps}^{-}(z(1))=\lambda\sigma_0, \tag{A.49}$$

and

$$Y_{ps}^{+}(z(1))=\lambda\sigma_1\frac{1-\Gamma_{ps}^{+}(1)e^{-2\lambda h_1}}{1+\Gamma_{ps}^{+}(1)e^{-2\lambda h_1}}. \tag{A.50}$$

Substituting equation (A.47) in equation (A.50), we obtain

$$Y_{ps}^{+}(z(1))=\lambda\sigma_1\frac{1-k_1e^{-2\lambda h_1}}{1+k_1e^{-2\lambda h_1}}, \tag{A.51}$$

where k_1 is defined as

$$k_1=\frac{\sigma_1-\sigma_H}{\sigma_1+\sigma_H}. \tag{A.52}$$

Substituting equations (A.49) and (A.51) in equation (A.48) yields

$$A_{ps}^{+}(1)=\frac{I}{2\lambda\sigma_1}\frac{\lambda\sigma_1+\lambda\sigma_1\dfrac{1-k_1e^{-2\lambda h_1}}{1+k_1e^{-2\lambda h_1}}}{\lambda\sigma_0+\lambda\sigma_1\dfrac{1-k_1e^{-2\lambda h_1}}{1+k_1e^{-2\lambda h_1}}}. \tag{A.53}$$

After simplification, we obtain equation (A.53) in the following form:

$$A_{ps}^{+}(1)=\frac{I}{\lambda}\frac{1}{\sigma_0(1+k_1e^{-2\lambda h_1})+\sigma_1(1-k_1e^{-2\lambda h_1})}. \tag{A.54}$$

From equations (A.42), (A.45), (A.50), and (A.52), we also obtain the coefficient $A_{ps}^{-}(1)$ as

$$A_{ps}^{-}(1)=\frac{I}{\lambda}\frac{k_1e^{-\lambda h_1}}{\sigma_0(1+k_1e^{-2\lambda h_1})+\sigma_1(1-k_1e^{-2\lambda h_1})}. \tag{A.55}$$

Substituting equations (A.54) and (A.55) in equation (A.43) yields

$$G(\bar{r}_p,\bar{r}_s')=\frac{I}{2\pi}\int_0^{\infty}\frac{(1+k_1e^{-2\lambda h_1})}{\sigma_0(1+k_1e^{-2\lambda h_1})+\sigma_1(1-k_1e^{-2\lambda h_1})}J_0(\lambda r_p)d\lambda. \tag{A.56}$$

Considering that the uppermost medium above the earth's surface is air, we have $\sigma_0=0$. Thus, for this case equation (A.56) is written as

$$G(\bar{r}_p,\bar{r}_s')=\frac{I}{2\pi\sigma_1}\int_0^{\infty}\frac{1+k_1e^{-2\lambda h_1}}{1-k_1e^{-2\lambda h_1}}J_0(\lambda r_p)d\lambda. \tag{A.57}$$

Using equations (A.1) and (A.4), we can write the expression for the Green's function $G(\bar{r}_m,\bar{r}_s')$, shown in Figure 2.6, as

$$G(\bar{r}_m,\bar{r}_s')=\frac{1}{2\pi}\int_0^{\infty}A_{ms}^{+}(2)e^{-\lambda(z_m-z(2))}J_0(\lambda r_m)\lambda d\lambda. \tag{A.58}$$

Considering Figure 2.6, we have $z(2)=z_s'+h_1$ where z_s' is the depth to the current point source at r_s'. Thus, we can write equation (A.58) in the following form:

$$G(\bar{r}_m,\bar{r}_s')=\frac{1}{2\pi}\int_0^{\infty}A_{ms}^{+}(2)e^{-\lambda(z_m-z_s'-h_1)}J_0(\lambda r_m)\lambda d\lambda. \tag{A.59}$$

In this case, using equation (A.40), we write

$$A_{ms}^{+}(2)=\frac{1+\Gamma_{ms}^{+}(1)}{1+\Gamma_{ms}^{+}(2)e^{-2\lambda h(2)}}A_{ms}^{+}(1)e^{-\lambda h_1}. \tag{A.60}$$

We know $h(2)=\infty$ (Figure 2.6), thus equation (A.60) can be written as

$$A_{ms}^{+}(2)=[1+\Gamma_{ms}^{+}(1)]A_{ms}^{+}(1)e^{-\lambda h_1}. \tag{A.61}$$

Also, using equation (A.36), we write

$$A_{ms}^{+}(1)=\frac{I}{2\lambda\sigma_1}\frac{\lambda\sigma_1+Y_{ms}^{+}(z(1))}{Y_{ms}^{-}(z(1))+Y_{ms}^{+}(z(1))}. \tag{A.62}$$

From equations (A.18) and (A.28) the input admittance at the source level $Y_{ms}^{-}(z(1))$ and $Y_{ms}^{+}(z(1))$ are obtained as

$$Y_{ms}^{-}(z(1))=\lambda\sigma_0, \tag{A.63}$$

and

$$Y_{ms}^{+}(z(1))=\lambda\sigma_1\frac{1-\Gamma_{ms}^{+}(1)e^{-2\lambda h_1}}{1+\Gamma_{ms}^{+}(1)e^{-2\lambda h_1}}, \tag{A.64}$$

respectively. From equation (A.27), we obtain $\Gamma_{ms}^{+}(1)$ as

$$\Gamma_{ms}^{+}(1)=\frac{\lambda\sigma_1-Y_{ms}^{+}(z(2))}{\lambda\sigma_1+Y_{ms}^{+}(z(2))}, \tag{A.65}$$

and using equation (A.20),

$$Y_{ms}^{+}(z(2)) = \lambda\sigma_H \,. \tag{A.66}$$

Substituting equation (A.66) in equation (A.65), we obtain

$$\Gamma_{ms}^{+}(1) = \frac{\sigma_1 - \sigma_H}{\sigma_1 + \sigma_H} = k_1 \,. \tag{A.67}$$

Substituting equation (A.67) in equation (A.64), we obtain

$$Y_{ms}^{+}(z(1)) = \lambda\sigma_1 \frac{1 - k_1 e^{-2\lambda h_1}}{1 + k_1 e^{-2\lambda h_1}} \,. \tag{A.68}$$

Equations (A.62), (A.63), and (A.68) yield

$$A_{ms}^{+}(1) = \frac{I}{\lambda} \frac{1}{\sigma_0(1 + k_1 e^{-2\lambda h_1}) + \sigma_1(1 - k_1 e^{-2\lambda h_1})} \,. \tag{A.69}$$

From equations (A.61), (A.67), and (A.69), we obtain

$$A_{ms}^{+}(2) = \frac{I}{\lambda} \frac{(1 + k_1) e^{-\lambda h_1}}{\sigma_0(1 + k_1 e^{-2\lambda h_1}) + \sigma_1(1 - k_1 e^{-2\lambda h_1})} \,. \tag{A.70}$$

Substituting equation (A.70) in equation (A.59), we obtain the expression for the Green's function $G(\bar{r}_m, \bar{r}_s')$ as

$$G(\bar{r}_m, \bar{r}_s') = \frac{I}{2\pi} \int_0^{\infty} \frac{(1 + k_1) e^{-\lambda(z_m - z_s')}}{\sigma_0(1 + k_1 e^{-2\lambda h_1}) + \sigma_1(1 - k_1 e^{-2\lambda h_1})} J_0(\lambda r_m) d\lambda \,. \tag{A.71}$$

Since the uppermost medium above the earth's surface is air, ie, we have $\sigma_0 = 0$. Thus, we can write equation (A.71) for this case as

$$G(\bar{r}_m,\bar{r}_s') = \frac{I}{2\pi\sigma_1}\int_0^\infty \frac{(1+k_1)e^{-\lambda(z_m-z_s')}}{1-k_1e^{-2\lambda h_1}} J_0(\lambda r_m)d\lambda . \tag{A.72}$$

Considering equations (A.1) and (A.4, the Green's function $G(\bar{r}_p,\bar{r}_n')$, shown in Figure 2.7, is of the same form as $G(\bar{r}_p,\bar{r}_s')$ but having different coefficients. Thus, we have

$$G(\bar{r}_p,\bar{r}_n') = \frac{1}{2\pi}\int_0^\infty [A_{pn}^+(1)+A_{pn}^-(1)e^{-\lambda h_1}]J_0(\lambda r_p)\lambda d\lambda . \tag{A.73}$$

In this case, using equation (A.38) we have

$$A_{pn}^-(1) = \frac{1+\Gamma_{pn}^-(2)}{1+\Gamma_{pn}^-(1)e^{-2\lambda h_1}} A_{pn}^-(2)e^{-\lambda h(2)}, \tag{A.74}$$

where $h(2) = z_n' - z(2)$ is the thickness of a part of the second layer, which is above the source level or source cell, and $z_n' = z'(n)$ is the depth of source element (Figure 2.7). Also, $z(2) = z_p + h_1$, thus $h(2) = z_n' - z_p - h_1$. Hence, equation (A.74) can be written in the following form

$$A_{pn}^-(1) = \frac{1+\Gamma_{pn}^-(2)}{1+\Gamma_{pn}^-(1)e^{-2\lambda h_1}} A_{pn}^-(2)e^{-\lambda(z_n'-z_p-h_1)}. \tag{A.75}$$

Also, using equation (A.39), we can write

$$A_{pn}^+(1) = \Gamma_{pn}^-(1)A_{pn}^-(1)e^{-\lambda h_1}, \tag{A.76}$$

and using equation (A.35), we have

$$A_{pn}^-(2) = \frac{I}{2\lambda\sigma_H}\frac{\lambda\sigma_H + Y_{pn}^-(z'(n))}{Y_{pn}^-(z'(n))+Y_{pn}^+(z'(n))}. \tag{A.77}$$

The input admittance $Y_{pn}^{+}(z'(n))$ and $Y_{pn}^{-}(z'(n))$, considering equations (A.20) and (A.23), are obtained, respectively, as

$$Y_{pn}^{+}(z'(n)) = \lambda\sigma_H , \tag{A.78}$$

and

$$Y_{pn}^{-}(z'(n)) = \lambda\sigma_H \frac{1-\Gamma_{pn}^{-}(2)e^{-2\lambda(z_n'-z(2))}}{1+\Gamma_{pn}^{-}(2)e^{-2\lambda(z_n'-z(2))}}. \tag{A.79}$$

Using equation (A.22), $\Gamma_{pn}^{-}(2)$ is obtained as

$$\Gamma_{pn}^{-}(2) = \frac{\lambda\sigma_H - Y_{pn}^{-}(z(2))}{\lambda\sigma_H + Y_{pn}^{-}(z(2))}, \tag{A.80}$$

where $Y_{pn}^{-}(z(2))$ is given from equation (A.23) as

$$Y_{pn}^{-}(z(2)) = \lambda\sigma_1 \frac{1-\Gamma_{pn}^{-}(1)e^{-2\lambda h_1}}{1+\Gamma_{pn}^{-}(1)e^{-2\lambda h_1}}. \tag{A.81}$$

Using equation (A.22), we obtain

$$\Gamma_{pn}^{-}(1) = \frac{\lambda\sigma_1 - Y_{pn}^{-}(z(1))}{\lambda\sigma_1 + Y_{pn}^{-}(z(1))}, \tag{A.82}$$

where from equation (A.18), we have $Y_{pn}^{-}(z(1)) = \lambda\sigma_0$. Thus, we obtain

$$\Gamma_{pn}^{-}(1) = \frac{\sigma_1 - \sigma_0}{\sigma_1 + \sigma_0}, \tag{A.83}$$

$$Y_{pn}^{-}(z(2)) = \lambda\sigma_1 \frac{1-\frac{\sigma_1-\sigma_0}{\sigma_1+\sigma_0}e^{-2\lambda h_1}}{1+\frac{\sigma_1-\sigma_0}{\sigma_1+\sigma_0}e^{-2\lambda h_1}}, \tag{A.84}$$

and then

$$\Gamma_{pn}^{-}(2) = \frac{-k_1+\frac{\sigma_1-\sigma_0}{\sigma_1+\sigma_0}e^{-2\lambda h_1}}{1-k_1\frac{\sigma_1-\sigma_0}{\sigma_1+\sigma_0}e^{-2\lambda h_1}}. \tag{A.85}$$

Substituting equation (A.85) in equation (A.79) yields [considering $z(2) = z_p + h_1$]

$$Y_{pn}^{-}(z'(n)) = \lambda\sigma_H \frac{(1-k_1\frac{\sigma_1-\sigma_0}{\sigma_1+\sigma_0}e^{-2\lambda h_1}) - e^{-2\lambda(z_n'-z_p-h_1)}(\frac{\sigma_1-\sigma_0}{\sigma_1+\sigma_0}e^{-2\lambda h_1}-k_1)}{(1-k_1\frac{\sigma_1-\sigma_0}{\sigma_1+\sigma_0}e^{-2\lambda h_1}) + e^{-2\lambda(z_n'-z_p-h_1)}(\frac{\sigma_1-\sigma_0}{\sigma_1+\sigma_0}e^{-2\lambda h_1}-k_1)}. \tag{A.86}$$

From equations (A.77), (A.78) and (A.86), we obtain

$$A_{pn}^{-}(2) = \frac{I}{2\lambda\sigma_H}. \tag{A.87}$$

Also, from equations (A.75), (A.83), (A.85) and (A.87), we obtain

$$A_{pn}^{-}(1) = \frac{I}{2\lambda\sigma_H}\frac{(1-k_1)e^{-\lambda(z_n'-z_p-h_1)}}{1-k_1\frac{\sigma_1-\sigma_0}{\sigma_1+\sigma_0}e^{-2\lambda h_1}}, \tag{A.88}$$

and then, substituting equations (A.83) and (A.88) in equation (A.76) yields

$$A_{pn}^{+}(1)=\frac{I}{2\lambda\sigma_H}\frac{(1-k_1)\dfrac{\sigma_1-\sigma_0}{\sigma_1+\sigma_0}e^{-\lambda(z_n'-z_p)}}{1-k_1\dfrac{\sigma_1-\sigma_0}{\sigma_1+\sigma_0}e^{-2\lambda h_1}}. \tag{A.89}$$

From equations (A.73), (A.88) and (A.89) we get

$$G(\bar{r}_p,\bar{r}_n')=\frac{I}{4\pi\sigma_H}\int_0^{\infty}\frac{(1-k_1)\dfrac{2\sigma_1}{\sigma_1+\sigma_0}e^{-\lambda(z_n'-z_p)}}{1-k_1\dfrac{\sigma_1-\sigma_0}{\sigma_1+\sigma_0}e^{-2\lambda h_1}}J_0(\lambda r_p)d\lambda. \tag{A.90}$$

Considering that the uppermost medium above the earth's surface is air, ie, $\sigma_0=0$, we can write equation (A.90) for this case as

$$G(\bar{r}_p,\bar{r}_n')=\frac{I}{4\pi\sigma_H}\int_0^{\infty}\frac{(1-k_1)2e^{-\lambda(z_n'-z_p)}}{1-k_1e^{-2\lambda h_1}}J_0(\lambda r_p)d\lambda. \tag{A.91}$$

To obtain the Green's function $G(\bar{r}_m,\bar{r}_n')$, we consider Figure 2.7, in which both the field point $\bar{r}_m$ and the source at $\bar{r}_n'$, are located in the lower half-space of a two-layered earth. As shown in Figure 2.7, three depth locations of the field point $\bar{r}_m$ above, at the same level, and below the source element are considered. The Green's functions $G(\bar{r}_m,\bar{r}_n')$ corresponding to these locations are

$$G(\bar{r}_m,\bar{r}_n')=\frac{1}{2\pi}\int_0^{\infty}[A_{mn}^{+}(2)e^{-\lambda(z_m-z(2))}+A_{mn}^{-}(2)e^{-\lambda(z_n'-z_m)}]J_0(\lambda r_m)\lambda d\lambda \quad \text{for} \quad z_m<z_n', \tag{A.92}$$

or

$$G(\bar{r}_m,\bar{r}_n')=\frac{1}{2\pi}\int_0^{\infty}A_{mn}^{+}(n)e^{-\lambda(z_m-z_n')}J_0(\lambda r_m)\lambda d\lambda \quad \text{for} \quad z_m\geq z_n', \tag{A.93}$$

where z_m is the depth to the field point $\bar{r}_m$ and z_n' is the depth to the source element (Figure 2.7). In the case that the field point is located above the source element, the Green's function $G(\bar{r}_m, \bar{r}_n')$ is expressed by equation (A.92). In this case, the coefficients $A_{mn}^{-}(2)$ and $A_{mn}^{+}(2)$ are determined using equations (A.35) and (A.39). Thus, we obtain

$$A_{mn}^{-}(2) = \frac{I}{2\lambda\sigma_H} \frac{\lambda\sigma_H + Y_{mn}^{-}(z'(n))}{Y_{mn}^{-}(z'(n)) + Y_{mn}^{+}(z'(n))}, \tag{A.94}$$

and

$$A_{mn}^{+}(2) = \Gamma_{mn}^{-}(2) A_{mn}^{-}(2) e^{-\lambda h(2)}, \tag{A.95}$$

where $h(2) = z_n' - z(2)$ (Figure 2.7), thus equation (A.95) can be written in the following form:

$$A_{mn}^{+}(2) = \Gamma_{mn}^{-}(2) A_{mn}^{-}(2) e^{-\lambda(z_n' - z(2))}. \tag{A.96}$$

The input admittance $Y_{mn}^{+}(z'(n))$ and $Y_{mn}^{-}(z'(n))$ from equations (A.20) and (A.23) are obtained as

$$Y_{mn}^{+}(z'(n)) = \lambda\sigma_H, \tag{A.97}$$

and

$$Y_{mn}^{-}(z'(n)) = \lambda\sigma_H \frac{1 - \Gamma_{mn}^{-}(2) e^{-2\lambda(z_n' - z(2))}}{1 + \Gamma_{mn}^{-}(2) e^{-2\lambda(z_n' - z(2))}}. \tag{A.98}$$

Using equation (A.22), $\Gamma_{mn}^{-}(2)$ is obtained as

$$\Gamma_{mn}^{-}(2)=\frac{\lambda\sigma_H - Y_{mn}^{-}(z(2))}{\lambda\sigma_H + Y_{mn}^{-}(z(2))}. \tag{A.99}$$

Using equation (A.23), we obtain

$$Y_{mn}^{-}(z(2))=\lambda\sigma_1\frac{1-\Gamma_{mn}^{-}(1)e^{-2\lambda h_1}}{1+\Gamma_{mn}^{-}(1)e^{-2\lambda h_1}}. \tag{A.100}$$

From equation (A.22) $\Gamma_{mn}^{-}(1)$ is obtained as

$$\Gamma_{mn}^{-}(1)=\frac{\lambda\sigma_1 - Y_{mn}^{-}(z(1))}{\lambda\sigma_1 + Y_{mn}^{-}(z(1))}. \tag{A.101}$$

As before from equation (A.18) we find $Y_{mn}^{-}(z(1))=\lambda\sigma_0$. Thus, we obtain $\Gamma_{mn}^{-}(1)=\frac{\sigma_1-\sigma_0}{\sigma_1+\sigma_0}$, and then, equations (A.100), (A.99) and (98), respectively, convert to

$$Y_{mn}^{-}(z(2))=\lambda\sigma_1\frac{1-\frac{\sigma_1-\sigma_0}{\sigma_1+\sigma_0}e^{-2\lambda h_1}}{1+\frac{\sigma_1-\sigma_0}{\sigma_1+\sigma_0}e^{-2\lambda h_1}}, \tag{A.102}$$

$$\Gamma_{mn}^{-}(2)=\frac{\frac{\sigma_1-\sigma_0}{\sigma_1+\sigma_0}e^{-2\lambda h_1}-k_1}{1-k_1\frac{\sigma_1-\sigma_0}{\sigma_1+\sigma_0}e^{-2\lambda h_1}}, \tag{A.103}$$

$$Y_{mn}^{-}(z'(n))=\lambda\sigma_H\frac{(1-k_1\frac{\sigma_1-\sigma_0}{\sigma_1+\sigma_0}e^{-2\lambda h_1})-e^{-2\lambda(z_n'-z(2))}(\frac{\sigma_1-\sigma_0}{\sigma_1+\sigma_0}e^{-2\lambda h_1}-k_1)}{(1-k_1\frac{\sigma_1-\sigma_0}{\sigma_1+\sigma_0}e^{-2\lambda h_1})+e^{-2\lambda(z_n'-z(2))}(\frac{\sigma_1-\sigma_0}{\sigma_1+\sigma_0}e^{-2\lambda h_1}-k_1)}. \tag{A.104}$$

From equations (A.94), (A.97) and (A.104) we obtain

$$A_{mn}^{-}(2)=\frac{I}{2\lambda\sigma_H}, \tag{A.105}$$

and substituting equations (A.103) and (A.105) in equation (A.96) yields

$$A_{mn}^{+}(2)=\frac{I}{2\lambda\sigma_H}\frac{(\frac{\sigma_1-\sigma_0}{\sigma_1+\sigma_0}e^{-2\lambda h_1}-k_1)e^{-\lambda(z_n'-z(2))}}{1-k_1\frac{\sigma_1-\sigma_0}{\sigma_1+\sigma_0}e^{-2\lambda h_1}}. \tag{A.106}$$

Substituting equations (A.105) and (A.106) in equation (A.92) yields

$$G(\bar{r}_m,\bar{r}_n')=\frac{I}{4\pi\sigma_H}\int_0^{\infty}\frac{(1-k_1\frac{\sigma_1-\sigma_0}{\sigma_1+\sigma_0}e^{-2\lambda h_1})e^{-\lambda(z_n'-z_m)}+(\frac{\sigma_1-\sigma_0}{\sigma_1+\sigma_0}e^{-2\lambda h_1}-k_1)e^{-\lambda(z_m+z_n'-2z(2))}}{1-k_1\frac{\sigma_1-\sigma_0}{\sigma_1+\sigma_0}e^{-2\lambda h_1}}$$
$$J_0(\lambda r_m)d\lambda \quad \text{for} \quad z_m<z_n'. \tag{A.107}$$

Equation (A.107) can be written in the following form:

$$G(\bar{r}_m,\bar{r}_n')=\frac{I}{4\pi\sigma_H}\int_0^{\infty}\frac{(1-k_1\frac{\sigma_1-\sigma_0}{\sigma_1+\sigma_0}e^{-2\lambda h_1})e^{-\lambda|z_m-z_n'|}+(\frac{\sigma_1-\sigma_0}{\sigma_1+\sigma_0}e^{-2\lambda h_1}-k_1)e^{-\lambda(z_m+z_n'-2z(2))}}{1-k_1\frac{\sigma_1-\sigma_0}{\sigma_1+\sigma_0}e^{-2\lambda h_1}}$$
$$J_0(\lambda r_m)d\lambda \quad \text{for } z_m<z_n'. \tag{A.108}$$

Considering that the uppermost medium above the earth's surface is air, we have $\sigma_0=0$. Thus, equation (A.108) for this case is written as

$$G(\bar{r}_m,\bar{r}_n')=\frac{I}{4\pi\sigma_H}\int_0^{\infty}\frac{(1-k_1e^{-2\lambda h_1})e^{-\lambda|z_m-z_n'|}+(e^{-2\lambda h_1}-k_1)e^{-\lambda(z_m+z_n'-2z(2))}}{1-k_1e^{-2\lambda h_1}}J_0(\lambda r_m)d\lambda.$$
$$\text{for} \quad z_m<z_n' \tag{A.109}$$

For the case that the field point is located below or at the same level as the source element, the Green's function $G(\bar{r}_m, \bar{r}_n')$ is expressed by equation (A.93). In this case, the coefficient $A_{mn}^{+}(n)$ is obtained using equation (A.36), i.e.

$$A_{mn}^{+}(n) = \frac{I}{2\lambda\sigma_H} \frac{\lambda\sigma_H + Y_{mn}^{+}(z'(n))}{Y_{mn}^{-}(z'(n)) + Y_{mn}^{+}(z'(n))}. \tag{A.110}$$

The input admittance $Y_{mn}^{+}(z'(n))$ and $Y_{mn}^{-}(z'(n))$ are obtained using equations (A.20) and (A.23), respectively, i.e.

$$Y_{mn}^{+}(z'(n)) = \lambda\sigma_H, \tag{A.111}$$

and

$$Y_{mn}^{-}(z'(n)) = \lambda\sigma_H \frac{1 - \Gamma_{mn}^{-}(2) e^{-2\lambda(z_n' - z(2))}}{1 + \Gamma_{mn}^{-}(2) e^{-2\lambda(z_n' - z(2))}}. \tag{A.112}$$

Using equation (A.22), $\Gamma_{mn}^{-}(2)$ is obtained as

$$\Gamma_{mn}^{-}(2) = \frac{\lambda\sigma_H - Y_{mn}^{-}(z(2))}{\lambda\sigma_H + Y_{mn}^{-}(z(2))}. \tag{A.113}$$

Using equation (A.23), we obtain

$$Y_{mn}^{-}(z(2)) = \lambda\sigma_1 \frac{1 - \Gamma_{mn}^{-}(1) e^{-2\lambda h_1}}{1 + \Gamma_{mn}^{-}(1) e^{-2\lambda h_1}}. \tag{A.114}$$

Using equation (A.22) $\Gamma_{mn}^{-}(1)$ is obtained as

$$\Gamma_{mn}^{-}(1)=\frac{\lambda\sigma_1-Y_{mn}^{-}(z(1))}{\lambda\sigma_1+Y_{mn}^{-}(z(1))}. \tag{A.115}$$

Using equation (A.18) we find $Y_{mn}^{-}(z(1))=\lambda\sigma_0$). Thus, we obtain $\Gamma_{mn}^{-}(1)=\dfrac{\sigma_1-\sigma_0}{\sigma_1+\sigma_0}$,

and then,

$$Y_{mn}^{-}(z(2))=\lambda\sigma_1\frac{1-\dfrac{\sigma_1-\sigma_0}{\sigma_1+\sigma_0}e^{-2\lambda h_1}}{1+\dfrac{\sigma_1-\sigma_0}{\sigma_1+\sigma_0}e^{-2\lambda h_1}}, \tag{A.116}$$

$$\Gamma_{mn}^{-}(2)=\frac{\dfrac{\sigma_1-\sigma_0}{\sigma_1+\sigma_0}e^{-2\lambda h_1}-k_1}{1-k_1\dfrac{\sigma_1-\sigma_0}{\sigma_1+\sigma_0}e^{-2\lambda h_1}}, \tag{A.117}$$

$$Y_{mn}^{-}(z'(n))=\lambda\sigma_H\frac{(1-k_1\dfrac{\sigma_1-\sigma_0}{\sigma_1+\sigma_0}e^{-2\lambda h_1})-e^{-2\lambda(z_n'-z(2))}(\dfrac{\sigma_1-\sigma_0}{\sigma_1+\sigma_0}e^{-2\lambda h_1}-k_1)}{(1-k_1\dfrac{\sigma_1-\sigma_0}{\sigma_1+\sigma_0}e^{-2\lambda h_1})+e^{-2\lambda(z_n'-z(2))}(\dfrac{\sigma_1-\sigma_0}{\sigma_1+\sigma_0}e^{-2\lambda h_1}-k_1)}. \tag{A.118}$$

From equations (A.110), (A.111) and (A.118), we obtain

$$A_{mn}^{+}(n)=\frac{I}{2\lambda\sigma_H}\frac{(1-k_1\dfrac{\sigma_1-\sigma_0}{\sigma_1+\sigma_0}e^{-2\lambda h_1})+(\dfrac{\sigma_1-\sigma_0}{\sigma_1+\sigma_0}e^{-2\lambda h_1}-k_1)e^{-2\lambda z'}}{1-k_1\dfrac{\sigma_1-\sigma_0}{\sigma_1+\sigma_0}e^{-2\lambda h_1}e^{-2\lambda h_1}}. \tag{A.119}$$

Substituting equation (A.119) in equation (A.93), we obtain

$$G(\bar{r}_m,\bar{r}_n')=\frac{I}{4\pi\sigma_H}\int_0^{\infty}\frac{(1-k_1\frac{\sigma_1-\sigma_0}{\sigma_1+\sigma_0}e^{-2\lambda h_1})e^{-\lambda(z_m-z_n')}+(\frac{\sigma_1-\sigma_0}{\sigma_1+\sigma_0}e^{-2\lambda h_1}-k_1)e^{-\lambda(z_m+z_n'-2z(2))}}{1-k_1\frac{\sigma_1-\sigma_0}{\sigma_1+\sigma_0}e^{-2\lambda h_1}}$$

$$J_0(\lambda r_m)d\lambda \quad \text{for} \quad z_m \geq z_n'. \tag{A.120}$$

Equation (A.120) can be written in the following form:

$$G(\bar{r}_m,\bar{r}_n')=\frac{I}{4\pi\sigma_H}\int_0^{\infty}\frac{(1-k_1\frac{\sigma_1-\sigma_0}{\sigma_1+\sigma_0}e^{-2\lambda h_1})e^{-\lambda|z_m-z_n'|}+(\frac{\sigma_1-\sigma_0}{\sigma_1+\sigma_0}e^{-2\lambda h_1}-k_1)e^{-\lambda(z_m+z_n'-2z(2))}}{1-k_1\frac{\sigma_1-\sigma_0}{\sigma_1+\sigma_0}e^{-2\lambda h_1}}$$

$$J_0(\lambda r_m)d\lambda \quad \text{for } z_m \geq z_n'. \tag{A.121}$$

Equation (A.121), which is the expression for the Green's function $G(\bar{r}_m,\bar{r}_n')$ for the case of $z_m \geq z_n'$, is exactly the same as equation (A.108) for the case of $z_m < z_n'$. Considering that the uppermost medium above the earth's surface is air, we have $\sigma_0 = 0$. Thus, equation (A.121) for this case is written as

$$G(\bar{r}_m,\bar{r}_n')=\frac{I}{4\pi\sigma_H}\int_0^{\infty}\frac{(1-k_1e^{-2\lambda h_1})e^{-\lambda|z_m-z_n'|}+(e^{-2\lambda h_1}-k_1)e^{-\lambda(z_m+z_n'-2z(2))}}{1-k_1e^{-2\lambda h_1}}J_0(\lambda r_m)d\lambda.$$

$$\text{for } z_m \geq z_n' \tag{A.122}$$

Thus, the Green's function $G(\bar{r}_m,\bar{r}_n')$ for the case of $z_m \geq z_n'$, where $\sigma_0 = 0$ is expressed by equation (A.122), which is also exactly the same as equation (A.109) for the case of $z_m < z_n'$.

As shown in this Appendix, we used a procedure introduced by the recently developed spectral formalism to present the mathematical expressions for the required Green's functions used in the 3-D resistivity modelling computations. The expressions for the Green's functions $G(\bar{r}_p,\bar{r}_s')$, $G(\bar{r}_p,\bar{r}_n')$, $G(\bar{r}_m,\bar{r}_s')$, and $G(\bar{r}_m,\bar{r}_n')$,

presented above, are used to compute, respectively, the layered earth potential, the anomalous potential, the electric field, and the elements of the K matrix [see equations (2.47)-(2.48) in Chapter 2].

Appendix B

TRANSITIONAL ZONE MATHEMATICS - LINEAR VARIATION OF RESISTIVITY WITH DEPTH

In this Appendix, we present a new mathematical formulation for obtaining the resistivity response of a 3-D body embedded in a layered earth containing a transitional layer in which the resistivity (or conductivity) varies linearly with depth. Here, we specify a linearly changing *resistivity* with depth for the transitional layer, as it is more common than linearly varying *conductivity* with depth in nature. It is quite obvious that if the resistivity of a transitional layer varies linearly with depth, then the conductivity of the transitional layer must fail to do so since the one is the reciprocal of the other. However, the method of formulation of the problem for the case of linear conductivity variation with depth is the same as for the case of linear resistivity variation with depth.

B.1 Computation of the primary layered-earth potential

Koefoed (1979b) solved the problem of determining the apparent resistivity function for a transitional layer, which has a linear change of resistivity with depth, in a layered earth. He obtained the solution in the form of a modification of the recurrence relation that was derived by Pekris (1940) for homogeneous layers. He also obtained the general expression for the primary layered-earth potential due to an electric current point source on the ground surface. However, the expression contains unknown coefficients, which need to be determined to obtain the explicit expression for the primary layered-earth potential. Although Koefoed (1979b) presented in his paper the boundary conditions, which can be used for obtaining the unknown coefficients, he preferred to obtain the expression for the resistivity transform, and not for the primary layered-earth potential for the case of linear transitional layer. In

the following, we present a mathematical summary and the expression for the primary layered-earth potential for the case of a transitional layer, with a linear change of resistivity with depth, in a layered earth. We approach the problem in the same way as for the exponential transitional layer case given in section 4.2.1 of Chapter 4.

In an M-layered earth, as shown in Figure 2.1, if the ith layer is homogeneous and has a constant resistivity (or conductivity), the general layered earth potential expression for this layer is given by equation (4.12).

If the ith layer is transitional and has a resistivity ρ_i, which varies linearly with depth, we can write

$$\rho_i(z) = \rho_a + \beta(z - z_{i-1}), \quad \text{for} \quad z_{i-1} \le z \le z_i; \quad i = 1, 2, ..., M-1, \tag{B.1}$$

where ρ_a is the resistivity of the transitional layer at the interface between the $(i-1)$th and ith layers (i.e. the resistivity at the top level of the transitional layer where $z = z_{i-1}$), and β, which is a constant with the same dimension as resistance (i.e. Ω), is the rate of change (or the gradient) of resistivity with depth. If $\rho_{i-1} = \rho_a$, then the resistivity is continuous at the interface between the $(i-1)$th and ith layers, otherwise there is a discontinuity at the interface. If ρ_b is the resistivity of the transitional layer at the interface between the ith and $(i+1)$th layers (i.e. the resistivity at the bottom side of the transitional layer where $z = z_i$), then we have

$$\beta = \frac{\rho_b - \rho_a}{z_i - z_{i-1}}. \tag{B.2}$$

Using equation (B.1), we can write equation (4.6) in the following form:

$$\frac{\partial^2 V}{\partial r^2} + \frac{1}{r}\frac{\partial V}{\partial r} + \frac{\partial^2 V}{\partial z^2} - \frac{\beta}{\rho_a + \beta(z - z_{i-1})}\frac{\partial V}{\partial z} = 0. \tag{B.3}$$

The solution of differential equation (B.3) for the potential V_i in the transitional layer is given by Koefoed (1979b) in the following form:

$$V_i(r,z) = \int_0^\infty [A_i(\lambda)\rho_i I_1(\frac{\lambda\rho_i}{\beta}) + B_i(\lambda)\rho_i K_1(\frac{\lambda\rho_i}{\beta})]J_0(\lambda r)d\lambda, \quad \text{for } z_{i-1} \le z \le z_i;$$

$$i = 1, 2, ..., M-1, \quad \text{(B.4)}$$

where $A_i(\lambda)$ and $B_i(\lambda)$ are coefficients, ρ_i is the resistivity of the transitional layer given by equation (B.1), and I_1 and K_1 are the modified Bessel functions of the first and second kinds of order one. If the lowermost layer M is a transitional layer in which the resistivity varies linearly with depth, $A_M(\lambda) = 0$, and thus, the layered earth potential $V_M(r,z)$ for the transitional layer M is given by

$$V_M(r,z) = \int_0^\infty B_M(\lambda)\rho_i K_1(\frac{\lambda\rho_i}{\beta})J_0(\lambda r)d\lambda, \qquad \text{for } z_{M-1} \le z < \infty. \qquad \text{(B.5)}$$

The coefficients $A_i(\lambda)$, $B_i(\lambda)$ [where $i = 1, 2, ..., M-1$], and $B_M(\lambda)$ are to be determined from boundary conditions.

Two-layered case

Once again, for simplicity we consider a two-layered earth as shown in Figure 4.1 in order to establish the mathematical relations governing in the case of linear transitional overburden layer. The isotropic, homogeneous lower half-space (second layer) of the two-layered earth hosts a 3-D body. The overburden layer has a resistivity ρ_1, which varies linearly with depth, i.e.

$$\rho_1(z) = \rho_0 + \beta z, \qquad \text{for} \quad 0 \le z \le z_t, \qquad \text{(B.6)}$$

where z is the depth from the ground surface, z_1 is the depth to the homogeneous lower half-space or second layer (host medium), ρ_0 is the resistivity of the transitional overburden at the ground surface (where $z=0$), and β, which is a constant, is the gradient of resistivity with depth. Considering $z=0$ at the ground surface, we can write $z_1 = h_1$ (Figure 4.1) where h_1 is the thickness of the transitional overburden layer. In this case, we write the layered earth potential for the transitional overburden and the second layer (host medium) as

$$V_1(r,z) = \int_0^\infty [A_1(\lambda)\rho_1 I_1(\frac{\lambda\rho_1}{\beta}) + B_1(\lambda)\rho_1 K_1(\frac{\lambda\rho_1}{\beta})]J_0(\lambda r)d\lambda, \quad \text{for } 0 \le z \le h_1, \quad \text{(B.7)}$$

and

$$V_2(r,z) = \int_0^\infty B_2(\lambda)e^{-\lambda z}J_0(\lambda r)d\lambda, \qquad \text{for} \quad h_1 \le z < \infty. \qquad \text{(B.8)}$$

Here, ρ_1 is the resistivity of the transitional overburden layer given by equation (B.6). The coefficients $A_1(\lambda)$, $B_1(\lambda)$, and $B_2(\lambda)$ are determined from the following boundary conditions:

1) The normal current density at the surface ($z=0$) is satisfied by the following expression:

$$J_z\Big|_{z=0} = -\sigma_1 \frac{\partial V_1}{\partial z}\Big|_{z=0} = -\frac{1}{\rho_1}\frac{\partial V_1}{\partial z}\Big|_{z=0} = \frac{I}{2\pi r}\delta(r), \qquad \text{(B.9)}$$

where I is the electric current, r is the distance between the current source point and the potential measuring location, and $\delta(r)$ is the Dirac delta function. For differentiation of the potential V_1, defined in equation (B.7), we use the following rules for differentiation of modified Bessel functions I_1 and K_1 (Watson, 1958):

$$\frac{dI_1(x)}{dx} = I_0(x) - \frac{I_1(x)}{x}, \tag{B.10}$$

and

$$\frac{dK_1(x)}{dx} = -K_0(x) - \frac{K_1(x)}{x}, \tag{B.11}$$

where I_0 and K_0 are the modified Bessel functions of the first and second kinds of order zero. Using these rules, differentiating the potential V_1 with respect to z and substituting it in equation (B.9) yields

$$-\frac{1}{\rho_0}\int_0^\infty [A_1(\lambda)\rho_0\lambda I_0(\frac{\lambda\rho_0}{\beta}) - B_1(\lambda)\rho_0\lambda K_0(\frac{\lambda\rho_0}{\beta})]J_0(\lambda r)d\lambda = \frac{I}{2\pi r}\delta(r). \tag{B.12}$$

Note that ρ_1 at $z=0$ is equal to ρ_0 [see equation (B.6)]. Equation (B.12) can be simplified to obtain the following equation:

$$\int_0^\infty [A_1(\lambda)I_0(\frac{\lambda\rho_0}{\beta}) - B_1(\lambda)K_0(\frac{\lambda\rho_0}{\beta})]\lambda J_0(\lambda r)d\lambda = \frac{-I}{2\pi}\frac{\delta(r)}{r}, \tag{B.13}$$

which, when inverted with the help of the Fourier Bessel integral (Watson, 1958), yields

$$A_1(\lambda)I_0(\frac{\lambda\rho_0}{\beta}) - B_1(\lambda)K_0(\frac{\lambda\rho_0}{\beta}) = \frac{-I}{2\pi}. \tag{B.14}$$

2) Continuity of the potential at the interface between the first (overburden) and second (host medium) layers, i.e. $V_1 = V_2$ at $z = h_1$. Thus, using equations (B.7) and (B.8), we obtain

$$A_1(\lambda)\rho^* I_1(\frac{\lambda\rho^*}{\beta}) + B_1(\lambda)\rho^* K_1(\frac{\lambda\rho^*}{\beta}) - B_2(\lambda)e^{-\lambda h_1} = 0, \tag{B.15}$$

where

$$\rho^* = \rho_0 + \beta h_1. \tag{B.16}$$

3) Continuity of the normal current density at the interface between the first and second layers i.e. $\frac{1}{\rho_1}\frac{\partial V_1}{\partial z}\Big|_{z=h_1} = \frac{1}{\rho_2}\frac{\partial V_2}{\partial z}\Big|_{z=h_1}$. Thus, differentiating equations (B.7) and (B.8) with respect to z, we have

$$\frac{1}{\rho_1}\int_0^\infty [A_1(\lambda)\rho^*\lambda I_0(\frac{\lambda\rho^*}{\beta}) - B_1(\lambda)\rho^*\lambda K_0(\frac{\lambda\rho^*}{\beta})]J_0(\lambda r)d\lambda = \frac{1}{\rho_2}\int_0^\infty [-\lambda B_2(\lambda)e^{-\lambda h_1}]J_0(\lambda r)d\lambda, \tag{B.17}$$

where ρ^* is given by equation (B.16). Considering ρ_1 at the interface between the first and second layers (i.e. $z = z_1 = h_1$) is equal to ρ^*, we obtain the following expression from equation (B.17):

$$A_1(\lambda)I_0(\frac{\lambda\rho^*}{\beta}) - B_1(\lambda)K_0(\frac{\lambda\rho^*}{\beta}) + \frac{1}{\rho_2}B_2(\lambda)e^{-\lambda h_1} = 0. \tag{B.18}$$

$A_1(\lambda)$, $B_1(\lambda)$, and $B_2(\lambda)$ are evaluated from the set of equations (B.14), (B.15), and (B.18). We can write this set of equations in the form of a matrix equation, and obtain the values $A_1(\lambda)$, $B_1(\lambda)$, and $B_2(\lambda)$ using Cramer's rule. Consequently, we obtain

$$A_1(\lambda)=\frac{-\frac{I}{2\pi}[\frac{\rho^*}{\rho_2}K_1(\frac{\lambda\rho^*}{\beta})-K_0(\frac{\lambda\rho^*}{\beta})]}{[\frac{\rho^*}{\rho_2}K_1(\frac{\lambda\rho^*}{\beta})-K_0(\frac{\lambda\rho^*}{\beta})]I_0(\frac{\lambda\rho_0}{\beta})+[\frac{\rho^*}{\rho_2}I_1(\frac{\lambda\rho^*}{\beta})+I_0(\frac{\lambda\rho^*}{\beta})]K_0(\frac{\lambda\rho_0}{\beta})},$$

(B.19)

$$B_1(\lambda)=\frac{\frac{I}{2\pi}[\frac{\rho^*}{\rho_2}I_1(\frac{\lambda\rho^*}{\beta})+I_0(\frac{\lambda\rho^*}{\beta})]}{[\frac{\rho^*}{\rho_2}K_1(\frac{\lambda\rho^*}{\beta})-K_0(\frac{\lambda\rho^*}{\beta})]I_0(\frac{\lambda\rho_0}{\beta})+[\frac{\rho^*}{\rho_2}I_1(\frac{\lambda\rho^*}{\beta})+I_0(\frac{\lambda\rho^*}{\beta})]K_0(\frac{\lambda\rho_0}{\beta})},$$

(B.20)

$$B_2(\lambda)=\frac{\frac{\rho^* I}{2\pi}[I_1(\frac{\lambda\rho^*}{\beta})K_0(\frac{\lambda\rho^*}{\beta})+I_0(\frac{\lambda\rho^*}{\beta})K_1(\frac{\lambda\rho^*}{\beta})]}{[\frac{\rho^*}{\rho_2}K_1(\frac{\lambda\rho^*}{\beta})-K_0(\frac{\lambda\rho^*}{\beta})]I_0(\frac{\lambda\rho_0}{\beta})e^{-\lambda h_1}+[\frac{\rho^*}{\rho_2}I_1(\frac{\lambda\rho^*}{\beta})+I_0(\frac{\lambda\rho^*}{\beta})]K_0(\frac{\lambda\rho_0}{\beta})e^{-\lambda h_1}},$$

(B.21)

where ρ^* is given by equation (B.16). Substituting equations (B.19) and (B.20) in equation (B.7), we obtain the layered earth potential. Therefore, the layered earth potential at the ground surface ($z=0$), represented by $V_l(r,0)$, is given by

$$V_l(r,0)=\frac{\rho_0 I}{2\pi}\int_0^\infty \frac{[I_0(\frac{\lambda\rho^*}{\beta})+\frac{\rho^*}{\rho_2}I_1(\frac{\lambda\rho^*}{\beta})]K_1(\frac{\lambda\rho_0}{\beta})+[K_0(\frac{\lambda\rho^*}{\beta})-\frac{\rho^*}{\rho_2}K_1(\frac{\lambda\rho^*}{\beta})]I_1(\frac{\lambda\rho_0}{\beta})}{[I_0(\frac{\lambda\rho^*}{\beta})+\frac{\rho^*}{\rho_2}I_1(\frac{\lambda\rho^*}{\beta})]K_0(\frac{\lambda\rho_0}{\beta})-[K_0(\frac{\lambda\rho^*}{\beta})-\frac{\rho^*}{\rho_2}K_1(\frac{\lambda\rho^*}{\beta})]I_0(\frac{\lambda\rho_0}{\beta})}J_0(\lambda r)d\lambda.$$

(B.22)

Dividing the numerator and denominator of the kernel function in equation (B.22) by $I_0(\frac{\lambda\rho^*}{\beta})+\frac{\rho^*}{\rho_2}I_1(\frac{\lambda\rho^*}{\beta})$, we can write equation (B.22) in the following form:

$$V_l(r,0)=\frac{\rho_0 I}{2\pi}\int_0^\infty \frac{K_1(\frac{\lambda\rho_0}{\beta})+UI_1(\frac{\lambda\rho_0}{\beta})}{K_0(\frac{\lambda\rho_0}{\beta})-UI_0(\frac{\lambda\rho_0}{\beta})}J_0(\lambda r)d\lambda,$$

(B.23)

where

$$U = \frac{K_0(\frac{\lambda\rho^*}{\beta}) - \frac{\rho^*}{\rho_2} K_1(\frac{\lambda\rho^*}{\beta})}{I_0(\frac{\lambda\rho^*}{\beta}) + \frac{\rho^*}{\rho_2} I_1(\frac{\lambda\rho^*}{\beta})}. \tag{B.24}$$

B.2 Computation of Green's functions, electric field, anomalous potential and other parameters involved in the integral equation approach

For computation of the resistivity response of a body embedded in a layered earth with a transitional overburden of linearly varying resistivity with depth (Figure 4.1), as in the transitional layer case of exponentially varying resistivity with depth, we need to obtain the total electric potential. The total electric potential is expressed as the sum of the layered earth potential V_l and the anomalous electric potential V_a [see equation (4.41)]. The mathematical expression for computing the layered earth potential was given by equation (B.23). To compute the anomalous electric potential due to the electric charge distribution on the surface of the body, we discretise the surface of the body into small elementary cells and apply the integral equation method. As for the earlier case of an exponentially varying transitional layer, the unknown electric charge Q on the surface of each cell is computed using equation (4.40) after computing the other parameters in the equation, i.e. the electric field E and the elements of the matrix K. Then, the anomalous electric potential is computed using equation (4.43). Thus, in this transitional case for computing the electric field E, matrix K, and anomalous electric potential V_a, which involve the evaluation of the relevant Green's functions, we use the same equations as used in the other transitional case (i.e. exponential variation) or the homogeneous case (discussed in Chapter 2). The difference between these cases in the computations of the above parameters is in the expressions for the involved Green's functions (Figure 4.2). In this case, the Green's functions, as shown in Figure 4.2, account for the

effect of the transitional overburden, in which the resistivity varies linearly with depth. In the following, we obtain the Green's functions for this transitional case.

The layered earth potential V_l can be expressed by equation (4.42), which involves the Green's function $G(\bar{r}_p, \bar{r}_s')$. Thus, comparing this equation with equation (B.23), we can express the Green's function $G(\bar{r}_p, \bar{r}_s')$ for the case of the transitional overburden with linearly changing resistivity with depth in the following form:

$$G(\bar{r}_p, \bar{r}_s') = \int_0^\infty \frac{K_1(\frac{\lambda\rho_0}{\beta}) + UI_1(\frac{\lambda\rho_0}{\beta})}{K_0(\frac{\lambda\rho_0}{\beta}) - UI_0(\frac{\lambda\rho_0}{\beta})} J_0(\lambda r_p) d\lambda, \tag{B.25}$$

where U is given by equation (B.24). $\bar{r}_p$ is a point on the ground surface where a potential measuring electrode is set up, and $\bar{r}_s'$ is the location of the current source electrode (Figure 4.2).

For computation of the electric field $\bar{E}$, the expression given in equation (4.46) is used in which the Green's function $G(\bar{r}_m, \bar{r}_s')$, for the electric field at the centre $\bar{r}_m$ of a surface cell due to the current point source at $\bar{r}_s'$ (Figure 4.3), is defined by equation (4.49), i.e.

$$G(\bar{r}_m, \bar{r}_s') = \int_0^\infty B_2(\lambda) e^{-\lambda z} J_0(\lambda r_m) d\lambda, \tag{B.26}$$

where $B_2(\lambda)$ is given by equation (B.21). Equation (B.26), using equation (B.21), can be written in the following form:

$$G(\bar{r}_m,\bar{r}_s')=\frac{\rho_0 I}{2\pi}\int_0^{\infty}\frac{\frac{\rho^*}{\rho_0}[I_1(\frac{\lambda\rho^*}{\beta})K_0(\frac{\lambda\rho^*}{\beta})+I_0(\frac{\lambda\rho^*}{\beta})K_1(\frac{\lambda\rho^*}{\beta})]}{[\frac{\rho^*}{\rho_0}K_1(\frac{\lambda\rho^*}{\beta})-K_0(\frac{\lambda\rho^*}{\beta})]I_0(\frac{\lambda\rho_0}{\beta})e^{-\lambda h_1}+[\frac{\rho^*}{\rho_0}I_1(\frac{\lambda\rho^*}{\beta})-I_0(\frac{\lambda\rho^*}{\beta})]K_0(\frac{\lambda\rho_0}{\beta})e^{-\lambda h_1}}$$
$$e^{-\lambda z}J_0(\lambda r_m)d\lambda. \tag{B.27}$$

We can write the integral in the following form:

$$G(\bar{r}_m,\bar{r}_s')=\frac{\rho_0 I}{2\pi}\int_0^{\infty}\{1+\frac{\frac{\rho^*}{\rho_0}[I_1(\frac{\lambda\rho^*}{\beta})K_0(\frac{\lambda\rho^*}{\beta})+I_0(\frac{\lambda\rho^*}{\beta})K_1(\frac{\lambda\rho^*}{\beta})]}{[\frac{\rho^*}{\rho_0}K_1(\frac{\lambda\rho^*}{\beta})-K_0(\frac{\lambda\rho^*}{\beta})]I_0(\frac{\lambda\rho_0}{\beta})e^{-\lambda h_1}+[\frac{\rho^*}{\rho_0}I_1(\frac{\lambda\rho^*}{\beta})-I_0(\frac{\lambda\rho^*}{\beta})]K_0(\frac{\lambda\rho_0}{\beta})e^{-\lambda h_1}}$$
$$\frac{-[\frac{\rho^*}{\rho_0}K_1(\frac{\lambda\rho^*}{\beta})-K_0(\frac{\lambda\rho^*}{\beta})]I_0(\frac{\lambda\rho_0}{\beta})e^{-\lambda h_1}-[\frac{\rho^*}{\rho_0}I_1(\frac{\lambda\rho^*}{\beta})-I_0(\frac{\lambda\rho^*}{\beta})]K_0(\frac{\lambda\rho_0}{\beta})e^{-\lambda h_1}}{}\}e^{-\lambda z}J_0(\lambda r_m)d\lambda.$$
(B.28)

or

$$G(\bar{r}_m,\bar{r}_s')=\frac{\rho_0 I}{4\pi}\int_0^{\infty}\{e^{-\lambda z}+\frac{\{\frac{2\rho^*}{\rho_0}[I_1(\frac{\lambda\rho^*}{\beta})K_0(\frac{\lambda\rho^*}{\beta})+I_0(\frac{\lambda\rho^*}{\beta})K_1(\frac{\lambda\rho^*}{\beta})]}{[\frac{\rho^*}{\rho_0}K_1(\frac{\lambda\rho^*}{\beta})-K_0(\frac{\lambda\rho^*}{\beta})]I_0(\frac{\lambda\rho_0}{\beta})e^{-\lambda h_1}+[\frac{\rho^*}{\rho_0}I_1(\frac{\lambda\rho^*}{\beta})}$$
$$\frac{-[\frac{\rho^*}{\rho_0}K_1(\frac{\lambda\rho^*}{\beta})-K_0(\frac{\lambda\rho^*}{\beta})]I_0(\frac{\lambda\rho_0}{\beta})e^{-\lambda h_1}-[\frac{\rho^*}{\rho_0}I_1(\frac{\lambda\rho^*}{\beta})-I_0(\frac{\lambda\rho^*}{\beta})]K_0(\frac{\lambda\rho_0}{\beta})e^{-\lambda h_1}\}e^{-\lambda z}}{-I_0(\frac{\lambda\rho^*}{\beta})]K_0(\frac{\lambda\rho_0}{\beta})e^{-\lambda h_1}}\}J_0(\lambda r_m)d\lambda.$$
(B.29)

The first term inside the integral in equation (B.29) represents the whole space term $G^W(\bar{r}_m,\bar{r}_s')$, and the second term inside the integral represents the reflected term $G^R(\bar{r}_m,\bar{r}_s')$. Thus,

$$G^W(\bar{r}_m,\bar{r}_s')=\int_0^{\infty}e^{-\lambda z}J_0(\lambda r_m)d\lambda=\frac{1}{\sqrt{r_m{}^2+z^2}}, \tag{B.30}$$

and

$$G^R(\bar{r}_m,\bar{r}_s')=\int_0^\infty \frac{\{\frac{2\rho^*}{\rho_0}[I_1(\frac{\lambda\rho^*}{\beta})K_0(\frac{\lambda\rho^*}{\beta})+I_0(\frac{\lambda\rho^*}{\beta})K_1(\frac{\lambda\rho^*}{\beta})]}{[\frac{\rho^*}{\rho_0}K_1(\frac{\lambda\rho^*}{\beta})-K_0(\frac{\lambda\rho^*}{\beta})]I_0(\frac{\lambda\rho_0}{\beta})e^{-\lambda h_1}+[\frac{\rho^*}{\rho_0}I_1(\frac{\lambda\rho^*}{\beta})-I_0(\frac{\lambda\rho^*}{\beta})]K_0(\frac{\lambda\rho_0}{\beta})e^{-\lambda h_1}}$$
$$\frac{-[\frac{\rho^*}{\rho_0}K_1(\frac{\lambda\rho^*}{\beta})-K_0(\frac{\lambda\rho^*}{\beta})]I_0(\frac{\lambda\rho_0}{\beta})e^{-\lambda h_1}-[\frac{\rho^*}{\rho_0}I_1(\frac{\lambda\rho^*}{\beta})-I_0(\frac{\lambda\rho^*}{\beta})]K_0(\frac{\lambda\rho_0}{\beta})e^{-\lambda h_1}\}e^{-\lambda z}}{}J_0(\lambda r_m)d\lambda. \tag{B.31}$$

Using a Cartesian coordinate system with the same origin and z-axis as those of the cylindrical coordinate system used earlier, we can specify the coordinates of $\bar{r}_m$ and $\bar{r}_s'$ in the Cartesian coordinate system by (x,y,z) and (x',y',z'), respectively. In this case, the current source point $\bar{r}_s'$ is located on the surface, thus $z'=0$. Hence, equation (B.30) can be written as

$$G^W(\bar{r}_m,\bar{r}_s')=\frac{1}{R}, \tag{B.32}$$

where R is given by equation (4.58).

Differentiating equation (B.29), with respect to x, y and z, and substituting it in equation (4.46), we obtain the normal components of the electric field at the centre of each elementary surface cell as

$$E_x^i=\rho_0 I\Big\{\frac{(x-x')}{R^3}+$$
$$\frac{(x-x')}{r}\int_0^\infty \frac{\{\frac{2\rho^*}{\rho_0}[I_1(\frac{\lambda\rho^*}{\beta})K_0(\frac{\lambda\rho^*}{\beta})+I_0(\frac{\lambda\rho^*}{\beta})K_1(\frac{\lambda\rho^*}{\beta})]}{[\frac{\rho^*}{\rho_0}K_1(\frac{\lambda\rho^*}{\beta})-K_0(\frac{\lambda\rho^*}{\beta})]I_0(\frac{\lambda\rho_0}{\beta})e^{-\lambda h_1}+[\frac{\rho^*}{\rho_0}I_1(\frac{\lambda\rho^*}{\beta})-I_0(\frac{\lambda\rho^*}{\beta})]K_0(\frac{\lambda\rho_0}{\beta})e^{-\lambda h_1}}$$
$$\frac{-[\frac{\rho^*}{\rho_0}K_1(\frac{\lambda\rho^*}{\beta})-K_0(\frac{\lambda\rho^*}{\beta})]I_0(\frac{\lambda\rho_0}{\beta})e^{-\lambda h_1}-[\frac{\rho^*}{\rho_0}I_1(\frac{\lambda\rho^*}{\beta})-I_0(\frac{\lambda\rho^*}{\beta})]K_0(\frac{\lambda\rho_0}{\beta})e^{-\lambda h_1}\}e^{-\lambda z}}{}\lambda J_1(\lambda r)d\lambda, \tag{B.33}$$

with a similar equation for the $y-$component with y and y' replacing, respectively, x and x', and finally

$$E_z^i = \rho_0 I\left\{\frac{(z-z')}{R^3}+\right.$$

$$\int_0^\infty \frac{\{\frac{2\rho^*}{\rho_0}[I_1(\frac{\lambda\rho^*}{\beta})K_0(\frac{\lambda\rho^*}{\beta})+I_0(\frac{\lambda\rho^*}{\beta})K_1(\frac{\lambda\rho^*}{\beta})]}{[\frac{\rho^*}{\rho_0}K_1(\frac{\lambda\rho^*}{\beta})-K_0(\frac{\lambda\rho^*}{\beta})]I_0(\frac{\lambda\rho_0}{\beta})e^{-\lambda h_1}+[\frac{\rho^*}{\rho_0}I_1(\frac{\lambda\rho^*}{\beta})-I_0(\frac{\lambda\rho^*}{\beta})]K_0(\frac{\lambda\rho_0}{\beta})e^{-\lambda h_1}}$$

$$\left.\frac{-[\frac{\rho^*}{\rho_0}K_1(\frac{\lambda\rho^*}{\beta})-K_0(\frac{\lambda\rho^*}{\beta})]I_0(\frac{\lambda\rho_0}{\beta})e^{-\lambda h_1}-[\frac{\rho^*}{\rho_0}I_1(\frac{\lambda\rho^*}{\beta})-I_0(\frac{\lambda\rho^*}{\beta})]K_0(\frac{\lambda\rho_0}{\beta})e^{-\lambda h_1}\}e^{-\lambda z}}{}\right. \lambda J_0(\lambda r)d\lambda.$$

(B.34)

The integrals in equations (B.33) and (B.34) are solved using digital linear filters designed for Hankel J_0 and J_1 transforms discussed in Chapter 2.

To obtain the expression for the Green's function $G(\bar{r}_p,\bar{r}_n')$, used in the computation of the anomalous potential $V_a(\bar{r}_p)$ due to the electric charges developed on the surface of each cell, and also, the expression for the Green's function $G(\bar{r}_m,\bar{r}_n')$, used in the computation of the elements of matrix K^{mn}, we consider the situation shown in Figure 4.4. Both the field point $\bar{r}_m$ and the source at $\bar{r}_n'$ are located in the lower half-space of the two-layered earth shown in Figure 4.4, while the potential point $\bar{r}_p$ is located on the ground surface. The Green's function $G(\bar{r}_p,\bar{r}_n')$ represents the potential at point $\bar{r}_p$ due to source at $\bar{r}_n'$, thus it can be defined as the potential V_1 of the first layer at point $\bar{r}_p$ on the ground surface (where $z=0$) due to source at $\bar{r}_n'$. Also, the Green's function $G(\bar{r}_m,\bar{r}_n')$ represents the potential at field point $\bar{r}_m$ due to source at $\bar{r}_n'$, thus it can be defined as the potential V_2 of the second layer at point $\bar{r}_m$ due to source at $\bar{r}_n'$. Therefore, we can write

$$G(\bar{r}_p,\bar{r}_n') = V_1\Big|_{z=0} = \int_0^\infty [A_1(\lambda)\rho_1 I_1(\frac{\lambda\rho_1}{\beta}) + B_1(\lambda)\rho_1 K_1(\frac{\lambda\rho_1}{\beta})]J_0(\lambda r_p)d\lambda\Big|_{z=0}, \quad \text{(B.35)}$$

and

$$G(\bar{r}_m,\bar{r}_n') = V_2 = \int_0^\infty [e^{-\lambda|z-z'|} + B_2(\lambda)e^{-\lambda z}]J_0(\lambda r_m)d\lambda. \quad \text{(B.36)}$$

Applying the following boundary conditions, we obtain the coefficients $A_1(\lambda)$, $B_1(\lambda)$, and $B_2(\lambda)$:

1) The normal current density at the surface ($z=0$):

$$J_z\Big|_{z=0} = -\frac{1}{\rho_1}\frac{\partial V_1}{\partial z}\Big|_{z=0} = 0. \quad \text{(B.37)}$$

Note that in this case, the source is located in the second layer. Differentiating V_1, given by equation (B.35), with respect to z and substituting it in equation (B.37) yields

$$-\frac{1}{\rho_0}\int_0^\infty [A_1(\lambda)\rho_0\lambda I_0(\frac{\lambda\rho_0}{\beta}) - B_1(\lambda)\rho_0\lambda K_0(\frac{\lambda\rho_0}{\beta})]J_0(\lambda r)d\lambda = 0. \quad \text{(B.38)}$$

Note that ρ_1 at $z=0$ is equal to ρ_0 [see equation (B.6)]. Equation (B.38) can be simplified to obtain the following equation:

$$\int_0^\infty [A_1(\lambda)I_0(\frac{\lambda\rho_0}{\beta}) - B_1(\lambda)K_0(\frac{\lambda\rho_0}{\beta})]\lambda J_0(\lambda r)d\lambda = 0, \quad \text{(B.39)}$$

From this equation, we can conclude

$$A_1(\lambda)I_0(\frac{\lambda\rho_0}{\beta}) - B_1(\lambda)K_0(\frac{\lambda\rho_0}{\beta}) = 0. \tag{B.40}$$

Then,

$$B_1(\lambda) = \frac{I_0(\frac{\lambda\rho_0}{\beta})}{K_0(\frac{\lambda\rho_0}{\beta})} A_1(\lambda). \tag{B.41}$$

2) $V_1 = V_2$ at the interface between the first and second layers (i.e. at $z = h_1$). Thus, using equations (B.35) and (B.36), we obtain

$$A_1(\lambda)\rho^* I_1(\frac{\lambda\rho^*}{\beta}) + B_1(\lambda)\rho^* K_1(\frac{\lambda\rho^*}{\beta}) = e^{-\lambda(z'-h_1)} + B_2(\lambda)e^{-\lambda h_1}. \tag{B.42}$$

where ρ^* is given by equation (B.16). Substituting equation (B.41) in equation (B.42), we obtain

$$B_2(\lambda) = A_1(\lambda)[\rho^* I_1(\frac{\lambda\rho^*}{\beta}) + \frac{I_0(\frac{\lambda\rho_0}{\beta})}{K_0(\frac{\lambda\rho_0}{\beta})}\rho^* K_1(\frac{\lambda\rho^*}{\beta})]e^{\lambda h_1} - e^{-\lambda(z'-2h_1)}. \tag{B.43}$$

3) $\frac{1}{\rho_1}\frac{\partial V_1}{\partial z} = \frac{1}{\rho_2}\frac{\partial V_2}{\partial z}$ at the interface between the first and second layers (i.e. at $z = h_1$). Thus, differentiating equations (B.35) and (B.36) with respect to z, and considering $\rho_1 = \rho^*$ at the interface between the first and second layers (i.e. $z = h_1$), we obtain

$$A_1(\lambda)I_0(\frac{\lambda\rho^*}{\beta}) - B_1(\lambda)K_0(\frac{\lambda\rho^*}{\beta}) = \frac{1}{\rho_2}[e^{-\lambda(z'-h_1)} - B_2(\lambda)e^{-\lambda h_1}]. \tag{B.44}$$

Substituting equations (B.41) and (B.43) in equation (B.44), we finally have

$$A_1(\lambda) = \frac{2e^{-\lambda(z'-h_1)}K_0(\frac{\lambda\rho_0}{\beta})}{\rho^* I_1(\frac{\lambda\rho^*}{\beta})K_0(\frac{\lambda\rho_0}{\beta}) + \rho_2 I_0(\frac{\lambda\rho^*}{\beta})K_0(\frac{\lambda\rho_0}{\beta}) + [\rho^* K_1(\frac{\lambda\rho^*}{\beta}) - \rho_2 K_0(\frac{\lambda\rho^*}{\beta})]I_0(\frac{\lambda\rho_0}{\beta})}. \quad \text{(B.45)}$$

Substituting (B.45) in (B.41), we obtain

$$B_1(\lambda) = \frac{2e^{-\lambda(z'-h_1)}I_0(\frac{\lambda\rho_0}{\beta})}{\rho^* I_1(\frac{\lambda\rho^*}{\beta})K_0(\frac{\lambda\rho_0}{\beta}) + \rho_2 I_0(\frac{\lambda\rho^*}{\beta})K_0(\frac{\lambda\rho_0}{\beta}) + [\rho^* K_1(\frac{\lambda\rho^*}{\beta}) - \rho_2 K_0(\frac{\lambda\rho^*}{\beta})]I_0(\frac{\lambda\rho_0}{\beta})}. \quad \text{(B.46)}$$

Similarly, substituting (B.45) in (B.43), we obtain

$$B_2(\lambda) = \frac{e^{-\lambda(z'-2h_1)}[\rho^* I_1(\frac{\lambda\rho^*}{\beta})K_0(\frac{\lambda\rho_0}{\beta}) + \rho^* I_0(\frac{\lambda\rho_0}{\beta})K_1(\frac{\lambda\rho^*}{\beta}) - \rho_2 I_0(\frac{\lambda\rho^*}{\beta})K_0(\frac{\lambda\rho_0}{\beta})}{\rho^* I_1(\frac{\lambda\rho^*}{\beta})K_0(\frac{\lambda\rho_0}{\beta}) + \rho_2 I_0(\frac{\lambda\rho^*}{\beta})K_0(\frac{\lambda\rho_0}{\beta}) + [\rho^* K_1(\frac{\lambda\rho^*}{\beta}) - \rho_2 K_0(\frac{\lambda\rho^*}{\beta})]I_0(\frac{\lambda\rho_0}{\beta}) + \rho_2 I_0(\frac{\lambda\rho_0}{\beta})K_0(\frac{\lambda\rho^*}{\beta})]}. \quad \text{(B.47)}$$

Substituting equation (B.47) in equation (B.36), we obtain the expression for the Green's function $G(\vec{r}_m, \vec{r}_n')$ in the following form:

$$G(\bar{r}_m,\bar{r}_n') = \int_0^\infty \{e^{-\lambda|z-z'|} + \frac{e^{-\lambda(z+z'-2h_1)}[\rho^* I_1(\frac{\lambda\rho^*}{\beta})K_0(\frac{\lambda\rho_0}{\beta}) + \rho^* I_0(\frac{\lambda\rho_0}{\beta})K_1(\frac{\lambda\rho^*}{\beta}) - \rho_2 I_0(\frac{\lambda\rho^*}{\beta})K_0(\frac{\lambda\rho_0}{\beta})}{\rho^* I_1(\frac{\lambda\rho^*}{\beta})K_0(\frac{\lambda\rho_0}{\beta}) + \rho_2 I_0(\frac{\lambda\rho^*}{\beta})K_0(\frac{\lambda\rho_0}{\beta}) + [\rho^* K_1(\frac{\lambda\rho^*}{\beta}) - \rho_2 K_0(\frac{\lambda\rho^*}{\beta})]I_0(\frac{\lambda\rho_0}{\beta}) + \rho_2 I_0(\frac{\lambda\rho_0}{\beta})K_0(\frac{\lambda\rho^*}{\beta})]}\} J_0(\lambda r_m)d\lambda. \tag{B.48}$$

The first exponential term inside the integral represents the whole space term $G^W(\bar{r}_m,\bar{r}_n')$. Defining the coordinates of $\bar{r}_m$ and $\bar{r}_n'$ respectively by (x,y,z) and (x',y',z') in the Cartesian coordinate system used, we can write represents the whole space term $G^W(\bar{r}_m,\bar{r}_n')$ as

$$G^W(\bar{r}_m,\bar{r}_n') = \int_0^\infty e^{-\lambda|z-z'|} J_0(\lambda r_m)d\lambda = \frac{1}{R}, \tag{B.49}$$

where R is given by equation (4.58). The second term inside the integral in equation (B.48) includes the reflection contribution to the Green's function $G(\bar{r}_m,\bar{r}_n')$, represented by $G^R(\bar{r}_m,\bar{r}_n')$, i.e.

$$G^R(\bar{r}_m,\bar{r}_n') = \int_0^\infty \frac{e^{-\lambda(z+z'-2h_1)}[\rho^* I_1(\frac{\lambda\rho^*}{\beta})K_0(\frac{\lambda\rho_0}{\beta}) + \rho^* I_0(\frac{\lambda\rho_0}{\beta})K_1(\frac{\lambda\rho^*}{\beta}) - \rho_2 I_0(\frac{\lambda\rho^*}{\beta})K_0(\frac{\lambda\rho_0}{\beta})}{\rho^* I_1(\frac{\lambda\rho^*}{\beta})K_0(\frac{\lambda\rho_0}{\beta}) + \rho_2 I_0(\frac{\lambda\rho^*}{\beta})K_0(\frac{\lambda\rho_0}{\beta}) + [\rho^* K_1(\frac{\lambda\rho^*}{\beta}) - \rho_2 K_0(\frac{\lambda\rho^*}{\beta})]I_0(\frac{\lambda\rho_0}{\beta}) + \rho_2 I_0(\frac{\lambda\rho_0}{\beta})K_0(\frac{\lambda\rho^*}{\beta})]} J_0(\lambda r_m)d\lambda. \tag{B.50}$$

For computation of the elements of matrix K^{mn}, we use equations (4.79) – (4.81), in which Γ^{mn} for $m \neq n$ (Figure 4.4) includes both whole space and reflection contributions to the Green's function $G(\bar{r}_m,\bar{r}_n')$, given by equations (B.49) and

(B.50). For $m = n$, Γ^{mn} includes only the reflected term of the Green's function $G(\bar{r}_m, \bar{r}_n')$, i.e. $\Gamma^{mn} = \Gamma_R^{mn}$ for $m = n$. Computation of Γ_W^{mn} [i.e. the first integral on the right-hand side of equation (4.82)], using equations (B.49) is achieved exactly over the surface of the body. For computing Γ_R^{mn} [i.e. the second integral on the right-hand side of equation (4.82)], we assume the integrand to be constant. Differentiating equation (B.50) with respect to x, y and z, and substituting it in equation (4.85), we obtain the various components of Γ_R^{mn} as follows:

$$\Gamma_{R,x}^{mn} = -\frac{\Delta S(x-x')}{r}\int_0^\infty \frac{e^{-\lambda(z+z'-2h_1)}[\rho^* I_1(\frac{\lambda\rho^*}{\beta})K_0(\frac{\lambda\rho_0}{\beta}) + \rho^* I_0(\frac{\lambda\rho_0}{\beta})K_1(\frac{\lambda\rho^*}{\beta})}{\rho^* I_1(\frac{\lambda\rho^*}{\beta})K_0(\frac{\lambda\rho_0}{\beta}) + \rho_2 I_0(\frac{\lambda\rho^*}{\beta})K_0(\frac{\lambda\rho_0}{\beta}) + [\rho^* K_1(\frac{\lambda\rho^*}{\beta}) - \rho_2 I_0(\frac{\lambda\rho^*}{\beta})K_0(\frac{\lambda\rho_0}{\beta}) + \rho_2 I_0(\frac{\lambda\rho_0}{\beta})K_0(\frac{\lambda\rho^*}{\beta})]}{-\rho_2 K_0(\frac{\lambda\rho^*}{\beta})]I_0(\frac{\lambda\rho_0}{\beta})} \lambda J_1(\lambda r)d\lambda. \tag{B.51}$$

with a similar equation for the $y-$component with y and y' replacing, respectively, x and x', and finally

$$\Gamma_{R,z}^{mn} = -\Delta S\int_0^\infty \frac{e^{-\lambda(z+z'-2h_1)}[\rho^* I_1(\frac{\lambda\rho^*}{\beta})K_0(\frac{\lambda\rho_0}{\beta}) + \rho^* I_0(\frac{\lambda\rho_0}{\beta})K_1(\frac{\lambda\rho^*}{\beta})}{\rho^* I_1(\frac{\lambda\rho^*}{\beta})K_0(\frac{\lambda\rho_0}{\beta}) + \rho_2 I_0(\frac{\lambda\rho^*}{\beta})K_0(\frac{\lambda\rho_0}{\beta}) + [\rho^* K_1(\frac{\lambda\rho^*}{\beta}) - \rho_2 K_0(\frac{\lambda\rho^*}{\beta})]I_0(\frac{\lambda\rho_0}{\beta}) - \rho_2 I_0(\frac{\lambda\rho^*}{\beta})K_0(\frac{\lambda\rho_0}{\beta}) + \rho_2 I_0(\frac{\lambda\rho_0}{\beta})K_0(\frac{\lambda\rho^*}{\beta})]} \lambda J_0(\lambda r)d\lambda. \tag{B.52}$$

The above integrals are solved using digital linear filters designed for Hankel J_0 and J_1 transforms (see Chapter 2).

The expression for the Green's function $G(\bar{r}_p, \bar{r}_n')$, used in the computation of the anomalous electric potential V_a at $\bar{r}_p$ on the ground surface due to the surface charge density at $\bar{r}_n'$, is obtained by substituting equations (B.45) and (B.46) in equation (B.35). Then after simplification, we finally obtain

$$G(\bar{r}_p, \bar{r}_n') = (1-k)\left\{\frac{1}{R} + \int_0^\infty \frac{[\rho_0 I_1(\frac{\lambda\rho_0}{\beta})K_0(\frac{\lambda\rho_0}{\beta}) + \rho_2 I_0(\frac{\lambda\rho_0}{\beta})K_1(\frac{\lambda\rho_0}{\beta})]e^{-\lambda(z'-h_1)} - e^{-\lambda z'}\{[\rho^* I_1(\frac{\lambda\rho^*}{\beta}) + [\rho^* I_1(\frac{\lambda\rho^*}{\beta}) + \rho_2 I_0(\frac{\lambda\rho^*}{\beta})]K_0(\frac{\lambda\rho_0}{\beta}) + [\rho^* K_1(\frac{\lambda\rho^*}{\beta}) - \rho_2 K_0(\frac{\lambda\rho^*}{\beta})]I_0(\frac{\lambda\rho_0}{\beta})}{\rho_2 I_0(\frac{\lambda\rho^*}{\beta})]K_0(\frac{\lambda\rho_0}{\beta}) + [\rho^* K_1(\frac{\lambda\rho^*}{\beta}) - \rho_2 K_0(\frac{\lambda\rho^*}{\beta})]I_0(\frac{\lambda\rho_0}{\beta})\}} J_0(\lambda r_p)d\lambda\right\}. \quad \text{(B.53)}$$

In equation (B.53),

$$k = \frac{\rho_2 - \rho_0}{\rho_2 + \rho_0}, \quad \text{(B.54)}$$

and R is given by equation (4.58) considering the coordinates of $\bar{r}_p$ and $\bar{r}_n'$ in the Cartesian coordinate system to be respectively (x, y, z) and (x', y', z'). Also, as for the other Green's functions, the Green's function $G(\bar{r}_p, \bar{r}_n')$, given by equation (4.89) can be shown in two parts: whole space part $G^W(\bar{r}_p, \bar{r}_n')$ and reflected part $G^R(\bar{r}_p, \bar{r}_n')$. The term $\frac{1}{R}$ in equation (B.53) represents the whole space part $G^W(\bar{r}_p, \bar{r}_n')$, while the integral in equation (B.53) represents the reflected part $G^R(\bar{r}_p, \bar{r}_n')$. Substituting equation (B.53) in equation (4.43), we obtain the anomalous potential $V_a(\bar{r}_p)$. This anomalous potential can be shown as the sum of the whole space contribution $V_a^W(\bar{r}_p)$ [which includes whole space term $G^W(\bar{r}_p, \bar{r}_n')$]

and the reflection contribution $V_a^R(\bar{r}_p)$ [which includes reflected term $G^R(\bar{r}_p,\bar{r}_n')$] to the anomalous potential [see equation (4.91)]. For this transitional case of linearly changing resistivity with depth, the whole space part $V_a^W(\bar{r}_p)$ is computed using equation (4.92), which was given for the case of transitional case of exponentially varying resistivity with depth. Thus the computation of $V_a^W(\bar{r}_p)$ for these two cases is the same. The reflected part $V_a^R(\bar{r}_p)$ for the linear case of transitional layer is obtained by substituting the reflected term of Green's function $G^R(\bar{r}_p,\bar{r}_n')$ [i.e. the integral in equation (B.53)] in equation (4.43). Thus, we obtain

$$V_a^R(\bar{r}_p)=\frac{1}{4\pi}(1-k)\sum_{n=1}^{N}Q(\bar{r}_n')\Delta S.$$
$$\int_0^\infty \frac{[\rho_0 I_1(\frac{\lambda\rho_0}{\beta})K_0(\frac{\lambda\rho_0}{\beta})+\rho_2 I_0(\frac{\lambda\rho_0}{\beta})K_1(\frac{\lambda\rho_0}{\beta})]e^{-\lambda(z'-h_1)}-e^{-\lambda z'}\{[\rho^* I_1(\frac{\lambda\rho^*}{\beta})+}{[\rho^* I_1(\frac{\lambda\rho^*}{\beta})+\rho_2 I_0(\frac{\lambda\rho^*}{\beta})]K_0(\frac{\lambda\rho_0}{\beta})+[\rho^* K_1(\frac{\lambda\rho^*}{\beta})-\rho_2 K_0(\frac{\lambda\rho^*}{\beta})]I_0(\frac{\lambda\rho_0}{\beta})}$$
$$\frac{\rho_2 I_0(\frac{\lambda\rho^*}{\beta})]K_0(\frac{\lambda\rho_0}{\beta})+[\rho^* K_1(\frac{\lambda\rho^*}{\beta})-\rho_2 K_0(\frac{\lambda\rho^*}{\beta})]I_0(\frac{\lambda\rho_0}{\beta})\}}{}J_0(\lambda r_p)d\lambda.$$

(B.55)

The integral in equation (B.55) is solved using a digital linear filter for Hankel J_0 transforms.

The above formulation was developed for computation of the resistivity response where a 3-D body is situated in the lower half-space of a two-layered earth, with a transitional overburden layer in which the resistivity varies linearly with depth.

Appendix C

COMPUTER PROGRAMS

In this Appendix, two Fortran programs are presented.

The first program, trw3d.for, on page 237 computes the Wenner and two-electrode apparent resistivities, and also the corresponding apparent resistivity residual responses for a layered model containing an anomalous 3-D body under a transitional overburden of exponentially varying conductivity or resistivity with depth. By setting BETA in the input file of the program equal to zero, the responses for the case of a homogeneous overburden are obtained.

The second program, trs3d.for, on page 260 computes the Schlumberger and equatorial dipole-dipole apparent resistivities, and also the corresponding apparent resistivity residual responses for a layered model containing an anomalous 3-D body under a transitional overburden of exponentially varying conductivity or resistivity with depth. For this program also, by setting BETA in the input file of the program equal to zero, the responses for the case of a homogeneous overburden are obtained.

These two programs look very similar to each other as the basic equations used in the computations are the same, and only the geometry and design of these two programs are different. Although we could make them into one program, for research convenience we left them as separate programs.

```
C       ********************************************************************
C       *                                                                  *
C       * Program "trw3d.for" by Abolghasem Kamkar-Rouhani                 *
C       *                                                                  *
C       * This programme computes the Wenner and two-electrode             *
C       * apparent resistivities as well as the corresponding              *
C       * apparent resistivity residual responses.                         *
C       *                                                                  *
C       ********************************************************************
C
        PROGRAM MAIN
        EXTERNAL SEXP
        EXTERNAL ATAN2
C
        REAL MPOINT,MN,MPOT,NPOT
C
        REAL  A(152,152),DC(152),E(152),XA(152),XB(152),YA(152),
     *  YB(152),ZA(152),ZB(152),XLENTH(152),YLENTH(152),ZLENTH(152),
     *  KERNL(140), SURFAC(152),  X(152), Y(152), Z(152),  XELEC(205),
     *  YELEC(40), J0(120),  J1(140),  DGS(21),  XPLOT(40),  AII(152),
     *  AJ(152), VL(205,205), VB(205,205), V(205,205), APPR(205,205),
     *  APPREST(205,205), APPRESW(205,205,205), APPRDIF(205,205,205),
     *  AAR(152,152), SA(46209)
C
        INTEGER FIELD,SOURCE,ROW,COL,TYPEAB,TYPEMN,IJA(46209),NMAX
C
        DOUBLE PRECISION XD(152),DSA(46209)
C
C       For old filters: J0(61) and J1(14)
C
        CHARACTER*80 AA(10)
C
        OPEN ( 2,FILE= 'INTRW.3DR',STATUS= 'OLD')
        OPEN ( 1,FILE= 'OUTTRW.3DR',STATUS='UNKNOWN')
        OPEN ( 3,FILE= 'RESTRW.3D',STATUS='UNKNOWN')
C
        DATA DGS/.00004415,-.0007067,.00020028,-.00006335,.00051191,
     *      .00054246,.00200018,.00428432,.01082827,.02608353,.06171465,
     *      .14470387,.30370453,.53037187,.35186747,-.636663,.24659151,
     *      -.05591765,.01101434,-.0019857,.00023703/
C
C
        READ(2,1500) AA(1)
        READ(2,1)NELEM,NXELEC,NYELEC,LST,LEND,NMODEL,TYPEAB,TYPEMN
        READ(2,1500) AA(2)
        READ(2,2)(XA(I),XB(I),YA(I),YB(I),ZA(I),ZB(I),I=1,NELEM)
        READ(2,1500) AA(3)
        READ(2,7) (DC(I),I=1,NELEM)
        READ(2,1500) AA(4)
C        READ(2,3) (J0(I),I=1,61)
        READ(2,3) (J0(I),I=1,120)
        READ(2,1500) AA(5)
C        READ(2,4) (J1(I),I=1,14)
        READ(2,3) (J1(I),I=1,140)
        READ(2,1500) AA(6)
        READ(2,2) AB,THETA,MN,AMSEPA,XLEFT,XRIGHT
        READ(2,1500) AA(7)
        READ(2,2) (XELEC(I),I=1,NXELEC)
        READ(2,1500) AA(8)
        READ(2,2) (YELEC(I),I=1,NYELEC)
C
```

```
C         WRITE(1,2) (XA(I),XB(I),YA(I),YB(I),ZA(I),ZB(I),I=1,NELEM)
C
          WRITE(1,*) 'J0 filters'
          WRITE(1,823) (J0(I),I=1,120)
          WRITE(1,*) 'J1 filters'
          WRITE(1,823) (J1(I),I=1,140)
 823      FORMAT(3E19.11)
          ST= 0.0
          DO 119 I=1,120
          ST= ST + J0(I)
 119      CONTINUE
C
          WRITE(1,*) 'Sum of J0 filter weights'
          WRITE(1,*) ST
C
          SS= 0.0
          DO 118 I=1,140
          SS= SS+ J1(I)
 118      CONTINUE
          WRITE(1,*) 'Sum of J1 filter weights'
          WRITE(1,*) SS
C
          EPS=1.E-6
C
          DO 110 I=1,NELEM
          X(I)= (XA(I)+XB(I))/2.
          Y(I)= (YA(I)+YB(I))/2.
          Z(I)= (ZA(I)+ZB(I))/2.
          XLENTH(I)= ABS(XA(I)-XB(I))
          YLENTH(I)= ABS(YA(I)-YB(I))
          ZLENTH(I)= ABS(ZA(I)-ZB(I))
          IF(XLENTH(I).EQ.0.)SURFAC(I)=YLENTH(I)*ZLENTH(I)
          IF(YLENTH(I).EQ.0.)SURFAC(I)=XLENTH(I)*ZLENTH(I)
 110      IF(ZLENTH(I).EQ.0.)SURFAC(I)=XLENTH(I)*YLENTH(I)
          PI=3.14159265
          THETA=PI/180.*THETA
          PI2=2.*PI
          PI4=4.*PI
          AM1=AMSEPA
C
          READ(2,1500) AA(9)
          DO 333 IMODEL=1,NMODEL
C
          READ(2,209) RHO1,RHO2,RHOBDY,H1,BETA
C
C         If resistivity is continuous at the interface between the
C         the first and second layers, then
C          READ(2,209) RHO1,RHOBDY,H1,BETA
C          RHO2=RHO1*SEXP(-BETA*H1)
C
          WRITE(1,5)NELEM,TYPEAB,TYPEMN,RHO1,RHO2,RHOBDY,H1,BETA
          WRITE(*,5)NELEM,TYPEAB,TYPEMN,RHO1,RHO2,RHOBDY,H1,BETA
    5     FORMAT(////1X,24HNUMBER OF ELEMENTS USED=,I5,/1X,
         *  45HNO. OF ACTIVE CURRENT & POTENTIAL ELECTRODES=,2I10,
         *  /1X,39HRESISTIVITY OF OVERBURDEN,HOST & BODY =,3F10.2,2X,
         *  5HOHM-M,/1X,28HTHICKNESS OF THE OVERBURDEN=,F6.1,2X,6HMETERS,
         *  /1X,11HBETA VALUE=,F9.3)
C
          C=PI2*(RHOBDY+RHO2)/(RHOBDY-RHO2)
C         If RHOBDY=RHO2, then C=infinity. So, if this case is decided,
C         try to avoid the overflow problem by
```

```
C       choosing RHOBDY=RHO2 + or - 0.0001.
        RHOPI2=RHO1/((RHO1+RHO2)*PI2)
        ROW=1
        DO 101 FIELD=1,NELEM
        COL=1
        DO 100 SOURCE=1,NELEM
        XDIST=X(FIELD)-X(SOURCE)
        YDIST=Y(FIELD)-Y(SOURCE)
        ZDIST=Z(FIELD)-Z(SOURCE)
        XDIST2=XDIST*XDIST
        YDIST2=YDIST*YDIST
        ZDIST2=ZDIST*ZDIST
        RDIST=SQRT(XDIST2+YDIST2)
        IF(RDIST.EQ.0.)RDIST=0.1
        RDIST2=RDIST*RDIST
        RDIST3=RDIST2*RDIST
        RDIST4=RDIST3*RDIST
        XXA=X(FIELD)-XA(SOURCE)
        XXB=X(FIELD)-XB(SOURCE)
        YYA=Y(FIELD)-YA(SOURCE)
        YYB=Y(FIELD)-YB(SOURCE)
        ZZA=Z(FIELD)-ZA(SOURCE)
        ZZB=Z(FIELD)-ZB(SOURCE)
        ZH2D=Z(FIELD)+Z(SOURCE)-2.*H1
        XXA2=XXA*XXA
        XXB2=XXB*XXB
        YYA2=YYA*YYA
        YYB2=YYB*YYB
        ZZA2=ZZA*ZZA
        ZZB2=ZZB*ZZB
        XDYBZB=SQRT(XDIST2+YYB2+ZZB2)
        XDYBZA=SQRT(XDIST2+YYB2+ZZA2)
        XDYAZB=SQRT(XDIST2+YYA2+ZZB2)
        XDYAZA=SQRT(XDIST2+YYA2+ZZA2)
        XBYDZB=SQRT(XXB2+YDIST2+ZZB2)
        XAYDZB=SQRT(XXA2+YDIST2+ZZB2)
        XBYDZA=SQRT(XXB2+YDIST2+ZZA2)
        XAYDZA=SQRT(XXA2+YDIST2+ZZA2)
        XBYBZD=SQRT(XXB2+YYB2+ZDIST2)
        XAYBZD=SQRT(XXA2+YYB2+ZDIST2)
        XBYAZD=SQRT(XXB2+YYA2+ZDIST2)
        XAYAZD=SQRT(XXA2+YYA2+ZDIST2)
        XAZB=XXA*ZZB
        XBZA=XXB*ZZA
        XAZA=XXA*ZZA
        XBZB=XXB*ZZB
        YBZA=YYB*ZZA
        YAZB=YYA*ZZB
        YAZA=YYA*ZZA
        YBZB=YYB*ZZB
        XBYA=XXB*YYA
        XAYB=XXA*YYB
        XAYA=XXA*YYA
        XBYB=XXB*YYB
        AREA=SURFAC(SOURCE)
        IF(SOURCE.EQ.FIELD)GOTO 8
        IF(YLENTH(FIELD).EQ.0.)GOTO 94
        IF(XLENTH(FIELD).EQ.0.)GOTO 95
        IF(ZLENTH(FIELD).EQ.0.)GOTO 96
  94    IF(Y(FIELD).EQ.YA(SOURCE).AND.Y(FIELD).EQ.YB(SOURCE))GOTO 97
        IF(XLENTH(SOURCE).EQ.0.)PRIMRY=ALOG((ZZB+XDYBZB)*(ZZA+XDYAZA)
```

```
     *       /((ZZA+XDYBZA)*(ZZB+XDYAZB)))
             IF(YLENTH(SOURCE).EQ.0.)PRIMRY=
     *       ATAN(XAZB/(YDIST*XAYDZB))+ATAN(XBZA/(YDIST*XBYDZA))-ATAN(
     *       XAZA/(YDIST*XAYDZA))-ATAN(XBZB/(YDIST*XBYDZB))
 142         FORMAT(2F6.1,10X,3E12.4)
             IF(ZLENTH(SOURCE).EQ.0.)PRIMRY=ALOG((XXB+XBYBZD)*(XXA+XAYAZD)
     *       /((XXA+XAYBZD)*(XXB+XBYAZD)))
             GOTO 93
  95         IF(X(FIELD).EQ.XA(SOURCE).AND.X(FIELD).EQ.XB(SOURCE))GOTO 97
             IF(XLENTH(SOURCE).EQ.0.) PRIMRY=
     1       ATAN(YBZA/(XDIST*XDYBZA))+ATAN(YAZB/(XDIST*XDYAZB))
     2       -ATAN(YAZA/(XDIST*XDYAZA))-ATAN(YBZB/(XDIST*XDYBZB))
             IF(YLENTH(SOURCE).EQ.0.)PRIMRY=ALOG((ZZB+XBYDZB)*(ZZA+XAYDZA)
     1       /((ZZA+XBYDZA)*(ZZB+XAYDZB)))
             IF(ZLENTH(SOURCE).EQ.0.)PRIMRY=ALOG((YYB+XBYBZD)*(YYA+
     1       XAYAZD)/((YYA+XBYAZD)*(YYB+XAYBZD)))
  93         KLM=0
             MM=3
             MP=10
C             MT=14
             MT=140
             DS=ALOG(10.)/6.
             SHIFT=0.13433155
             AH=-7.91001919000
             SH= 0.0879671439570
             CALL KERNEL(KLM,MM,MP,DS,SHIFT,RDIST,RHO1,RHO2,H1,BETA,ZDIST,
     1       KERNL,ZH2D,AH,SH,MT)
             SECOND=0.
             K=MT+1
             DO 92 JONE=1,MT
C             NJ=K-JONE
C  92         SECOND=SECOND+KERNL(NJ)*J1(JONE)
  92         SECOND=SECOND+KERNL(JONE)*J1(JONE)
C             SECOND=AREA*SECOND/RDIST3
             SECOND=AREA*SECOND/RDIST2
             IF(YLENTH(FIELD).EQ.0.)SECOND=-YDIST*SECOND
             IF(XLENTH(FIELD).EQ.0.)SECOND=-XDIST*SECOND
             GOTO 91
  96         IF(Z(FIELD).EQ.ZA(SOURCE).AND.Z(FIELD).EQ.ZB(SOURCE)) GOTO 21
             IF(XLENTH(SOURCE).EQ.0.) PRIMRY=ALOG((YYB+XDYBZB)*(YYA+XDYAZA)
     1       /((YYA+XDYAZB)*(YYB+XDYBZA)))
             IF(YLENTH(SOURCE).EQ.0.) PRIMRY=ALOG((XXB+XBYDZB)*(XXA+XAYDZA)
     1       /((XXA+XAYDZB)*(XXB+XBYDZA)))
             IF(ZLENTH(SOURCE).EQ.0.) PRIMRY=
     1       ATAN(XBYA/(ZDIST*XBYAZD))+ATAN(XAYB/(ZDIST*XAYBZD))
     2       -ATAN(XAYA/(ZDIST*XAYAZD))-ATAN(XBYB/(ZDIST*XBYBZD))
             CALL DIGDAR(RDIST,J0,RHO1,RHO2,H1,ZDIST,ZH2D,AREA,SECOND)
C             WRITE(1,15) ROW,COL,PRIMRY,SECOND
  91         A(ROW,COL)=(PRIMRY+SECOND)*DC(FIELD)
C             WRITE(1,15) ROW,COL,PRIMRY,SECOND
             GOTO 99
  97         A(ROW,COL)=0.
             GOTO 99
  21         CALL DIGDAR(RDIST,J0,RHO1,RHO2,H1,ZDIST,ZH2D,AREA,SECOND)
C             WRITE(1,15) ROW,COL,PRIMRY,SECOND
             A(ROW,COL)=SECOND*DC(FIELD)
             GOTO 99
   8         IF(ZLENTH(SOURCE).GT.EPS) GOTO 98
             CALL DIGDAR(RDIST,J0,RHO1,RHO2,H1,ZDIST,ZH2D,AREA,SECOND)
             A(ROW,COL)=SECOND*DC(FIELD)-C
             GOTO 99
```

```
   98     A(ROW,COL)=-C
   99     COL=COL+1
C          WRITE(1,15)ROW,COL,PRIMRY,SECOND
  100     CONTINUE
C          WRITE(1,16) (A(ROW,II),II=1,NELEM)
          ROW=ROW+1
          WRITE (*,987) FIELD
  987     FORMAT(/20X,I3,' field point is completed for all elements')
  101     CONTINUE
          WRITE (*,986)
  986     FORMAT(///20X,' ******  Matrix A (N,N) is complete ******')
C         Matrix A (N,N) is the same matrix K in equation E=KQ
C         If the LU decomposition is used instead of the biconjugate
C         gradient method, then (N.B. it has not been used here):
C          CALL LUDCOM(A,NELEM)
C          WRITE( *,985)
C 985     FORMAT(///20X,'   ------  LU Decomposition is over ------')
          DO 82 IP=1,NELEM
C          WRITE(1,16) (A(IP,IC),IC=1,NELEM)
   82     CONTINUE
C
          DO 302 JY=1,NYELEC
C
          WRITE(1,301) YELEC(JY)
          WRITE(3,301) YELEC(JY)
C
          JI=1
          DO 700 IS=1,NXELEC
          DO 800 IR=1,NXELEC
          IF (IS .EQ. IR) GO TO 800
          IF (IS .GT. IR) GO TO 750
          BMSEPA=AM1-AB
          NXEL=NXELEC
C          DO 333 IK=LST,LEND
          IK=ABS(IS-IR)
          AMSEPA=IK*BMSEPA+AB
          IF(TYPEAB.EQ.1) AMSEPA=IK*AM1
          XM=XELEC(JI)+AMSEPA*COS(THETA)
          YM=YELEC(JI)+AMSEPA*SIN(THETA)
          XN=XM+MN*COS(THETA)
          YN=YM+MN*SIN(THETA)
          PPOTMN=0.
          GF=0.
          XELEJ=XELEC(JI)
          YELEJ=YELEC(JI)
          DO 109 NAB=1,TYPEAB
          IF(NAB-2) 83,84,84
   84     XELEJ=XELEJ+AB*COS(THETA)
          YELEJ=YELEJ+AB*SIN(THETA)
   83     XAM=XM-XELEJ
          YAM=YM-YELEJ
          XAN=XN-XELEJ
          YAN=YN-YELEJ
          AM=SQRT(XAM*XAM+YAM*YAM)
          AN=SQRT(XAN*XAN+YAN*YAN)
          GF=-GF-(1./AM-1./AN)
          IF(TYPEAB.EQ.1) GF=-GF
          IF(TYPEAB.EQ.1.AND.TYPEMN.EQ.1) GF=1./AM
          CALL PRIME (AM,AN,J0,DGS,RHO1,RHO2,H1,BETA,PI2,TYPEMN,PPMN)
C          WRITE(1,16)AM,AN,PPMN
          PPOTMN=-PPOTMN-PPMN
```

```
 109     CONTINUE
         IF(TYPEAB.EQ.1)PPOTMN=-PPOTMN
         VL(IS,IR)=PPOTMN
         GF=PI2/GF
         APPRLR=GF*PPOTMN
C        Thus, the primary layered-earth potential was computed.
C
         XM=XELEC(IS)+AMSEPA*COS(THETA)
         YM=YELEC(JY)+AMSEPA*SIN(THETA)
         XN=XM+MN*COS(THETA)
         YN=YM+MN*SIN(THETA)
         AELECT=XELEC(IS)
         BELECT=AELECT+AB*COS(THETA)
         ELECM=XM
         ELECN=XN
         POSA=XELEC(IS)
         POSM=XELEC(IR)
C         XPLOT(J)=(BELECT+XM)/2.
C         WRITE(1,6)AELECT,BELECT,ELECM,ELECN
         IF(BELECT.GE.XLEFT.AND.BELECT.LT.XRIGHT) GOTO 30
         IF(AELECT.GE.XLEFT.AND.AELECT.LT.XRIGHT) GO TO 30
 211     GOTO 112
  30     XM=AELECT
         XN=BELECT
         AELECT=ELECM
 112     DO 106 I=1,NELEM
         XELEJ=AELECT
         YELEJ=YELEC(JY)
         EINCI=0.
         DO 10 IELEC=1,TYPEAB
         IF(IELEC-2) 14,12,12
  12     XELEJ=XELEJ+AB*COS(THETA)
         YELEJ=YELEJ+AB*SIN(THETA)
C         IF(XELEC(J).GE.XLEFT.AND.XELEC(J).LT.XRIGHT)XELEJ=ELECN
  14     XSEPA=X(I)-XELEJ
         YSEPA=Y(I)-YELEJ
         ZSEPA=Z(I)
         RDIST=SQRT(XSEPA*XSEPA+YSEPA*YSEPA)
         IF(RDIST.EQ.0.)RDIST=1.E-6
         R2=RDIST*RDIST
         R3=R2*RDIST
         DIST=SQRT(XSEPA*XSEPA+YSEPA*YSEPA+ZSEPA*ZSEPA)
         DIST3=DIST*DIST*DIST
         IF(XLENTH(I).EQ.0. .OR. YLENTH(I).EQ.0.) GOTO 102
         IF(ZLENTH(I).EQ.0.) GOTO 104
 102     IF(XSEPA.EQ.0.) GOTO 9
         MM=3
         MP=10
C         MT=14
         MT=140
         DS=ALOG(10.)/6.
         SHIFT=0.1343155
         AH=-7.91001919000
         SH= 0.0879671439570
         CALL XYINKR(MM,MP,DS,SHIFT,RDIST,RHO1,RHO2,H1,BETA,ZSEPA,KERNL,
     $               AH,SH,MT)
         SECINC=0.
         K=MT+1
         DO 105 JONE=1,MT
C         NJ=K-JONE
C 105     SECINC=SECINC+KERNL(NJ)*J1(JONE)
```

```
 105     SECINC=SECINC+KERNL(JONE)*J1(JONE)
C         SECINC=SECINC/R3
         SECINC=SECINC/R2
         PRINC=1./DIST3
C        WRITE(1,1) I
C        WRITE(1,16) XELEJ,PRINC,SECINC
         IF(YLENTH(I).EQ.0.)EINC=RHO1*YSEPA*(1./DIST3+SECINC)
         IF(XLENTH(I).EQ.0.)EINC=RHO1*XSEPA*(1./DIST3+SECINC)
         GOTO 10
   9     EINC=0.
         GOTO 10
 104     MM=30
         MP=30
C         MT=61
         MT=120
         DS=ALOG(10.)/10.
         SHIFT=0.00424
         AH=-8.38850000000
         SH= 0.0904226468670
         CALL ZINCKR(MM,MP,DS,SHIFT,RDIST,RHO1,RHO2,H1,BETA,ZSEPA,KERNL,
     $               AH,SH,MT)
         SECINC=0.
         K=62
C         DO 107 JZERO=1,61
         DO 107 JZERO=1,MT
C         NJ=K-JZERO
C 107     SECINC=SECINC+KERNL(NJ)*J0(JZERO)
 107     SECINC=SECINC+KERNL(JZERO)*J0(JZERO)
         PRINC=ZSEPA/DIST3
         EINC=RHO1*(PRINC+SECINC/RDIST)
C         WRITE(1,1) I
C         WRITE(1,16) XELEJ,PRINC,SECINC
  10     EINCI=-EINCI-EINC
         E(I)=EINCI*DC(I)
         IF(TYPEAB.EQ.1) E(I)=EINC*DC(I)
C         WRITE(1,16) E(I)
 106     CONTINUE
C        Thus, the vector matrix E was computed.
C         WRITE(1,19) XELEC(J),(E(NG),NG=1,NELEM)
  19     FORMAT(2X,7E11.4)
C
         IF((XELEC(IS) .EQ. 0.) .AND. (IR .EQ. (IS+1))) THEN
         WRITE(1,263) (E(NG),NG=1,NELEM)
 263     FORMAT(/2X,'S.P.=0 & E =',6F11.8)
         ELSE
         ENDIF
C         CALL FIELDS(A,E,NELEM)
         CALL XSPRSIN(A,NELEM,NMAX,DSA,IJA)
C
         CALL XLINBCG(NELEM,NMAX,DSA,IJA,E,XD)
C
         WRITE(*,984) IS
C         WRITE(*,984) J
 984     FORMAT(//,'** surface charges of the elements are completed ',
     *   'for ',I3,' source position(s)')
C
         DO 178 IEN=1, NELEM
         E(IEN)=SNGL(XD(IEN))
 178     CONTINUE
C
C         WRITE(1,26) XELEC(J),(E(KI),KT=1,NELEM)
```

```
  26    FORMAT(//4X,F6.0/,6E11.4///)
C       Thus, column vector matrix Q was computed.
  17    SPOTMN=0.
        DO 1006 IELEM=1,NELEM
        CALL WHOLSP(IELEM,X,Y,Z,XM,YM,XN,YN,XA,XB,YA,YB,ZA,ZB,TYPEAB,
     *      TYPEMN,XLENTH,ZLENTH,WHOLMN,YLENTH)
        IF ( IELEM. EQ. NELEM) WRITE(*,980)
 980    FORMAT('** Primary potential at MN is completed')
        ZSC=Z(IELEM)
        XEM=XM-X(IELEM)
        YEM=YM-Y(IELEM)
        XEN=XN-X(IELEM)
        YEN=YN-Y(IELEM)
C        WRITE(1,16) XEM,XEN,YEM,YEN,ZSC,RHO1,RHO2
        CALL SCAT(XEM,YEM,XEN,YEN,ZSC,J0,H1,BETA,TYPEMN,RHO1,RHO2,
     *            SCATMN)
        AREA=SURFAC(IELEM)
        ERHO=E(IELEM)*RHOPI2
        SCATMN=SCATMN*AREA
C
        IF ( IELEM .EQ. NELEM) WRITE(*,979)
 979    FORMAT('** Scattered potential at MN is completed')
        AII(IELEM)=SCATMN
        AJ(IELEM)=WHOLMN
        TOT=WHOLMN+SCATMN
        PRO=TOT*E(IELEM)
C        WRITE(1,142) XM,XN,TOT,E(IELEM),PRO
        SPOTMN=SPOTMN+(WHOLMN+SCATMN)*ERHO
 1006   CONTINUE
        WRITE(*,983) IS
C        WRITE(*,983) J
 983    FORMAT('** Total potential for current electrode position = ',
     *  I3,' is completed')
C        WRITE(1,161)  ((AII(IEE),IEE=1,NELEM),(AJ(IEE),IEE=1,NELEM))
 161    FORMAT(8E12.4)
C        WRITE(*,981) XPLOT(J) , J
 981    FORMAT('**APPARENT RESISTIVITY AT ',F5.0,' meters FOR CURRENT',
     *  ' ELECTRODE POSITION = ',I3)
        VB(IS,IR)=SPOTMN
C
        V(IS,IR)=VL(IS,IR) + VB(IS,IR)
        TOTLMN=PPOTMN+SPOTMN
C       Thus, the total potential was computed.
C        APPR(J)=TOTLMN*GF
        APPR(IS,IR)=TOTLMN*GF
        WRITE(1,350) IS, IR, XELEC(IS), XELEC(IR), VL(IS,IR),
     *               VB(IS,IR), V(IS,IR)
        GO TO 800
C
 350    FORMAT(2X,2I3,2X,2F9.2,2X,3F15.10)
   6    FORMAT(//8X,4F8.1)
 301    FORMAT(//4X,17HPROFILE OFF-SET =,F6.1,2X,6HMETERS/)
C
 750    VL(IS,IR)=VL(IR,IS)
        VB(IS,IR)=VB(IR,IS)
        V(IS,IR)=V(IR,IS)
        WRITE(1,350) IS, IR, XELEC(IS), XELEC(IR), VL(IS,IR),
     *               VB(IS,IR), V(IS,IR)
 800    CONTINUE
 700    CONTINUE
C
```

```
      CALL APPRTWO (NXELEC, NYELEC, XELEC, IS, IR, AM1, V)
      CALL APPRWEN (NXELEC, NYELEC, XELEC, IS, IR, AM1, V)
C
      CALL DIFAPPR (NXELEC, NYELEC, XELEC, IS, IR, AM1, V,
     $              APPREST, APPRESW)
C
 302  CONTINUE
 333  CONTINUE
   1  FORMAT(8I10)
   2  FORMAT(12F6.0)
  22  FORMAT(6F6.0)
 222  FORMAT(3F6.0,F7.2)
 209  FORMAT(4F6.0,F9.3)
C 209  FORMAT(3F6.0,F8.2)
C   3  FORMAT(8F10.6)
   3  FORMAT(3E19.11)
   4  FORMAT(8F10.4)
   7  FORMAT(20F4.0)
  15  FORMAT(2I4,10E11.4)
  16  FORMAT(10F8.2)
1500  FORMAT(A80)
 150  STOP
      END
C
C
C     If the LU decomposition method is used, then
C     (N.B. it has not been used here):
C      SUBROUTINE LUDCOM(A,N)
C      This subroutine uses the LU decomposition method (unused).
C      INTEGER R
C      REAL A(152,152)
C      R=1
C      LP=R+1
C      DO 80 J=LP,N
C      A(J,R)=A(J,R)/A(R,R)
C  80  CONTINUE
C      DO 70 R=2,N
C      DO 40 M=R,N
C      SUMROW=0.
C      SUM COL=0.
C      LM=R-1
C      DO 30 I=1,LM
C      SUMROW=SUMROW+A(R,I)*A(I,M)
C      IF(M.EQ.N) GOTO 30
C      SUMCOL=SUMCOL+A(I,R)*A(M+1,I)
C  30  CONTINUE
C      A(R,M)=A(R,M)-SUMROW
C      IF(M.EQ.N) GOTO 40
C      A(M+1,R)=A(M+1,R)-SUMCOL
C  40  CONTINUE
C      IF(R.EQ.N) GOTO 70
C      LP=R+1
C      DO 60 J=LP,N
C  60  A(J,R)=A(J,R)/A(R,R)
C  70  CONTINUE
C      RETURN
C      END
C
C      SUBROUTINE FIELDS(A,B,N)
C      This subroutine evaluate Q by the LU decomposition method
C     (unused).
```

```
C         REAL A(152,152),B(152)
C         DO 101 J=2,N
C         SUM=0.
C         L=J-1
C         DO 100 I=1,L
C 100     SUM=SUM+A(J,I)*B(I)
C 101     B(J)=B(J)-SUM
C         B(N)=B(N)/A(N,N)
C         J=N-1
C         LL=1
C  80     SUM=0.
C         N1=N
C         DO 90 I=1,LL
C         SUM=SUM+A(J,N1)*B(N1)
C         N1=N1-1
C  90     CONTINUE
C         B(J)=(B(J)-SUM)/A(J,J)
C         J=J-1
C         LL=LL+1
C         IF(J.GE.1) GOTO 80
C         RETURN
C         END
C
          SUBROUTINE XSPRSIN(A,NELEM,NMAX,DSA,IJA)
C         This subroutine converts matrix A (=K) from 2-D to two
C         1-D matrices.
          REAL A(152,152),AAR(152,152),SA(46209)
          INTEGER NP,NMAX,I,J,MSIZE,IJA(46209)
          DOUBLE PRECISION DA(152,152),DAA(152,152),DSA(46209),THRESH
          NP=NELEM
          NMAX=2*NP*NP+1
          DO 171 J=1,NP
            DO 172 I=1,NP
            DA(I,J)=DBLE(A(I,J))
 172        CONTINUE
 171      CONTINUE
C
          THRESH=1.D-9
          CALL SPRSIN(DA,NP,NP,THRESH,NMAX,DSA,IJA)
          MSIZE=IJA(IJA(1)-1)-1
          SA(NP+1)=0.0
          DSA(NP+1)=0.D0
C          WRITE(*,'(T4,A,T18,A,T24,A)') 'INDEX','IJA','DSA'
C          WRITE(1,'(T4,A,T18,A,T24,A)') 'INDEX','IJA','DSA'
          DO 11 I=1,MSIZE
C          WRITE(*,'(T2,I4,T16,I4,T20,F16.9)') I,IJA(I),DSA(I)
C          WRITE(1,'(T2,I4,T16,I4,T20,F16.9)') I,IJA(I),DSA(I)
  11      CONTINUE
          DO 13 I=1,NP
            DO 12 J=1,NP
             DAA(I,J)=0.D0
  12        CONTINUE
  13      CONTINUE
          DO 15 I=1,NP
            DAA(I,I)=DSA(I)
              DO 14 J=IJA(I),IJA(I+1)-1
                DAA(I,IJA(J))=DSA(J)
  14          CONTINUE
  15       CONTINUE
C          WRITE(*,*)'ORIGINAL MATRIX:'
C          WRITE(1,*)'ORIGINAL MATRIX:'
```

```
C         WRITE(*,'(5F12.6)') ((DA(I,J),J=1,NP),I=1,NP)
C         WRITE(1,'(5F12.6)') ((DA(I,J),J=1,NP),I=1,NP)
C         WRITE(*,*)'RECONSTRUCTED MATRIX:'
C         WRITE(1,*)'RECONSTRUCTED MATRIX:'
C         WRITE(*,'(5F12.6)') ((DAA(I,J),J=1,NP),I=1,NP)
C         WRITE(1,'(5F12.6)') ((DAA(I,J),J=1,NP),I=1,NP)
          RETURN
          END
C
          SUBROUTINE SPRSIN(DA,N,NP,THRESH,NMAX,DSA,IJA)
C         This subroutine is related to subroutine XSPRSIN.
          INTEGER N,NMAX,NP,IJA(46209)
          DOUBLE PRECISION THRESH,DA(152,152),DSA(46209)
          INTEGER I,J,K
          N=NP
          DO 11 J=1,N
          DSA(J)=DA(J,J)
 11       CONTINUE
          IJA(1)=N+2
          K=N+1
          DO 13 I=1,N
          DO 12 J=1,N
           IF(ABS(DA(I,J)).GE.THRESH)THEN
              IF(I.NE.J)THEN
                K=K+1
                IF(K.GT.NMAX)PAUSE 'NMAX TOO SMALL IN SPRSIN'
                DSA(K)=DA(I,J)
                IJA(K)=J
              ENDIF
           ENDIF
 12       CONTINUE
          IJA(I+1)=K+1
 13       CONTINUE
          RETURN
          END
C
          SUBROUTINE XLINBCG(NELEM,NMAX,DSA,IJA,E,XD)
C         This subroutine evaluates vector matrix Q using the
C         biconjugate gradient method.
          INTEGER NP,NMAX,ITOL,ITMAX,I,ITER,IJA(46209)
          REAL E(152)
          DOUBLE PRECISION TOL,B(152),DE(152),XD(152),BCMP(152),ERR,
     $    DSA(46209)
          NP=NELEM
          NMAX=2*NP*NP+1
          ITOL=1
          TOL=1.D-9
          ITMAX=4*NP
C
          DO 173 I=1,NP
          DE(I)=DBLE(E(I))
 173      CONTINUE
          DO 17 IJO=1,NP
          B(IJO)=DE(IJO)
  17      CONTINUE
          DO 11 I=1,NP
          XD(I)=0.D0
C         B(I)=1.D0
  11      CONTINUE
          CALL LINBCG(NP,NMAX,B,XD,ITOL,TOL,ITMAX,ITER,ERR,DSA,IJA)
          WRITE(*,'(/1X,A,E15.6)') 'ESTIMATED ERROR:',ERR
```

```
      WRITE(1,'(/1X,A,E15.6)') 'ESTIMATED ERROR:',ERR
      WRITE(*,'(/1X,A,I6)') 'ITERATIONS NEEDED:',ITER
      WRITE(1,'(/1X,A,I6)') 'ITERATIONS NEEDED:',ITER
C      WRITE(*,'(/1X,A)') 'SOLUTION VECTOR:'
C      WRITE(1,'(/1X,A)') 'SOLUTION VECTOR:'
C      WRITE(*,'(/1X,5F12.6)') (XD(I),I=1,NP)
C      WRITE(1,'(/1X,5F12.6)') (XD(I),I=1,NP)
      CALL DSPRSAX(DSA,IJA,XD,BCMP,NP)
C      THIS IS A DOUBLE PRECISION VERSION OF SPRSAX
C      WRITE(*,'(/1X,A/T8,A,T22,A)') 'TEST OF SOLUTION VECTOR:',
C     $       'A*X','B'
C      WRITE(1,'(/1X,A/T8,A,T22,A)') 'TEST OF SOLUTION VECTOR:',
C     $       'A*X','B'
      DO 12 I=1,NP
C      WRITE(*,'(1X,2F12.6)') BCMP(I),B(I)
C      WRITE(1,'(1X,2F12.6)') BCMP(I),B(I)
 12   CONTINUE
      RETURN
      END
C
      SUBROUTINE LINBCG(N,NMAX,B,XD,ITOL,TOL,ITMAX,ITER,ERR,DSA,IJA)
C     This subroutine is related to subroutine XLINBCG.
      INTEGER ITER,ITMAX,ITOL,N,NMAX,IJA(46209),J
      DOUBLE PRECISION ERR,TOL,B(*),XD(*),EPS
      DOUBLE PRECISION AK,AKDEN,BK,BKDEN,BKNUM,BNRM,DXNRM,XNRM,ZM1NRM,
     *  ZNRM,P(46209),PP(46209),R(46209),RR(46209),ZD(46209),ZZ(46209),
     *  SNRM,DSA(46209)
      EPS=1.D-14
      ITER=0
      CALL ATIMES(N,XD,R,0,DSA,IJA)
      DO 11 J=1,N
      R(J)=B(J)-R(J)
      RR(J)=R(J)
 11   CONTINUE
      ZNRM=1.D0
      IF(ITOL.EQ.1) THEN
      BNRM=SNRM(N,B,ITOL)
      ELSE IF (ITOL.EQ.2) THEN
      CALL ASOLVE(N,B,ZD,0,DSA,IJA)
      BNRM=SNRM(N,ZD,ITOL)
      ELSE IF (ITOL.EQ.3.OR.ITOL.EQ.4) THEN
      CALL ASOLVE(N,B,ZD,0,DSA,IJA)
      BNRM=SNRM(N,ZD,ITOL)
      CALL ASOLVE(N,R,ZD,0,DSA,IJA)
      ZNRM=SNRM(N,ZD,ITOL)
      ELSE
      PAUSE 'ILLEGAL ITOL IN LINBCG'
      ENDIF
      CALL ASOLVE(N,R,ZD,0,DSA,IJA)
 100  IF (ITER.LE.ITMAX) THEN
      ITER=ITER+1
      ZM1NRM=ZNRM
      CALL ASOLVE(N,RR,ZZ,1,DSA,IJA)
      BKNUM=0.D0
      DO 12 J=1,N
        BKNUM=BKNUM+ZD(J)*RR(J)
 12   CONTINUE
      IF(ITER.EQ.1) THEN
        DO 13 J=1,N
          P(J)=ZD(J)
          PP(J)=ZZ(J)
```

```
 13       CONTINUE
        ELSE
          BK=BKNUM/BKDEN
          DO 14 J=1,N
            P(J)=BK*P(J)+ZD(J)
            PP(J)=BK*PP(J)+ZZ(J)
 14       CONTINUE
        ENDIF
        BKDEN=BKNUM
        CALL ATIMES(N,P,ZD,0,DSA,IJA)
        AKDEN=0.D0
        DO 15 J=1,N
          AKDEN=AKDEN+ZD(J)*PP(J)
 15     CONTINUE
        AK=BKNUM/AKDEN
        CALL ATIMES(N,PP,ZZ,1,DSA,IJA)
        DO 16 J=1,N
          XD(J)=XD(J)+AK*P(J)
          R(J)=R(J)-AK*ZD(J)
          RR(J)=RR(J)-AK*ZZ(J)
 16     CONTINUE
        CALL ASOLVE(N,R,ZD,0,DSA,IJA)
        IF(ITOL.EQ.1.OR.ITOL.EQ.2)THEN
          ZNRM=1.D0
          ERR=SNRM(N,R,ITOL)/BNRM
        ELSE IF(ITOL.EQ.3.OR.ITOL.EQ.4)THEN
          ZNRM=SNRM(N,ZD,ITOL)
          IF(ABS(ZM1NRM-ZNRM).GT.EPS*ZNRM) THEN
            DXNRM=ABS(AK)*SNRM(N,P,ITOL)
            ERR=ZNRM/ABS(ZM1NRM-ZNRM)*DXNRM
          ELSE
            ERR=ZNRM/BNRM
            GOTO 100
          ENDIF
          XNRM=SNRM(N,XD,ITOL)
          IF(ERR.LE.0.5D0*XNRM) THEN
            ERR=ERR/XNRM
          ELSE
            ERR=ZNRM/BNRM
            GOTO 100
          ENDIF
        ENDIF
C        WRITE (*,*) ' ITER=',ITER,' ERR=',ERR
C        WRITE (1,*) ' ITER=',ITER,' ERR=',ERR
        IF(ERR.GT.TOL) GOTO 100
        ENDIF
        RETURN
        END
C
        FUNCTION SNRM(N,SX,ITOL)
        INTEGER N,ITOL,I,ISAMAX
        DOUBLE PRECISION SX(*),SNRM
        IF(ITOL .LE. 3) THEN
        SNRM=0.D0
        DO 11 I=1,N
        SNRM=SNRM+SX(I)**2
 11     CONTINUE
        SNRM=SQRT(SNRM)
        ELSE
        ISAMAX=1
        DO 12 I=1,N
```

```
      IF(ABS(SX(I)).GT.ABS(SX(ISAMAX))) ISAMAX=I
 12   CONTINUE
      SNRM=ABS(SX(ISAMAX))
      ENDIF
      RETURN
      END
C
      SUBROUTINE ATIMES(N,XD,R,ITRNSP,DSA,IJA)
C     This subroutine is related to subroutine LINBCG.
      INTEGER N,ITRNSP,IJA(*),NMAX
      DOUBLE PRECISION XD(*),R(*),DSA(*)
      NMAX=2*N*N+1
      IF (ITRNSP.EQ.0) THEN
      CALL DSPRSAX(DSA,IJA,XD,R,N)
      ELSE
      CALL DSPRSTX(DSA,IJA,XD,R,N)
      ENDIF
      RETURN
      END
C
      SUBROUTINE ASOLVE(N,B,XD,ITRNSP,DSA,IJA)
C     This subroutine is related to subroutine LINBCG.
      INTEGER N,ITRNSP,IJA(*),NMAX,I
      DOUBLE PRECISION XD(*),B(*),DSA(*)
      NMAX=2*N*N+1
      DO 11 I=1,N
      XD(I)=B(I)/DSA(I)
 11   CONTINUE
      RETURN
      END
C
      SUBROUTINE DSPRSAX(DSA,IJA,XD,B,N)
C     This subroutine is related to subroutine XLINBCG.
      INTEGER N,IJA(*)
      DOUBLE PRECISION B(*),DSA(*),XD(*)
      INTEGER I,K
      IF (IJA(1).NE.N+2) PAUSE 'MISMATCHED VECTOR AND MATRIX IN
     $ SPRSAX'
      DO 12 I=1,N
      B(I)=DSA(I)*XD(I)
      DO 11 K=IJA(I),IJA(I+1)-1
        B(I)=B(I)+DSA(K)*XD(IJA(K))
 11   CONTINUE
 12   CONTINUE
      RETURN
      END
C
      SUBROUTINE DSPRSTX(DSA,IJA,XD,B,N)
C     This subroutine is related to subroutine ATIMES.
      INTEGER N,IJA(*)
      DOUBLE PRECISION B(*),DSA(*),XD(*)
      INTEGER I,J,K
      IF (IJA(1).NE.N+2) PAUSE 'MISMATCHED VECTOR AND MATRIX IN
     $ SPRSTX'
      DO 11 I=1,N
      B(I)=DSA(I)*XD(I)
 11   CONTINUE
      DO 13 I=1,N
      DO 12 K=IJA(I),IJA(I+1)-1
        J=IJA(K)
        B(J)=B(J)+DSA(K)*XD(I)
```

```
 12     CONTINUE
 13     CONTINUE
        RETURN
        END
C
        SUBROUTINE XYINKR(MM,MP,DS,SHIFT,RDIST,RHO1,RHO2,H1,BETA,Z,KRNL,
     $                    AH,SH,MT)
C       This subroutine computes the kernel for E (x- and y-components).
        REAL KRNL(140),LAMDA
        EXTERNAL SEXP
        DO 447 I=1,MT
        RT1= (AH + (I-1)*SH)
        RT2= (10.0)**RT1
        LAMDA=(1./RDIST)*RT2
        EXD=SEXP(-2.*LAMDA*H1)
        EXZ=SEXP(-LAMDA*Z)
        EXDK1=K1*EXD
        M=-MP
C  1     EP=RDIST*SEXP(FLOAT(M)*DS-SHIFT)
C        LAMDA=1./EP
        SIGMA0=1./RHO1
        SIGMA2=1./RHO2
        BETL=SQRT((BETA*BETA)+(4.*LAMDA*LAMDA))
        ALPHA1=(-BETA+BETL)/2.
        ALPHA2=(-BETA-BETL)/2.
        EXDLA2=SEXP(H1*(ALPHA2+LAMDA))
        EXDB=SEXP(BETA*H1)
        EXDA1M=SEXP(-ALPHA1*H1)
        EXDA2=SEXP(ALPHA2*H1)
        STERM1=2.*LAMDA*(ALPHA1-ALPHA2)*SIGMA0*EXDB*EXDLA2
        STERM2=(LAMDA*ALPHA1*SIGMA2+ALPHA1*ALPHA2*SIGMA0*EXDB)*
     $         EXDA2*EXDA1M
        STERM3=(LAMDA*ALPHA2*SIGMA2+ALPHA1*ALPHA2*SIGMA0*EXDB)
C       I=M+MP+1
        KRNL(I)=(EXZ*(STERM1-STERM2+STERM3))/(STERM2-STERM3)
C        M=M+1
C        IF(M.LE.MM) GOTO 1
 447    CONTINUE
        RETURN
        END
C
        SUBROUTINE ZINCKR(MM,MP,DS,SHIFT,RDIST,RHO1,RHO2,H1,BETA,Z,KRNL,
     $                    AH,SH,MT)
C       This subroutine computes Kernel for E (z-component).
C        REAL KRNL(61),LAMDA,K1
        REAL KRNL(140),LAMDA
        EXTERNAL SEXP
C        K1=(RHO2-RHO1)/(RHO2+RHO1)
C        M=-MP
C   1    EP=RDIST*SEXP(FLOAT(M)*DS-SHIFT)
C        LAMDA=1./EP
        DO 448 I=1,MT
        RT1= (AH + (I-1)*SH)
        RT2= (10.0)**RT1
C        RLAMB(I)= (1./R)*RT2
        LAMDA=(1./RDIST)*RT2
        SIGMA0=1./RHO1
        SIGMA2=1./RHO2
        BETL=SQRT((BETA*BETA)+(4.*LAMDA*LAMDA))
        ALPHA1=(-BETA+BETL)/2.
        ALPHA2=(-BETA-BETL)/2.
```

```
      EXDLA2=SEXP(H1*(ALPHA2+LAMDA))
      EXDB=SEXP(BETA*H1)
      EXDA1M=SEXP(-ALPHA1*H1)
      EXDA2=SEXP(ALPHA2*H1)
      EXZ=SEXP(-LAMDA*Z)
      STERM1=2.*LAMDA*(ALPHA1-ALPHA2)*SIGMA0*EXDB*EXDLA2
      STERM2=(LAMDA*ALPHA1*SIGMA2+ALPHA1*ALPHA2*SIGMA0*EXDB)*
     $        EXDA2*EXDA1M
      STERM3=(LAMDA*ALPHA2*SIGMA2+ALPHA1*ALPHA2*SIGMA0*EXDB)
C      I=M+MP+1
      KRNL(I)=LAMDA*(EXZ*(STERM1-STERM2+STERM3))/(STERM2-STERM3)
C      M=M+1
C      IF(M.LE.MM) GOTO 1
 448  CONTINUE
      RETURN
      END
C
      SUBROUTINE DIGDAR(RD,J0,R1,R2,H,Z,ZH,AREA,SECOND)
C     This subroutine computes the kernel function for z-component of
C     reflected part of Gamma.
      REAL KERNL(61),J0(61)
      KLM=10
      MM=30
      RHO1=R1
      RHO2=R2
      ZDIST=Z
      H1=H
      ZH2D=ZH
      MP=30
      SHIFT=0.00424
      DS=ALOG(10.)/10.
      AH=-8.38850000000
      SH=0.0904226468670
      RDIST=RD
C      MT=61
      MT=120
      CALL KERNEL(KLM,MM,MP,DS,SHIFT,RDIST,RHO1,RHO2,H1,BETA,ZDIST,
     *  KERNL,ZH2D,AH,SH,MT)
      SECOND=0.
C      K=62
C      DO 90 JZERO=1,61
      DO 90 JZERO=1,MT
C      NJ=K-JZERO
C  90  SECOND=SECOND+KERNL(NJ)*J0(JZERO)
  90  SECOND=SECOND+KERNL(JZERO)*J0(JZERO)
      SECOND=-AREA*SECOND/RDIST
      RETURN
      END
C
      SUBROUTINE KERNEL(KLM,MM,MP,DS,SHIFT,RDIST,RHO1,RHO2,H1,BETA,
     *  ZDIST,KRNL,ZH2D,AH,SH,MT)
C     This subroutine computes the kernel function for computation of
C     reflected part of Gamma.
C      REAL KRNL(61),LAMDA,K1
      REAL KRNL(140),LAMDA
      EXTERNAL SEXP
C      K1=(RHO2-RHO1)/(RHO2+RHO1)
C       M=-MP
C    1  EP=RDIST*SEXP(FLOAT(M)*DS-SHIFT)
C       LAMDA=1./EP
      DO 446 I=1,MT
```

```
      RT1= (AH + (I-1)*SH)
      RT2= (10.0)**RT1
C      RLAMB(I)= (1./R)*RT2
      LAMDA=(1./RDIST)*RT2
C      EX=SEXP(-2.*LAMDA*H1)
      SIGMA0=1./RHO1
      SIGMA2=1./RHO2
      BETL=SQRT((BETA*BETA)+(4.*LAMDA*LAMDA))
      ALPHA1=(-BETA+BETL)/2.
      ALPHA2=(-BETA-BETL)/2.
C      EXDL=SEXP(LAMDA*H1)
      EXDB=SEXP(BETA*H1)
C      EXDA1=SEXP(ALPHA1*H1)
      EXDA1M=SEXP(-ALPHA1*H1)
      EXDA2=SEXP(ALPHA2*H1)
C      EXZ=SEXP(-LAMDA*Z)
      EXZH2D=SEXP(-LAMDA*ZH2D)
      GTERM1=((LAMDA*SIGMA2)-(ALPHA1*SIGMA0*EXDB))*ALPHA2
      GTERM2=((LAMDA*SIGMA2)-(ALPHA2*SIGMA0*EXDB))*ALPHA1
      GTERM3=(GTERM1*EXZH2D)-(GTERM2*EXZH2D*EXDA2*EXDA1M)
      GTERM4=((LAMDA*SIGMA2)+(ALPHA1*SIGMA0*EXDB))*ALPHA2
      GTERM5=((LAMDA*SIGMA2)+(ALPHA2*SIGMA0*EXDB))*ALPHA1
C     I=M+MP+1
      KRNL(I)=GTERM3/(GTERM4-(GTERM5*EXDA2*EXDA1M))
      IF(KLM.EQ.10)KRNL(I)=LAMDA*KRNL(I)
C      M=M+1
C      IF(M.LE.MM) GOTO 1
 446  CONTINUE
      RETURN
      END
C
      SUBROUTINE PRIME (S,S1,J0,DGS,RHO1,RHO2,H1,BETA,PI2,
     $                  TYPEMN,POTMN)
C     This subroutine computes the primary layered-earth potential.
      INTEGER TYPEMN
      REAL J0(120),DGS(21),T(120),R(2),H(1),LAMDA
C      REAL J0(61),DGS(21),T(61),R(2),H(1)
      EXTERNAL SEXP
      N=2
      R(1)=RHO1
      R(2)=RHO2
      H(1)=H1
      MM=30
      MP=30
C      MN=61
      MN=120
      SHIFT=0.00424
      DS=ALOG(10.)/10.
C      MM=11
C      MP=9
C      MN=21
C      SHIFT=-.175072768
C      DS=ALOG(10.)/5.16500849
      AH=-8.38850000000
      SH=0.0904226468670
      AM=S
      DO 50 L=1,TYPEMN
C        M=-MP
C    8   EP=AM*SEXP(FLOAT(M)*DS-SHIFT)
      DO 454 I=1,MN
      RT1= (AH + (I-1)*SH)
```

```
      RT2= (10.0)**RT1
C      RLAMB(I)= (1./R)*RT2
      LAMDA=(1./AM)*RT2
C        NN=N
C        TN=R(NN)
C        DTN=0.
      SIGMA0=1./RHO1
      SIGMA2=1./RHO2
      BETL=SQRT((BETA*BETA)+(4.*LAMDA*LAMDA))
      ALPHA1=(-BETA+BETL)/2.
      ALPHA2=(-BETA-BETL)/2.
C      EXDL=SEXP(LAMDA*H1)
      EXDB=SEXP(BETA*H1)
CC       EXDA1=SEXP(ALPHA1*H1)
      EXDA2=SEXP(ALPHA2*H1)
C      EXZ=SEXP(-LAMDA*Z)
      EXDA1M=SEXP(-ALPHA1*H1)
      EXDA2A1=SEXP((ALPHA2-ALPHA1)*H1)
      PTERM1=(LAMDA*SIGMA2)+(ALPHA2*SIGMA0*EXDB)
      PTERM2=(LAMDA*SIGMA2)+(ALPHA1*SIGMA0*EXDB)
      PTERM3=(PTERM1/PTERM2)*EXDA2*EXDA1M
C     I=M+MP+1
      T(I)=(LAMDA*(1.-PTERM3))/((ALPHA1*PTERM3)-ALPHA2)
C
C      M=M+1
C      IF(M.LE.MM) GOTO 8
 454    CONTINUE
      POT=0.
C      K=22
      K=62
      DO 9 J=1,MN
   9  POT=POT+T(K-J)*J0(J)
      IF(L.EQ.2) GOTO 50
C      POTM=POT/(PI2*AM*AM)
      POTM=POT/(PI2*SIGMA0*AM)
      AM=S1
  50  CONTINUE
C      POTN=POT/(PI2*AM*AM)
      POTN=POT/(PI2*SIGMA0*AM)
      IF(TYPEMN.EQ.1)POTN=0.
      POTMN=POTM-POTN
      RETURN
      END
C
      SUBROUTINE WHOLSP(IELEM,X,Y,Z,XM,YM,XN,YN,XA,XB,YA,YB,ZA,ZB,
     *     TYPEAB,TYPEMN,XLENTH,ZLENTH,WHOLE,YLENTH)
C     This subroutine computes the whole-space part of the anomalous
C     potential.
      INTEGER TYPEAB,TYPEMN
      REAL X(1),Y(1),Z(1),XA(1),XB(1),YA(1),YB(1),ZA(1),
     *     ZB(1),XLENTH(1),YLENTH(1),ZLENTH(1)
      EXTERNAL ATAN2
      WHOLE=0.
      TNFORM=0.
      N=IELEM
      XMM=XM
      XNN=XN
      YMM=YM
      YNN=YN
      DO 11 NB=1,TYPEMN
C      WRITE(1,16)N,X(N),Y(N),Z(N),XA(N),XB(N),YA(N),YB(N),ZA(N),ZB(N)
```

```
C     *     ,XLENTH(N),YLENTH(N),ZLENTH(N),XMM,XNN,YMM,YNN
      XMXA=XMM-XA(IELEM)
      XMXB=XMM-XB(IELEM)
      YMYA=YMM-YA(IELEM)
      YMYB=YMM-YB(IELEM)
      ZMZA=-ZA(IELEM)
      ZMZB=-ZB(IELEM)
      XEM=XMM-X(IELEM)
      YEM=YMM-Y(IELEM)
      ZEM=-Z(IELEM)
      XEM2=XEM*XEM
      YEM2=YEM*YEM
      ZEM2=ZEM*ZEM
      XMXA2=XMXA*XMXA
      XMXB2=XMXB*XMXB
      YMYA2=YMYA*YMYA
      YMYB2=YMYB*YMYB
      ZMZA2=ZMZA*ZMZA
      ZMZB2=ZMZB*ZMZB
      RDBB=SQRT(XEM2+YMYB2+ZMZB2)
      RDBA=SQRT(XEM2+YMYB2+ZMZA2)
      RDAB=SQRT(XEM2+YMYA2+ZMZB2)
      RDAA=SQRT(XEM2+YMYA2+ZMZA2)
      RBDB=SQRT(XMXB2+YEM2+ZMZB2)
      RBDA=SQRT(XMXB2+YEM2+ZMZA2)
      RADA=SQRT(XMXA2+YEM2+ZMZA2)
      RADB=SQRT(XMXA2+YEM2+ZMZB2)
      RABD=SQRT(XMXA2+YMYB2+ZEM2)
      RBAD=SQRT(XMXB2+YMYA2+ZEM2)
      RBBD=SQRT(XMXB2+YMYB2+ZEM2)
      RAAD=SQRT(XMXA2+YMYA2+ZEM2)
      IF(XLENTH(IELEM).EQ.0.) GOTO 6
      IF(ZLENTH(IELEM).EQ.0.) GOTO 8
      TERM1=ZMZB*ALOG((XMXB+RBDB)/(XMXA+RADB))-ZMZA*ALOG((XMXB+RBDA)
     *     /(XMXA+RADA))
      IF(XMXB.EQ.0.)TERM2=-XMXA*ALOG((ZMZB+RADB)/(ZMZA+RADA))
      IF(XMXA.EQ.0.)TERM2=XMXB*ALOG((ZMZB+RBDB)/(ZMZA+RBDA))
      IF(XMXA.EQ.0. .OR. XMXB.EQ.0.) GOTO 5
      TERM2=XMXB*ALOG((ZMZB+RBDB)/(ZMZA+RBDA))-XMXA*ALOG((ZMZB+RADB)
     *     /(ZMZA+RADA))
    5 IF(YEM.EQ.0.) GOTO 12
      TERM3=YEM*(ATAN2(XMXB*ZMZB/(YEM*RBDB))-ATAN2(XMXB*ZMZA
     *     /(YEM*RBDA))
     *     -ATAN2(XMXA*ZMZB/(YEM*RADB))+ATAN2(XMXA*ZMZA/(YEM*RADA)))
      GOTO 9
   12 TERM3=0.
      GOTO 9
    6 TERM1=ZMZB*ALOG((YMYB+RDBB)/(YMYA+RDAB))-ZMZA*ALOG((YMYB+RDBA)
     *     /(YMYA+RDAA))
      IF(YMYB.EQ.0.)TERM2=-YMYA*ALOG((ZMZB+RDAB)/(ZMZA+RDAA))
      IF(YMYA.EQ.0.)TERM2=YMYB*ALOG((ZMZB+RDBB)/(ZMZA+RDBA))
      IF(YMYA.EQ.0. .OR. YMYB.EQ.0.) GOTO 7
      TERM2=YMYB*ALOG((ZMZB+RDBB)/(ZMZA+RDBA))-YMYA*ALOG((ZMZB+RDAB)
     *     /(ZMZA+RDAA))
    7 IF(XEM.EQ.0.) GOTO 14
      TERM3=XEM*(ATAN2(ZMZB*YMYB/(XEM*RDBB))-ATAN2(ZMZB*YMYA
     *     /(XEM*RDAB))
     *     -ATAN2(ZMZA*YMYB/(XEM*RDBA))+ATAN2(ZMZA*YMYA/(XEM*RDAA)))
      GOTO 9
   14 TERM3=0.
      GOTO 9
```

```
    8     TERM1=YMYB*ALOG((XMXB+RBBD)/(XMXA+RABD))-YMYA*ALOG((XMXB+RBAD)
     *       /(XMXA+RAAD))
          TERM2=XMXB*ALOG((YMYB+RBBD)/(YMYA+RBAD))-XMXA*ALOG((YMYB+RABD)
     *       /(YMYA+RAAD))
          TERM3=ZEM*(ATAN2(XMXB*YMYB/(ZEM*RBBD))-ATAN2(XMXB*YMYA
     *       /(ZEM*RBAD))
     *       -ATAN2(XMXA*YMYB/(ZEM*RABD))+ATAN2(XMXA*YMYA/(ZEM*RAAD)))
    9     WHOLE=-WHOLE-(TERM1+TERM2-TERM3)
   16     FORMAT(///8X,I3/,3F8.1/,3(2F8.1/),3F8.1,//2(2F8.1))
          XMM=XNN
          YMM=YNN
          IF(TYPEMN.EQ.1) WHOLE=-WHOLE
   11     CONTINUE
          RETURN
          END
C
          SUBROUTINE SCAT(XM,YM,XN,YN,Z,J0,H1,BETA,TYPEMN,RHO1,RHO2,SPMN)
C         This subroutine computes the reflected part of the anomalous
C         potential.
          INTEGER TYPEMN
          REAL LAMDA,K1,MPOT,NPOT
C          REAL T(61),J0(61)
          REAL T(120),J0(120)
          EXTERNAL SEXP
          K1=(RHO2-RHO1)/(RHO2+RHO1)
          MM=30
          MP=30
C          MN=61
          MN=120
          SHIFT=0.00424
          DS=ALOG(10.)/10.
          AH=-8.38850000000
          SH=0.0904226468670
          DO 50 L=1,TYPEMN
          REM=SQRT(XM*XM+YM*YM)+1.E-6
C         WRITE(1,16)XM,XN,YM,YN,REM
   16     FORMAT(//// 8X,3(2F8.1/))
          DO 456 I=1,MN
          RT1= (AH + (I-1)*SH)
          RT2= (10.0)**RT1
CC          RLAMB(I)= (1./R)*RT2
          LAMDA=(1./REM)*RT2
C          M=-MP
C    8     EP=REM*SEXP(FLOAT(M)*DS-SHIFT)
C          LAMDA=1./EP
C          T(M+MP+1)=(SEXP(-LAMDA*Z)+K1*SEXP(-LAMDA*(Z+2.*H1)))/
C      *   (1.-K1*SEXP(-2.*LAMDA*H1))
          SIGMA0=1./RHO1
          SIGMA2=1./RHO2
          BETL=SQRT((BETA*BETA)+(4.*LAMDA*LAMDA))
          ALPHA1=(-BETA+BETL)/2.
          ALPHA2=(-BETA-BETL)/2.
C          EXDL=SEXP(LAMDA*H1)
          EXDB=SEXP(BETA*H1)
          EXDA1M=SEXP(-ALPHA1*H1)
          EXDA2=SEXP(ALPHA2*H1)
C          EXZ=SEXP(-LAMDA*Z)
C          EXDA1M=SEXP(-ALPHA1*H1)
          EXH=SEXP(-LAMDA*Z)
          EXHD=SEXP(-LAMDA*(Z-H1))
          RTERM1=(1.+K1)*EXDB*ALPHA1*ALPHA2*(1.-EXDA2*EXDA1M)
```

```
      RTERM2=LAMDA*(1.-K1)*(ALPHA2-(ALPHA1*EXDA2*EXDA1M))
      RTERM3=RTERM1+RTERM2
      RTERM4=2.*(ALPHA2-ALPHA1)*LAMDA*EXHD*EXDA1M
C      I=M+MP+1
      T(I)=(RTERM4-(EXH*RTERM3))/RTERM3
C      M=M+1
C      IF(M.LE.MM) GOTO 8
 456  CONTINUE
C      K=62
      POT=0.
      DO 9 J=1,MN
C   9   POT=POT+T(K-J)*J0(J)
    9  POT=POT+T(J)*J0(J)
      IF(L.EQ.2) GOTO 50
      MPOT=POT/REM
      XM=XN
      YM=YN
   50 CONTINUE
      NPOT=POT/REM
      IF(TYPEMN.EQ.1) NPOT=0.
      SPMN=MPOT-NPOT
C      WRITE(1,16) MPOT,NPOT,SPMN
      RETURN
      END
C
C                                                  *************** APPRES
C
      SUBROUTINE APPRTWO (NXELEC, NYELEC, XELEC, IS, IR, AM1, V)
C     This subroutine calculates the two-electrode apparent
C     resistivity.
      REAL V(99,99), APPREST(99,99), XELEC(99)
      CURRNT = 1.
      WRITE(1,*)'TWO-ELECTRODE ARRAY'
      WRITE(3,*)'TWO-ELECTRODE ARRAY'
      WRITE(1,*)'S, R, PS, PR, AM (m) & APPARENT RESISTIVITY (ohm-m)'
      WRITE(3,*)'AM , Midpsr & APPARENT RESISTIVITY (ohm-m)'
      PI2 = 2. * 3.14159265
C      DO 100 IN=1,NXELEC-1
      DO 100 IN=1,2
      DO 10 IS=1,NXELEC
      IR = IS + IN
      IF (IS .EQ. IR) THEN
      GO TO 10
      ELSE
      ENDIF
C
      IF (IR .GT. NXELEC) THEN
      GO TO 10
      ELSE
      ENDIF
      HAM=ABS(IS-IR)
      AM=HAM*AM1
      GF=PI2/(1./AM)
      DELTAV = V(IS,IR)
      APPREST(IS,IR) = GF * DELTAV / CURRNT
      PMAM = (XELEC(IS)+XELEC(IR))/2.
C      WRITE (1, 854) IS, IR, XELEC(IS), XELEC(IR), AM, APPREST(IS,IR)
      WRITE (3, 853) AM, PMAM, APPREST(IS,IR)
  853 FORMAT(2F8.2,F15.6)
  854 FORMAT(2I3,3F8.2,F15.6)
   10 CONTINUE
```

```
  100   CONTINUE
        RETURN
        END
C
C                                                    ******************
        SUBROUTINE APPRWEN (NXELEC, NYELEC, XELEC, IS, IR, AM1, V)
C       This subroutine calculates the Wenner apparent resistivity.
        REAL V(99,99), APPRESW(99,99,99), XELEC(99)
        CURRNT = 1.
        PI2 = 2. * 3.14159265
C        PI4 = 4. * 3.14159265
C
        WRITE(1,*)'WENNER ARRAY'
        WRITE(3,*)'WENNER ARRAY'
        WRITE(1,75)
        WRITE(3,74)
 74     FORMAT(1X,42HAM, Centpar & APPARENT RESISTIVITY (ohm-m)/)
 75     FORMAT(1X,49HS1, S2, R1, R2, PS1, PS2, PR1, PR2, SEPARATION(m),
     $  1X,30H& APPARENT RESISTIVITY (ohm-m)/)
C
C        JX=NXELEC-1
C        IX=JX/3
        IX=1
        DO 90 IN=1,IX
        DO 85 IR1=2,(NXELEC-2)
        IR2=IR1+IN
        IS1=IR1-IN
        IS2=IR2+IN
        IF((IS2 .GT. NXELEC) .OR. (IS1 .LT. 1)) GO TO 85
C
        HAM = ABS(IS1-IR1)
        HAN = ABS(IS1-IR2)
        HBM = ABS(IS2-IR1)
        HBN = ABS(IS2-IR2)
        AM = HAM * AM1
        AN = HAN * AM1
        BM = HBM * AM1
        BN = HBN * AM1
        GEOFAC = PI2 / (1./AM - 1./BM - 1./AN + 1./BN)
        DELTAV = V(IS1,IR1) - V(IS1,IR2) - V(IS2,IR1) + V(IS2,IR2)
        APPRESW(IS1,IR1,IR2) = GEOFAC * DELTAV / CURRNT
        PMMNW = (XELEC(IR1)+XELEC(IR2))/2.
C        WRITE(1,854)IS1,IS2,IR1,IR2,XELEC(IS1),XELEC(IS2),
C     $  XELEC(IR1), XELEC(IR2), AM, APPRESW(IS1,IR1,IR2)
        WRITE (3, 853) AM, PMMNW, APPRESW(IS1,IR1,IR2)
  853   FORMAT(2F8.2,F15.5)
  854   FORMAT(4I3,5F8.2,F15.5)
C
  85    CONTINUE
C
  90    CONTINUE
        RETURN
        END
C
        SUBROUTINE DIFAPPR (NXELEC, NYELEC, XELEC, IS, IR, AM1, V,
     $       APPREST, APPRESW)
C       This subroutine calculate the apparent resistivity residual.
        REAL V(99,99),  XELEC(99),  APPREST(99,99),
     $  APPRESW(99,99,99), APPRDIF(99,99,99)
        CURRNT = 1.
        PI2 = 2. * 3.14159265
```

```
        PI4 = 4. * 3.14159265
        WRITE(1,35)
C        WRITE(3,35)
        WRITE(3,34)
 34     FORMAT(1X,48HSEPARATION, CENTRE & APP. RES. DIFFERENCE(ohm-m)/)
 35     FORMAT(1X,49HS1, S2, R1, R2, PS1, PS2, PR1, PR2, SEPARATION(m),
     $  1X,30H& APP. RES. DIFFERENCE (ohm-m)/)
C        JX=NXELEC-1
C        IX=JX/3
        IX=1
        DO 90 IN=1,IX
        DO 85 IR1=2,(NXELEC-2)
        IR2=IR1+IN
        IS1=IR1-IN
        IS2=IR2+IN
        IF((IS2 .GT. NXELEC) .OR. (IS1 .LT. 1)) GO TO 85
        HAM = ABS(IS1-IR1)
        HAN = ABS(IS1-IR2)
        HBM = ABS(IS2-IR1)
        HBN = ABS(IS2-IR2)
        AM = HAM * AM1
        AN = HAN * AM1
        BM = HBM * AM1
        BN = HBN * AM1
        GEOFAC = PI2 / (1./AM - 1./BM - 1./AN + 1./BN)
        DELTAV = V(IS1,IR1) - V(IS1,IR2) - V(IS2,IR1) + V(IS2,IR2)
        APPRESW(IS1,IR1,IR2) = GEOFAC * DELTAV / CURRNT
        GF1 = PI2/(1./AM)
        GF2 = PI2/(1./AN)
        DELTAV1 = V(IS1,IR1)
        DELTAV2 = V(IS1,IR2)
        APPREST(IS1,IR1) = GF1 * DELTAV1 / CURRNT
        APPREST(IS1,IR2) = GF2 * DELTAV2 / CURRNT
        APPRDIF(IS1,IR1,IR2) = APPRESW(IS1,IR1,IR2) -
     $     (2 * APPREST(IS1,IR1)) + APPREST(IS1,IR2)
        PMMNW = (XELEC(IR1)+XELEC(IR2))/2.
C        WRITE(1,854)IS1,IS2,IR1,IR2,XELEC(IS1),XELEC(IS2),
C     $  XELEC(IR1), XELEC(IR2), AM, APPRDIF(IS1,IR1,IR2)
        WRITE (3, 853) AM, PMMNW, APPRDIF(IS1,IR1,IR2)
  853   FORMAT(2F8.2,F15.5)
  854   FORMAT(4I3,5F8.2,F15.5)
  85    CONTINUE
C
  90    CONTINUE
        RETURN
        END
C
        REAL FUNCTION SEXP(W)
        SEXP=0.
C        IF(W.LT.-30.) RETURN
        IF(W.LT.-300.) RETURN
        SEXP=EXP(W)
        RETURN
        END
C
        REAL FUNCTION ATAN2(Z)
        ATAN2=ATAN(Z)
        IF(Z.GE.0.) RETURN
        ATAN2=-ATAN(-Z)
        RETURN
        END
```

```
C       ****************************************************************
C       *                                                              *
C       * Program "trs3d.for" by Abolghasem Kamkar-Rouhani             *
C       *                                                              *
C       * This programme computes the Schlumberger and equatorial      *
C       * dipole-dipole apparent resistivities as well as the          *
C       * the corresponding apparent resistivity residual responses.   *
C       *                                                              *
C       ****************************************************************
C
        PROGRAM MAIN
        EXTERNAL SEXP
        EXTERNAL ATAN2
C
        REAL MPOINT,MN,MPOT,NPOT
C
        REAL  A(152,152),DC(152),E(152),XA(152),XB(152),YA(152),
     *  YB(152),ZA(152),ZB(152),XLENTH(152),YLENTH(152),ZLENTH(152),
     *  KERNL(140), SURFAC(152),  X(152), Y(152), Z(152),  XELEC(205),
     *  YELEC(40), J0(120),  J1(140),  DGS(21),  XPLOT(40),  AII(152),
     *  AJ(152), VL(2002,2002), VB(2002,2002), V(2002,2002),
     *  APPRESS(2002,2002), APPRESE(2002,2002) ,
     *  DIFSCED(2002,2002), APPR(2002,2002),
     *  VS(2002,2002), VP(2002,2002),
     *  VQ(2002,2002)
C
        INTEGER FIELD,SOURCE,ROW,COL,TYPEAB,TYPEMN,IJA(46209),NMAX
C
        DOUBLE PRECISION XD(152),DSA(46209)
C
C       For old filters: J0(61) and J1(14)
C
        CHARACTER*80 AA(10)
C
        OPEN ( 2,FILE= 'INTRS.3DR',STATUS= 'OLD')
        OPEN ( 1,FILE= 'OUTTRS.3DR',STATUS='UNKNOWN')
        OPEN ( 3,FILE= 'RESTRS.3D',STATUS='UNKNOWN')
C
C
        DATA DGS/.00004415,-.0007067,.00020028,-.00006335,.00051191,
     *      .00054246,.00200018,.00428432,.01082827,.02608353,.06171465,
     *      .14470387,.30370453,.53037187,.35186747,-.636663,.24659151,
     *      -.05591765,.01101434,-.0019857,.00023703/
C
C
        READ(2,1500) AA(1)
        READ(2,1)NELEM,NXELEC,NYELEC,LST,LEND,NMODEL,TYPEAB,TYPEMN
        READ(2,1500) AA(2)
        READ(2,2)(XA(I),XB(I),YA(I),YB(I),ZA(I),ZB(I),I=1,NELEM)
        READ(2,1500) AA(3)
        READ(2,7) (DC(I),I=1,NELEM)
        READ(2,1500) AA(4)
C        READ(2,3) (J0(I),I=1,61)
        READ(2,3) (J0(I),I=1,120)
        READ(2,1500) AA(5)
C        READ(2,4) (J1(I),I=1,14)
        READ(2,3) (J1(I),I=1,140)
        READ(2,1500) AA(6)
C        READ(2,2) AB,THETA,MN,AMSEPA,XLEFT,XRIGHT
        READ(2,181) AB,THETA,MN,AMSEPA,XLEFT,XRIGHT
        READ(2,1500) AA(7)
```

```
C        READ(2,2) (XELEC(I),I=1,NXELEC)
        READ(2,2) (XELEC(I),I=1,NXELEC)
        READ(2,1500) AA(8)
        READ(2,2) (YELEC(I),I=1,NYELEC)
C
C        WRITE(1,2) (XA(I),XB(I),YA(I),YB(I),ZA(I),ZB(I),I=1,NELEM)
C
        WRITE(1,*) 'J0 filters'
        WRITE(1,823) (J0(I),I=1,120)
        WRITE(1,*) 'J1 filters'
        WRITE(1,823) (J1(I),I=1,140)
 823    FORMAT(3E19.11)
        ST= 0.0
        DO 119 I=1,120
        ST= ST + J0(I)
 119    CONTINUE
C
        WRITE(1,*) 'Sum of J0 filter weights'
        WRITE(1,*) ST
C
        SS= 0.0
        DO 118 I=1,140
        SS= SS+ J1(I)
 118    CONTINUE
        WRITE(1,*) 'Sum of J1 filter weights'
        WRITE(1,*) SS
C
        EPS=1.E-6
C
        DO 110 I=1,NELEM
        X(I)= (XA(I)+XB(I))/2.
        Y(I)= (YA(I)+YB(I))/2.
        Z(I)= (ZA(I)+ZB(I))/2.
        XLENTH(I)= ABS(XA(I)-XB(I))
        YLENTH(I)= ABS(YA(I)-YB(I))
        ZLENTH(I)= ABS(ZA(I)-ZB(I))
        IF(XLENTH(I).EQ.0.)SURFAC(I)=YLENTH(I)*ZLENTH(I)
        IF(YLENTH(I).EQ.0.)SURFAC(I)=XLENTH(I)*ZLENTH(I)
 110    IF(ZLENTH(I).EQ.0.)SURFAC(I)=XLENTH(I)*YLENTH(I)
        PI=3.14159265
        THETA=PI/180.*THETA
        PI2=2.*PI
        PI4=4.*PI
        AM1=AMSEPA
C
        READ(2,1500) AA(9)
        DO 333 IMODEL=1,NMODEL
C
        READ(2,209) RHO1,RHO2,RHOBDY,H1,BETA
C
C       If resistivity is continuous at the interface between the
C       the first and second layers, then
C        READ(2,209) RHO1,RHOBDY,H1,BETA
C        RHO2=RHO1*SEXP(-BETA*H1)
C
        WRITE(1,5)NELEM,TYPEAB,TYPEMN,RHO1,RHO2,RHOBDY,H1,BETA
        WRITE(*,5)NELEM,TYPEAB,TYPEMN,RHO1,RHO2,RHOBDY,H1,BETA
   5    FORMAT(////1X,24HNUMBER OF ELEMENTS USED=,I5,/1X,
     *  45HNO. OF ACTIVE CURRENT & POTENTIAL ELECTRODES=,2I10,
     *  /1X,39HRESISTIVITY OF OVERBURDEN,HOST & BODY =,3F10.2,2X,
     *  5HOHM-M,/1X,28HTHICKNESS OF THE OVERBURDEN=,F6.1,2X,6HMETERS,
```

```
     *   /1X,11HBETA VALUE=,F9.3)
C
          C=PI2*(RHOBDY+RHO2)/(RHOBDY-RHO2)
C         If RHOBDY=RHO2, then C=infinity. So, if this case is decided,
C         try to avoid the overflow problem by
C         choosing RHOBDY=RHO2 + or - 0.0001.
          RHOPI2=RHO1/((RHO1+RHO2)*PI2)
          ROW=1
          DO 101 FIELD=1,NELEM
          COL=1
          DO 100 SOURCE=1,NELEM
          XDIST=X(FIELD)-X(SOURCE)
          YDIST=Y(FIELD)-Y(SOURCE)
          ZDIST=Z(FIELD)-Z(SOURCE)
          XDIST2=XDIST*XDIST
          YDIST2=YDIST*YDIST
          ZDIST2=ZDIST*ZDIST
          RDIST=SQRT(XDIST2+YDIST2)
          IF(RDIST.EQ.0.)RDIST=0.1
          RDIST2=RDIST*RDIST
          RDIST3=RDIST2*RDIST
          RDIST4=RDIST3*RDIST
          XXA=X(FIELD)-XA(SOURCE)
          XXB=X(FIELD)-XB(SOURCE)
          YYA=Y(FIELD)-YA(SOURCE)
          YYB=Y(FIELD)-YB(SOURCE)
          ZZA=Z(FIELD)-ZA(SOURCE)
          ZZB=Z(FIELD)-ZB(SOURCE)
          ZH2D=Z(FIELD)+Z(SOURCE)-2.*H1
          XXA2=XXA*XXA
          XXB2=XXB*XXB
          YYA2=YYA*YYA
          YYB2=YYB*YYB
          ZZA2=ZZA*ZZA
          ZZB2=ZZB*ZZB
          XDYBZB=SQRT(XDIST2+YYB2+ZZB2)
          XDYBZA=SQRT(XDIST2+YYB2+ZZA2)
          XDYAZB=SQRT(XDIST2+YYA2+ZZB2)
          XDYAZA=SQRT(XDIST2+YYA2+ZZA2)
          XBYDZB=SQRT(XXB2+YDIST2+ZZB2)
          XAYDZB=SQRT(XXA2+YDIST2+ZZB2)
          XBYDZA=SQRT(XXB2+YDIST2+ZZA2)
          XAYDZA=SQRT(XXA2+YDIST2+ZZA2)
          XBYBZD=SQRT(XXB2+YYB2+ZDIST2)
          XAYBZD=SQRT(XXA2+YYB2+ZDIST2)
          XBYAZD=SQRT(XXB2+YYA2+ZDIST2)
          XAYAZD=SQRT(XXA2+YYA2+ZDIST2)
          XAZB=XXA*ZZB
          XBZA=XXB*ZZA
          XAZA=XXA*ZZA
          XBZB=XXB*ZZB
          YBZA=YYB*ZZA
          YAZB=YYA*ZZB
          YAZA=YYA*ZZA
          YBZB=YYB*ZZB
          XBYA=XXB*YYA
          XAYB=XXA*YYB
          XAYA=XXA*YYA
          XBYB=XXB*YYB
          AREA=SURFAC(SOURCE)
          IF(SOURCE.EQ.FIELD)GOTO 8
```

```
      IF(YLENTH(FIELD).EQ.0.)GOTO 94
      IF(XLENTH(FIELD).EQ.0.)GOTO 95
      IF(ZLENTH(FIELD).EQ.0.)GOTO 96
 94   IF(Y(FIELD).EQ.YA(SOURCE).AND.Y(FIELD).EQ.YB(SOURCE))GOTO 97
      IF(XLENTH(SOURCE).EQ.0.)PRIMRY=ALOG((ZZB+XDYBZB)*(ZZA+XDYAZA)
     *     /((ZZA+XDYBZA)*(ZZB+XDYAZB)))
      IF(YLENTH(SOURCE).EQ.0.)PRIMRY=
     *     ATAN(XAZB/(YDIST*XAYDZB))+ATAN(XBZA/(YDIST*XBYDZA))-ATAN(
     *     XAZA/(YDIST*XAYDZA))-ATAN(XBZB/(YDIST*XBYDZB))
142   FORMAT(2F6.1,10X,3E12.4)
      IF(ZLENTH(SOURCE).EQ.0.)PRIMRY=ALOG((XXB+XBYBZD)*(XXA+XAYAZD)
     *     /((XXA+XAYBZD)*(XXB+XBYAZD)))
      GOTO 93
 95   IF(X(FIELD).EQ.XA(SOURCE).AND.X(FIELD).EQ.XB(SOURCE))GOTO 97
      IF(XLENTH(SOURCE).EQ.0.) PRIMRY=
     1     ATAN(YBZA/(XDIST*XDYBZA))+ATAN(YAZB/(XDIST*XDYAZB))
     2     -ATAN(YAZA/(XDIST*XDYAZA))-ATAN(YBZB/(XDIST*XDYBZB))
      IF(YLENTH(SOURCE).EQ.0.)PRIMRY=ALOG((ZZB+XBYDZB)*(ZZA+XAYDZA)
     1     /((ZZA+XBYDZA)*(ZZB+XAYDZB)))
      IF(ZLENTH(SOURCE).EQ.0.)PRIMRY=ALOG((YYB+XBYBZD)*(YYA+
     1     XAYAZD)/((YYA+XBYAZD)*(YYB+XAYBZD)))
 93   KLM=0
      MM=3
      MP=10
C      MT=14
      MT=140
      DS=ALOG(10.)/6.
      SHIFT=0.13433155
      AH=-7.91001919000
      SH= 0.0879671439570
      CALL KERNEL(KLM,MM,MP,DS,SHIFT,RDIST,RHO1,RHO2,H1,BETA,ZDIST,
     1 KERNL,ZH2D,AH,SH,MT)
      SECOND=0.
      K=MT+1
      DO 92 JONE=1,MT
C       NJ=K-JONE
C 92    SECOND=SECOND+KERNL(NJ)*J1(JONE)
 92   SECOND=SECOND+KERNL(JONE)*J1(JONE)
C       SECOND=AREA*SECOND/RDIST3
      SECOND=AREA*SECOND/RDIST2
      IF(YLENTH(FIELD).EQ.0.)SECOND=-YDIST*SECOND
      IF(XLENTH(FIELD).EQ.0.)SECOND=-XDIST*SECOND
      GOTO 91
 96   IF(Z(FIELD).EQ.ZA(SOURCE).AND.Z(FIELD).EQ.ZB(SOURCE)) GOTO 21
      IF(XLENTH(SOURCE).EQ.0.) PRIMRY=ALOG((YYB+XDYBZB)*(YYA+XDYAZA)
     1     /((YYA+XDYAZB)*(YYB+XDYBZA)))
      IF(YLENTH(SOURCE).EQ.0.) PRIMRY=ALOG((XXB+XBYDZB)*(XXA+XAYDZA)
     1     /((XXA+XAYDZB)*(XXB+XBYDZA)))
      IF(ZLENTH(SOURCE).EQ.0.) PRIMRY=
     1     ATAN(XBYA/(ZDIST*XBYAZD))+ATAN(XAYB/(ZDIST*XAYBZD))
     2     -ATAN(XAYA/(ZDIST*XAYAZD))-ATAN(XBYB/(ZDIST*XBYBZD))
      CALL DIGDAR(RDIST,J0,RHO1,RHO2,H1,ZDIST,ZH2D,AREA,SECOND)
C       WRITE(1,15) ROW,COL,PRIMRY,SECOND
 91   A(ROW,COL)=(PRIMRY+SECOND)*DC(FIELD)
C       WRITE(1,15) ROW,COL,PRIMRY,SECOND
      GOTO 99
 97   A(ROW,COL)=0.
      GOTO 99
 21   CALL DIGDAR(RDIST,J0,RHO1,RHO2,H1,ZDIST,ZH2D,AREA,SECOND)
C       WRITE(1,15) ROW,COL,PRIMRY,SECOND
      A(ROW,COL)=SECOND*DC(FIELD)
```

```
        GOTO 99
    8   IF(ZLENTH(SOURCE).GT.EPS) GOTO 98
        CALL DIGDAR(RDIST,J0,RHO1,RHO2,H1,ZDIST,ZH2D,AREA,SECOND)
        A(ROW,COL)=SECOND*DC(FIELD)-C
        GOTO 99
   98   A(ROW,COL)=-C
   99   COL=COL+1
C        WRITE(1,15)ROW,COL,PRIMRY,SECOND
  100   CONTINUE
C       WRITE(1,16) (A(ROW,II),II=1,NELEM)
        ROW=ROW+1
        WRITE (*,987) FIELD
  987   FORMAT(/20X,I3,' field point is completed for all elements')
  101   CONTINUE
        WRITE (*,986)
  986   FORMAT(///20X,' *********  Matrix A (N,N) is complete ********')
C       Matrix A (N,N) is the same matrix K in equation E=KQ
C       If the LU decomposition is used instead of the biconjugate
C       gradient method, then (N.B. it has not been used here):
C        CALL LUDCOM(A,NELEM)
C        WRITE( *,985)
C 985    FORMAT(///20X,'   ------  LU Decomposition is over ------')
        DO 82 IP=1,NELEM
C       WRITE(1,16) (A(IP,IC),IC=1,NELEM)
   82   CONTINUE
C
        JN=0
        JA=1
        JB=1
        DO 302 JY=1,NYELEC
        WRITE(1,301) YELEC(JY)
        WRITE(3,301) YELEC(JY)
  301   FORMAT(//4X,17HPROFILE OFF-SET =,F6.1,2X,6HMETERS/)
C        WRITE(1,450)
  450   FORMAT(42Hsource, receiver., pos. of s. & rec., pot.,
     *  1X,33Hdue to lay. & body and total pot./)
        JB=(-1)**JA
        JI=1
        JP=JY+1
        JQ=JY-1
        NXEL=NXELEC
        DISMN=AM1
        OM=DISMN/2.
        SEP=ABS(YELEC(JY)-YELEC(JQ))
        IF(SEP .EQ. 0.) SEP=ABS(XELEC(JI+1)-XELEC(JI))
        IF(JY .EQ. 1) SEP=ABS(YELEC(JP)-YELEC(JY))
        SIM=SEP/OM
        IM=INT(SIM)
        CN=ABS(XELEC(NXELEC)-XELEC(JI))
        CNCN=CN/OM
        NC=INT(CNCN)
        NCC=NC+1
C
        DO 700 IS=1,NCC
        IF(IS .EQ. 1) GO TO 782
        LR=IS/IM
        IF((IS .GT. (IM*LR+2)) .AND. (IS .LT. (IM*(LR+1)))) GO TO 700
  782   IL1=1
  783   DO 800 IR=IL1,NCC,IM
C
        IF((ABS(IR-IS)) .GT. 122) GO TO 800
```

```
C
      IF((JY .EQ. (2+JN*3)) .AND. (IS .EQ. IR)) GO TO 800
C
      IF((JY .EQ. (2+JN*3)) .AND. (IS .GT. IR)) GO TO 750
C      DO 333 IK=LST,LEND
      IK=ABS(IS-IR)
      AMSEPA=IK*OM
      IF(JY .EQ. (1+JN*3)) THEN
      AMSEPA=SQRT(((YELEC(JY)-YELEC(JP))**2) + ((IK*OM)**2))
      ELSE
      ENDIF
C
      IF(JY .EQ. (JN*3)) THEN
C     AMSEPA=SQRT(((YELEC(JY)-YELEC(JQ))**2) + ((IK*OM)**2))
      AMSEPA=SQRT((SEP*SEP) + ((IK*OM)**2))
      ELSE
      ENDIF
C
      XM=XELEC(JI)+IK*OM*COS(THETA)
      YM=YELEC(JY)+IK*OM*SIN(THETA)
      XN=XM+MN*COS(THETA)
      YN=YM+MN*SIN(THETA)
      PPOTMN=0.
      GF=0.
      XELEJ=XELEC(JI)
      YELEJ=YELEC(JY)
      DO 109 NAB=1,TYPEAB
      IF(NAB-2) 83,84,84
   84 XELEJ=XELEJ+AB*COS(THETA)
      YELEJ=YELEJ+AB*SIN(THETA)
   83 XAM=XM-XELEJ
C
      IF(JY .EQ. (1+JN*3)) THEN
      XAM=SQRT(((YELEC(JY)-YELEC(JP))**2) + ((IK*OM)**2))
      ELSE
      ENDIF
C
      IF(JY .EQ. (JN*3)) THEN
C     XAM=SQRT(((YELEC(JY)-YELEC(JQ))**2) + ((IK*OM)**2))
      XAM=SQRT((SEP*SEP) + ((IK*OM)**2))
      ELSE
      ENDIF
C
      YAM=YM-YELEJ
C      XAN=XN-XELEJ
      XAN=XAM
      YAN=YN-YELEJ
      AM=SQRT(XAM*XAM+YAM*YAM)
      AN=SQRT(XAN*XAN+YAN*YAN)
      GF=-GF-(1./AM-1./AN)
      IF(TYPEAB.EQ.1) GF=-GF
      IF(TYPEAB.EQ.1.AND.TYPEMN.EQ.1) GF=1./AM
      CALL PRIME (AM,AN,J0,DGS,RHO1,RHO2,H1,BETA,PI2,TYPEMN,PPMN)
C      WRITE(1,16)AM,AN,PPMN
      PPOTMN=-PPOTMN-PPMN
  109 CONTINUE
      IF(TYPEAB.EQ.1)PPOTMN=-PPOTMN
      VL(IS,IR)=PPOTMN
      GF=PI2/GF
      APPRLR=GF*PPOTMN
C     Thus, the primary layered-earth potential was computed.
```

```
C
      XM=((IS-1)*OM)+XELEC(JI)+IK*OM*COS(THETA)
      YM=YELEC(JY)+IK*OM*SIN(THETA)
      IF(JY .EQ. (1+JN*3)) THEN
      YM=YELEC(JP)+IK*OM*SIN(THETA)
      ELSE
      ENDIF
      IF(JY .EQ. (JN*3)) THEN
      YM=YELEC(JQ)+IK*OM*SIN(THETA)
      ELSE
      ENDIF
C
      XN=XM+MN*COS(THETA)
      YN=YM+MN*SIN(THETA)
      AELECT=((IS-1)*OM)+XELEC(JI)
      BELECT=AELECT+AB*COS(THETA)
      ELECM=XM
      ELECN=XN
      POSA=XELEC(IS)
      POSM=XELEC(IR)
C      WRITE(1,6)AELECT,BELECT,ELECM,ELECN
      IF(BELECT.GE.XLEFT.AND.BELECT.LT.XRIGHT) GOTO 30
      IF(AELECT.GE.XLEFT.AND.AELECT.LT.XRIGHT) GO TO 30
 211  GOTO 112
  30  XM=AELECT
      XN=BELECT
      AELECT=ELECM
 112  DO 106 I=1,NELEM
      XELEJ=AELECT
      YELEJ=YELEC(JY)
      IF(JY .EQ. (1+JN*3)) THEN
      YELEJ=YELEC(JP)
      ELSE
      ENDIF
      IF(JY .EQ. (JN*3)) THEN
      YELEJ=YELEC(JQ)
      ELSE
      ENDIF
      EINCI=0.
      DO 10 IELEC=1,TYPEAB
      IF(IELEC-2) 14,12,12
  12  XELEJ=XELEJ+AB*COS(THETA)
      YELEJ=YELEJ+AB*SIN(THETA)
C      IF(XELEC(IS).GE.XLEFT.AND.XELEC(IS).LT.XRIGHT)XELEJ=ELECN
  14  XSEPA=X(I)-XELEJ
      YSEPA=Y(I)-YELEJ
      ZSEPA=Z(I)
      RDIST=SQRT(XSEPA*XSEPA+YSEPA*YSEPA)
      IF(RDIST.EQ.0.)RDIST=1.E-6
      R2=RDIST*RDIST
      R3=R2*RDIST
      DIST=SQRT(XSEPA*XSEPA+YSEPA*YSEPA+ZSEPA*ZSEPA)
      DIST3=DIST*DIST*DIST
      IF(XLENTH(I).EQ.0. .OR. YLENTH(I).EQ.0.) GOTO 102
      IF(ZLENTH(I).EQ.0.) GOTO 104
 102  IF(XSEPA.EQ.0.) GOTO 9
      MM=3
      MP=10
C      MT=14
      MT=140
      DS=ALOG(10.)/6.
```

```
      SHIFT=0.1343155
      AH=-7.91001919000
      SH= 0.0879671439570
      CALL XYINKR(MM,MP,DS,SHIFT,RDIST,RHO1,RHO2,H1,BETA,ZSEPA,KERNL,
     $            AH,SH,MT)
      SECINC=0.
      K=MT+1
      DO 105 JONE=1,MT
C      NJ=K-JONE
C 105  SECINC=SECINC+KERNL(NJ)*J1(JONE)
 105  SECINC=SECINC+KERNL(JONE)*J1(JONE)
C      SECINC=SECINC/R3
      SECINC=SECINC/R2
      PRINC=1./DIST3
C      WRITE(1,1) I
C      WRITE(1,16) XELEJ,PRINC,SECINC
      IF(YLENTH(I).EQ.0.)EINC=RHO1*YSEPA*(1./DIST3+SECINC)
      IF(XLENTH(I).EQ.0.)EINC=RHO1*XSEPA*(1./DIST3+SECINC)
      GOTO 10
   9  EINC=0.
      GOTO 10
 104  MM=30
      MP=30
C      MT=61
      MT=120
      DS=ALOG(10.)/10.
      SHIFT=0.00424
      AH=-8.38850000000
      SH= 0.0904226468670
      CALL ZINCKR(MM,MP,DS,SHIFT,RDIST,RHO1,RHO2,H1,BETA,ZSEPA,KERNL,
     $            AH,SH,MT)
      SECINC=0.
      K=62
C      DO 107 JZERO=1,61
      DO 107 JZERO=1,MT
C      NJ=K-JZERO
C 107  SECINC=SECINC+KERNL(NJ)*J0(JZERO)
 107  SECINC=SECINC+KERNL(JZERO)*J0(JZERO)
      PRINC=ZSEPA/DIST3
      EINC=RHO1*(PRINC+SECINC/RDIST)
C      WRITE(1,1) I
C      WRITE(1,16) XELEJ,PRINC,SECINC
  10  EINCI=-EINCI-EINC
      E(I)=EINCI*DC(I)
      IF(TYPEAB.EQ.1) E(I)=EINC*DC(I)
C      WRITE(1,16) E(I)
C      WRITE(3,169) I, E(I)
 106  CONTINUE
C     Thus, the vector matrix E was computed.
C      WRITE(1,19) XELEC(J),(E(NG),NG=1,NELEM)
  19  FORMAT(2X,7E11.4)
C
      IF((XELEC(IS) .EQ. 0.) .AND. (IR .EQ. (IS+1))) THEN
      WRITE(1,263) (E(NG),NG=1,NELEM)
 263  FORMAT(/2X,'S.P.=0 & E =',6F11.8)
      ELSE
      ENDIF
C      CALL FIELDS(A,E,NELEM)
      CALL XSPRSIN(A,NELEM,NMAX,DSA,IJA)
C
      CALL XLINBCG(NELEM,NMAX,DSA,IJA,E,XD)
```

```
C
      WRITE(*,984) IS
C      WRITE(*,984) J
 984  FORMAT(//,'** surface charges of the elements are completed ',
     * 'for ',I3,' source position(s)')
C
      DO 178 IEN=1, NELEM
      E(IEN)=SNGL(XD(IEN))
 178  CONTINUE
C
C     WRITE(1,26) XELEC(J),(E(KI),KT=1,NELEM)
  26  FORMAT(//4X,F6.0/,6E11.4///)
C     Thus, column vector matrix Q was computed.
  17  SPOTMN=0.
      DO 1006 IELEM=1,NELEM
      CALL WHOLSP(IELEM,X,Y,Z,XM,YM,XN,YN,XA,XB,YA,YB,ZA,ZB,TYPEAB,
     *     TYPEMN,XLENTH,ZLENTH,WHOLMN,YLENTH)
      IF ( IELEM. EQ. NELEM) WRITE(*,980)
 980  FORMAT('** Primary potential at MN is completed')
      ZSC=Z(IELEM)
      XEM=XM-X(IELEM)
      YEM=YM-Y(IELEM)
      XEN=XN-X(IELEM)
      YEN=YN-Y(IELEM)
C      WRITE(1,16) XEM,XEN,YEM,YEN,ZSC,RHO1,RHO2
      CALL SCAT(XEM,YEM,XEN,YEN,ZSC,J0,H1,BETA,TYPEMN,RHO1,RHO2,
     *          SCATMN)
      AREA=SURFAC(IELEM)
      ERHO=E(IELEM)*RHOPI2
      SCATMN=SCATMN*AREA
C
      IF ( IELEM .EQ. NELEM) WRITE(*,979)
 979  FORMAT('** Scattered potential at MN is completed')
      AII(IELEM)=SCATMN
      AJ(IELEM)=WHOLMN
      TOT=WHOLMN+SCATMN
      PRO=TOT*E(IELEM)
C      WRITE(1,142) XM,XN,TOT,E(IELEM),PRO
      SPOTMN=SPOTMN+(WHOLMN+SCATMN)*ERHO
 1006 CONTINUE
      WRITE(*,983) IS
C      WRITE(*,983) J
 983  FORMAT('** Total potential for current electrode position = ',
     * I4,' is completed')
C     WRITE(1,161)  ((AII(IEE),IEE=1,NELEM),(AJ(IEE),IEE=1,NELEM))
 161  FORMAT(8E12.4)
C      WRITE(*,981) XPLOT(J) , J
 981  FORMAT('**APPARENT RESISTIVITY AT ',F5.0,' meters FOR CURRENT',
     * ' ELECTRODE POSITION = ',I3)
      VB(IS,IR)=SPOTMN
C
      V(IS,IR)=VL(IS,IR) + VB(IS,IR)
      TOTLMN=PPOTMN+SPOTMN
C     Thus, the total potential was computed.
C      APPR(J)=TOTLMN*GF
C      WRITE(1,350) IS, IR, XELEC(IS), XELEC(IR), VL(IS,IR),
C     *              VB(IS,IR), V(IS,IR)
 350  FORMAT(2X,2I3,2X,2F9.2,2X,3F15.10)
C      WRITE(1,16)AM,PPOTMN,SPOTMN,TOTLMN,APPRLR
   6  FORMAT(//8X,4F8.1)
C
```

```
        IF(JY .EQ. (2+JN*3)) THEN
        VS(IS,IR)=V(IS,IR)
        ELSE
        ENDIF
C
        IF(JY .EQ. (1+JN*3)) THEN
        VP(IS,IR)=V(IS,IR)
        ELSE
        ENDIF
C
        IF(JY .EQ. (JN*3)) THEN
        VQ(IS,IR)=V(IS,IR)
C        JA=JA+1
        ELSE
        ENDIF
C
 750    IF((JY .EQ. (2+JN*3)) .AND. (IS .GT. IR)) THEN
        VS(IS,IR)=VS(IR,IS)
        ELSE
        ENDIF
C
 800    CONTINUE
        IF(IL1 .EQ. (IM+2)) GO TO 700
        IF(IL1 .EQ. IM) THEN
        IL1=IL1+2
        ELSE
        ENDIF
        IF(IL1 .EQ. (IM+2)) GO TO 783
        IF(IL1 .EQ. 1) THEN
        IL1=IL1+IM-1
        ELSE
        ENDIF
        IF(IL1 .EQ. IM) GO TO 783
C
 700    CONTINUE
C
        IF((JY .EQ. (1+JN*3)) .AND. (JB .EQ. -1)) THEN
        JA=JA+1
        ELSE
        ENDIF
C
        IF((JY .EQ. (1+JN*3)) .AND. (JB .EQ. 1)) THEN
        JA=JA+1
        ELSE
        ENDIF
C
        IF((JY .EQ. (JN*3)) .AND. (JB .EQ. -1)) THEN
        JA=JA+1
        ELSE
        ENDIF
C
        IF(JY .EQ. (JN*3)) THEN
        CALL APPRDEQ ( XELEC, YELEC, AM1, VP, VQ, NXELEC, NYELEC,
     $   JY, IS, IR, JN, SEP, OM, NCC)
C
        ELSE
        ENDIF
C
        IF(JY .NE. (2+JN*3)) GO TO 196
        IF(JY .EQ. (2+JN*3)) THEN
        CALL APPRSCH (NXELEC, NYELEC, XELEC, JY, IS, IR, AM1, VS,
```

```
     $                SEP, OM, NCC)
        JN=JN+1
        JA=JA+1
C
        ELSE
        ENDIF
        GO TO 302
C
 196    IF(JY .EQ. (JN*3)) THEN
        CALL APPRSCD (NXELEC, NYELEC, XELEC, JY, YELEC, IS, IR,
     $    AM1, VS, VP, VQ, APPRSCH, APPRDEQ, JN, SEP, OM, NCC)
        ELSE
        ENDIF
C
        IF((JY .EQ. (JN*3)) .AND. (JB .EQ. 1)) THEN
        JA=JA+1
        ELSE
        ENDIF
 302    CONTINUE
 333    CONTINUE
   1    FORMAT(8I10)
   2    FORMAT(12F6.0)
  22    FORMAT(6F6.0)
 222    FORMAT(3F6.0,F7.2)
C 209    FORMAT(4F6.0,F8.2)
 209    FORMAT(4F6.0,F9.3)
C   3    FORMAT(8F10.6)
   3    FORMAT(3E19.11)
   4    FORMAT(8F10.4)
   7    FORMAT(20F4.0)
 181    FORMAT(3F6.0,F7.1,2F6.0)
 188    FORMAT(F7.1,11F6.1)
  18    FORMAT(2F6.0,F8.3,F4.0)
  15    FORMAT(2I4,10E11.4)
  16    FORMAT(10F8.2)
  169   FORMAT(I5,F14.9)
 1500   FORMAT(A80)
 150    STOP
        END
C
C
C        If the LU decomposition method is used, then
C        (N.B. it has not been used here):
C        SUBROUTINE LUDCOM(A,N)
C        This subroutine uses the LU decomposition method (unused).
C        INTEGER R
C        REAL A(152,152)
C        R=1
C        LP=R+1
C        DO 80 J=LP,N
C        A(J,R)=A(J,R)/A(R,R)
C  80    CONTINUE
C        DO 70 R=2,N
C        DO 40 M=R,N
C        SUMROW=0.
C        SUM COL=0.
C        LM=R-1
C        DO 30 I=1,LM
C        SUMROW=SUMROW+A(R,I)*A(I,M)
C        IF(M.EQ.N) GOTO 30
C        SUMCOL=SUMCOL+A(I,R)*A(M+1,I)
```

```
C  30     CONTINUE
C        A(R,M)=A(R,M)-SUMROW
C        IF(M.EQ.N) GOTO 40
C        A(M+1,R)=A(M+1,R)-SUMCOL
C  40    CONTINUE
C        IF(R.EQ.N) GOTO 70
C        LP=R+1
C        DO 60 J=LP,N
C  60    A(J,R)=A(J,R)/A(R,R)
C  70    CONTINUE
C        RETURN
C        END
C
C        SUBROUTINE FIELDS(A,B,N)
C        This subroutine evaluate Q by the LU decomposition method
C        (unused).
C        REAL A(152,152),B(152)
C        DO 101 J=2,N
C        SUM=0.
C        L=J-1
C        DO 100 I=1,L
C 100    SUM=SUM+A(J,I)*B(I)
C 101    B(J)=B(J)-SUM
C        B(N)=B(N)/A(N,N)
C        J=N-1
C        LL=1
C  80    SUM=0.
C        N1=N
C        DO 90 I=1,LL
C        SUM=SUM+A(J,N1)*B(N1)
C        N1=N1-1
C  90    CONTINUE
C        B(J)=(B(J)-SUM)/A(J,J)
C        J=J-1
C        LL=LL+1
C        IF(J.GE.1) GOTO 80
C        RETURN
C        END
C
       SUBROUTINE XSPRSIN(A,NELEM,NMAX,DSA,IJA)
C      This subroutine converts matrix A (=K) from 2-D to two
C      1-D matrices.
       REAL A(152,152),AAR(152,152),SA(46209)
       INTEGER NP,NMAX,I,J,MSIZE,IJA(46209)
       DOUBLE PRECISION DA(152,152),DAA(152,152),DSA(46209),THRESH
       NP=NELEM
       NMAX=2*NP*NP+1
       DO 171 J=1,NP
         DO 172 I=1,NP
         DA(I,J)=DBLE(A(I,J))
 172     CONTINUE
 171   CONTINUE
C
       THRESH=1.D-9
       CALL SPRSIN(DA,NP,NP,THRESH,NMAX,DSA,IJA)
       MSIZE=IJA(IJA(1)-1)-1
       SA(NP+1)=0.0
       DSA(NP+1)=0.D0
C       WRITE(*,'(T4,A,T18,A,T24,A)') 'INDEX','IJA','DSA'
C       WRITE(1,'(T4,A,T18,A,T24,A)') 'INDEX','IJA','DSA'
       DO 11 I=1,MSIZE
```

```
C         WRITE(*,'(T2,I4,T16,I4,T20,F16.9)') I,IJA(I),DSA(I)
C         WRITE(1,'(T2,I4,T16,I4,T20,F16.9)') I,IJA(I),DSA(I)
  11     CONTINUE
         DO 13 I=1,NP
           DO 12 J=1,NP
            DAA(I,J)=0.D0
  12       CONTINUE
  13     CONTINUE
         DO 15 I=1,NP
           DAA(I,I)=DSA(I)
             DO 14 J=IJA(I),IJA(I+1)-1
               DAA(I,IJA(J))=DSA(J)
  14         CONTINUE
  15      CONTINUE
C          WRITE(*,*)'ORIGINAL MATRIX:'
C          WRITE(1,*)'ORIGINAL MATRIX:'
C          WRITE(*,'(5F12.6)') ((DA(I,J),J=1,NP),I=1,NP)
C          WRITE(1,'(5F12.6)') ((DA(I,J),J=1,NP),I=1,NP)
C          WRITE(*,*)'RECONSTRUCTED MATRIX:'
C          WRITE(1,*)'RECONSTRUCTED MATRIX:'
C          WRITE(*,'(5F12.6)') ((DAA(I,J),J=1,NP),I=1,NP)
C          WRITE(1,'(5F12.6)') ((DAA(I,J),J=1,NP),I=1,NP)
         RETURN
         END
C
         SUBROUTINE SPRSIN(DA,N,NP,THRESH,NMAX,DSA,IJA)
C        This subroutine is related to subroutine XSPRSIN.
         INTEGER N,NMAX,NP,IJA(46209)
         DOUBLE PRECISION THRESH,DA(152,152),DSA(46209)
         INTEGER I,J,K
         N=NP
         DO 11 J=1,N
         DSA(J)=DA(J,J)
  11     CONTINUE
         IJA(1)=N+2
         K=N+1
         DO 13 I=1,N
         DO 12 J=1,N
          IF(ABS(DA(I,J)).GE.THRESH)THEN
             IF(I.NE.J)THEN
               K=K+1
               IF(K.GT.NMAX)PAUSE 'NMAX TOO SMALL IN SPRSIN'
               DSA(K)=DA(I,J)
               IJA(K)=J
             ENDIF
          ENDIF
  12     CONTINUE
         IJA(I+1)=K+1
  13     CONTINUE
         RETURN
         END
C
         SUBROUTINE XLINBCG(NELEM,NMAX,DSA,IJA,E,XD)
C        This subroutine evaluates vector matrix Q using the
C        biconjugate gradient method.
         INTEGER NP,NMAX,ITOL,ITMAX,I,ITER,IJA(46209)
         REAL E(152)
         DOUBLE PRECISION TOL,B(152),DE(152),XD(152),BCMP(152),ERR,
     $   DSA(46209)
         NP=NELEM
         NMAX=2*NP*NP+1
```

```
      ITOL=1
      TOL=1.D-9
      ITMAX=4*NP
C
      DO 173 I=1,NP
      DE(I)=DBLE(E(I))
 173  CONTINUE
      DO 17 IJO=1,NP
      B(IJO)=DE(IJO)
  17  CONTINUE
      DO 11 I=1,NP
      XD(I)=0.D0
C     B(I)=1.D0
  11  CONTINUE
      CALL LINBCG(NP,NMAX,B,XD,ITOL,TOL,ITMAX,ITER,ERR,DSA,IJA)
      WRITE(*,'(/1X,A,E15.6)') 'ESTIMATED ERROR:',ERR
      WRITE(1,'(/1X,A,E15.6)') 'ESTIMATED ERROR:',ERR
      WRITE(*,'(/1X,A,I6)') 'ITERATIONS NEEDED:',ITER
      WRITE(1,'(/1X,A,I6)') 'ITERATIONS NEEDED:',ITER
C      WRITE(*,'(/1X,A)') 'SOLUTION VECTOR:'
C      WRITE(1,'(/1X,A)') 'SOLUTION VECTOR:'
C      WRITE(*,'(/1X,5F12.6)') (XD(I),I=1,NP)
C      WRITE(1,'(/1X,5F12.6)') (XD(I),I=1,NP)
      CALL DSPRSAX(DSA,IJA,XD,BCMP,NP)
C     THIS IS A DOUBLE PRECISION VERSION OF SPRSAX
C      WRITE(*,'(/1X,A/T8,A,T22,A)') 'TEST OF SOLUTION VECTOR:',
C     $       'A*X','B'
C      WRITE(1,'(/1X,A/T8,A,T22,A)') 'TEST OF SOLUTION VECTOR:',
C     $       'A*X','B'
      DO 12 I=1,NP
C      WRITE(*,'(1X,2F12.6)') BCMP(I),B(I)
C      WRITE(1,'(1X,2F12.6)') BCMP(I),B(I)
  12  CONTINUE
      RETURN
      END
C
      SUBROUTINE LINBCG(N,NMAX,B,XD,ITOL,TOL,ITMAX,ITER,ERR,DSA,IJA)
C     This subroutine is related to subroutine XLINBCG.
      INTEGER ITER,ITMAX,ITOL,N,NMAX,IJA(46209),J
      DOUBLE PRECISION ERR,TOL,B(*),XD(*),EPS
      DOUBLE PRECISION AK,AKDEN,BK,BKDEN,BKNUM,BNRM,DXNRM,XNRM,ZM1NRM,
     *  ZNRM,P(46209),PP(46209),R(46209),RR(46209),ZD(46209),ZZ(46209),
     *  SNRM,DSA(46209)
      EPS=1.D-14
      ITER=0
      CALL ATIMES(N,XD,R,0,DSA,IJA)
      DO 11 J=1,N
      R(J)=B(J)-R(J)
      RR(J)=R(J)
 11   CONTINUE
      ZNRM=1.D0
      IF(ITOL.EQ.1) THEN
      BNRM=SNRM(N,B,ITOL)
      ELSE IF (ITOL.EQ.2) THEN
      CALL ASOLVE(N,B,ZD,0,DSA,IJA)
      BNRM=SNRM(N,ZD,ITOL)
      ELSE IF (ITOL.EQ.3.OR.ITOL.EQ.4) THEN
      CALL ASOLVE(N,B,ZD,0,DSA,IJA)
      BNRM=SNRM(N,ZD,ITOL)
      CALL ASOLVE(N,R,ZD,0,DSA,IJA)
      ZNRM=SNRM(N,ZD,ITOL)
```

```
      ELSE
      PAUSE 'ILLEGAL ITOL IN LINBCG'
      ENDIF
      CALL ASOLVE(N,R,ZD,0,DSA,IJA)
100   IF (ITER.LE.ITMAX) THEN
      ITER=ITER+1
      ZM1NRM=ZNRM
      CALL ASOLVE(N,RR,ZZ,1,DSA,IJA)
      BKNUM=0.D0
      DO 12 J=1,N
        BKNUM=BKNUM+ZD(J)*RR(J)
12    CONTINUE
      IF(ITER.EQ.1) THEN
        DO 13 J=1,N
          P(J)=ZD(J)
          PP(J)=ZZ(J)
13      CONTINUE
      ELSE
        BK=BKNUM/BKDEN
        DO 14 J=1,N
          P(J)=BK*P(J)+ZD(J)
          PP(J)=BK*PP(J)+ZZ(J)
14      CONTINUE
      ENDIF
      BKDEN=BKNUM
      CALL ATIMES(N,P,ZD,0,DSA,IJA)
      AKDEN=0.D0
      DO 15 J=1,N
        AKDEN=AKDEN+ZD(J)*PP(J)
15    CONTINUE
      AK=BKNUM/AKDEN
      CALL ATIMES(N,PP,ZZ,1,DSA,IJA)
      DO 16 J=1,N
        XD(J)=XD(J)+AK*P(J)
        R(J)=R(J)-AK*ZD(J)
        RR(J)=RR(J)-AK*ZZ(J)
16    CONTINUE
      CALL ASOLVE(N,R,ZD,0,DSA,IJA)
      IF(ITOL.EQ.1.OR.ITOL.EQ.2)THEN
        ZNRM=1.D0
        ERR=SNRM(N,R,ITOL)/BNRM
      ELSE IF(ITOL.EQ.3.OR.ITOL.EQ.4)THEN
        ZNRM=SNRM(N,ZD,ITOL)
        IF(ABS(ZM1NRM-ZNRM).GT.EPS*ZNRM) THEN
          DXNRM=ABS(AK)*SNRM(N,P,ITOL)
          ERR=ZNRM/ABS(ZM1NRM-ZNRM)*DXNRM
        ELSE
          ERR=ZNRM/BNRM
          GOTO 100
        ENDIF
        XNRM=SNRM(N,XD,ITOL)
        IF(ERR.LE.0.5D0*XNRM) THEN
          ERR=ERR/XNRM
        ELSE
          ERR=ZNRM/BNRM
          GOTO 100
        ENDIF
      ENDIF
C      WRITE (*,*) ' ITER=',ITER,' ERR=',ERR
C      WRITE (1,*) ' ITER=',ITER,' ERR=',ERR
      IF(ERR.GT.TOL) GOTO 100
```

```
      ENDIF
      RETURN
      END
C
      FUNCTION SNRM(N,SX,ITOL)
      INTEGER N,ITOL,I,ISAMAX
      DOUBLE PRECISION SX(*),SNRM
      IF(ITOL .LE. 3) THEN
      SNRM=0.D0
      DO 11 I=1,N
      SNRM=SNRM+SX(I)**2
 11   CONTINUE
      SNRM=SQRT(SNRM)
      ELSE
      ISAMAX=1
      DO 12 I=1,N
      IF(ABS(SX(I)).GT.ABS(SX(ISAMAX))) ISAMAX=I
 12   CONTINUE
      SNRM=ABS(SX(ISAMAX))
      ENDIF
      RETURN
      END
C
      SUBROUTINE ATIMES(N,XD,R,ITRNSP,DSA,IJA)
C     This subroutine is related to subroutine LINBCG.
      INTEGER N,ITRNSP,IJA(*),NMAX
      DOUBLE PRECISION XD(*),R(*),DSA(*)
      NMAX=2*N*N+1
      IF (ITRNSP.EQ.0) THEN
      CALL DSPRSAX(DSA,IJA,XD,R,N)
      ELSE
      CALL DSPRSTX(DSA,IJA,XD,R,N)
      ENDIF
      RETURN
      END
C
      SUBROUTINE ASOLVE(N,B,XD,ITRNSP,DSA,IJA)
C     This subroutine is related to subroutine LINBCG.
      INTEGER N,ITRNSP,IJA(*),NMAX,I
      DOUBLE PRECISION XD(*),B(*),DSA(*)
      NMAX=2*N*N+1
      DO 11 I=1,N
      XD(I)=B(I)/DSA(I)
 11   CONTINUE
      RETURN
      END
C
      SUBROUTINE DSPRSAX(DSA,IJA,XD,B,N)
C     This subroutine is related to subroutine XLINBCG.
      INTEGER N,IJA(*)
      DOUBLE PRECISION B(*),DSA(*),XD(*)
      ITEGER I,K
      IF (IJA(1).NE.N+2) PAUSE 'MISMATCHED VECTOR AND MATRIX IN
     $ SPRSAX'
      DO 12 I=1,N
      B(I)=DSA(I)*XD(I)
      DO 11 K=IJA(I),IJA(I+1)-1
        B(I)=B(I)+DSA(K)*XD(IJA(K))
 11   CONTINUE
 12   CONTINUE
      RETURN
```

```
      END
C
      SUBROUTINE DSPRSTX(DSA,IJA,XD,B,N)
C     This subroutine is related to subroutine ATIMES.
      INTEGER N,IJA(*)
      DOUBLE PRECISION B(*),DSA(*),XD(*)
      INTEGER I,J,K
      IF (IJA(1).NE.N+2) PAUSE 'MISMATCHED VECTOR AND MATRIX IN
     $ SPRSTX'
      DO 11 I=1,N
       B(I)=DSA(I)*XD(I)
 11   CONTINUE
      DO 13 I=1,N
      DO 12 K=IJA(I),IJA(I+1)-1
        J=IJA(K)
        B(J)=B(J)+DSA(K)*XD(I)
 12   CONTINUE
 13   CONTINUE
      RETURN
      END
C
      SUBROUTINE XYINKR(MM,MP,DS,SHIFT,RDIST,RHO1,RHO2,H1,BETA,Z,KRNL,
     $                  AH,SH,MT)
C     This subroutine computes the kernel for E (x- and y-components).
C      REAL KRNL(61),LAMDA,K1
      REAL KRNL(61),LAMDA
      EXTERNAL SEXP
C      K1=(RHO2-RHO1)/(RHO2+RHO1)
      DO 447 I=1,MT
      RT1= (AH + (I-1)*SH)
      RT2= (10.0)**RT1
      LAMDA=(1./RDIST)*RT2
      EXD=SEXP(-2.*LAMDA*H1)
      EXZ=SEXP(-LAMDA*Z)
      EXDK1=K1*EXD
C     M=-MP
C  1  EP=RDIST*SEXP(FLOAT(M)*DS-SHIFT)
C     LAMDA=1./EP
      SIGMA0=1./RHO1
      SIGMA2=1./RHO2
      BETL=SQRT((BETA*BETA)+(4.*LAMDA*LAMDA))
      ALPHA1=(-BETA+BETL)/2.
      ALPHA2=(-BETA-BETL)/2.
      EXDLA2=SEXP(H1*(ALPHA2+LAMDA))
      EXDB=SEXP(BETA*H1)
      EXDA1M=SEXP(-ALPHA1*H1)
      EXDA2=SEXP(ALPHA2*H1)
      STERM1=2.*LAMDA*(ALPHA1-ALPHA2)*SIGMA0*EXDB*EXDLA2
      STERM2=(LAMDA*ALPHA1*SIGMA2+ALPHA1*ALPHA2*SIGMA0*EXDB)*
     $       EXDA2*EXDA1M
      STERM3=(LAMDA*ALPHA2*SIGMA2+ALPHA1*ALPHA2*SIGMA0*EXDB)
C     I=M+MP+1
      KRNL(I)=(EXZ*(STERM1-STERM2+STERM3))/(STERM2-STERM3)
C      M=M+1
C      IF(M.LE.MM) GOTO 1
 447  CONTINUE
      RETURN
      END
C
      SUBROUTINE ZINCKR(MM,MP,DS,SHIFT,RDIST,RHO1,RHO2,H1,BETA,Z,KRNL,
     $                  AH,SH,MT)
```

```
C       This subroutine computes Kernel for E (z-component).
C        REAL KRNL(61),LAMDA,K1
        REAL KRNL(140),LAMDA
        EXTERNAL SEXP
C        K1=(RHO2-RHO1)/(RHO2+RHO1)
C        M=-MP
C   1    EP=RDIST*SEXP(FLOAT(M)*DS-SHIFT)
C        LAMDA=1./EP
        DO 448 I=1,MT
        RT1= (AH + (I-1)*SH)
        RT2= (10.0)**RT1
C        RLAMB(I)= (1./R)*RT2
        LAMDA=(1./RDIST)*RT2
        SIGMA0=1./RHO1
        SIGMA2=1./RHO2
        BETL=SQRT((BETA*BETA)+(4.*LAMDA*LAMDA))
        ALPHA1=(-BETA+BETL)/2.
        ALPHA2=(-BETA-BETL)/2.
        EXDLA2=SEXP(H1*(ALPHA2+LAMDA))
        EXDB=SEXP(BETA*H1)
        EXDA1M=SEXP(-ALPHA1*H1)
        EXDA2=SEXP(ALPHA2*H1)
        EXZ=SEXP(-LAMDA*Z)
        STERM1=2.*LAMDA*(ALPHA1-ALPHA2)*SIGMA0*EXDB*EXDLA2
        STERM2=(LAMDA*ALPHA1*SIGMA2+ALPHA1*ALPHA2*SIGMA0*EXDB)*
     $          EXDA2*EXDA1M
        STERM3=(LAMDA*ALPHA2*SIGMA2+ALPHA1*ALPHA2*SIGMA0*EXDB)
C       I=M+MP+1
        KRNL(I)=LAMDA*(EXZ*(STERM1-STERM2+STERM3))/(STERM2-STERM3)
C        M=M+1
C        IF(M.LE.MM) GOTO 1
 448    CONTINUE
        RETURN
        END
C
        SUBROUTINE DIGDAR(RD,J0,R1,R2,H,Z,ZH,AREA,SECOND)
C       This subroutine computes the kernel function for z-component of
C       reflected part of Gamma.
        REAL KERNL(61),J0(61)
        KLM=10
        MM=30
        RHO1=R1
        RHO2=R2
        ZDIST=Z
        H1=H
        ZH2D=ZH
        MP=30
        SHIFT=0.00424
        DS=ALOG(10.)/10.
        AH=-8.38850000000
        SH=0.0904226468670
        RDIST=RD
C        MT=61
        MT=120
        CALL KERNEL(KLM,MM,MP,DS,SHIFT,RDIST,RHO1,RHO2,H1,BETA,ZDIST,
     *  KERNL,ZH2D,AH,SH,MT)
        SECOND=0.
C        K=62
C        DO 90 JZERO=1,61
        DO 90 JZERO=1,MT
C        NJ=K-JZERO
```

```
C  90     SECOND=SECOND+KERNL(NJ)*J0(JZERO)
   90    SECOND=SECOND+KERNL(JZERO)*J0(JZERO)
         SECOND=-AREA*SECOND/RDIST
         RETURN
         END
C
         SUBROUTINE KERNEL(KLM,MM,MP,DS,SHIFT,RDIST,RHO1,RHO2,H1,BETA,
     *   ZDIST,KRNL,ZH2D,AH,SH,MT)
C        This subroutine computes the kernel function for computation of
C        reflected part of Gamma.
C         REAL KRNL(61),LAMDA,K1
         REAL KRNL(140),LAMDA
         EXTERNAL SEXP
C         K1=(RHO2-RHO1)/(RHO2+RHO1)
C          M=-MP
C    1     EP=RDIST*SEXP(FLOAT(M)*DS-SHIFT)
C          LAMDA=1./EP
         DO 446 I=1,MT
         RT1= (AH + (I-1)*SH)
         RT2= (10.0)**RT1
CC         RLAMB(I)= (1./R)*RT2
         LAMDA=(1./RDIST)*RT2
C         EX=SEXP(-2.*LAMDA*H1)
         SIGMA0=1./RHO1
         SIGMA2=1./RHO2
         BETL=SQRT((BETA*BETA)+(4.*LAMDA*LAMDA))
         ALPHA1=(-BETA+BETL)/2.
         ALPHA2=(-BETA-BETL)/2.
C         EXDL=SEXP(LAMDA*H1)
         EXDB=SEXP(BETA*H1)
C         EXDA1=SEXP(ALPHA1*H1)
         EXDA1M=SEXP(-ALPHA1*H1)
         EXDA2=SEXP(ALPHA2*H1)
C         EXZ=SEXP(-LAMDA*Z)
         EXZH2D=SEXP(-LAMDA*ZH2D)
         GTERM1=((LAMDA*SIGMA2)-(ALPHA1*SIGMA0*EXDB))*ALPHA2
         GTERM2=((LAMDA*SIGMA2)-(ALPHA2*SIGMA0*EXDB))*ALPHA1
         GTERM3=(GTERM1*EXZH2D)-(GTERM2*EXZH2D*EXDA2*EXDA1M)
         GTERM4=((LAMDA*SIGMA2)+(ALPHA1*SIGMA0*EXDB))*ALPHA2
         GTERM5=((LAMDA*SIGMA2)+(ALPHA2*SIGMA0*EXDB))*ALPHA1
C        I=M+MP+1
         KRNL(I)=GTERM3/(GTERM4-(GTERM5*EXDA2*EXDA1M))
         IF(KLM.EQ.10)KRNL(I)=LAMDA*KRNL(I)
C         M=M+1
C         IF(M.LE.MM) GOTO 1
 446     CONTINUE
         RETURN
         END
C
         SUBROUTINE PRIME (S,S1,J0,DGS,RHO1,RHO2,H1,BETA,PI2,
     $                     TYPEMN,POTMN)
C        This subroutine computes the primary layered-earth potential.
         INTEGER TYPEMN
         REAL J0(120),DGS(21),T(120),R(2),H(1),LAMDA
C         REAL J0(61),DGS(21),T(61),R(2),H(1)
         EXTERNAL SEXP
         N=2
         R(1)=RHO1
         R(2)=RHO2
         H(1)=H1
         MM=30
```

```
      MP=30
C      MN=61
      MN=120
      SHIFT=0.00424
      DS=ALOG(10.)/10.
C     MM=11
C     MP=9
C     MN=21
C     SHIFT=-.175072768
C     DS=ALOG(10.)/5.16500849
      AH=-8.38850000000
      SH=0.0904226468670
      AM=S
      DO 50 L=1,TYPEMN
C       M=-MP
C    8  EP=AM*SEXP(FLOAT(M)*DS-SHIFT)
      DO 454 I=1,MN
      RT1= (AH + (I-1)*SH)
      RT2= (10.0)**RT1
C      RLAMB(I)= (1./R)*RT2
      LAMDA=(1./AM)*RT2
C       NN=N
C       TN=R(NN)
C       DTN=0.
      SIGMA0=1./RHO1
      SIGMA2=1./RHO2
      BETL=SQRT((BETA*BETA)+(4.*LAMDA*LAMDA))
      ALPHA1=(-BETA+BETL)/2.
      ALPHA2=(-BETA-BETL)/2.
C      EXDL=SEXP(LAMDA*H1)
      EXDB=SEXP(BETA*H1)
C      EXDA1=SEXP(ALPHA1*H1)
      EXDA2=SEXP(ALPHA2*H1)
C      EXZ=SEXP(-LAMDA*Z)
      EXDA1M=SEXP(-ALPHA1*H1)
      EXDA2A1=SEXP((ALPHA2-ALPHA1)*H1)
      PTERM1=(LAMDA*SIGMA2)+(ALPHA2*SIGMA0*EXDB)
      PTERM2=(LAMDA*SIGMA2)+(ALPHA1*SIGMA0*EXDB)
      PTERM3=(PTERM1/PTERM2)*EXDA2*EXDA1M
C     I=M+MP+1
      T(I)=(LAMDA*(1.-PTERM3))/((ALPHA1*PTERM3)-ALPHA2)
C
C      M=M+1
C      IF(M.LE.MM) GOTO 8
 454   CONTINUE
      POT=0.
C     K=22
      K=62
      DO 9 J=1,MN
    9 POT=POT+T(K-J)*J0(J)
      IF(L.EQ.2) GOTO 50
C     POTM=POT/(PI2*AM*AM)
      POTM=POT/(PI2*SIGMA0*AM)
      AM=S1
   50 CONTINUE
C     POTN=POT/(PI2*AM*AM)
      POTN=POT/(PI2*SIGMA0*AM)
      IF(TYPEMN.EQ.1)POTN=0.
      POTMN=POTM-POTN
      RETURN
      END
```

```
C
      SUBROUTINE WHOLSP(IELEM,X,Y,Z,XM,YM,XN,YN,XA,XB,YA,YB,ZA,ZB,
     *  TYPEAB,TYPEMN,XLENTH,ZLENTH,WHOLE,YLENTH)
C     This subroutine computes the whole-space part of the anomalous
C     potential.
      INTEGER TYPEAB,TYPEMN
      REAL X(1),Y(1),Z(1),XA(1),XB(1),YA(1),YB(1),ZA(1),
     *     ZB(1),XLENTH(1),YLENTH(1),ZLENTH(1)
      EXTERNAL ATAN2
      WHOLE=0.
      TNFORM=0.
      N=IELEM
      XMM=XM
      XNN=XN
      YMM=YM
      YNN=YN
      DO 11 NB=1,TYPEMN
C      WRITE(1,16)N,X(N),Y(N),Z(N),XA(N),XB(N),YA(N),YB(N),ZA(N),ZB(N)
C     *     ,XLENTH(N),YLENTH(N),ZLENTH(N),XMM,XNN,YMM,YNN
      XMXA=XMM-XA(IELEM)
      XMXB=XMM-XB(IELEM)
      YMYA=YMM-YA(IELEM)
      YMYB=YMM-YB(IELEM)
      ZMZA=-ZA(IELEM)
      ZMZB=-ZB(IELEM)
      XEM=XMM-X(IELEM)
      YEM=YMM-Y(IELEM)
      ZEM=-Z(IELEM)
      XEM2=XEM*XEM
      YEM2=YEM*YEM
      ZEM2=ZEM*ZEM
      XMXA2=XMXA*XMXA
      XMXB2=XMXB*XMXB
      YMYA2=YMYA*YMYA
      YMYB2=YMYB*YMYB
      ZMZA2=ZMZA*ZMZA
      ZMZB2=ZMZB*ZMZB
      RDBB=SQRT(XEM2+YMYB2+ZMZB2)
      RDBA=SQRT(XEM2+YMYB2+ZMZA2)
      RDAB=SQRT(XEM2+YMYA2+ZMZB2)
      RDAA=SQRT(XEM2+YMYA2+ZMZA2)
      RBDB=SQRT(XMXB2+YEM2+ZMZB2)
      RBDA=SQRT(XMXB2+YEM2+ZMZA2)
      RADA=SQRT(XMXA2+YEM2+ZMZA2)
      RADB=SQRT(XMXA2+YEM2+ZMZB2)
      RABD=SQRT(XMXA2+YMYB2+ZEM2)
      RBAD=SQRT(XMXB2+YMYA2+ZEM2)
      RBBD=SQRT(XMXB2+YMYB2+ZEM2)
      RAAD=SQRT(XMXA2+YMYA2+ZEM2)
      IF(XLENTH(IELEM).EQ.0.) GOTO 6
      IF(ZLENTH(IELEM).EQ.0.) GOTO 8
      TERM1=ZMZB*ALOG((XMXB+RBDB)/(XMXA+RADB))-ZMZA*ALOG((XMXB+RBDA)
     *     /(XMXA+RADA))
      IF(XMXB.EQ.0.)TERM2=-XMXA*ALOG((ZMZB+RADB)/(ZMZA+RADA))
      IF(XMXA.EQ.0.)TERM2=XMXB*ALOG((ZMZB+RBDB)/(ZMZA+RBDA))
      IF(XMXA.EQ.0. .OR. XMXB.EQ.0.) GOTO 5
      TERM2=XMXB*ALOG((ZMZB+RBDB)/(ZMZA+RBDA))-XMXA*ALOG((ZMZB+RADB)
     *     /(ZMZA+RADA))
    5 IF(YEM.EQ.0.) GOTO 12
      TERM3=YEM*(ATAN2(XMXB*ZMZB/(YEM*RBDB))-ATAN2(XMXB*ZMZA
     *     /(YEM*RBDA))
```

```
     *      -ATAN2(XMXA*ZMZB/(YEM*RADB))+ATAN2(XMXA*ZMZA/(YEM*RADA)))
            GOTO 9
  12        TERM3=0.
            GOTO 9
   6        TERM1=ZMZB*ALOG((YMYB+RDBB)/(YMYA+RDAB))-ZMZA*ALOG((YMYB+RDBA)
     *      /(YMYA+RDAA))
            IF(YMYB.EQ.0.)TERM2=-YMYA*ALOG((ZMZB+RDAB)/(ZMZA+RDAA))
            IF(YMYA.EQ.0.)TERM2=YMYB*ALOG((ZMZB+RDBB)/(ZMZA+RDBA))
            IF(YMYA.EQ.0. .OR. YMYB.EQ.0.) GOTO 7
            TERM2=YMYB*ALOG((ZMZB+RDBB)/(ZMZA+RDBA))-YMYA*ALOG((ZMZB+RDAB)
     *      /(ZMZA+RDAA))
   7        IF(XEM.EQ.0.) GOTO 14
            TERM3=XEM*(ATAN2(ZMZB*YMYB/(XEM*RDBB))-ATAN2(ZMZB*YMYA
     *      /(XEM*RDAB))
     *      -ATAN2(ZMZA*YMYB/(XEM*RDBA))+ATAN2(ZMZA*YMYA/(XEM*RDAA)))
            GOTO 9
  14        TERM3=0.
            GOTO 9
   8        TERM1=YMYB*ALOG((XMXB+RBBD)/(XMXA+RABD))-YMYA*ALOG((XMXB+RBAD)
     *      /(XMXA+RAAD))
            TERM2=XMXB*ALOG((YMYB+RBBD)/(YMYA+RBAD))-XMXA*ALOG((YMYB+RABD)
     *      /(YMYA+RAAD))
            TERM3=ZEM*(ATAN2(XMXB*YMYB/(ZEM*RBBD))-ATAN2(XMXB*YMYA
     *      /(ZEM*RBAD))
     *      -ATAN2(XMXA*YMYB/(ZEM*RABD))+ATAN2(XMXA*YMYA/(ZEM*RAAD)))
   9        WHOLE=-WHOLE-(TERM1+TERM2-TERM3)
  16        FORMAT(///8X,I3/,3F8.1/,3(2F8.1/),3F8.1,//2(2F8.1))
            XMM=XNN
            YMM=YNN
            IF(TYPEMN.EQ.1) WHOLE=-WHOLE
  11        CONTINUE
            RETURN
            END
C
            SUBROUTINE SCAT(XM,YM,XN,YN,Z,J0,H1,BETA,TYPEMN,RHO1,RHO2,SPMN)
C           This subroutine computes the reflected part of the anomalous
C           potential.
            INTEGER TYPEMN
            REAL LAMDA,K1,MPOT,NPOT
C            REAL T(61),J0(61)
            REAL T(120),J0(120)
            EXTERNAL SEXP
            K1=(RHO2-RHO1)/(RHO2+RHO1)
            MM=30
            MP=30
C            MN=61
            MN=120
            SHIFT=0.00424
            DS=ALOG(10.)/10.
            AH=-8.38850000000
            SH=0.0904226468670
            DO 50 L=1,TYPEMN
            REM=SQRT(XM*XM+YM*YM)+1.E-6
C           WRITE(1,16)XM,XN,YM,YN,REM
  16        FORMAT(//// 8X,3(2F8.1/))
            DO 456 I=1,MN
            RT1= (AH + (I-1)*SH)
            RT2= (10.0)**RT1
CC            RLAMB(I)= (1./R)*RT2
            LAMDA=(1./REM)*RT2
C            M=-MP
```

```
C    8     EP=REM*SEXP(FLOAT(M)*DS-SHIFT)
C          LAMDA=1./EP
C          T(M+MP+1)=(SEXP(-LAMDA*Z)+K1*SEXP(-LAMDA*(Z+2.*H1)))/
C       *   (1.-K1*SEXP(-2.*LAMDA*H1))
           SIGMA0=1./RHO1
           SIGMA2=1./RHO2
           BETL=SQRT((BETA*BETA)+(4.*LAMDA*LAMDA))
           ALPHA1=(-BETA+BETL)/2.
           ALPHA2=(-BETA-BETL)/2.
C          EXDL=SEXP(LAMDA*H1)
           EXDB=SEXP(BETA*H1)
           EXDA1M=SEXP(-ALPHA1*H1)
           EXDA2=SEXP(ALPHA2*H1)
C          EXZ=SEXP(-LAMDA*Z)
C          EXDA1M=SEXP(-ALPHA1*H1)
           EXH=SEXP(-LAMDA*Z)
           EXHD=SEXP(-LAMDA*(Z-H1))
           RTERM1=(1.+K1)*EXDB*ALPHA1*ALPHA2*(1.-EXDA2*EXDA1M)
           RTERM2=LAMDA*(1.-K1)*(ALPHA2-(ALPHA1*EXDA2*EXDA1M))
           RTERM3=RTERM1+RTERM2
           RTERM4=2.*(ALPHA2-ALPHA1)*LAMDA*EXHD*EXDA1M
C          I=M+MP+1
           T(I)=(RTERM4-(EXH*RTERM3))/RTERM3
C          M=M+1
C          IF(M.LE.MM) GOTO 8
 456       CONTINUE
C          K=62
           POT=0.
           DO 9 J=1,MN
C    9      POT=POT+T(K-J)*J0(J)
     9     POT=POT+T(J)*J0(J)
           IF(L.EQ.2) GOTO 50
           MPOT=POT/REM
           XM=XN
           YM=YN
   50      CONTINUE
           NPOT=POT/REM
           IF(TYPEMN.EQ.1) NPOT=0.
           SPMN=MPOT-NPOT
C          WRITE(1,16) MPOT,NPOT,SPMN
           RETURN
           END
C
C                                                  *************** APPRES
C
           SUBROUTINE APPRSCH (NXELEC, NYELEC, XELEC, JY, IS, IR, AM1, VS,
      $                        SEP, OM, NCC)
C
           REAL VS(2002,2002), APPRESS(2002,2002) , XELEC(122)
C
           CURRNT = 1.
           PI2 = 2. * 3.14159265
           PI4 = 4. * 3.14159265
C
           WRITE(1,*)'SCHLUMBERGER ARRAY'
           WRITE(3,*)'SCHLUMBERGER ARRAY'
C          WRITE(3,*) ' AB/2 (m) and APPARENT RESISTIVITY (ohm-m)'
           WRITE(1,65)
           WRITE(3,64)
 64        FORMAT(1X,44HAB/2, Centpar & APPARENT RESISTIVITY (ohm-m)/)
C          WRITE(3,65)
```

```
 65     FORMAT(1X,46HS1, S2, R1, R2, PS1, PS2, PR1, PR2, AB/2 (m) &,
     $  1X,28HAPPARENT RESISTIVITY (ohm-m)/)
C
C        M=40
        SIM=SEP/OM
        IM=INT(SIM)
C        DO 45 IR1=10,(NXELEC-11)
C        DO 45 IR1=IX,NCC,IX
        DO 45 IR1=IM,(NCC-IM-1),IM
        IR2=IR1+2
        IN=IM-1
        IS1=IR1-IN
        IS2=IR2+IN
        IF((IS1 .LT. 1) .OR. (IS2 .GT. NCC)) GO TO 45
        HAM = ABS(IS1-IR1)
        HAN = ABS(IS1-IR2)
        HBM = ABS(IS2-IR1)
        HBN = ABS(IS2-IR2)
        HAB = ABS(IS2-IS1)
        AM = HAM * OM
        AN = HAN * OM
        BM = HBM * OM
        BN = HBN * OM
        DAB = HAB * OM
        HL = DAB/2.
        GEOFAC = PI2 / (1./AM - 1./BM - 1./AN + 1./BN)
C
        DELTAV = VS(IS1,IR1) - VS(IS1,IR2) - VS(IS2,IR1)
     $           + VS(IS2,IR2)
        APPRESS(IS1,IR1) = GEOFAC * DELTAV / CURRNT
        PIR1=((IR1-1)*OM)+XELEC(1)
        PIR2=((IR2-1)*OM)+XELEC(1)
        PMMNS = (PIR1+PIR2)/2
C
C
        IF(HL .LE. 50.) THEN
        WRITE (3, 853) HL, PMMNS, APPRESS(IS1,IR1)
        ELSE
        ENDIF
 853    FORMAT(2F8.2,F15.5)
C
 45     CONTINUE
        RETURN
        END
C
C        SUBROUTINE APPRDEQ (NXELEC, NYELEC, XELEC, JY, YELEC, IS,
C     $     IR, AM1, VP1, VP2, VQ1, VQ2, APPRSCH, APPRDEQ)
        SUBROUTINE APPRDEQ (XELEC, YELEC, AM1, VP, VQ, NXELEC,
     $   NYELEC, JY, IS, IR, JN, SEP, OM, NCC)
C
        REAL VP(2002,2002), VQ(2002,2002),
     $  APPRESE(2002,2002), XELEC(122), YELEC(40)
        CURRNT = 1.
        PI2 = 2. * 3.14159265
        PI4 = 4. * 3.14159265
        WRITE(1,*)'EQUATORIAL DIPOLE-DIPOLE ARRAY'
        WRITE(3,*)'EQUATORIAL DIPOLE-DIPOLE ARRAY'
C        WRITE(1,*) ' AB/2 (m) and APPARENT RESISTIVITY (ohm-m)'
C        WRITE(3,*) ' AB/2 (m) and APPARENT RESISTIVITY (ohm-m)'
        WRITE(1,65)
        WRITE(3,64)
```

```
 64     FORMAT(1X,46HOO', Pos. of O' & APPARENT RESISTIVITY (ohm-m)/)
C        WRITE(3,65)
 65     FORMAT(1X,43H AB=MN, Pos. O, Pos. O', Pos. O", OO' (m) &,
     $  1X,28HAPPARENT RESISTIVITY (ohm-m)/)
C
C
        IF (JY .EQ. (1+JN*3)) THEN
        JY1 = JY + 1
        ELSE
        ENDIF
        IF (JY .EQ. (JN*3)) THEN
        JY1 = JY - 1
        ELSE
        ENDIF
C
        SSRR=ABS(YELEC(JY)-YELEC(JY1))
        IF(SSRR .EQ. 0.) SSRR=SEP
        SIM=SEP/OM
        IM=INT(SEP/OM)
        DO 45 IS1=IM,(NCC-IM-1),IM
        IS2=IS1+2
        IR1=IS1
        IR2=IR1+2
        HAM = ABS(IR2-IR1)
C
        RRAM = HAM * OM
        AM = SSRR
        BN = AM
        AN = SQRT(AM*AM+RRAM*RRAM)
        BM = AN
        XIS1 = ((IS1-1)*OM)+XELEC(1)
        XIR1 = ((IR1-1)*OM)+XELEC(1)
        XIS2 = ((IS2-1)*OM)+XELEC(1)
        XIR2 = ((IR2-1)*OM)+XELEC(1)
        GEOFAC = PI2 / (1./AM - 1./BM - 1./AN + 1./BN)
        IF(IS2 .GT. IR1) THEN
        VP(IS2,IR1)=VQ(IR1,IS2)
        ELSE
        ENDIF
C
        DELTAV = VP(IS1,IR1) - VP(IS1,IR2)
     $           - VP(IS2,IR1) + VP(IS2,IR2)
C
        APPRESE(IS1,IR2) = GEOFAC * DELTAV / CURRNT
C
        PMRR = (XIR1+XIR2)/2.
        WRITE (3, 853) AM, PMRR, APPRESE(IS1,IR2)
 853    FORMAT(2F8.2,F15.5)
C
 45     CONTINUE
        RETURN
        END
C
C
        SUBROUTINE APPRSCD (NXELEC, NYELEC, XELEC, JY, YELEC, IS,
     $    IR, AM1, VS, VP, VQ, APPRSCH, APPRDEQ, JN, SEP,OM, NCC)
C
        REAL VS(2002,2002), VP(2002,2002),
     $  VQ(2002,2002), APPRESS(2002,2002),
     $  APPRESE(2002,2002) , DIFSCED(2002,2002) , XELEC(122),
     $  YELEC(40)
```

```
C        WRITE(3,*) ' PR1 and apparent resistivities difference'
         CURRNT = 1.
         PI2 = 2. * 3.14159265
         PI4 = 4. * 3.14159265
         WRITE(1,35)
C        WRITE(3,35)
         WRITE(3,34)
 34      FORMAT(1X,49HAB/2=OO', Midpoint & APP. RES. DIFFERENCE (ohm-m)/)
 35      FORMAT(1X,49HS1,S2, R1,R2, PS1,PS2, PR1,PR2, PO', AB/2=OO' (m),
     $   1X,30H& APP. RES. DIFFERENCE (ohm-m)/)
         IF (JY .EQ. (1+JN*3)) THEN
         JY1 = JY + 1
         ELSE
         ENDIF
         IF (JY .EQ. (JN*3)) THEN
         JY1 = JY - 1
         ELSE
         ENDIF
C
         SSRR=ABS(YELEC(JY)-YELEC(JY1))
         IF(SSRR .EQ. 0.) SSRR=SEP
         JX=NCC-1
         IX=JX/2
         SIM=SEP/OM
         IM=INT(SIM)
         DO 45 IR1=IM,(NCC-IM-1),IM
         IR2=IR1+2
         VAL=SSRR/OM
         IVAL=INT(VAL)
         IN=IVAL-1
         IS1=IR1-IN
         IS2=IR2+IN
C
         IF((IS1 .LT. 1) .OR. (IS2 .GT. NCC)) GO TO 45
C
         HAM = ABS(IS1-IR1)
         HAN = ABS(IS1-IR2)
         HBM = ABS(IS2-IR1)
         HBN = ABS(IS2-IR2)
         HAB = ABS(IS2-IS1)
         AM = HAM * OM
         AN = HAN * OM
         BM = HBM * OM
         BN = HBN * OM
         DAB = HAB * OM
         HL = DAB/2.
C
         HRS = SSRR
         RRD = ABS(IR2-IR1)
         RRDF = RRD * OM
         RSDI = HRS
         AM2 = RSDI
         BN2 = AM2
         AN2 = SQRT(RSDI*RSDI+RRDF*RRDF)
         BM2 = AN2
         XIS1 = ((IS1-1)*OM)+XELEC(1)
         XIS2 = ((IS2-1)*OM)+XELEC(1)
         XIR1 = ((IR1-1)*OM)+XELEC(1)
         XIR2 = ((IR2-1)*OM)+XELEC(1)
         PMRR = (XIR1+XIR2)/2.
         GEOFAC2 = PI2 / (1./AM2 - 1./BM2 - 1./AN2 + 1./BN2)
```

```
      IF(IR2 .GT. IR1) THEN
      VP(IR2,IR1)=VQ(IR1,IR2)
      ELSE
      ENDIF
C
      DELTAV2 = VP(IR1,IR1) - VP(IR1,IR2)
     $            - VP(IR2,IR1) + VP(IR2,IR2)
C
      APPRESE(IR1,IR2) = GEOFAC2 * DELTAV2 / CURRNT
      GEOFAC = PI2 / (1./AM - 1./BM - 1./AN + 1./BN)
      DELTAV = VS(IS1,IR1) - VS(IS1,IR2) - VS(IS2,IR1)
     $           + VS(IS2,IR2)
      APPRESS(IS1,IR1) = GEOFAC * DELTAV / CURRNT
C
      DIFSCED(IS1,IR2) = APPRESE(IR1,IR2)
     $                           - APPRESS(IS1,IR1)
      WRITE (3, 853) RSDI, PMRR, DIFSCED(IS1,IR2)
C
  853 FORMAT(2F8.2,F15.5)
C
  45  CONTINUE
C
      RETURN
      END
C
      REAL FUNCTION SEXP(W)
      SEXP=0.
C      IF(W.LT.-30.) RETURN
      IF(W.LT.-300.) RETURN
      SEXP=EXP(W)
      RETURN
      END
C
      REAL FUNCTION ATAN2(Z)
      ATAN2=ATAN(Z)
      IF(Z.GE.0.) RETURN
      ATAN2=-ATAN(-Z)
      RETURN
      END
```